

Nanotechnology for Tissue Engineering Applications

Guest Editors: Xiaojun Yu, Junping Wang, Yanan Du,
Zuwei Ma, and Wei He





Nanotechnology for Tissue Engineering Applications

Nanotechnology for Tissue Engineering Applications

Guest Editors: Xiaojun Yu, Junping Wang, Yanan Du,
Zuwei Ma, and Wei He



Copyright © 2011 Hindawi Publishing Corporation. All rights reserved.

This is a special issue published in volume 2011 of “Journal of Nanomaterials.” All articles are open access articles distributed under the Creative Commons Attribution License, which permits unrestricted use, distribution, and reproduction in any medium, provided the original work is properly cited.

Editorial Board

Katerina Aifantis, Greece
Nageh K. Allam, USA
Margarida Amaral, Portugal
Xuedong Bai, China
Enrico Bergamaschi, Italy
Theodorian Borca-Tasciuc, USA
C. Jeffrey Brinker, USA
Christian Brosseau, France
Xuebo Cao, China
Sang-Hee Cho, Republic of Korea
Shafiul Chowdhury, USA
Cui ChunXiang, China
Miguel A. Correa-Duarte, Spain
Shadi A. Dayeh, USA
Ali Eftekhari, USA
Claude Estournes, France
Alan Fuchs, USA Lian Gao, China
Russell E. Gorga, USA
Hongchen Chen Gu, China
Mustafa O. Guler, Turkey
John Zhanhu Guo, USA
Smrati Gupta, Germany
Michael Harris, USA
Zhongkui Hong, USA
Michael Z. Hu, USA
David Hui, USA
Y.-K. Jeong, Republic of Korea
Sheng-Rui Jian, Taiwan
Wanqin Jin, China
Rakesh K. Joshi, India

Zhenhui Kang, China
Fathallah Karimzadeh, Iran
Do Kyung Kim, Republic of Korea
Kin Tak Lau, Australia
Burtrand Lee, USA
Benxia Li, China
Jun Li, Singapore
Shijun Liao, China
Gong Ru Lin, Taiwan
J.-Y. Liu, USA Jun Liu, USA
Tianxi Liu, China
Songwei Lu, USA
Daniel Lu, China Jue Lu, USA
Ed Ma, USA Gaurav Mago, USA
Sanjay R. Mathur, Germany
A. McCormick, USA
Vikas Mittal, UAE
Weihai Ni, Germany
Sherine Obare, USA
Edward Andrew Payzant, USA
Kui-Qing Peng, China
Anukorn Phuruangrat, Thailand
Ugur Serincan, Turkey
Huaiyu Shao, Japan
Donglu Shi, USA
Suprakas Sinha Ray, South Africa
Vladimir Sivakov, Germany
Marinella Striccoli, Italy
Bohua Sun, South Africa
Saikat Talapatra, USA

Nairong Tao, China
Titipun Thongtem, Thailand
Somchai Thongtem, Thailand
Valeri P. Tolstoy, Russia
Tsung-Yen Tsai, Taiwan
Takuya Tsuzuki, Australia
Raquel Verdejo, Spain
Mat U. Wahit, Malaysia
Shiren Wang, USA
Yong Wang, USA
Cheng Wang, China
Zhenbo Wang, China
Jinquan Wei, China
Ching Ping Wong, USA
Xingcai Wu, China
Guodong Xia, Hong Kong
Zhi Li Xiao, USA Ping Xiao, UK
Shuangxi Xing, China
Yangchuan Xing, USA
N. Xu, China
Doron Yadlovker, Israel
Ying-Kui Yang, China
Khaled Youssef, USA
Kui Yu, Canada
Haibo Zeng, China
Tianyou Zhai, Japan
Renyun Zhang, Sweden
Yanbao Zhao, China
Lianxi Zheng, Singapore
Chunyi Zhi, Japan

Contents

Nanotechnology for Tissue Engineering Applications, Xiaojun Yu, Junping Wang, Yanan Du, Zuwei Ma, and Wei He

Volume 2011, Article ID 506574, 2 pages

Fabrication of Biodegradable Polyester Nanocomposites by Electrospinning for Tissue Engineering, Zhi-Cai Xing, Seung-Jin Han, Yong-Suk Shin, and Inn-Kyu Kang

Volume 2011, Article ID 929378, 18 pages

Electrospun Collagen: A Tissue Engineering Scaffold with Unique Functional Properties in a Wide Variety of Applications, Balendu Shekhar Jha, Chantal E. Ayres, James R. Bowman, Todd A. Telemeco, Scott A. Sell, Gary L. Bowlin, and David G. Simpson

Volume 2011, Article ID 348268, 15 pages

Quantitatively Controlled Fabrication of Uniaxially Aligned Nanofibrous Scaffold for Cell Adhesion, Suk Hee Park, Jung Woo Hong, Jennifer Hyunjong Shin, and Dong-Yol Yang

Volume 2011, Article ID 201969, 9 pages

Electrospinning of Poly(ethylene-co-vinyl alcohol) Nanofibres Encapsulated with Ag Nanoparticles for Skin Wound Healing, Chao Xu, Feng Xu, Bin Wang, and TianJian Lu

Volume 2011, Article ID 201834, 7 pages

Dependence of Spreading and Differentiation of Mesenchymal Stem Cells on Micropatterned Surface Area, Wei Song, Naoki Kawazoe, and Guoping Chen

Volume 2011, Article ID 265251, 9 pages

Surface Modification of Titanium with Heparin-Chitosan Multilayers via Layer-by-Layer Self-Assembly Technique, Yao Shu, Guomin Ou, Li Wang, Jingcai Zou, and Quanli Li

Volume 2011, Article ID 423686, 8 pages

Particle Size Control of $\text{Y}_2\text{O}_3:\text{Eu}^{3+}$ Prepared via a Coconut Water-Assisted Sol-Gel Method,

Maria de Andrade Gomes, Mário Ernesto Giroldo Valerio, and Zélia Soares Macedo

Volume 2011, Article ID 469685, 6 pages

BN Nanoparticles/ Si_3N_4 Wave-Transparent Composites with High Strength and Low Dielectric Constant, Dongliang Zhao, Yujun Zhang, Hongyu Gong, Baoxin Zhu, and Xiaoyu Zhang

Volume 2011, Article ID 246847, 5 pages

Analysis of Carbon Nanotubes on the Mechanical Properties at Atomic Scale, Xiaowen Lei, Toshiaki Natsuki, Jinxing Shi, and Qing-Qing Ni

Volume 2011, Article ID 805313, 10 pages

Some Observations on Carbon Nanotubes Susceptibility to Cell Phagocytosis, Aneta Fraczek-Szczypta, Elzbieta Menaszek, and Stanislaw Blazewicz

Volume 2011, Article ID 473516, 8 pages

Enhanced Photocatalytic Activity for Degradation of Methyl Orange over Silica-Titania, Yaping Guo, Shaogui Yang, Xuefei Zhou, Chunmian Lin, Yajun Wang, and Weifeng Zhang

Volume 2011, Article ID 296953, 9 pages

Editorial

Nanotechnology for Tissue Engineering Applications

Xiaojun Yu,¹ Junping Wang,² Yanan Du,³ Zuwei Ma,⁴ and Wei He⁵

¹ Department of Chemistry, Chemical Biology and Biomedical Engineering, Stevens Institute of Technology, Hoboken, NJ 07030, USA

² Xylos Corporation, Langhorne, PA 19047, USA

³ Department of Biomedical Engineering, School of Medicine, Tsinghua University, Beijing 100084, China

⁴ RainDance Technologies Inc., Lexington, MA 02421, USA

⁵ McGowan Institute for Regenerative Medicine, University of Pittsburgh, Pittsburgh, PA 15219, USA

Correspondence should be addressed to Xiaojun Yu, xyu@stevens.edu

Received 26 May 2011; Accepted 26 May 2011

Copyright © 2011 Xiaojun Yu et al. This is an open access article distributed under the Creative Commons Attribution License, which permits unrestricted use, distribution, and reproduction in any medium, provided the original work is properly cited.

Due to the tissue and organ shortage, tissue engineering strategies combining engineering principles and methods and biological sciences in creating implantable tissues have been viewed as the most promising technologies for regenerating damaged tissues and organs. As native tissues or organs are composed of proteins within nanoscale and cells directly interact with nanostructured extracellular matrices (ECM), nanobiomaterials such as nanofibers, nanotubes, nanoparticles and other nanofabricated devices with smaller than 100 nm in at least one dimension are capable of contributing to cell growth and tissue regeneration.

The aim of this special issue is to demonstrate the latest achievement of nanotechnology and its development in tissue engineering field. The eleven research articles comprising this special issue cover topics including the fabrication, characterization, and application of nanobiomaterials. Research articles on biomaterial surface technology, cell-biomaterials interaction and nanobiomaterials properties are also included in this issue.

Electrospinning is a well-established technique aiming at producing ultrafine fibers by electrically charging a suspended droplet of polymer melt or solution. There are various kinds of materials that can be electrospun into nanofibrous structures, which have promising applications in tissue engineering. The first four papers of this special issue discussed the electrospinning technique for tissue engineering application. The first paper “*Fabrication of biodegradable polyester nanocomposites by electrospinning for tissue engineering*” reviewed several biodegradable polyester-based nanocomposites for tissue engineering applications. The second paper “*Electrospun collagen: a tissue engineering scaffold with unique functional properties in a wide variety*

of applications” specifically focused on the collagen-based electrospun nanomaterials with variable applications. The third paper “*Quantitatively controlled fabrication of uniaxially aligned nanofibrous scaffold for cell adhesion*” developed uniaxially aligned nanofibers via quantitatively controlled fabrication method. The fourth paper “*Electrospinning of poly (ethylene-co-vinyl alcohol) nanofibres encapsulated with Ag nanoparticles for skin wound healing*” achieved fabrication of an anti-inflammatory nanofibrous scaffold with the encapsulation of Ag nanoparticles in poly (ethylene-co-vinyl alcohol) nanofibers.

The following two papers are related to surface morphology and micropatterning technology. Specifically, the fifth paper “*Dependence of spreading and differentiation of mesenchymal stem cells on micropatterned surface area*” discussed the effect of micropatterning technology on the differentiation of Mesenchymal stem cells (MSCs). The sixth paper “*Surface modification of titanium with heparin-chitosan multilayers via layer-by-layer self-assembly technique*” showed a surface modification method via chitosan-heparin layer-by-layer self-assembly technique.

In the seventh paper, “*Particle size control of 1/2O₃: Eu³⁺ prepared via a coconut water-assisted sol-gel method*,” a type of Eu³⁺-doped Y₂O₃ nanoparticle was produced through protein sol-gel technique and the adjustment of pH was tested in order to control the particle size of the powders. In the eighth paper, “*BN nanoparticles/Si₃N₄ wave-transparent composites with high strength and low dielectric constant*,” the addition of the BNnp/Si₃N₄ nanoparticles improved the dielectric properties of BNnp/Si₃N₄ composites and decreased the mechanical properties. The ninth and tenth papers “*Analysis of carbon nanotubes on the mechanical*

properties at atomic scale” and “*Some observations on carbon nanotubes susceptibility to cell phagocytosis*” discussed the carbon nanotubes in terms of their mechanical properties and their susceptibility to cell phagocytosis. The eleventh paper “*Enhanced photocatalytic activity for degradation of methyl orange over silica-titania*” reported a method of constructing silica-modified titania (SMT) powders with enhanced photocatalytic activity.

Acknowledgments

The editors appreciate all the authors and coauthors of these articles comprising the special issue for their scientific contribution. Moreover, the editors would like to express their thanks to all the reviewers for their effort and dedication. They hope that this special issue will attract a wide range of the readers who are working or will join this challenging and fast-developing field and continuously motivate their research and work.

*Xiaojun Yu
Junping Wang
Yanan Du
Zuwei Ma
Wei He*

Review Article

Fabrication of Biodegradable Polyester Nanocomposites by Electrospinning for Tissue Engineering

Zhi-Cai Xing, Seung-Jin Han, Yong-Suk Shin, and Inn-Kyu Kang

Department of Polymer Science and Engineering, Kyungpook National University, Daegu 702-701, Republic of Korea

Correspondence should be addressed to Inn-Kyu Kang, ikkang@knu.ac.kr

Received 1 October 2010; Accepted 28 January 2011

Academic Editor: Xiaojun Yu

Copyright © 2011 Zhi-Cai Xing et al. This is an open access article distributed under the Creative Commons Attribution License, which permits unrestricted use, distribution, and reproduction in any medium, provided the original work is properly cited.

Recently, nanocomposites have emerged as an efficient strategy to upgrade the structural and functional properties of synthetic polymers. Polyesters have attracted wide attention because of their biodegradability and biocompatibility. A logic consequence has been the introduction of natural extracellular matrix (ECM) molecules, organic or inorganic nanostructures to biodegradable polymers to produce nanocomposites with enhanced properties. Consequently, the improvement of the interfacial adhesion between biodegradable polymers and natural ECM molecules or nanostructures has become the key technique in the fabrication of nanocomposites. Electrospinning has been employed extensively in the design and development of tissue engineering scaffolds to generate nanofibrous substrates of synthetic biodegradable polymers and to simulate the cellular microenvironment. In this paper, several types of biodegradable polyester nanocomposites were prepared by electrospinning, with the aim of being used as tissue engineering scaffolds. The combination of biodegradable nanofibrous polymers and natural ECM molecules or nanostructures opens new paradigms for tissue engineering applications.

1. Introduction

Tissue engineering (TE) is a multidisciplinary field focused on the development and application of knowledge in engineering, life and clinical sciences for the solution of critical medical problems, such as tissue loss and organ failure [1]. It involves the fundamental understanding of structure-function relationships in normal and pathological tissues and the development of biological substitutes that restore, maintain, or improve tissue function [2]. For *in vitro* engineering of living tissues, cultured cells are grown on bioactive degradable scaffolds that provide the physical and chemical cues to guide their proliferation, differentiation, and assembly into three-dimensional structures. One of the most critical issues in TE is the realization of scaffolds with specific physical, mechanical, and biological properties. Scaffolds act as a substrate for cellular growth, proliferation, and support for new tissue formation.

Materials used for TE applications must be designed to stimulate specific cell response at the molecular level. They should elicit specific interactions within cells and thereby direct cell attachment, proliferation, differentiation, and

extracellular matrix production and organization. The selection of biomaterials constitutes a key point for the success of TE practice [3]. The fundamental requirements of the biomaterials used in tissue regeneration are to have biocompatible surfaces and have favorable mechanical properties. Conventional single polymer materials cannot satisfy these requirements. In fact, although various polymeric materials have been available and investigated for TE, no single biodegradable polymer can meet all of these requirements. Therefore, the design and preparation of the multicomponent polymer systems represent a viable strategy in order to develop innovative multifunctional biomaterials. In particular, the introduction of biomolecules or inorganic molecules into biodegradable polymer matrices is effective to obtain composites with specific properties.

Composite materials using synthetic and natural-based materials are increasingly proposed for biomedical applications [4–6]. Natural polymers such as collagen [7], chitosan [8], soy [9], alginate [10], silk [11], or starch [12] have already been proposed in many biomedical applications. The biological environment is prepared to recognize these biopolymers and to interact with them metabolically.

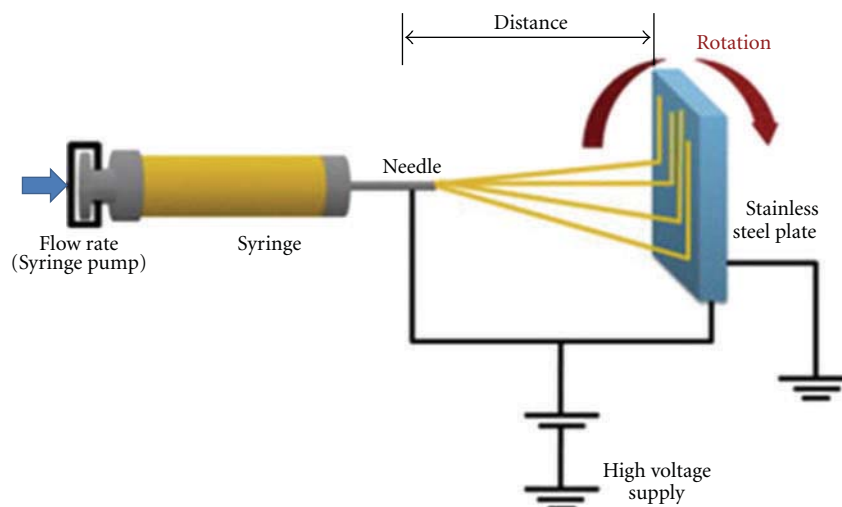


FIGURE 1: Schematic illustration of the electrospinning setup. The mandrel can be rotated at various speeds to achieve different fiber orientations. Reproduced from Biomaterials with permission from Elsevier [21].

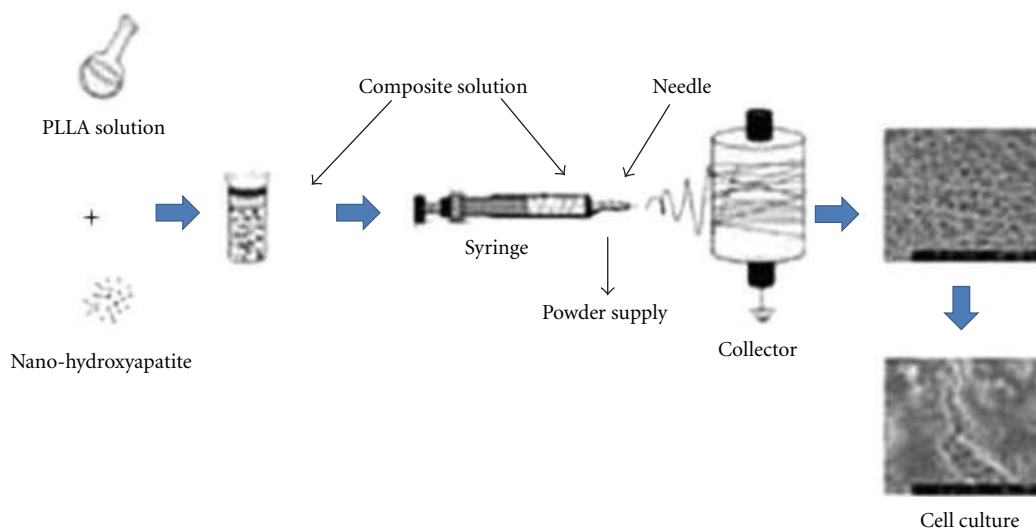


FIGURE 2: Schematic illustration of the preparation of the PLA/HA nanofibrous scaffolds by electrospinning technique. reproduced from Macromolecular Bioscience with permission from Wiley-VCH Verlag GmbH & Co. [51].

Another attractive feature of natural polymers is their ability to be cleaved by naturally occurring enzymes, facilitating degradation by physiological mechanisms [13]. Synthetic biodegradable polymers are already used extensively in the biomaterials field including biodegradable aliphatic polyesters, such as poly(lactic acid) (PLA), poly(glycolic acid) (PGA), poly(caprolactone) (PCL), or poly(hydroxyl butyrate) (PHB) and its copolymers. These biodegradable materials have already been shown to have excellent biological performance both *in vitro* and *in vivo* for bone and for cartilage tissue engineering applications. Most synthetic polymers are degraded via hydrolysis. The polyester bonds of synthetic polymers are hydrolysed in nontoxic natural metabolites and are eliminated from the body by the normal physiological processes [14]. Therefore, composite materials

using synthetic and natural-based polymer materials are increasingly being developed and designed to improve their biological performance [4, 6].

Electrospinning has been explored as an efficient process for obtaining nanofibers with diameters in the sub-micrometer range [15]. The interesting properties of electrospun fibers include increased surface-area-to-volume ratio as a consequence of the diameter, and the high interconnectivity and porosity of the nanofiber scaffolds at the micrometer length scale [16]. Another inherent feature of the electrospun nanofibers is their ability to mimic the extracellular matrix (ECM) of a variety of tissues, which can create a more favorable microenvironment for the cells [11]. Thus, their use in tissue/organ repair and regeneration as biocompatible and biodegradable medical implant devices

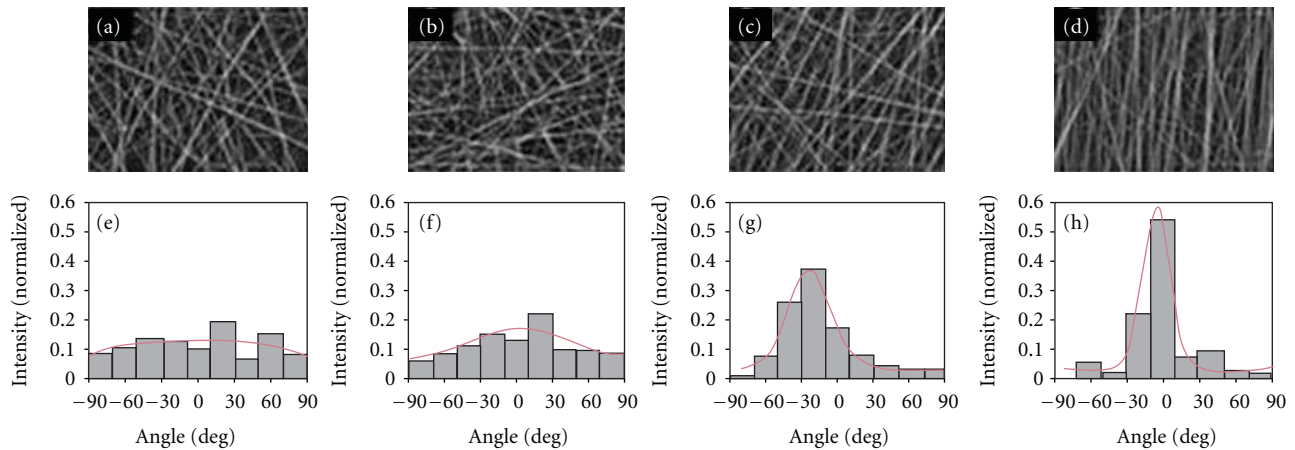


FIGURE 3: Fiber angles for the different rates of rotation: (a)–(d) SEM images of electrospun PCL/collagen nanofibers ($\times 4.0$ k magnification) and (e)–(h) normalized histograms of fiber angle, (a), (e) static, (b), (f) 800 rpm, (c), (g) 1500 rpm, and (d), (h) 2350 rpm. Reproduced from Biomaterials with permission from Elsevier [21].

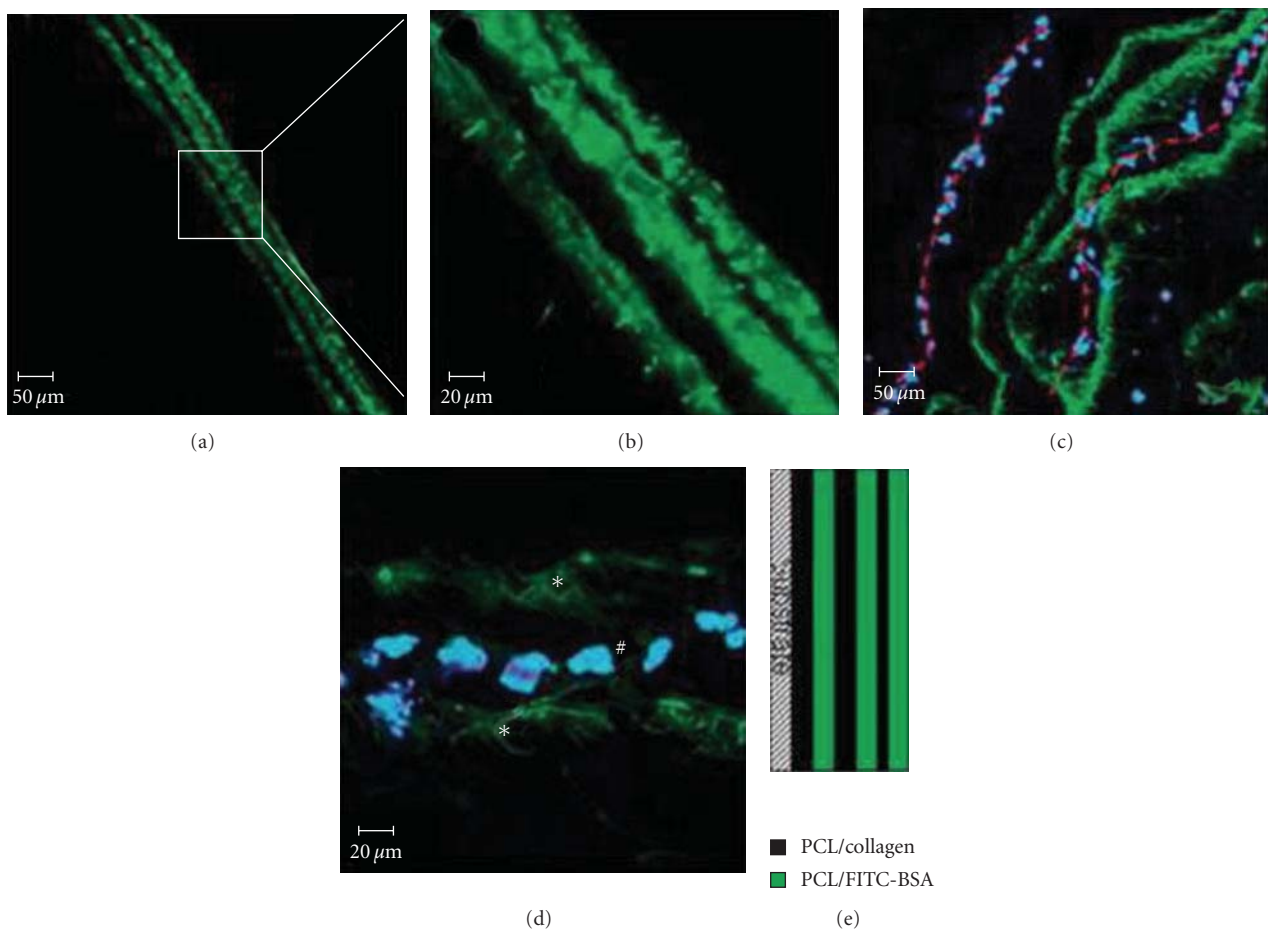
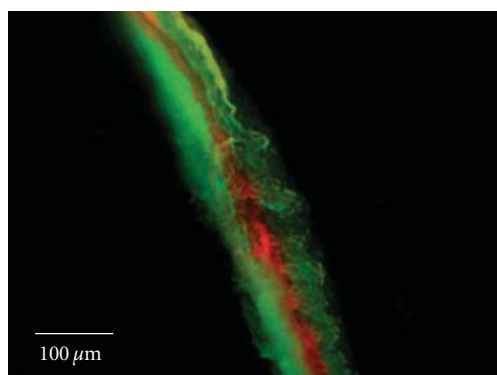


FIGURE 4: Fluorescence images of transverse sections of the nanofibrous structure. (a) and (b) Multifunctional scaffolds prepared by sequentially electrospinning of solutions as designated. (b) High magnification highlighting the clear layers. (c) Cell cultured in multifunctional scaffolds composed of PCL/collagen fibrous layer (outlined by red broken line) and PCL/BSA-FITC (green). High magnification (d) clearly showed cells attached onto PCL/collagen layers (#), but not onto PCL/BSA-FITC (*). Cell nuclei stained blue with DAPI. Scale bar: (a) and (c), 50 μm ; (b), and (d), 20 μm . Reproduced from Journal of Experimental Nanoscience with permission from Taylor & Francis [20].



■ PCL/BSA-TRITC
■ PCL/BSA-FITC

FIGURE 5: Fluorescence images of transverse sections of the three-layer nanofibrous scaffold. Red: PCL/BSA-TRITC. Green: PCL/BSA-FITC. Reproduced from Journal of Experimental Nanoscience with permission from Taylor & Francis [20].

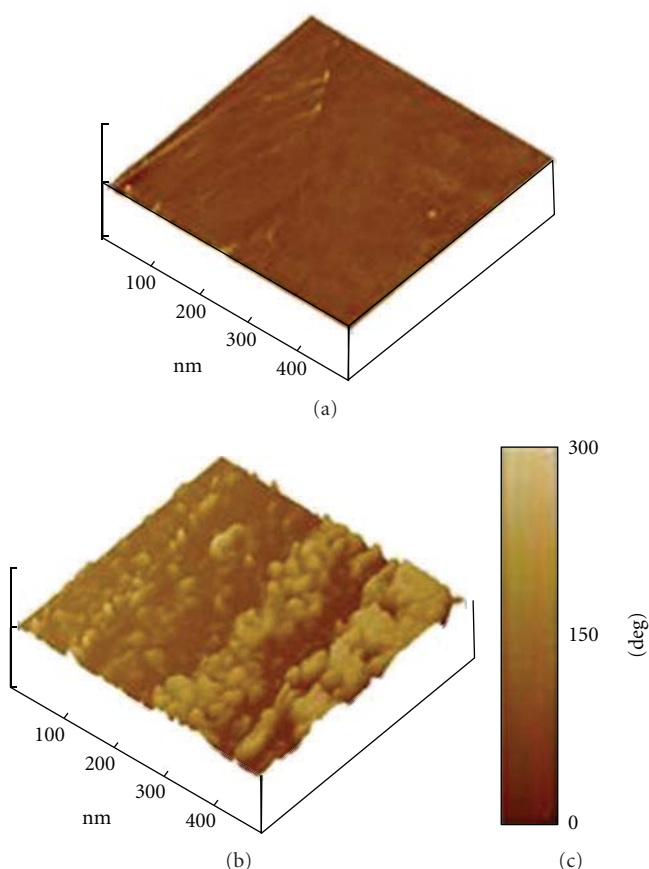


FIGURE 6: AFM images represented by phase mode: (a) PHBV fiber (b) PHBV/gelatin fiber. Reproduced from Journal of Materials Science: Materials in Medicine with permission from Springer [32].

has been suggested by many authors [17–19]. The nanoscale size of the biodegradable fibers may also offer advantages in inducing a specific kind of degradation.

Many review papers on polymer nanofibers by electrospinning and their applications in nanocomposites have been published. Huang et al. [20] summarized the processing conditions for electrosponing of ultrafine fibers and discussed the technology limitations, research challenges, and future trends. Yoo et al. [21] reviewed that the surfaces of nanofibrous meshes can be modified by plasma treatment, wet chemical method, surface graft polymerization, and co-electrospinning in order to obtain high functionalities of electrospun nanofibers, concluded that surface-engineered nanofibrous meshes are expected to have high potentials for drug and gene delivery and TE applications. Jang et al. [22] described the electrospun materials targeted for bone regeneration, including polymers, inorganics, and their composited/hybridized compositions, and aimed at employing nanofibrous matrices for drug delivery and tissue engineering by surface functionalization, drug encapsulation and 3D scaffolding technique. Armentano et al. [23] reported on the materials, processing, experimental results, and possible interpretations of those results for polymer matrix nanocomposites. In this paper, a review has been presented on fabrication, characterization, *in vitro* biodegradation and cell-nanocomposite interactions of the biodegradable polyester nanocomposites by electrospinning technique for TE applications.

Recently, many researchers have focused on the developments of biodegradable polyester nanocomposites by electrospinning for TE applications. Yang et al. [24] prepared the PCL solutions (8% w/v) containing different amounts of bovine serum albumin (BSA) with or without collagen and electrospun into nanofibrous scaffolds. They demonstrated the feasibility of producing multiscale scaffolds with diverse functionality and tunable distribution of bioactive molecules (BSA, collagen) across the nanofibrous scaffolds. Choi et al. [25] fabricated the PCL/collagen composite nanofibrous scaffolds by electrospinning and concluded that the scaffolds are biocompatible, biodegradable, easily fabricated, and are able to support cell adhesion, proliferation, and differentiation. Yin et al. [26] proved that PLA/silk fibroin (SF)-gelatin fiber membranes, in particular, the scaffold of PLA/SF-gelatin (50:50), which had both a good toughness and pliability, could provide a good environment for cell growth and proliferation of cells. Spadaccio et al. [27] demonstrated that electrospun poly (L-lactic acid)/hydroxyapatite (PLLA/HA) nanocomposites can induce differentiation of human mesenchymal stem cells (hMSCs) in chondrocyte-like cells that produce proteoglycan-based matrix. Xing et al. [28] prepared the poly (3-hydroxybutyrate-co-3-hydroxyvalerate)/silver (PHBV/Ag) nanocomposites and showed that the PHBV/Ag composites nanofibrous scaffolds inhibited the proliferation of bacteria, whereas the composites did not show *in vitro* cell cytotoxicity.

The aim of this paper is to put in evidence the evolution and potentiality of emergent biodegradable polyester nanocomposite approaches by electrospinning technique for TE applications. Therefore, this paper reviews current research

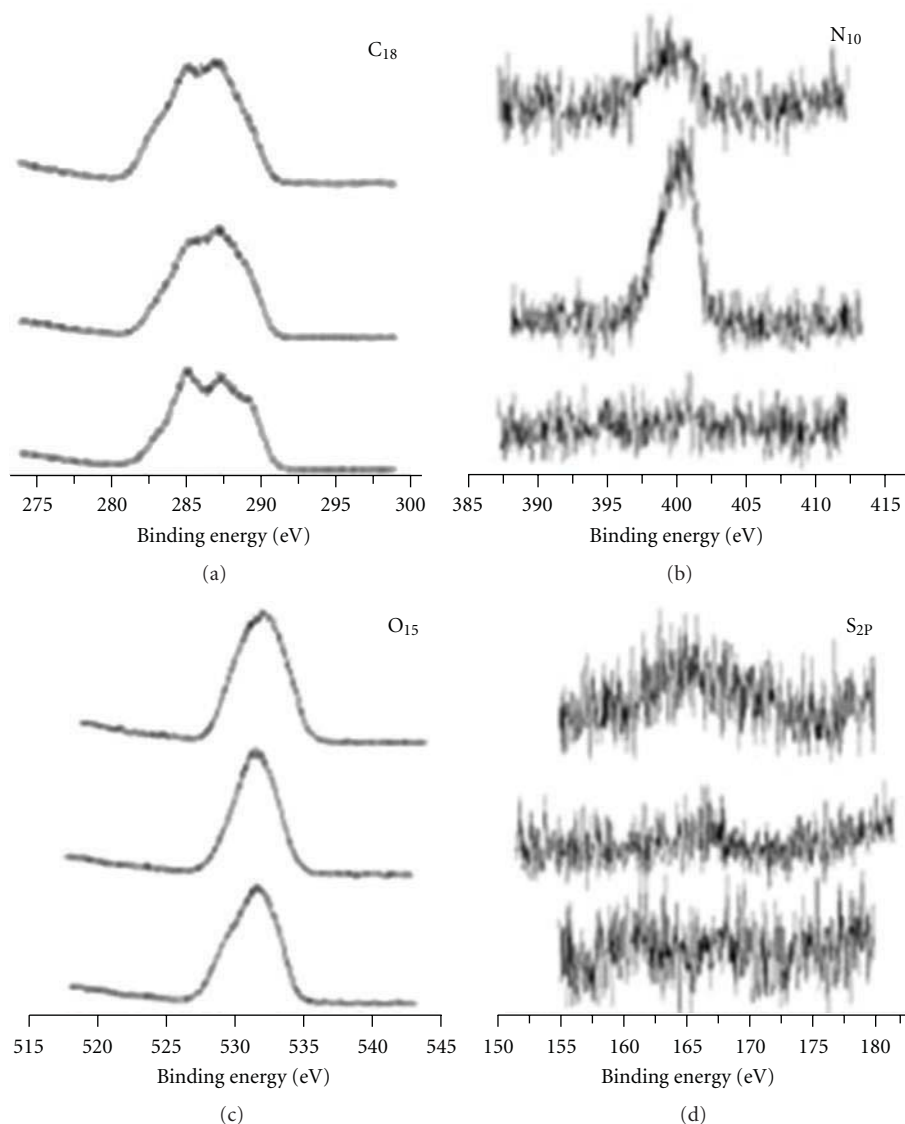


FIGURE 7: Electron spectroscopy for the chemical analysis survey scan spectra of mats (upper trace: PLA/keratin; middle trace: PLA/gelatin; lower trace: PLA). Reproduced from Polymer International with permission from John Wiley and Sons [34].

trends on relevant electrospun polyester nanocomposite materials for TE applications: biodegradable polymers, natural ECM molecules, organic/inorganic nanostructures, matrix-structure interaction, including strategies for fabrication of polyester composite nanofibrous scaffolds. The characterizations of electrospun biodegradable polyester nanocomposites are reviewed. Moreover, the *in vitro* degradation behaviors of nanofibrous scaffold composites for TE applications and cell-nanocomposite interactions are also discussed.

2. Structures for Electrospun Biodegradable Polyester Nanocomposites

In Table 1, the biodegradable polyester nanocomposites by electrospinning technique for tissue engineering were summarized.

2.1. Natural ECM Molecules. Molecules that are naturally occurring in the ECM are ideal materials for cell attachment, proliferation, and differentiation. In addition, substrate interactions between cells and ECM molecules may modulate certain cell functions. Biofunctional nanofibers can be directly fabricated by electrospinning natural ECM molecules alone or a blend of synthetic polymers and natural ECM molecules (Table 1). Nanofibrous composites generally have a benefit from improved physical properties due to polymer components and improved bioactivity due to the natural ECM components [29, 30].

Collagen is a natural ECM component of tissues, such as skin, bone, tendon, ligament, and other connective tissues. Therefore, it has a more native surface which favors cellular attachment as well as being chemotactic to cells when compared to synthetic polymers. It is well known that collagen plays an essential role in providing a scaffold for cellular

TABLE 1: Summary of biodegradable polyester nanocomposites by electrospinning technique for tissue engineering.

Composition		Solvent	Concentration	Perspective applications	Ref.
Main component	Abbreviation				
Natural ECM molecules	Collagen-PCL	1,1,1,3,3,3-hexafluoro-2-propanol (HFIP)	8 wt%,	Tissue engineering,	[24]
			5 wt%,	Skeletal muscle defects,	[25]
			3 wt%	Biomedical application	[31]
	Collagen-PHBV	HFIP	6 wt%	Biological dressing,	[32]
				Tissue engineering	[33]
	Gelatin-PCL	HFIP	6 wt%	Nerve tissue engineering	[34]
	Gelatin-PHBV	HFIP	6 wt%	Biological dressing,	[32]
				Tissue engineering	[35]
	Gelatin-PLA	2,2,2-trifluoroethanol (TFE) HFIP	15 wt%	Tissue regeneration,	[36]
				Tissue engineering	[37]
Hydroxyapatite	HA-PLLA	Dichloromethane	0.2 mg/mL	Cartilage tissue engineering,	[27]
					[40]
		Tetrahydrofuran	0.05 g/mL	Bone tissue regeneration, Tissue engineering	[41]
					[42]
Metal nanoparticles	Ag-PHBV	TFE	6 wt%	Joint arthroplasty	[28]
	Ag-PLGA	HFIP	4 wt%	Tissue engineering	[43]

support and thereby affecting cell attachment, migration, proliferation, differentiation, and survival. Collagen has been used in a variety of TE applications [44, 45]. Composite nanofibrous scaffolds containing collagen and biodegradable polymers such as PCL are easily fabricated by electrospinning when both materials are dissolved in the same solvent [46]. In the nanocomposites containing collagen and PCL, collagen was well dispersed as small spherical aggregates at low concentrations (10 wt%) and much larger irregular shapes at higher concentrations (50 wt%) [31]. Cells cultured on biodegradable nanofibers blended with collagen have shown better attachment, growth, and ECM production than nanofibers without collagen incorporation [32, 33].

Among the natural biopolymers, gelatin can be obtained by denaturing collagen and has almost an identical composition and biological properties as those of the parent collagen. Much attention has been focused on the use of gelatin as a TE material due to its low cost. Gelatin nanofiber composites could be electrospun by the combination of gelatin and other biodegradable polymers in one solution with a variety of fiber diameters. Cells attached and proliferated better on biodegradable nanofibers when they were blended with gelatin [32, 34–36]. Increases in cell attachment and proliferation have been shown to be a function of the ratio of gelatin in the fiber blends [30]. PCL nanofibers blended with gelatin also enhanced nerve differentiation as compared to plain PCL nanofibrous scaffolds [34].

Keratin is a chief component found in hair, skin, fur, wool, horns, and feathers. Reinforced with calcium salts, it is also found in hooves, nails, claws, and beaks [47]. Keratin can be used in a variety of biomedical applications due to its biocompatibility and biodegradability. Keratin containing composite nanofibrous scaffolds can be obtained by electrospinning of keratin and other biodegradable polymers such as PLA [37] in one solution. The keratin containing biodegradable composites could increase the cell adhesion and accelerate the cell proliferation when compared to the biodegradable polymeric nanofibrous scaffolds [37, 38].

Dextran is highly soluble in an aqueous environment, but photocrosslinked methacrylated dextran nanofibers form stable hydrogels in an aqueous environment [48]. Blended PLGA/dextran nanofibers have also been fabricated and have demonstrated favorable TE properties [39].

2.2. Hydroxyapatite. Hydroxyapatite ($\text{Ca}_{10}(\text{PO}_4)_6(\text{OH})_2$) (HA) is the major mineral component (69% wt.) of human hard tissues. It could be natural or synthetic, and it possesses excellent biocompatibility with bones, teeth, skin, and muscles, both *in vitro* and *in vivo*. HA promotes faster bone regeneration, and direct bonding to regenerated bones without intermediate connective tissues. HA has been developed as a bone graft substitute and it is currently used in clinical applications [49–52]. Recent research suggested that better osteoconductivity would be achieved if synthetic

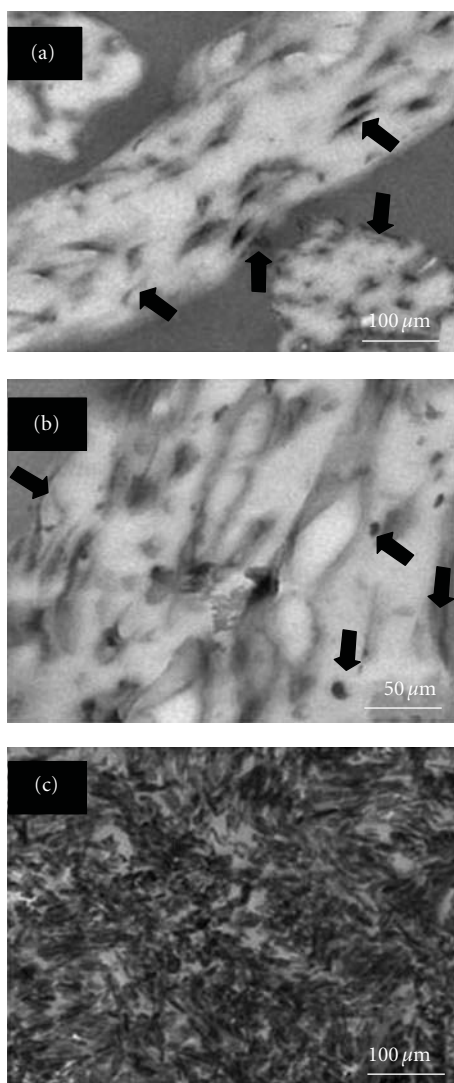


FIGURE 8: TEM micrographs of (a) PLA-HA1, (b) PLA-HA2, and (c) HA nanopowders. The arrows indicate the HA nanoparticles embedded within the PLA/HA composite nanofibers. Reproduced from *Macromolecular bioscience* with permission from Wiley-VCH Verlag GmbH & Co. [51].

HA could resemble bone minerals in composition, size, and morphology [53]. However, due to the brittleness of the HA and the lack of interaction with the polymer, the ceramic nanoparticles may present deleterious effects on the mechanical properties, when added at high loadings.

The incorporation of HA in a polymeric matrix has to overcome processing and dispersion challenges since it is of a great interest to the biomedical community (Table 1). Consequently, a desirable material in TE should be a biodegradable structure that induces and promotes new formation at the required site. Sui et al. [40] fabricated PLLA/HA composite scaffolds via electrospinning and concluded that the cell adhesion and growth on the PLLA/HA composite scaffolds were far better than those on the pure PLLA scaffolds. Jeong et al. [42] prepared the PLA/HA composite nanofibrous

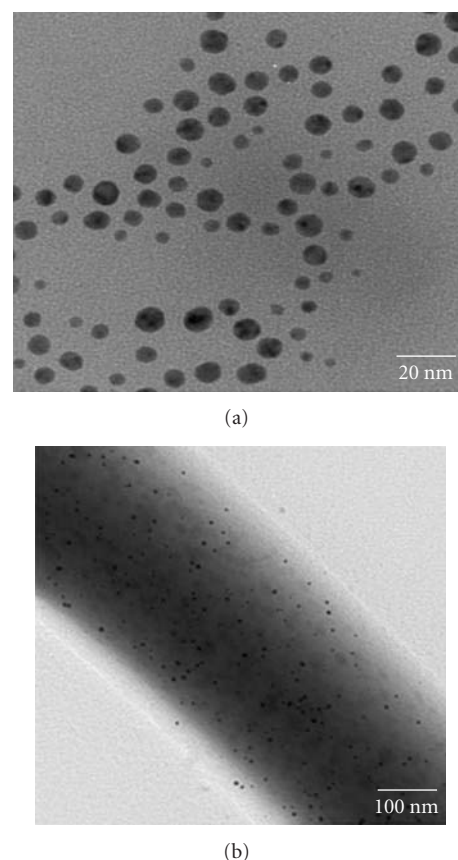


FIGURE 9: TEM images of (a) free silver nanoparticles, and (b) silver nanoparticles distributed to the PHBV nanofibrous scaffolds (PHBV/Ag 1.0). Reproduced from *Biomacromolecules* with permission from American Chemical Society [24].

scaffolds and showed that MC3T3-E1 cells maintained viability and proliferated continuously for up to 21 days, suggesting that the PLA/HA composites are effective scaffolds for the growth of osteoblasts. The electrospun PLLA/HA nanocomposites [27] could be an amenable alternative for cartilage TE in combination with bone marrow hMSCs. This functionalized scaffold would provide both a surrogate of the native ECM and the correct sequence of signals to allow a harmonic ongoing lineage-specific differentiation of multipotent precursor cells.

2.3. Metal Nanoparticles. Biomedical applications of metal nanoparticles have been dominated by the use of nanobioconjugates that started in 1971 after the discovery of immunogold labeling by Faulk and Taylor [54]. Currently metal-based nanoconjugates are used in various biomedical applications such as drug delivery (vehicle for delivering drugs, proteins, peptides, DNAs, etc.), detection, diagnosis, and therapy. However biological properties of metal nanoparticles have remained largely unexplored. Therefore, in this paper the novel biological properties and applications of silver nanoparticles in the nanofibrous polyester composites are discussed (Table 1).

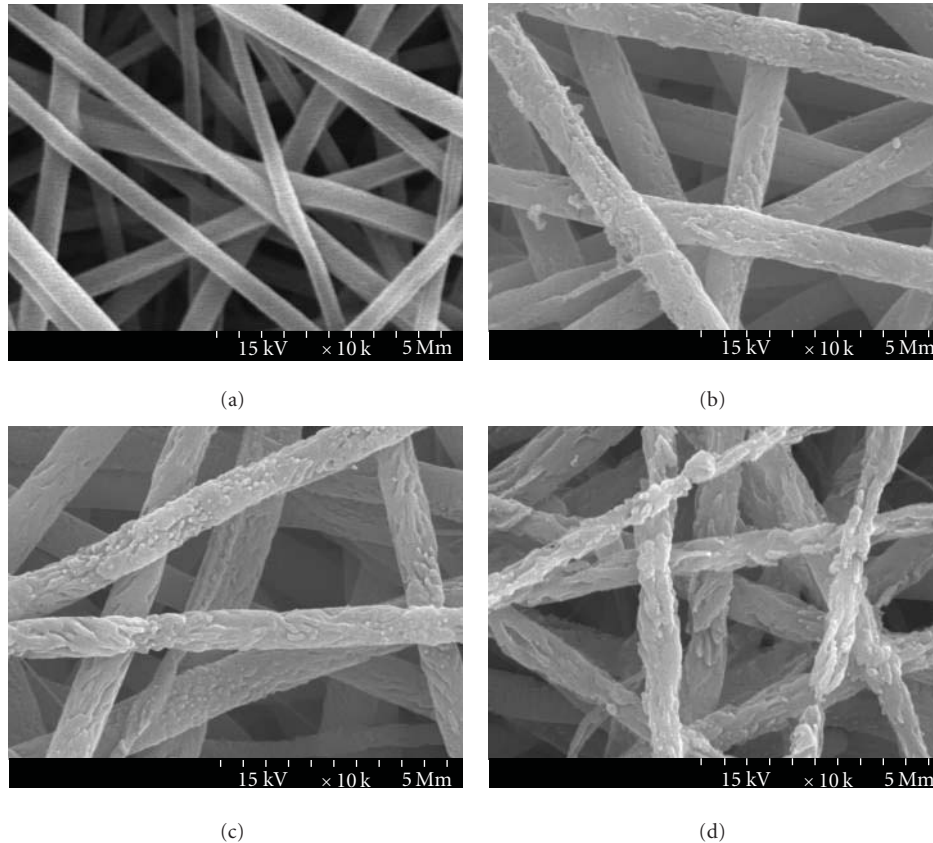


FIGURE 10: Biodegradation of PHBV/gelatin (50/50) nanofibrous scaffold by PHB depolymerase solution as a function of incubation time: (a) 0 h, (b) 1 h, (c) 4 h, and (d) 6 h. Reproduced from Journal of Materials Science: Materials in Medicine with permission from Springer [32].

Silver (Ag) nanoparticles have drawn considerable interest for their capability to release silver ions in a controlled manner which in turn leads to a powerful antibacterial activity against a large number of bacteria [55, 56]. It has been shown that the use of nanostructured Ag materials enhances the inhibitory capacity. Most likely this is because the nanostructured materials have a high surface area to contact [55–57]. However, they are easily aggregated because of their high surface free energy, and they can be oxidized or contaminated in air. Embedding of Ag nanoparticles into biodegradable polymer matrices represents a valid solution to these stabilization problems and permits a controlled antibacterial effect [58]. Xing et al. [28] successfully prepared PHBV/Ag composite scaffolds via an electrospinning technique. They demonstrated that the PHBV composite scaffolds having silver nanoparticles with less than 1.0 wt% completely inhibited the proliferation of the *Staphylococcus aureus* (Gram-positive) and the *Klebsiella pneumonia* (Gram-negative) bacteria, whereas the scaffolds did not show *in vitro* cell cytotoxicity. The Ag-containing polyester composite nanofibrous scaffolds may have a high interest in total joint arthroplasty, particularly because of their effect against multiresistant bacteria [28, 43].

3. Fabrication of Electrospun Biodegradable Polyester Nanocomposites

The nanocomposite scaffolds composed of ECM molecules such as collagen, gelatin, keratin, and biodegradable polyesters such as PCL, PLA, and PHBV are easily fabricated by electrospinning when both materials are dissolved in the same solvent (Table 1). Choi et al. [25] fabricated the PCL/collagen biodegradable composite nanofibrous scaffolds using a blend of PCL and collagen with a ratio of 1 : 1 in weight. Both PCL and collagen were dissolved in 1,1,1,3,3,3-hexafluoro-2-propanol (HFP) at a total concentration of 5% (wt/vol). Then the PCL/collagen blend solution was electrospun using a high voltage power supply at 20 kV potential between the solution and the grounded surface. The solution was delivered with a 5 mL polypropylene syringe through an 18.5 gauge blunt tip needle at a flow rate of 3.0 mL/h using a syringe pump. Fibers were collected onto a grounded mandrel at a distance of 10 cm from the syringe tip. The mandrel, consisting of a stainless steel plate, was rotated at various speeds to achieve different fiber orientations (Figure 1).

HA-containing biodegradable composite nanofibrous scaffolds were obtained by the incorporation of HA nanoparticles into the biodegradable polyester nanofibers (Table 1).

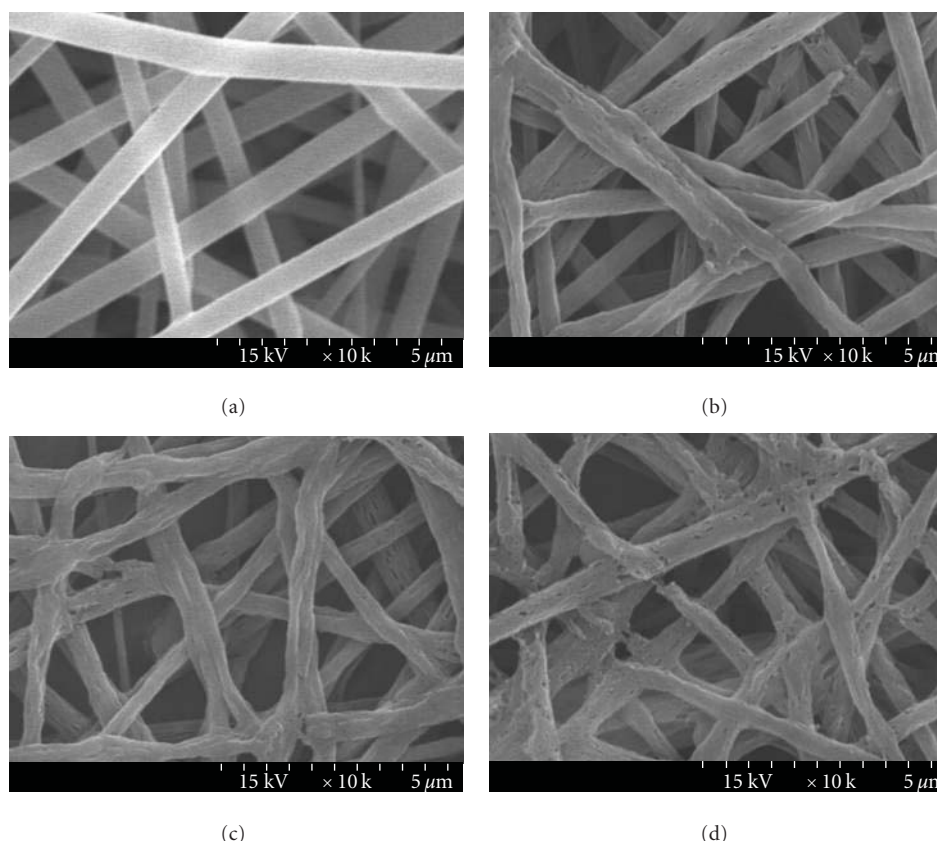


FIGURE 11: Biodegradation of PHBV/gelatin nanofibrous scaffold by collagenase solution as a function of incubation time: (a) 0 h, (b) 12 h, (c) 24 h, and (d) 48 h. Reproduced from Journal of Materials Science: Materials in Medicine with permission from Springer [32].

Jeong et al. [42] prepared the PLA/HA composite scaffolds directly on glass coverslips using an electrospinning technique. Briefly, PLA was dissolved in 2,2,2-trifluoroethyl alcohol (TFE, 10 wt%), and HA nanoparticles were then added to the PLA solution and mixed vigorously. The resulting concentrations of HA were 5 and 20 wt% (in PLA). The PLA/HA mixture was loaded in a 20 mL glass syringe equipped with a blunt 23 gauge needle. The glass syringe was then placed in a syringe pump and the needle was connected to the positive output of a high voltage power supply. Glass coverslips were attached to aluminum foil using a double-sided tape, which wrapped around the ground collector (9 cm in diameter) located at a fixed distance of 15 cm from the needle. The flow rate of the solution, applied voltage, and the spinning time were set to 0.85 mL/h, 18–20 kV, and 8 h, respectively (Figure 2). Following the spinning process, nanofibrous scaffolds were rinsed with distilled water three times to remove any residual chemicals, and dried at 60°C overnight.

Silver-containing biodegradable composite nanofibrous scaffolds were obtained by suspending the Ag nanoparticles in a biodegradable polymer solution. Xing et al. [28] prepared the PHBV/Ag composite scaffolds using electrospinning technique (Table 1). PHBV (hydroxyvaleric acid content: 5 wt%) was dissolved in TFE at a concentration of 5 wt%, and then the solution was stirred overnight at room

temperature to ensure complete dissolution. Then, certain amounts of Ag nanoparticles (0.1 to 1 wt%, the percentage of Ag nanoparticles to PHBV) were mixed with PHBV solution and stirred by magnetic stirring for 24 h to get the silver-containing PHBV solution. The solution was further homogenized with an ultrasonic for 2 h. The electrospinning experiments were performed at room temperature, and the apparatus for the electrospinning was assembled based on the study carried out by Lee et al. [41].

4. Characterization of Electrospun Biodegradable Polyester Nanocomposites

The morphologies of the nanofibrous polymer composites could be observed by using a field emission scanning electron microscope (FE-SEM). FE-SEM images of the PCL/collagen composite fibers [25] showed nanoscaled fiber diameters and controlled fiber orientations (Figures 3(a)–3(d)). The nanofibrous composites of the PCL/collagen blend were produced from the solution having a total polymer concentration ranging from 3 to 10% (wt/vol) in HFP. The nanofibrous composites showed a linear relationship between the solution concentrations and the fiber diameters of the PCL/collagen nanofiber scaffolds with different fiber angles being produced by electrospinning at various rotation rates of 0 (static), 800, 1500, and 2350 rpm. Progressive

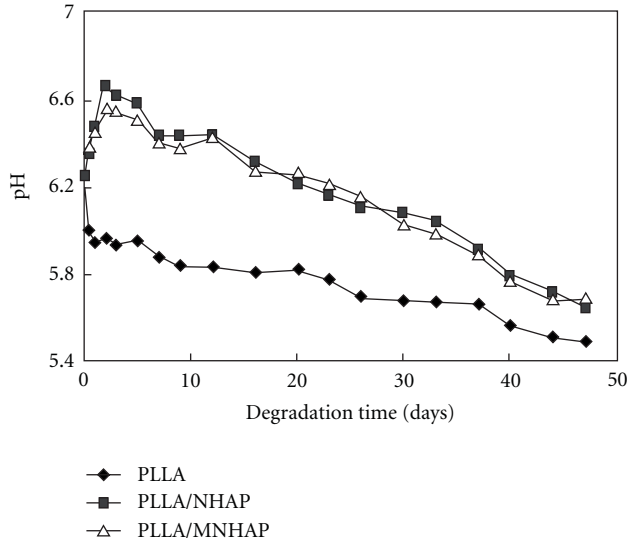


FIGURE 12: pH changes of PLLA, PLLA/NHAP (80 : 20, w/w) and PLLA/MNHAP (80 : 20, w/w) scaffold during *in vitro* degradation. Reproduced from Medical Engineering & Physics with permission from Elsevier [56].

increase in fiber orientation was observed as the rotation rate increased (Figures 3(e)–3(h)).

To test the capability of manipulating sequential deposition of different layers of fibers into a spatially graded composite nanofibrous scaffolds, a study [24] was performed using PCL only and PCL/Collagen-containing fluorescein isothiocyanate (FITC)-labeled BSA. The sequence was shown in Figure 4 and sequentially deposited multiple layers were directly collected on aluminum foil (substrate). It was found that different nanofiber materials were comparably layered as designed sequence by examining the cross-sections of collected scaffolds under a fluorescence microscope. By controlling the electrospinning time at a constant flow rate (10 mL/min), each layer could be altered with a designated thickness, from several micro-meters to several tens of micro meters.

A more confirmative result [24] was obtained by using PCL nanofibers containing either tetramethyl rhodamine isothiocyanate (TRITC)-labelled BSA or FITC-labelled BSA for sequential deposition (Figure 5). Despite the fact that each layer was thinner on the circumferential edge of the multilayered scaffolds, the majority (5 cm in diameter in the experimental setup) remained uniform and kept the deposition sequence as designed. The results indicated that the bioactive molecules can be incorporated into nanofibers and thereafter spatially arranged in a high order to form multifunctional scaffolds.

An atomic force microscope (AFM) was used to study the surface morphologies of the electrospun nanocomposites. AFM image of PHBV/gelatin composite nanofibers [35] was examined using a tapping mode and expressed as phase images. On the PHBV nanofiber surface, a relative homogeneous pattern was observed as shown in Figure 6(a). On the PHBV/gelatin composite nanofiber surface (Figure 6(b)),

TABLE 2: Chemical composition of the fiber mats calculated from ESCA survey scan spectra.

Mat	Composition (atom %)			
	C	O	N	S
PLA	63.1	36.9	0	0
PLA/gelatin	64.0	33.4	2.6	0
PLA/keratin	63.9	34.4	1.3	0.4

a phase-separated structure appeared showing the distribution of gelatin on the PHBV matrix. The phase-separated structures are probably attributed to the globular structure and hydrophilicity of gelatin.

Electron spectroscopy for chemical analysis (ESCA) survey scans were used to investigate the changes in the chemical structure of the electrospun composite scaffolds. Figure 7 shows ESCA survey scan spectra of PLA/keratin, PLA/gelatin and PLA nanofibers. PLA shows two separated peaks corresponding to C 1s (binding energy, 285 eV) and oxygen (binding energy, 532 eV) peaks (Figures 7(a) and 7(c)). The nitrogen (N 1s) peaks of gelatin and keratin newly appear at 400 eV (Figure 7(b)) [37]. The other new peak at 168 eV is attributed to sulfur (S 2p) of keratin (Figure 7(d)). Changes in the chemical structure of the nanofibrous mats were investigated using ESCA. The chemical compositions of the nanofibrous mats were calculated from a survey scan spectra and shown in Table 2. The oxygen content (36.9%) of PLA was reduced by the incorporation of proteins. Also, nitrogen (2.6 and 1.3%) was found on the composite mats, which is attributed to the presence of gelatin and keratin. Furthermore, a small quantity of sulfur (0.4%) was also found on the PLA/keratin.

Transmission electron microscopy (TEM) images were used to analyze the morphologies of the nanoparticles-containing biodegradable composites. As shown in Figures 8(a) and 8(b), HA nanoparticles (approximate diameter 35 nm) were uniformly and homogeneously dispersed in the organic phase of PLA nanofibers [42]. HA nanoparticles embedded within the nanofibers demonstrated spherical and elongated shapes, which are similar to those of HA only, as shown in Figure 8(c). Figure 9 shows TEM images of free silver nanoparticles and silver nanoparticles-containing PHBV nanofibers. The diameter of silver nanoparticles is in the range from 5 to 13 nm, as shown in Figure 9(a). The spherical silver nanoparticles were randomly distributed in the PHBV nanofiber (Figure 9(b)) (PHBV/Ag 1.0) [28].

5. In Vitro Biodegradation of Electrospun Polyester Nanocomposites

Figure 10 illustrates the morphological changes of the nanofiber composites surfaces after incubation in phosphate buffered saline (PBS) with or without depolymerase (*Pseudomonas stutzeri* BM190) [35]. Before the depolymerase treatment, PHBV/gelatin composite (Figure 10(a)) exhibited a preserved nanofibrous structure. After 4–6 h of incubation

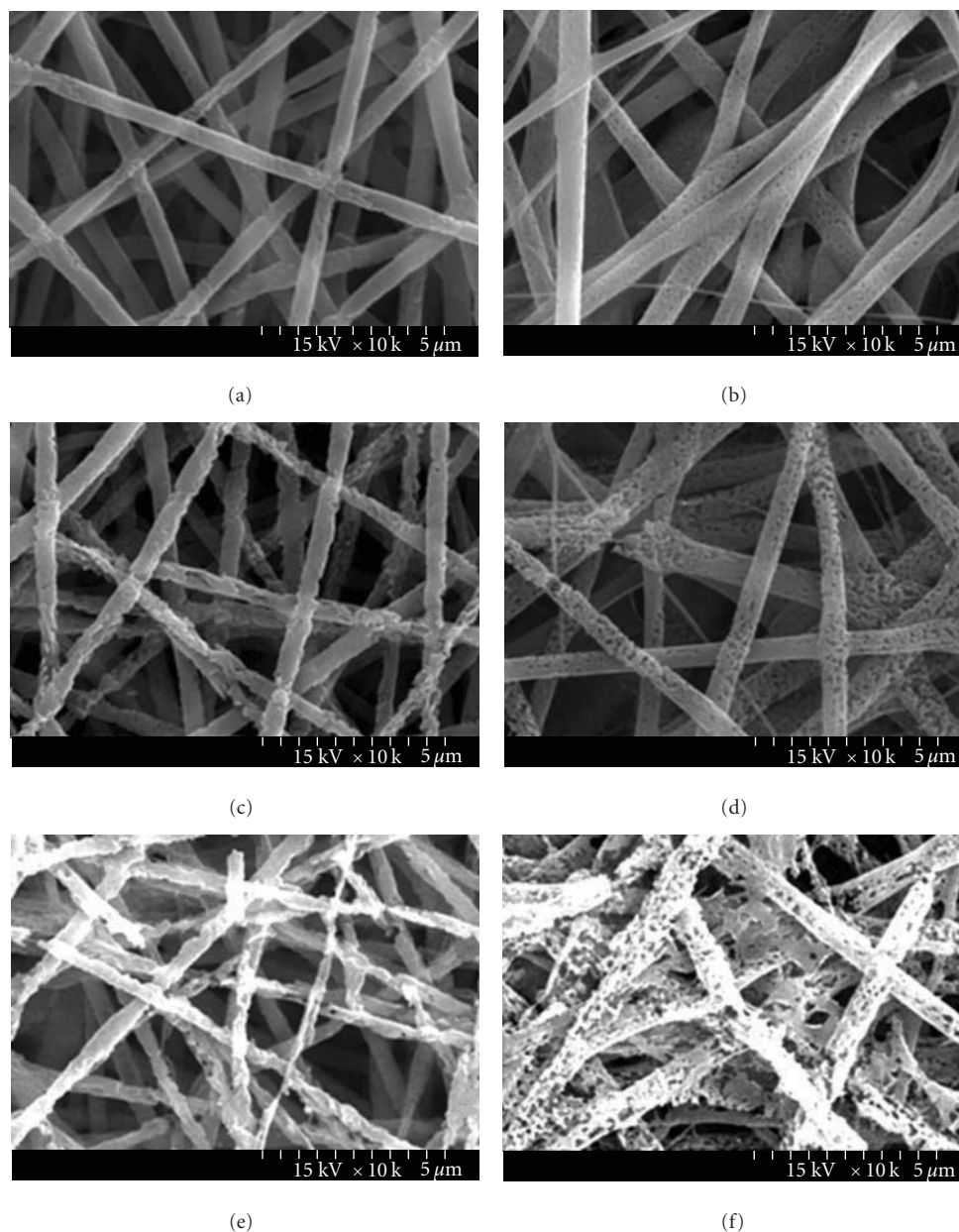


FIGURE 13: SEM images of (a), (c), (e) the PHBV and (b), (d), (f) PHBV/Ag 1.0 nanofibrous scaffolds incubated in PHB depolymerase aqueous for different lengths of time. (a), (b) 1 h, (c), (d) 6 h, and (e), (f) 24 h. Reproduced from Biomacromolecules with permission from American Chemical Society [24].

in depolymerase aqueous solution, the PHBV nanofiber showed many morphological changes (Figures 10(c) and 10(d)). On the other hand, after the collagenase treatment as shown in Figure 11, the PHBV/gelatin composite nanofibers broke down and partially adhered to each other after 24 and 48 h of incubation time.

The *in vitro* degradation of the PLLA/HA composite nanofibrous scaffolds is shown in Figure 12 [59]. It can be clearly seen that the pH of the pure PLLA degradation solution decreased remarkably from 6.25 to 5.89 in the first week, while those of the PLLA/silane-modified HA

(80:20, w/w) and PLLA/HA (80:20, w/w) composite scaffold increased to about 6.6 in the first 2 days, then gradually decreased after that. The increase of pH indicated that the degradation rate of HA was higher than that of PLLA in the first 2 days. During the testing period, it was obvious that the pH of the composite scaffold decreased more slowly than that of the pure PLLA scaffold. Moreover, the degradation process of PLLA became slower by the weakened acidic self-catalysis effect. Therefore, the pH of the PLLA/HA composite nanofibrous scaffold degradation curves declined more slowly than that of the pure PLLA

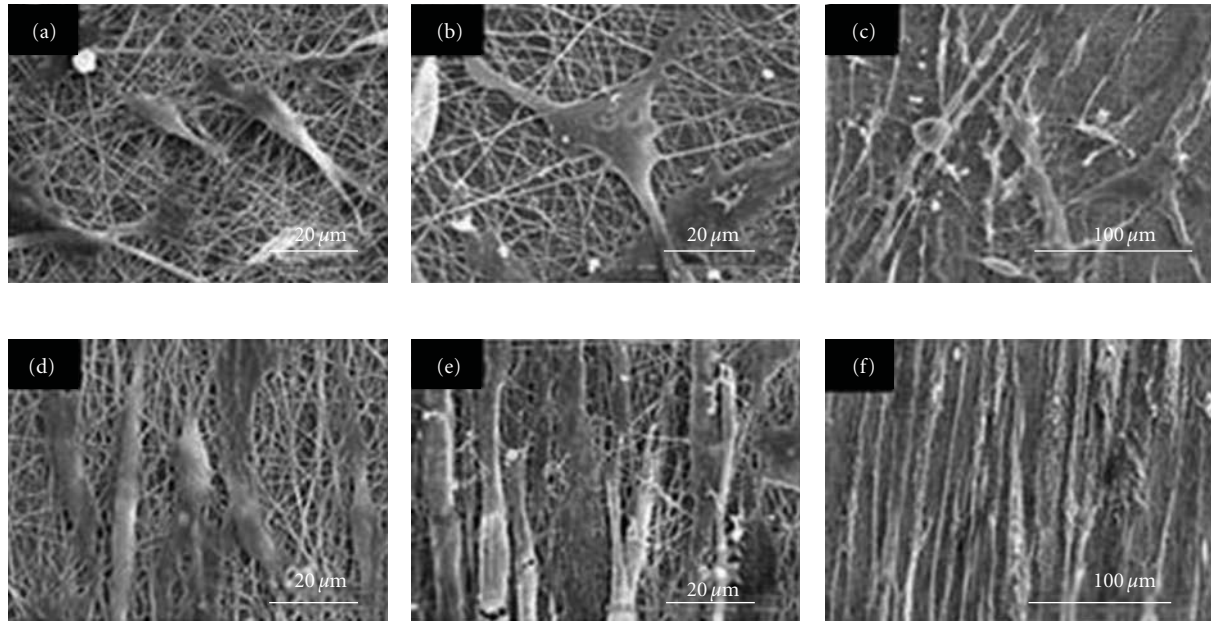


FIGURE 14: SEM images of hSkMCs on the electrospun PCL/collagen nanofiber meshes: (a)–(c) randomly oriented and (d)–(f) aligned electrospun meshes, (a), (d) 1 day and (b), (e) 3 days after cell seeding and (c), (f) 7 days after cell differentiation. Reproduced from Biomaterials with permission from Elsevier [21].

scaffold. The improved acidity atmosphere reduced the risk of indolent inflammatory reaction during the cultivation of the cell and tissue.

Figure 13 illustrates the morphological changes of the composite nanofibrous scaffold after incubation in a PBS containing PHB depolymerase for different times [28]. After 1 h of incubation, surface erosion appeared along the fiber axis of (a) the PHBV fibrous scaffold, whereas pores formed on the surface of (b) the PHBA/Ag 1.0 composite scaffold. Erosion of both the PHBV and the PHBV/Ag 1.0 composite scaffold increased with an increase in incubation time. However, the erosion rate of the PHBV/Ag 1.0 was faster than that of the PHBV control. It is considered that the rapid erosion of the PHBV/Ag 1.0 is due to the release of silver nanoparticles from the surface and then the subsequent biodegradation by PHB depolymerase.

6. Cell-Nanocomposites Interactions

In order to examine the effect of bioactive molecules incorporated into the scaffolds on cell adhesion, human dermal fibroblasts were seeded and cultured for 24 h on composite scaffolds composed of collagen-containing PCL fibers and PCL fibers [24]. Examination of the cross-sections of cultured constructs showed that human dermal fibroblasts had a preferential attachment to collagen-containing nanofibers, as illustrated in Figure 4 (bottom). The selective attachment of the dermal fibroblasts onto the PCL/Collagen nanofibers instead of the PCL nanofibers further demonstrated the advantage of collagen as it can promote the cell-nanofibers interaction.

SEM images taken at 1 and 3 days in the growth medium showed the presence of human skeletal muscle cells (hSkMCs) on the electrospun PCL/collagen composite nanofiber scaffolds [25] and the formation of myotubes at 7 days in the differentiation medium (Figure 14). The cells were aligned on the unidirectional oriented nanofibers after cell seeding. In contrast, the randomly oriented nanofiber scaffolds induced an irregular cellular orientation. The hSkMCs formed myotubes on the electrospun nanofibers at 7 days after cell differentiation. The myotubes formed on the oriented nanofiber scaffolds showed unidirectionally organized myotubes that are consistently aligned along the longitudinal axis of nanofibers, which is in contrast to the randomly oriented nanofiber scaffolds (Figures 14(c) and 14(f)).

Phenotypic expression of desmin, myosin heavy chain (MHC), and sarcomeric actin was confirmed on the aligned and randomly oriented nanofiber scaffolds (Figure 15) [25]. The hSkMCs were grown on the PCL/collagen composite nanofiber scaffolds in the growth medium for up to 3 days followed by incubation in the differentiation medium for up to 7 days which induced the formation of myotubes. Both the aligned and randomly oriented nanofiber scaffolds showed the maintenance of phenotypic expression of the skeletal muscle cells. In addition, the cells and myotubes were oriented along the longitudinal axis of the nanofiber direction (Figures 15(e)–15(g)). In contrast, the myotubes on the randomly oriented nanofiber scaffolds were mostly scattered in all directions (Figures 15(a)–15(c)). Confocal microscopic images confirmed that fiber orientation influenced the morphology and cytoskeletal of the hSkMCs on the nanofiber scaffolds (Figures 15(d) and 15(h)). Confocal microscopy

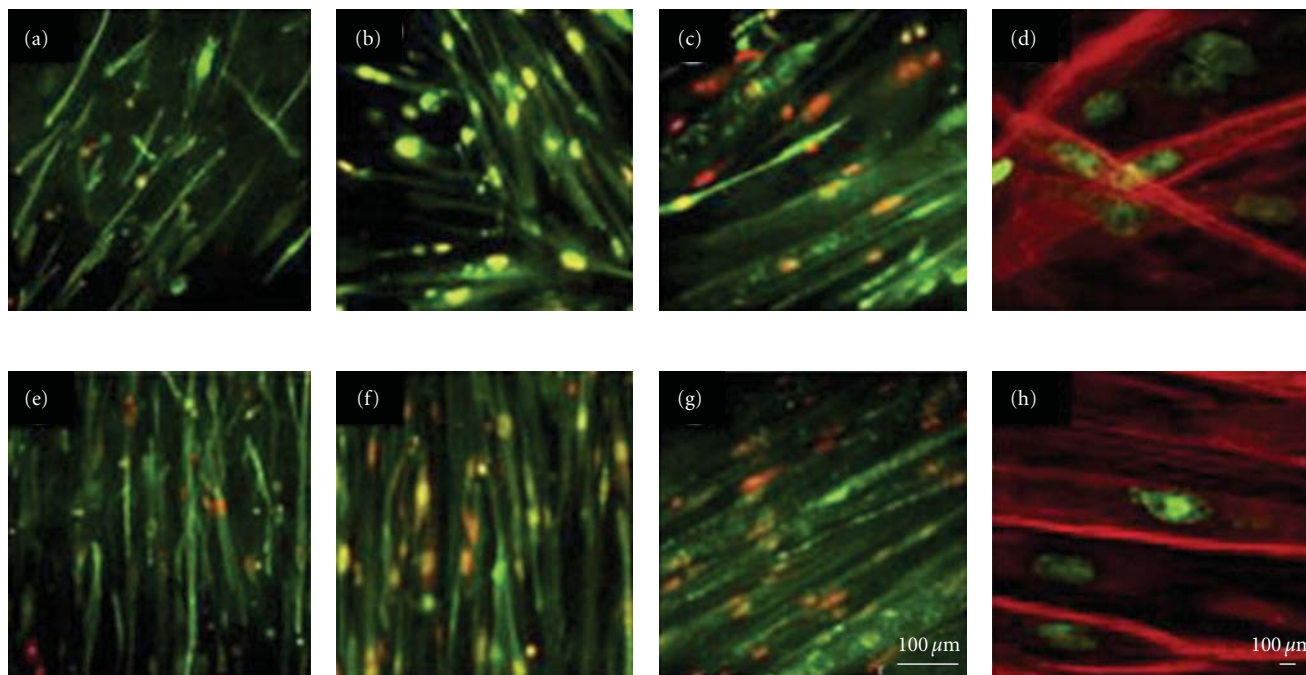


FIGURE 15: Immunofluorescent staining images of hSkMCs on the electrospun PCL/collagen nanofiber meshes: (a)–(c) randomly oriented and (e)–(g) aligned electrospun meshes; (a), (e) desmin-positive expression at 3 days after cell seeding, (b), (f) MHC-positive expression at 7 days after cell differentiation, and (c), (g) sarcomeric actin-positive expression at 7 days after cell differentiation. Laser confocal microscopy images of F-actin staining in hSkMCs seeded on the electrospun PCL/collagen nanofiber meshes ($\times 600$ magnification): (d) randomly oriented and (h) aligned electrospun meshes. Reproduced from *Biomaterials* with permission from Elsevier [21].

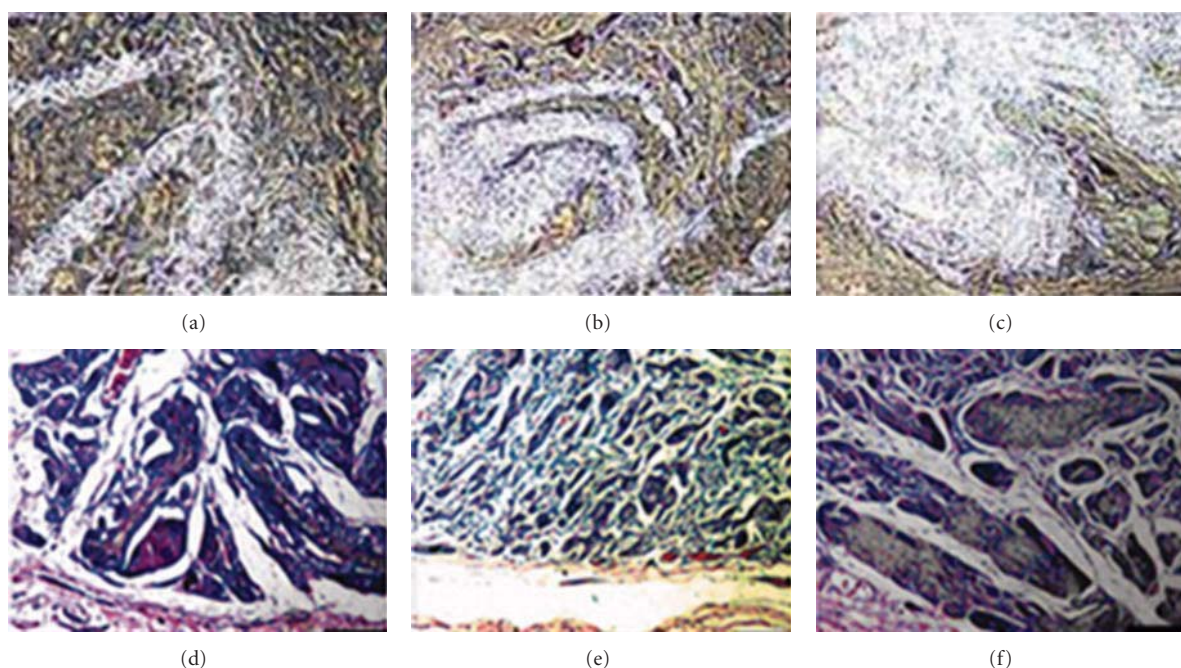


FIGURE 16: Representative photomicrographs of subcutaneous implants; PLA/SF (a), PLA/SF-gelatin (70:30) (b), and PLA/SF-gelatin (50:50) (c) at 1 month; PLA/SF (d), PLA/SF-gelatin (70:30) (e), and PLA/SF-gelatin (50:50) (f) at 3 months. Reproduced from *Journal of Biomedical Materials Research* with permission from John Wiley and Sons [22].

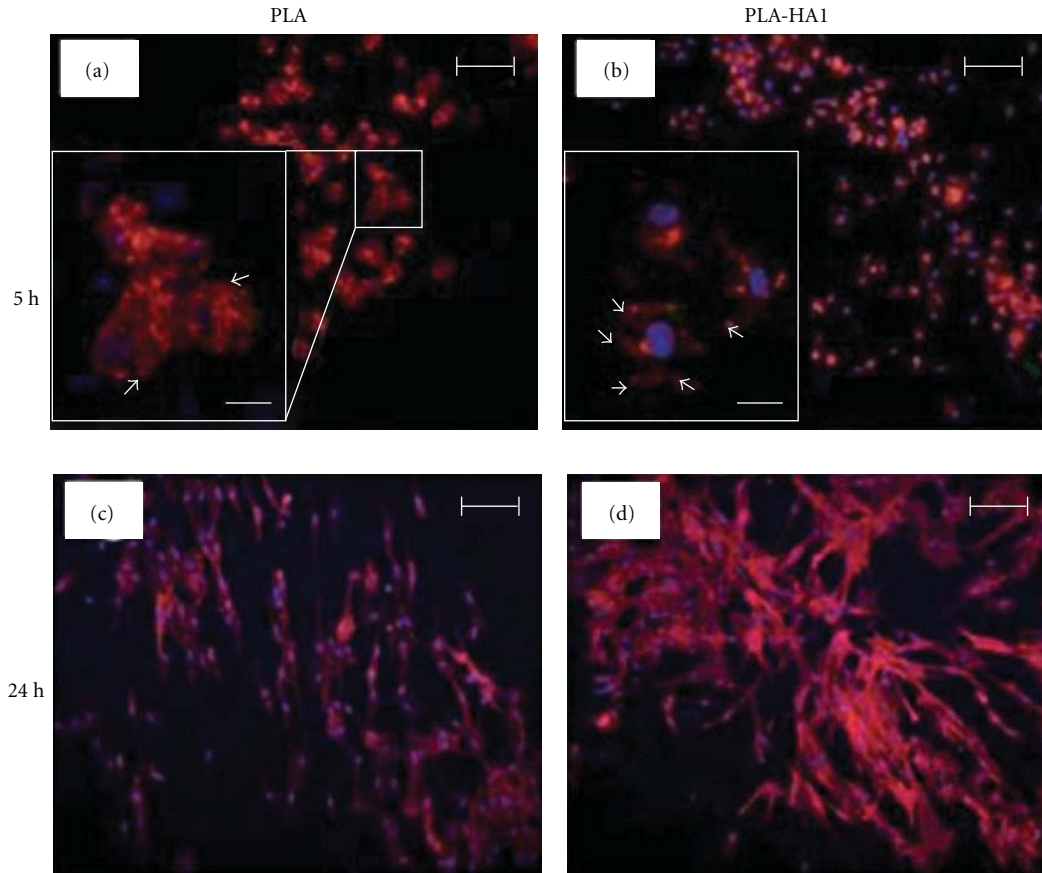


FIGURE 17: Immunofluorescence micrographs of MC3T3-E1 cells cultured on PLA (a) and (b) and PLA-HA1 (c) and (d) nanofibers for 5 and 24 h. Scale bars in insets of (a) and (c) represent 25 μ m. F-actin stress fibers were stained with rhodamine-phalloidin. Reproduced from *Macromolecular bioscience* with permission from Wiley-VCH Verlag GmbH & Co. [51].

images of the fluorescent stained F-actin on cell adhesion, proliferation, and differentiation demonstrated that the actin assembly appeared disordered on the randomly oriented nanofiber structure, whereas on the aligned nanofiber structures, the F-actin was oriented along the nanofiber direction in an organized fashion. The myotubes formed on the randomly oriented nanofiber scaffolds showed partial alignment locally and did not show a uniform cellular organization. In contrast, myotubes on the aligned nanofiber scaffolds organized within close proximity to the direction of the nanofiber direction and formed uniformly aligned myotubes.

After implantation of 1 month, Figure 16 showed that the PLA/SF-gelatin composite nanofibrous scaffolds were surrounded by the new tissue, and fewer macrophages, neutrophils, and lymphocytes were found, indicating that all three scaffold types have less inflammation and no significant rejection [26]. Furthermore, 3 months later, as shown in Figure 4, the scaffolds could guide the formation of connective vascular network tissue. Also, the shape of the implants became smaller, suggesting that PLA/SF-gelatin had good biocompatibility and biodegradation *in vivo*.

Cell adhesion to the PLA/HA composite nanofibrous scaffolds [42] was evaluated using MC3T3 E1 pre-osteoblast

cells that have been extensively characterized for their osteogenic differentiation potential [60–62]. The cytoskeletal organization of the cells attached on the nanofibers by fluorescently staining actin filaments of the adherent cells after up to 24 h of *in vitro* culture were first examined. At 5 h after cell seeding, preosteoblasts on the nanofiber scaffolds displayed a different degree of immature cytoskeletal structure as shown in Figures 17(a) and 17(c). The cells on the PLA/HA composite nanofibers formed an early stage of filopodial extension at the ends of intracellular actin stress fibers. On the other hand, the cells on the PLA nanofibers maintained spherical morphology and showed an accumulation of actin filaments only inside the cytoplasm, suggesting no indication of the extension of filopodia. After 24 h, the cells on all nanofibers displayed a spindle-shaped elongated morphology and extensive formation of actin stress fibers. Notably, they observed an interesting morphology of the pre-osteoblasts cultured on the PLA nanofiber featuring isotropic patterned elongation. On the other hand, the cells on the PLA/HA nanofiber showed anisotropic aggregation of a number of highly spread pre-osteoblasts with morphology that looked similar to viable osteoblasts. Taken together, despite varied cytoskeletal organization, the incorporation of HA with PLA did not

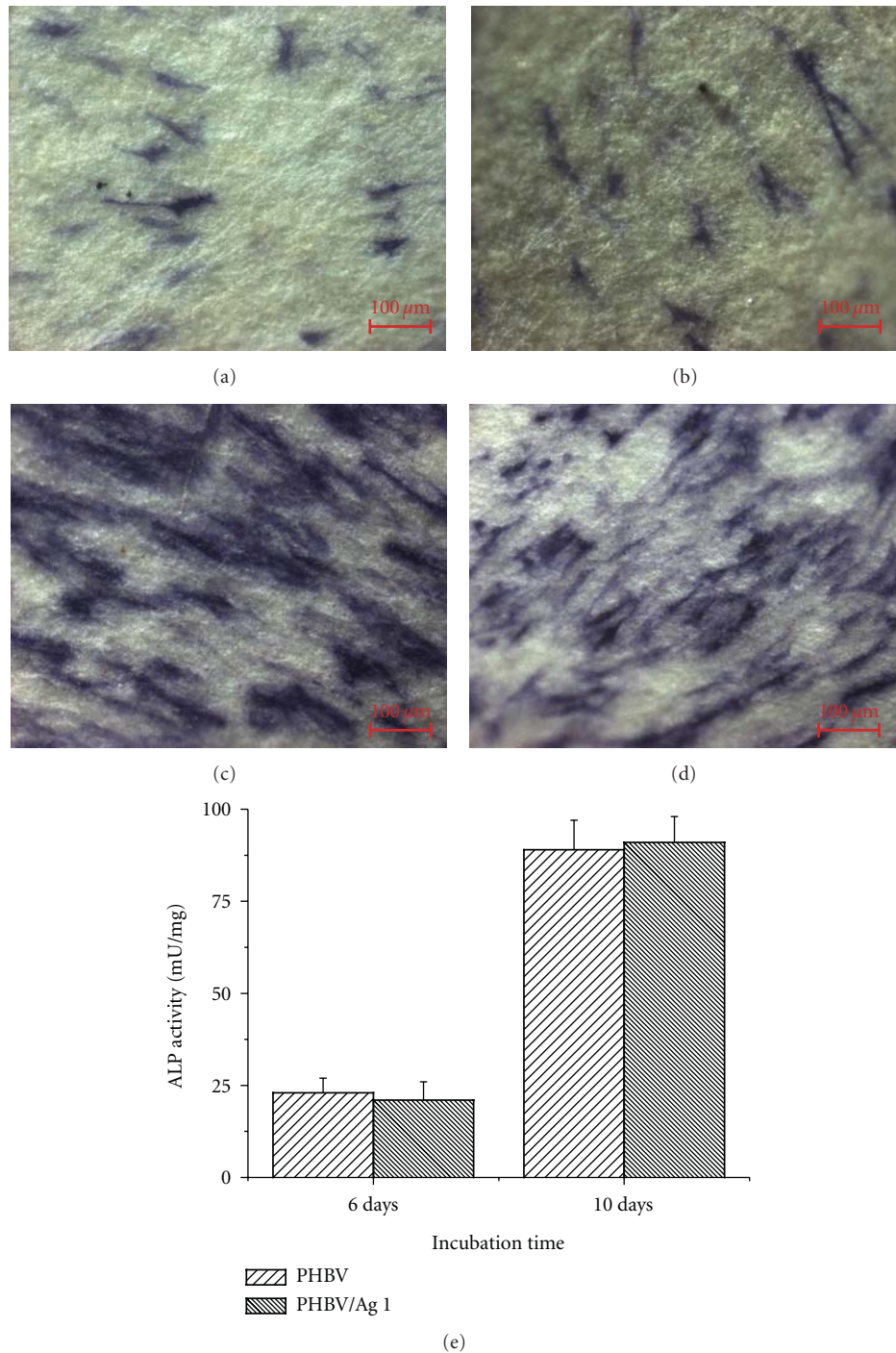


FIGURE 18: Alkaline phosphatase-(ALP-) stained (a) PHBV, (b) PHBV/Ag 1.0 nanofibrous scaffolds after 6 days of incubation of MC3T3-E1 osteoblasts, and (c) PHBV, (d) PHBV/Ag 1.0 nanofibrous scaffolds after 10 days incubation of MC3T3-E1 osteoblasts, and (e) ALP expression of MC3T3-E1 osteoblasts on the nanofibrous scaffolds. Reproduced from Biomacromolecules with permission from American Chemical Society [24].

seem to compromise cell viability. The slight difference in morphologies of adherent osteoblasts may be attributed to the different degree of pore distribution or to the chemical composition of underlying scaffolds or to both factors. Specifically, previous investigations have highlighted that

cytoskeletal organization and cell shape are regulated by the nanoscaled architecture of a scaffold [63, 64]. Cells can form a hierarchical cytoskeletal network by adaptation of the structure of underlying nanofiber that provides a different level of void pore space, and fiber diameters.

Because embedding HA nanoparticles into PLA alters the chemical composition as well as the size and distribution of the fibers, further study may be necessary to investigate the effect of these individual contributions on cellular responses.

Alkaline phosphatase (ALP) activity was determined to be an indicator of osteoblastic differentiation of MC3T3-E1 cultured on PHBV and PHBV/Ag 1.0 nanofibrous scaffolds [65]. As shown in Figure 18, the ALP activities of the cells on the PHBV and PHBV 1.0 nanofibrous scaffold increased with the increase of incubation time. The degree of ALP activity expressed by the PHBV scaffold was not significantly different from that of the PHBV/Ag 1.0 for 10 days (Figure 18(e)). Haimi et al. [66] fabricated three types of bioactive glass scaffolds (nontreated, thick, and thin Ca-P treated) and reported that the ALP activity of the cells cultured for 1 week on nontreated bioactive glass scaffolds was significantly higher than that of those cultured on both thin and thick Ca-P-treated scaffolds. However, these differences equalized between the three scaffolds by the 2-week time point. Therefore, they concluded that the osteogenic differentiation appears to be delayed on the Ca-P surface-treated scaffolds. Ge et al. [67] prepared the 3D poly-(lactic-co-glycolic acid) (PLGA) scaffolds and reported that the ALP activity expressed by the osteoblasts cultured on the PLGA scaffolds was almost the same as that on the open-cell polylactic acid (OPLA) and collagen scaffolds (Becton-Dickinson, Franklin Lakes, NJ). They concluded that the PLGA scaffold can support the proliferation of osteoblasts as well as the expression of genes, which is important for osteogenesis such as ALP, osteocalcin, collagen I, and osteopontin. The PHBV is a natural polyester polymerized by bacteria. The PHBV has a biological origin and environmentally more acceptable. In their study, it is considered that both the PHBV and the silver-containing PHBV nanofibrous scaffolds can support the expression of genes which is important for osteogenesis (ALP activity).

7. Conclusions

Novel generations of biodegradable nanocomposites are expected to be biofunctional, intelligent, and active components. Biopolymer matrix composites have the advantage of being very versatile, allowing for the tailoring of their final properties. Biodegradable polyester nanocomposites can be designed and produced with the electrospinning technique, using a wide range of biopolymeric matrices, reinforcements and processing routes. As a result, much of the work is still ongoing, and there is yet to be a definite conclusion on the effect of nano-sized inclusions on biodegradable polymer systems. In this paper, a review has been presented on the materials, processing, experimental results, and possible interpretations of those results for biodegradable polyester nanocomposites by an electrospinning technique. The mentioned studies suggest that the combination of biodegradable polymer and nature ECM molecules or nanostructures opens new perspective in the nanodevices for TE applications.

Acknowledgments

This research was supported by research Grants from the Biotechnology Development Project (2009-0090907) and by Grant 2010-0011125 from the Ministry of Education, Science, and Technology of Korea.

References

- [1] R. Langer and J. P. Vacanti, "Tissue engineering," *Science*, vol. 260, no. 5110, pp. 920–926, 1993.
- [2] R. Shalak and C. F. Fox, "Preface," in *Tissue Engineering*, R. Shalak and C. F. Fox, Eds., p. 26, Alan R. Liss, New York, NY, USA, 1988.
- [3] J. Jagur-Grodzinski, "Polymers for tissue engineering, medical devices, and regenerative medicine. Concise general review of recent studies," *Polymers for Advanced Technologies*, vol. 17, no. 6, pp. 395–418, 2006.
- [4] V. M. Correlo, L. F. Boesel, M. Bhattacharya, J. F. Mano, N. M. Neves, and R. L. Reis, "Properties of melt processed chitosan and aliphatic polyester blends," *Materials Science and Engineering A*, vol. 403, no. 1-2, pp. 57–68, 2005.
- [5] V. M. Correlo, L. F. Boesel, M. Bhattacharya, J. F. Mano, N. M. Neves, and R. L. Reis, "Hydroxyapatite reinforced chitosan and polyester blends for biomedical applications," *Macromolecular Materials and Engineering*, vol. 290, no. 12, pp. 1157–1165, 2005.
- [6] V. M. Correlo, L. F. Boesel, E. Pinho et al., "Melt-based compression-molded scaffolds from chitosan-polyester blends and composites: morphology and mechanical properties," *Journal of Biomedical Materials Research Part A*, vol. 91, no. 2, pp. 489–504, 2009.
- [7] P. Lee, R. Lin, J. Moon, and L. P. Lee, "Microfluidic alignment of collagen fibers for in vitro cell culture," *Biomedical Microdevices*, vol. 8, no. 1, pp. 35–41, 2006.
- [8] E. T. Baran, J. F. Mano, and R. L. Reis, "Starch-chitosan hydrogels prepared by reductive alkylation cross-linking," *Journal of Materials Science: Materials in Medicine*, vol. 15, no. 7, pp. 759–765, 2004.
- [9] C. M. Vaz, L. A. de Graaf, R. L. Reis, and A. M. Cunha, *Soy Protein-Based Systems for Different Tissue Regeneration Applications*, Nato Science Series, Kluwer, Dordrecht, The Netherlands, 2002.
- [10] N. Bhattarai, Z. Li, D. Edmondson, and M. Zhang, "Alginate-based nanofibrous scaffolds: structural, mechanical, and biological properties," *Advanced Materials*, vol. 18, no. 11, pp. 1463–1467, 2006.
- [11] C. Li, C. Vepari, H. J. Jin, H. J. Kim, and D. L. Kaplan, "Electrospun silk-BMP-2 scaffolds for bone tissue engineering," *Biomaterials*, vol. 27, no. 16, pp. 3115–3124, 2006.
- [12] G. A. Silva, A. Pedro, F. J. Costa, N. M. Neves, O. P. Coutinho, and R. L. Reis, "Soluble starch and composite starch Bioactive Glass 45S5 particles: synthesis, bioactivity, and interaction with rat bone marrow cells," *Materials Science and Engineering C*, vol. 25, no. 2, pp. 237–246, 2005.
- [13] J. F. Mano, G. A. Silva, H. S. Azevedo et al., "Natural origin biodegradable systems in tissue engineering and regenerative medicine: present status and some moving trends," *Journal of the Royal Society Interface*, vol. 4, no. 17, pp. 999–1030, 2007.
- [14] P. A. Gunatillake, R. Adhikari, and N. Gadegaard, "Biodegradable synthetic polymers for tissue engineering," *European Cells and Materials*, vol. 5, pp. 1–16, 2003.

- [15] J. Venugopal, P. Vadgama, T. S. S. Kumar, and S. Ramakrishna, "Biocomposite nanofibres and osteoblasts for bone tissue engineering," *Nanotechnology*, vol. 18, no. 5, Article ID 055101, 2007.
- [16] T. Lin, H. Wang, and X. Wang, "Self-crimping bicomponent nanofibers electrospun from polyacrylonitrile and elastomeric polyurethane," *Advanced Materials*, vol. 17, no. 22, pp. 2699–2703, 2005.
- [17] N. M. Neves, R. Campos, A. Pedro, J. Cunha, F. Macedo, and R. L. Reis, "Patterning of polymer nanofiber meshes by electrospinning for biomedical applications," *International Journal of Nanomedicine*, vol. 2, no. 3, pp. 433–448, 2007.
- [18] J. V. Araujo, A. Martins, I. B. Leonor, E. D. Pinho, R. L. Reis, and N. M. Neves, "Surface controlled biomimetic coating of polycaprolactone nanofiber meshes to be used as bone extracellular matrix analogues," *Journal of Biomaterials Science, Polymer Edition*, vol. 19, no. 10, pp. 1261–1278, 2008.
- [19] H. Yoshimoto, Y. M. Shin, H. Terai, and J. P. Vacanti, "A biodegradable nanofiber scaffold by electrospinning and its potential for bone tissue engineering," *Biomaterials*, vol. 24, no. 12, pp. 2077–2082, 2003.
- [20] Z. M. Huang, Y. Z. Zhang, M. Kotaki, and S. Ramakrishna, "A review on polymer nanofibers by electrospinning and their applications in nanocomposites," *Composites Science and Technology*, vol. 63, no. 15, pp. 2223–2253, 2003.
- [21] H. S. Yoo, T. G. Kim, and T. G. Park, "Surface-functionalized electrospun nanofibers for tissue engineering and drug delivery," *Advanced Drug Delivery Reviews*, vol. 61, no. 12, pp. 1033–1042, 2009.
- [22] J. H. Jang, O. Castano, and H. W. Kim, "Electrospun materials as potential platforms for bone tissue engineering," *Advanced Drug Delivery Reviews*, vol. 61, no. 12, pp. 1065–1083, 2009.
- [23] I. Armentano, M. Dottori, E. Fortunati, S. Mattioli, and J. M. Kenny, "Biodegradable polymer matrix nanocomposites for tissue engineering: a review," *Polymer Degradation and Stability*, vol. 95, no. 11, pp. 2126–2146, 2010.
- [24] X. Yang, K. R. Ogbolu, and H. Wang, "Multifunctional nanofibrous scaffold for tissue engineering," *Journal of Experimental Nanoscience*, vol. 3, no. 4, pp. 329–345, 2008.
- [25] J. S. Choi, S. J. Lee, G. J. Christ, A. Atala, and J. J. Yoo, "The influence of electrospun aligned poly(ϵ -caprolactone)/collagen nanofiber meshes on the formation of self-aligned skeletal muscle myotubes," *Biomaterials*, vol. 29, no. 19, pp. 2899–2906, 2008.
- [26] G. B. Yin, Y. Z. Zhang, S. D. Wang, D. B. Shi, Z. H. Dong, and W. G. Fu, "Study of the electrospun PLA/silk fibroin-gelatin composite nanofibrous scaffold for tissue engineering," *Journal of Biomedical Materials Research Part A*, vol. 93, no. 1, pp. 158–163, 2010.
- [27] C. Spadaccio, A. Rainer, M. Trombetta et al., "Poly-L-lactic acid/hydroxyapatite electrospun nanocomposites induce chondrogenic differentiation of human MSC," *Annals of Biomedical Engineering*, vol. 37, no. 7, pp. 1376–1389, 2009.
- [28] Z. C. Xing, W. P. Chae, J. Y. Baek, M. J. Choi, Y. Jung, and I. K. Kang, "In vitro assessment of antibacterial activity and cytocompatibility of silver-containing phbv nanofibrous scaffolds for tissue engineering," *Biomacromolecules*, vol. 11, no. 5, pp. 1248–1253, 2010.
- [29] F. Chen, X. Li, X. Mo, C. He, H. Wang, and Y. Ikada, "Electrospun chitosan-P(LLA-CL) nanofibers for biomimetic extracellular matrix," *Journal of Biomaterials Science, Polymer Edition*, vol. 19, no. 5, pp. 677–691, 2008.
- [30] S. I. Jeong, A. Y. Lee, Y. M. Lee, and H. Shin, "Electrospun gelatin/poly(L-lactide-co- ϵ -caprolactone) nanofibers for mechanically functional tissue-engineering scaffolds," *Journal of Biomaterials Science, Polymer Edition*, vol. 19, no. 3, pp. 339–357, 2008.
- [31] I. K. Kwon and T. Matsuda, "Co-electrospun nanofiber fabrics of poly(L-lactide-co- ϵ -caprolactone) with type I collagen or heparin," *Biomacromolecules*, vol. 6, no. 4, pp. 2096–2105, 2005.
- [32] I. Han, K. J. Shim, J. Y. Kim et al., "Effect of poly(3-hydroxybutyrate-co-3-hydroxyvalerate) nanofiber matrices cocultured with hair follicular epithelial and dermal cells for biological wound dressing," *Artificial Organs*, vol. 31, no. 11, pp. 801–808, 2007.
- [33] W. Meng, S. Y. Kim, J. Yuan et al., "Electrospun PHBV/collagen composite nanofibrous scaffolds for tissue engineering," *Journal of Biomaterials Science, Polymer Edition*, vol. 18, no. 1, pp. 81–94, 2007.
- [34] L. Ghasemi-Mobarakeh, M. P. Prabhakaran, M. Morshed, M. H. Nasr-Esfahani, and S. Ramakrishna, "Electrospun poly(ϵ -caprolactone)/gelatin nanofibrous scaffolds for nerve tissue engineering," *Biomaterials*, vol. 29, no. 34, pp. 4532–4539, 2008.
- [35] W. Meng, Z.-C. Xing, K.-H. Jung et al., "Synthesis of gelatin-containing PHBV nanofiber mats for biomedical application," *Journal of Materials Science: Materials in Medicine*, vol. 19, no. 8, pp. 2799–2807, 2008.
- [36] H.-W. Kim, H.-S. Yu, and H.-H. Lee, "Nanofibrous matrices of poly(lactic acid) and gelatin polymeric blends for the improvement of cellular responses," *Journal of Biomedical Materials Research Part A*, vol. 87, no. 1, pp. 25–32, 2008.
- [37] J. Yuan, J. Shen, and I.-K. Kang, "Fabrication of protein-doped PLA composite nanofibrous scaffolds for tissue engineering," *Polymer International*, vol. 57, no. 10, pp. 1188–1193, 2008.
- [38] J. Yuan, Z.-C. Xing, S.-W. Park et al., "Fabrication of PHBV/keratin composite nanofibrous mats for biomedical applications," *Macromolecular Research*, vol. 17, no. 11, pp. 850–855, 2009.
- [39] H. Pan, H. Jiang, and W. Chen, "Interaction of dermal fibroblasts with electrospun composite polymer scaffolds prepared from dextran and poly lactide-co-glycolide," *Biomaterials*, vol. 27, no. 17, pp. 3209–3220, 2006.
- [40] G. Sui, X. Yang, F. Mei et al., "Poly-L-lactic acid/hydroxyapatite hybrid membrane for bone tissue regeneration," *Journal of Biomedical Materials Research Part A*, vol. 82, no. 2, pp. 445–454, 2007.
- [41] K. H. Lee, H. Y. Kim, Y. J. Ryu, K. W. Kim, and S. W. Choi, "Mechanical behavior of electrospun fiber mats of poly(vinyl chloride)/polyurethane polyblends," *Journal of Polymer Science Part B*, vol. 41, no. 11, pp. 1256–1262, 2003.
- [42] S. I. Jeong, E. K. Ko, J. Yum, C. H. Jung, Y. M. Lee, and H. Shin, "Nanofibrous poly(lactic acid)/hydroxyapatite composite scaffolds for guided tissue regeneration," *Macromolecular Bioscience*, vol. 8, no. 4, pp. 328–338, 2008.
- [43] Z.-C. Xing, Y. P. Chae, M. W. Huh et al., "In vitro anti-bacterial and cytotoxic properties of silver-containing poly(L-lactide-co-glycolide) nanofibrous scaffolds," *Journal of Nanoscience and Nanotechnology*, vol. 11, no. 1, pp. 61–65, 2011.
- [44] X. Hu, W. Lui, L. Cui, M. Wang, and Y. Cao, "Tissue engineering of nearly transparent corneal stroma," *Tissue Engineering*, vol. 11, no. 11–12, pp. 1710–1717, 2005.
- [45] C. Yang, P. J. Hillas, J. A. Báez et al., "The application of recombinant human collagen in tissue engineering," *BioDrugs*, vol. 18, no. 2, pp. 103–119, 2004.
- [46] Z. C. C. Chen, A. K. Ekaputra, K. Gauthaman, P. G. Adaikan, H. Yu, and D. W. Huttmacher, "In vitro and in vivo analysis

- of co-electrospun scaffolds made of medical grade poly(ϵ -caprolactone) and porcine collagen," *Journal of Biomaterials Science, Polymer Edition*, vol. 19, no. 5, pp. 693–707, 2008.
- [47] E. A. MacGregor and C. T. Greenwood, *Polymers in Nature*, John Wiley & Sons Press, New York, NY, USA, 1980.
- [48] H. Jiang, D. Fang, B. S. Hsiao, B. Chu, and W. Chen, "Optimization and characterization of dextran membranes prepared by electrospinning," *Biomacromolecules*, vol. 5, no. 2, pp. 326–333, 2004.
- [49] A. Bianco, I. Cacciotti, M. Lombardi, L. Montanaro, and G. Gusmano, "Thermal stability and sintering behaviour of hydroxyapatite nanopowders," *Journal of Thermal Analysis and Calorimetry*, vol. 88, no. 1, pp. 237–243, 2007.
- [50] T. Koshino, T. Murase, T. Takagi, and T. Saito, "New bone formation around porous hydroxyapatite wedge implanted in opening wedge high tibial osteotomy in patients with osteoarthritis," *Biomaterials*, vol. 22, no. 12, pp. 1579–1582, 2001.
- [51] J. D. Bronzino, *The Biomedical Engineering Handbook*, CRC Press, Boca Raton, Fla, USA, 1995.
- [52] A. E. Porter, N. Patel, J. N. Skepper, S. M. Best, and W. Bonfield, "Effect of sintered silicate-substituted hydroxyapatite on remodelling processes at the bone-implant interface," *Biomaterials*, vol. 25, no. 16, pp. 3303–3314, 2004.
- [53] S. Gay, S. Arostegui, and J. Lemaitre, "Preparation and characterization of dense nanohydroxyapatite/PLLA composites," *Materials Science and Engineering C*, vol. 29, no. 1, pp. 172–177, 2009.
- [54] W. P. Faulk and G. M. Taylor, "Communication to the editors. An immunocolloid method for the electron microscope," *Immunochemistry*, vol. 8, no. 11, pp. 1081–1083, 1971.
- [55] E. Falletta, M. Bonini, E. Fratini et al., "Clusters of poly(acrylates) and silver nanoparticles: structure and applications for antimicrobial fabrics," *Journal of Physical Chemistry C*, vol. 112, no. 31, pp. 11758–11766, 2008.
- [56] D. D. Evanoff Jr. and G. Chumanov, "Synthesis and optical properties of silver nanoparticles and arrays," *ChemPhysChem*, vol. 6, no. 7, pp. 1221–1231, 2005.
- [57] M. Rai, A. Yadav, and A. Gade, "Silver nanoparticles as a new generation of antimicrobials," *Biotechnology Advances*, vol. 27, no. 1, pp. 76–83, 2009.
- [58] J. Y. Lee, Y. Liao, R. Nagahata, and S. Horiuchi, "Effect of metal nanoparticles on thermal stabilization of polymer/metal nanocomposites prepared by a one-step dry process," *Polymer*, vol. 47, no. 23, pp. 7970–7979, 2006.
- [59] X. J. Wang, G. J. Song, and T. Lou, "Fabrication and characterization of nano-composite scaffold of PLLA/silane modified hydroxyapatite," *Medical Engineering & Physics*, vol. 32, no. 2, pp. 391–397, 2010.
- [60] Y. Zhao, B. Zou, Z. Shi, Q. Wu, and G. Q. Chen, "The effect of 3-hydroxybutyrate on the in vitro differentiation of murine osteoblast MC3T3-E1 and in vivo bone formation in ovariectomized rats," *Biomaterials*, vol. 28, no. 20, pp. 3063–3073, 2007.
- [61] H. J. Kong, T. Boontheekul, and D. J. Mooney, "Quantifying the relation between adhesion ligand-receptor bond formation and cell phenotype," *Proceedings of the National Academy of Sciences of the United States of America*, vol. 103, no. 49, pp. 18534–18539, 2006.
- [62] R. A. Jackson, S. Murali, A. J. van Wijnen, G. S. Stein, V. Nurcombe, and S. M. Cool, "Heparan sulfate regulates the anabolic activity of MC3T3-E1 preosteoblast cells by induction of Runx2," *Journal of Cellular Physiology*, vol. 210, no. 1, pp. 38–50, 2007.
- [63] E. A. Cavalcanti-Adam, P. Tomakidi, M. Bezler, and J. P. Spatz, "Geometric organization of the extracellular matrix in the control of integrin-mediated adhesion and cell function in osteoblasts," *Progress in Orthodontics*, vol. 6, no. 2, pp. 232–237, 2005.
- [64] J. Y. Shen, M. B. E. Chan-Park, Z. Q. Feng, V. Chan, and Z. W. Feng, "UV-embossed microchannel in biocompatible polymeric film: application to control of cell shape and orientation of muscle cells," *Journal of Biomedical Materials Research Part B*, vol. 77, no. 2, pp. 423–430, 2006.
- [65] K. Isama and T. Tsuchiya, "Enhancing effect of poly(L-lactide) on the differentiation of mouse osteoblast-like MC3T3-E1 cells," *Biomaterials*, vol. 24, no. 19, pp. 3303–3309, 2003.
- [66] S. Haimi, L. Moimas, E. Pirhonen et al., "Calcium phosphate surface treatment of bioactive glass causes a delay in early osteogenic differentiation of adipose stem cells," *Journal of Biomedical Materials Research Part A*, vol. 91, no. 2, pp. 540–547, 2009.
- [67] Z. Ge, L. Wang, B. C. Heng et al., "Proliferation and differentiation of human osteoblasts within 3D printed poly-lactic-co-glycolic acid scaffolds," *Journal of Biomaterials Applications*, vol. 23, no. 6, pp. 533–547, 2009.

Research Article

Electrospun Collagen: A Tissue Engineering Scaffold with Unique Functional Properties in a Wide Variety of Applications

Balendu Shekhar Jha,¹ Chantal E. Ayres,² James R. Bowman,³ Todd A. Telemeco,⁴ Scott A. Sell,⁵ Gary L. Bowlin,² and David G. Simpson¹

¹ Department of Anatomy and Neurobiology, Virginia Commonwealth University, Richmond, VA 23298, USA

² Department of Biomedical Engineering, Virginia Commonwealth University, Richmond, VA 23298, USA

³ School of Medicine, Virginia Commonwealth University, Richmond, VA 23298, USA

⁴ Division of Physical Therapy, Shenandoah University, Winchester, VA 22601, USA

⁵ Physical Medicine and Rehabilitation Service, Hunter Holmes McGuire VA Medical Center, Richmond, VA 23249, USA

Correspondence should be addressed to David G. Simpson, dgsimpso@vcu.edu

Received 1 October 2010; Accepted 9 February 2011

Academic Editor: Wei He

Copyright © 2011 Balendu Shekhar Jha et al. This is an open access article distributed under the Creative Commons Attribution License, which permits unrestricted use, distribution, and reproduction in any medium, provided the original work is properly cited.

Type I collagen and gelatin, a derivative of Type I collagen that has been denatured, can each be electrospun into tissue engineering scaffolds composed of nano- to micron-scale diameter fibers. We characterize the biological activity of these materials in a variety of tissue engineering applications, including endothelial cell-scaffold interactions, the onset of bone mineralization, dermal reconstruction, and the fabrication of skeletal muscle prosthetics. Electrospun collagen (esC) consistently exhibited unique biological properties in these functional assays. Even though gelatin can be spun into fibrillar scaffolds that resemble scaffolds of esC, our assays reveal that electrospun gelatin (esG) lacks intact α chains and is composed of proinflammatory peptide fragments. In contrast, esC retains intact α chains and is enriched in the $\alpha 2(I)$ subunit. The distinct fundamental properties of the constituent subunits that make up esC and esG appear to define their biological and functional properties.

1. Introduction

Electrospinning has been used to fabricate a variety of polymers, including natural proteins [1–3], sugars [4], synthetic polymers [5, 6], and blends of native and synthetic polymers [7–9] into tissue engineering scaffolds composed of nano- to micron-scale diameter fibers, a size-scale that approaches the fiber diameters observed in the native extracellular matrix (ECM). The physical, biochemical, and biological properties of these unique biomaterials can be regulated at several sites in the electrospinning process. As this technology has matured, it has become apparent that many electrospun nanomaterials exhibit unusual, and often surprising, properties.

For many polymers, physical properties, including fiber diameter, pore dimension, and degree of scaffold anisotropy, can be regulated by controlling the composition of the electrospinning solvent, the air gap distance, accelerating voltage,

mandrel properties, and/or the identity, concentration, and degree of chain entanglements (viscosity) present in the starting solutions [10–12]. The ability to directly manipulate these fundamental variables can have a dramatic impact on the structural and functional properties of electrospun materials. This is especially true when considering native proteins and blends of synthetic polymers and native proteins.

Collagen represents the most abundant protein of the mammalian ECM. As such, this natural polymer has long been used as a biomaterial in a variety of tissue engineering applications. This crucial ECM protein, as well as a variety of other native proteins, can be electrospun into fibers that resemble the native state [1]. Not surprisingly, the fibers of electrospun collagen do not appear to fully reconstitute the structural or mechanical properties of the parent material [12]. Simultaneously, it is unclear to what extent the electrospun analog “must” recapitulate the native material

to be a functional tissue engineering scaffold. The nature of the electrospun collagen fiber is the subject of debate and there are conflicting reports in the literature concerning its structural and functional properties [7, 12–15]. In this study, we compare and contrast the functional characteristics of electrospun collagen and electrospun gelatin (denatured collagen) in a variety of tissue engineering applications. We then explore how the procedures used to isolate and prepare collagen for the electrospinning process might ultimately impact its functional profile once it has been processed into a tissue engineering scaffold. We believe that it is essential to develop a more complete functional map of these novel materials to fully exploit them in the development of clinically relevant products.

2. Materials and Methods

2.1. Collagen Preparation. Collagen was isolated at 4°C. Calf-skin corium (Lampire Biologics, Pipersville, PA) was cut into 1 mm² blocks and stirred for 24 hr in acetic acid (0.5 M), processed in a blender into a slurry, and stirred for an additional 24 hr. Solutions were filtered through cheesecloth, centrifuged at 10,000 × G for 12 hr; supernatant was recovered and dialyzed against ice cold, ultra pure 18 MΩ-cm water. Collagen isolates were frozen and lyophilized. Bovine gelatin Type B isolated from skin was purchased from Sigma (75 or 225 bloom).

2.2. Electrospinning: Collagen and Gelatin. Materials were purchased through Sigma unless noted. Lyophilized collagen (at 55 mg/mL) and gelatin (Sigma, 225 bloom at 110 mg/mL) were solubilized for 12 hr in 1,1,1,3,3,3-hexafluoro-2-propanol (HFP) and electrospun [1, 7, 10]. Conditions were adjusted to produce scaffolds composed of fiber diameters that were nominally 1 μm in cross-sectional diameter. Solutions were charged to 22 kV and delivered (3–7 mL/hr) across a 25 cm air gap. Electrospun samples, designated “recovered” electrospun collagen (rEC) or “recovered” electrospun gelatin (rEG) were produced by dissolving uncross-linked electrospun scaffolds immediately after spinning in ice cold, 18 MΩ-cm water; the final protein concentration was adjusted to 1.5 mg/mL. Collagen and gelatin starting electrospinning concentrations were manipulated to produce fibers of varying diameters. Where indicated, scaffolds were vapor cross-linked (1–12 hrs) in glutaraldehyde, blocked in 0.1 M glycine, rinsed in PBS, and disinfected in 70% alcohol prior to culture experimentation or implantation.

2.3. Cell Culture: Endothelial Cells. Electrospun scaffolds were cut into 12 mm diameter circular disks and cross-linked. A sterile 6 mm diameter glass cloning ring was placed on top of each disk and supplemented with 3,000 adult human microvascular endothelial cells (Invitrogen, C-011-5C) in a total volume of 100 μL. After 20 min the culture dishes were flooded with media to ensure that the cells were immersed. Cloning rings were removed after 24 hr of culture.

2.4. Cell Culture: Osteoblasts. Type I collagen and gelatin were electrospun across a 25 cm gap and directed at a grounded 6 in diameter circular steel plate. Tissue culture dishes were placed between the source electrospinning solutions and the grounded target to directly collect fibers on the culture surfaces. After cross-linking, equal numbers of osteoblasts (Clonetics, CC-2538) were plated onto each surface and cultured for 10 days in OBM basal media (CC-3208). As controls, cells were plated onto native tissue culture plastic or random gels composed of Type I collagen (Vitrogen: Cohesion Technologies), Simpson et al. [16]. For SEM imaging, osteoblasts were cultured directly on 6 mm diameter × 500 μm thick circular disks of electrospun collagen or gelatin (conditions optimized for 1 μm diameter fibers).

2.5. Dermal Reconstruction. Adult guinea pigs were brought to a surgical plane, fur was shaved and skin swabbed in betadine. Four 1 cm² full-thickness dermal injuries (complete removal of the dermis and hypodermis and bordered by the superficial fascia of the panniculus adiposus) were prepared on the dorsum of each animal. Injuries were treated with scaffolds composed of electrospun Type I collagen or gelatin (electrospinning conditions adjusted to produce scaffolds composed of fibers ranging from 250 nm to >2000 nm in average cross-sectional diameter). Scaffolds were vapor cross-linked to varying degrees. Each wound was treated with a candidate scaffold and covered with a piece of silver gauze that was sutured in place. Silver gauze remained in place for 5–7 days. Animals recovered on a warming pad and were provided with pain mitigation. Injuries were photographed at intervals. Data on wound closure was expressed as the percent injury surface area observed at the time of implantation. Representative samples were recovered for histological evaluation.

2.6. Muscle Fabrication. Three-day-old neonatal rats were decapitated, skin was removed. Skeletal muscle was removed, minced into 1 mm² pieces in sterile PBS and rinsed until clear of blood. Tissue was incubated in a sterile flask supplemented with 0.25% trypsin (Invitrogen) in a shaking (100 RPM) 37°C water bath. At 10 min intervals, tissue was cannulated and allowed to settle, and supernatant was removed and centrifuged at 800 × G for 6 min. Cell pellets were pooled in DMEM plus 10% FBS and 1.2% Antibiotic/Antimycotic (Invitrogen 15240). A 60 minute interval of differential adhesion to tissue culture plastic was used to reduce fibroblast contamination. Myoblasts were cultured for 3–5 days under conditions that minimized cell to cell contacts. In cell labeling assays, myoblast cultures were incubated in DiO (Invitrogen, L-7781) overnight according to manufacturer's recommendations.

Electrospun scaffolds were prepared on a 4 mm diameter round mandrel. With conditions optimized to produce 1 μm diameter fibers, cylindrical constructs were fabricated with a wall thickness of 200–400 μm [7]. Scaffolds were cross-linked. Myoblasts were recovered from culture and rinsed 2x in PBS by centrifugation (800 × G, 6 min). Electrospun

cylinders were sutured shut and suspended myoblasts were injected into the lumen of the constructs. Adult 150–180 gm Sprague Dawley rats were brought to a surgical plane. Fur on the hindlimb was shaved and skin was swabbed in betadine. In short-term studies (3 wks), a 4 mm × 15 mm long cylinder supplemented with cells was inserted directly into a channel (“intramuscular” position) prepared in the vastus lateralis muscle after the methods of Telemeco et al. [7]. In long term studies, a hemostat was passed deep to the quadriceps muscle group; engineered tissue (4 mm × 40 mm) was passed under the existing muscle mass and sutured (in an extramuscular position) to the proximal and distal tendons of origin and insertion for the quadriceps. Incisions were repaired, skin was stapled, and animals recovered on a warming pad.

2.7. Electrospinning: Nylon. To separate the fiber-forming properties of the different protein fractions from their fundamental biological properties, we applied collagen and gelatin fractions to electrospun scaffolds composed of nylon 66 (Ambion). Electrospun nylon has a high surface area and exhibits high protein binding capacity. Nylon was spun after the methods of Manis et al. [17]. Conditions were optimized to produce charged nylon fibers ranging 1.0–1.5 μm in diameter.

2.8. Cell Culture: Adult Human Dermal Fibroblasts. Dermal fibroblasts (HDF), (Cascade Biologics: C-013-5C) were passaged 3–5 times in basal dermal fibroblast medium 106 supplemented with a low serum growth kit (Cascade Biologics, S-003-K) prior to experimentation.

2.9. Cell Adhesion Assays. Electrospun nylon scaffolds were immersed in 20% methanol/phosphate buffered saline (PBS) [17], rinsed 3x in PBS and installed in a dot blotter manifold (Topac Model DHM-48). Wells were supplemented with 50 μL of collagen (control samples or fractions thermally denatured at 50, 60, 70, 80 or 90°C for 1 hr) or gelatin fractions containing equal amounts of protein. After 5 min, solutions were sucked through the membrane using a vacuum pump. Scaffolds coated with 1% bovine serum albumin (BSA) were used as controls. All wells were blocked with 100 μL of 1% BSA solution for 5 min and rinsed in PBS prior to use. In each assay, 3000 HDFs were suspended in 100 μL of media and applied to each surface for 1 hr at 37°C (dot blotter was used as a culture vessel; no vacuum was applied to the cell suspensions).

After the plating interval, the dot blotter was inverted to remove nonadherent cells, scaffolds were removed, rinsed in PBS, and fixed in ice cold methanol (20 min). For analysis, scaffolds were rinsed 5x in PBS plus 0.5% Triton, and incubated overnight at 4°C in primary goat antirabbit GAPDH antibody (Sigma # G9545, 1:5000). All antibodies were diluted in LiCor Odyssey Blocking Buffer (L-OiBB), and LOiBB plus 0.1% Tween-20 was used in all rinses. Cultures were rinsed 5x in L-OiBB, counter-stained with goat antirabbit IRDye 800 secondary antibody (LiCor 1:1000) for 1 hr and rinsed 5x. Data sets were captured at a line resolution of 169 μm using a Li-Cor Odyssey Infrared Imager.

Adhesion was expressed as “Integrated Intensity” (signal-mm²). Integrated intensity values were extrapolated to cell number using a standard curve of cells plated in parallel with the unknowns. Data sets were screened by one-way ANOVA ($P < .01$), Dunn’s Method ($P < .05$), and a Mann-Whitney Rank Sum test ($P < .001$) was used in *post hoc* analysis. In cyclic RGD competition experiments, HDFs (10,000 cells per treatment) were incubated for 15 min at 37°C with 0.01, 0.1, or 1 $\mu\text{g}/\text{mL}$ cyclic RGD peptide (Bachem, H-2574) or 1 $\mu\text{g}/\text{mL}$ control RGD peptide (Bachem, H-4088). The cells were then plated for 1 hr on the different surfaces and were processed to image GAPDH as described.

2.10. Alpha Chain Analysis. Collagen samples were diluted to 0.15 mg protein/mL in Laemmli sample buffer and separated by SDS interrupted gel electrophoresis using 10% polyacrylamide gels. Gels were run until the dye front reached the base of the stacking gel, 1 mL of Laemmli buffer supplemented with 20% β -mercaptoethanol was added to the gel stacker and incubated for 30 min at room temperature. The separation run was then completed. Gels were stained with Coomassie brilliant blue overnight, de-stained and photographed. Densitometric analysis was conducted with NIH ImageJ software.

2.11. Cross-Linking Assays. See Newton et al. [12] for details of this assay. Percent cross-linking was calculated from the formula

$$\% \text{ cross-linked} = 1 - \frac{\text{Abs}_c/\text{mass}_c}{\text{Abs}_{nc}/\text{mass}_{nc}}, \quad (1)$$

where Abs_c = absorbance of the controls at 345 nm; the unit of mass is given in mg. Abs_{nc} = absorbance of the unknowns at 345 nm; again the unit of mass is given in mg. All data is expressed as percent of cross-linking observed in electrospun scaffolds (controls) that have not been exposed to cross-linking reagents.

2.12. Scanning Electron Microscopy. Samples were sputter-coated and imaged with a Zeiss EVO 50 XVP scanning electron microscope (SEM) equipped with digital image acquisition. Average fiber diameter and pore area data was determined from representative samples using NIH ImageTool (UTHSCSA version 3). All fiber diameter measurements were taken perpendicular to the long axis of electrospun fibers [10, 11].

2.13. Transmission Electron Microscopy. Samples were immersed in 2% glutaraldehyde for 12 hr at 4°C and postfixed in 1.0% osmium plus or minus 2.5% potassium ferricyanide [6, 7]. All samples were subjected to a graded series of dehydration and embedded in Poly/Bed (Polysciences).

3. Results

3.1. Functional Performance of Electrospun Collagen. To compare and contrast the biological properties of electrospun

collagen and electrospun gelatin, we conducted a series of *in vitro* and *in vivo* functional assays.

3.1.1. Endothelial Cell Growth. Critical to the bioengineering paradigm is the development of tissue engineering scaffolds that can support the proliferation and penetration of vascular elements. To evaluate this characteristic *in vitro*, we plated microvascular endothelial cells onto electrospun scaffolds of Type I collagen and electrospun gelatin composed of varying fiber diameters. During the initial plating phase, and over time in culture, cell shape, on both surfaces (collagen and gelatin), was modulated by the fiber size (and likely the pore characteristics that “travel” with the fiber size that is present in an electrospun scaffolds [10]) (Figure 1). Electrospun scaffolds of collagen and gelatin composed of small diameter fibers induced the expression of a highly flattened and stellate cell shape. This cell shape was retained throughout the culture interval on both surfaces (e.g., Figure 1 compare (a) = day 1 with (b) = day 7 as well as (i) and (j)). With increasing fiber diameter, the cells assumed a more rounded and elongated phenotype. After 10 days, microvascular endothelial cells cultured on collagen- or gelatin-based scaffolds with average cross-sectional fiber diameter less than about 1.0–1.50 μm remained on the dorsal surfaces of the constructs (Figure 1 (q), (r), (u) and (v)). As fiber size exceeded this threshold value and pore size increased to about 10,000 nm^2 , the cells began to penetrate into the scaffolds (Figure 1 (s), (t), (w) and (x)). These results suggest that the physical arrangement of fibers (i.e., the pore characteristics) plays a role in regulating the infiltration of endothelial cells into an electrospun scaffold.

3.1.2. Osteoblast Differentiation. The 67 nm banding pattern typical of native Type I collagen is associated with the formation of nucleation and binding sites critical to the mineralization process in bone [18]. Superficially, electrospun fibers of collagen exhibit a similar structural motif. To examine the potential functional consequences of this motif, we plated osteoblasts onto surfaces coated with electrospun collagen and electrospun gelatin. Cultures plated onto surfaces coated with electrospun collagen exhibited low rates of proliferation and failed to form a confluent cell layer, even after 8 days. Phase bright crystals were present throughout these cultures (Figure 2). Cells plated onto surfaces coated with electrospun gelatin, Type I collagen gels, or native tissue culture plastic proliferated and formed a confluent cell layer over this same culture interval. Phase bright crystals were infrequently observed in any of these cultures. These data suggest electrospun collagen contains structural motifs necessary and sufficient to induce osteoblast differentiation and subsequent formation of hydroxyapatite crystals.

3.1.3. Dermal Reconstruction. From an architectural standpoint, tissue engineering electrospun scaffolds are theoretically very well suited for applications in dermal reconstruction. These constructs are deposited as nonwoven, fibrillar structures that exhibit an extensive void volume and pores that are completely interconnected with one another. To

evaluate the efficacy of using electrospun collagen as a dermal template, we treated full thickness dermal injuries with various permutations of this material. To track the healing process, we measured total wound surface area as a function of treatment and time. We have used this metric because interventions that reduce wound contraction (as measured by an *increased* retention of wound surface area once the injury is healed) are associated with less scarring and more complete tissue regeneration [19].

In the first series of experiments, we treated wounds (1 cm^2) with dermal templates fabricated from electrospun collagen under conditions that produced fibers ranging 750–1,000 nm. These scaffolds were postprocessed to cross-link approximately 50% of the available sites. Wound closure took place in 16 days with these constructs (Figure 3(a)). When the extent of cross-linking was increased to 70% in these constructs, wound healing was delayed modestly and wound surface area was dramatically increased, a feature indicative of increased regeneration (Figures 3(a) and 3(c)). Histological examination of the tissue reconstituted with templates composed of electrospun collagen consistently revealed a smooth continuum of infiltrating cells. There were no overt signs of inflammation or fibrosis along the interface of the implanted templates and the adjacent uninjured tissue, regardless of the fiber diameter composition present in electrospun constructs of Type I collagen (Figures 4(a)–4(c)). Our tissue culture experiments demonstrated that the intrinsic architectural features present in an electrospun scaffold can modulate the extent to which endothelial cells can penetrate into these constructs. We observed a similar trend in our dermal reconstruction experiments. Injuries treated with templates composed of fibers less than 500 nm in diameter were less densely populated than templates composed of fibers greater than 750–1000 nm in diameter (Figure 4).

In parallel experiments conducted with a wide variety of electrospun scaffolds composed of gelatin (average fiber diameters ranging from 250 nm to approximately 3000 nm), we were unable to replicate these results. Wounds treated with electrospun gelatin consistently healed in the classic X shaped configuration (Figure 3(d)) that develops in response to wound contraction, this feature developed regardless of the fiber diameter or the degree of cross-linking present in the gelatin-based scaffolds. These scaffolds were consistently infiltrated by foreign body giant cells, indicating an inflammatory response to the implanted electrospun gelatin (Figures 4(d)–4(f)). These data indicate that architectural features and the biochemical identity of an electrospun scaffold composed of collagen interact to define its unique functional characteristics.

3.1.4. Muscle Engineering. To evaluate the efficacy of using electrospun collagen in a cell-based tissue engineering application, we used an *in situ* strategy to fabricate skeletal muscle prosthetics. In these experiments we electrospun Type I collagen onto a rotating 4 mm diameter mandrel; this resulted in the formation of a hollow cylinder with walls composed of 1 μm diameter fibers of electrospun collagen. These cylinders

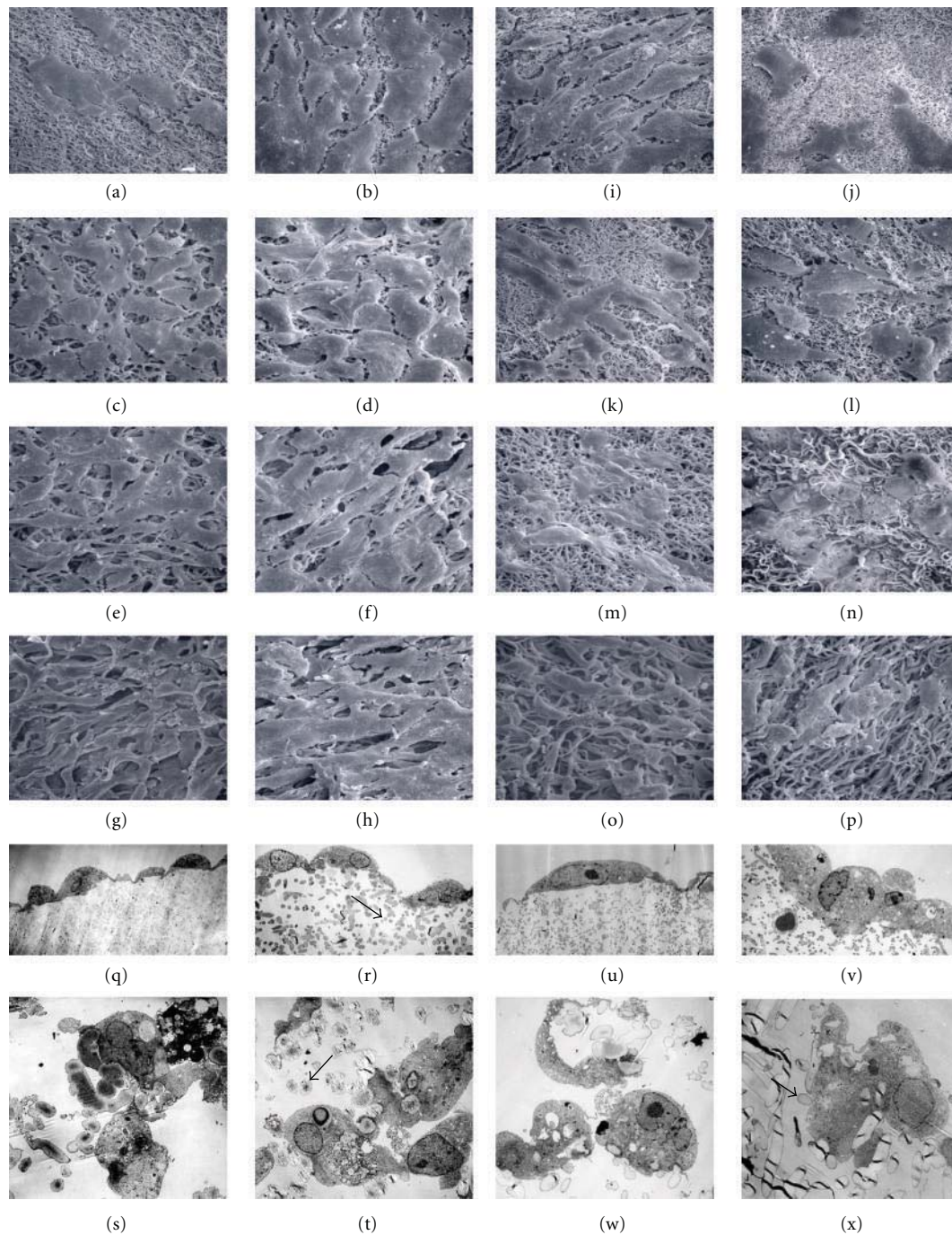


FIGURE 1: Endothelial interactions with electrospun collagen ((a)–(h)) and gelatin ((i)–(p)). Endothelial cell shape varied as a function of increasing fiber diameter on both electrospun collagen (Day 1: (a), (c), (e), (g) & Day 7: (b), (d), (f), (h)) and electrospun gelatin (Day 1: (i), (k), (m), (o) & Day 7: (j), (l), (n), (p)). Cell shape established during the early stages of plating persisted throughout the entire culture interval (e.g., for each scaffold cells at day 1 appeared to exhibit a similar cell shape after 7 days of culture). Cells expressed and retained a highly flattened and stellate shape when plated onto scaffolds composed of fibers less than 1,500 nm ((a)–(l)). At larger fiber sizes the cells exhibited a more elongated phenotype, this was especially evident on the collagen-based scaffolds ((e), (f), (g) and (h)). Penetration into the scaffolds was primarily regulated by average fiber diameter and pore size. TEMs of cross-sectional images of cells plated onto electrospun collagen ((q)–(t)) and electrospun gelatin ((u)–(x)) for 10 days. Average fiber diameters for collagen (a) & (q) = 449 ± 122 nm, (c) & (r) = $1,187 \pm 297$ nm, (e) & (s) = $1,886 \pm 513$ nm and (g) & (t) = $2,756 \pm 855$ nm. In gelatin (i) & (u) = 198 ± 50 nm, (k) & (v) = 491 ± 114 nm, (m) & (w) = $1,252 \pm 302$ nm, and (o) & (x) = $1,619 \pm 414$ nm (all fiber measurements from dry scaffolds prior to processing for cross-linking). Note that penetration was not evident until a nominal average fiber diameter of about 1,800 nm was achieved in the scaffolds (arrows in (r), (t), (x) indicate fibers in cross section). Scale bar in (a) = $20 \mu\text{m}$.

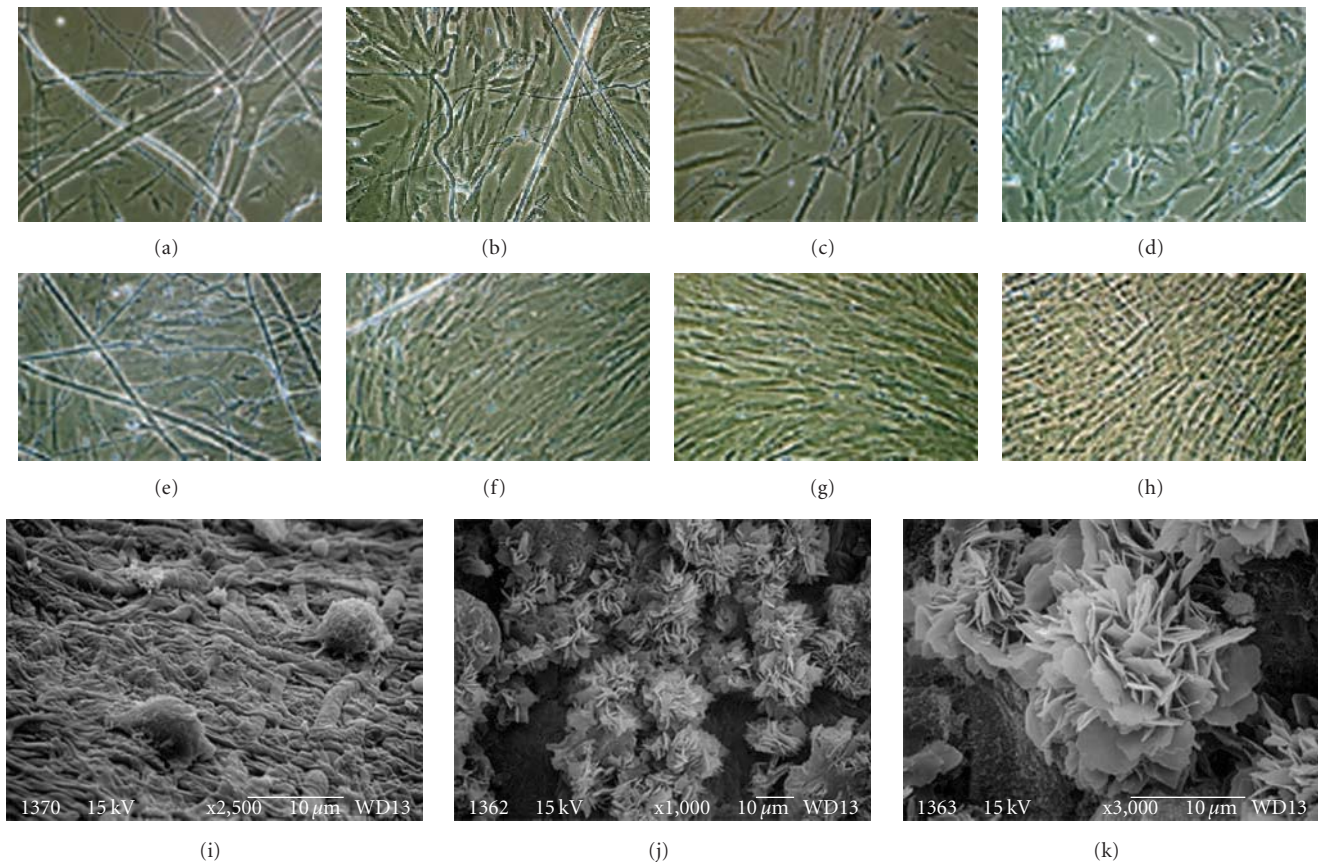


FIGURE 2: Osteoblast interactions with electrospun collagen and electrospun gelatin. Human osteoblasts plated for 1 (a)–(d) or 8 days (e)–(h). Cells plated on electrospun collagen ((a), (e)), electrospun gelatin ((b), (f)), collagen gel ((c), (g)), or tissue culture plastic ((d), (h)). Cells plated onto electrospun collagen remain subconfluent after 8 days of culture (e) and accumulated phase bright crystals. At the ultrastructural level, osteoblasts plated onto electrospun gelatin expressed a rounded cell shape (i); when plated onto electrospun collagen, the cells were covered with elaborate arrays of plate-like structures typical of hydroxyapatite crystals ((j), (k)).

were then supplemented with myoblasts and implanted directly into the vastus lateralis muscle. After 3 weeks, tissue fabricated with electrospun collagen was densely populated with cells. Nascent myotubes and functional blood vessels were evident throughout these implants (Figure 5). As with the dermal-templates, we observed a smooth continuum between the surrounding tissue and the engineered muscle with no evidence of fibrosis. In contrast to these results, tissue fabricated with gelatin based materials was necrotic, exhibited extensive fibrosis at the tissue interface and a massive infiltration of lymphocytes.

Given these results we next prepared engineered muscle tissue fabricated with electrospun collagen and directly sutured the constructs to the tendons of origin and insertion for the quadriceps muscle. These constructs were placed in an extramuscular position; in effect we are converting the quadriceps muscle into a “quintriceps” muscle. After 8 weeks, the engineered muscle was densely packed with fully differentiated myotubes that were distributed into stacked and linear parallel arrays that mimicked native tissue (Figure 6). This developing muscle tissue displayed well-formed myofibrillar elements. However, a range of cytoskeletal structural

patterns was observed. For example, some areas of the tissue displayed loosely packed arrays of myofibrils (Figures 6(d) and 6(e)); other domains differentially took up the stains used to enhance contrast for light (Figure 6(g)) and transmission electron microscopy (Figure 6(h)). We suspect this differential staining is a reflection of protein density or protein identity with respect to the myofibrillar subunits. Collagen bundles were evident along the borders of the implanted tissue.

3.2. Analysis of Collagen Alpha Chain Structure and Function

3.2.1. Protein Analysis. We next conducted experiments to characterize how various processing conditions impact acid-soluble collagen and how these manipulations might regulate the evolution of the functional properties of an electrospun fiber. We first examined the effects of thermal denaturation on Type I collagen. These experiments were conducted to provide us with a benchmark for the evaluation of collagen structure and its α chain content in response to various steps in the electrospinning process. Collagen was isolated from calfskin corium using classical acid extraction methods,

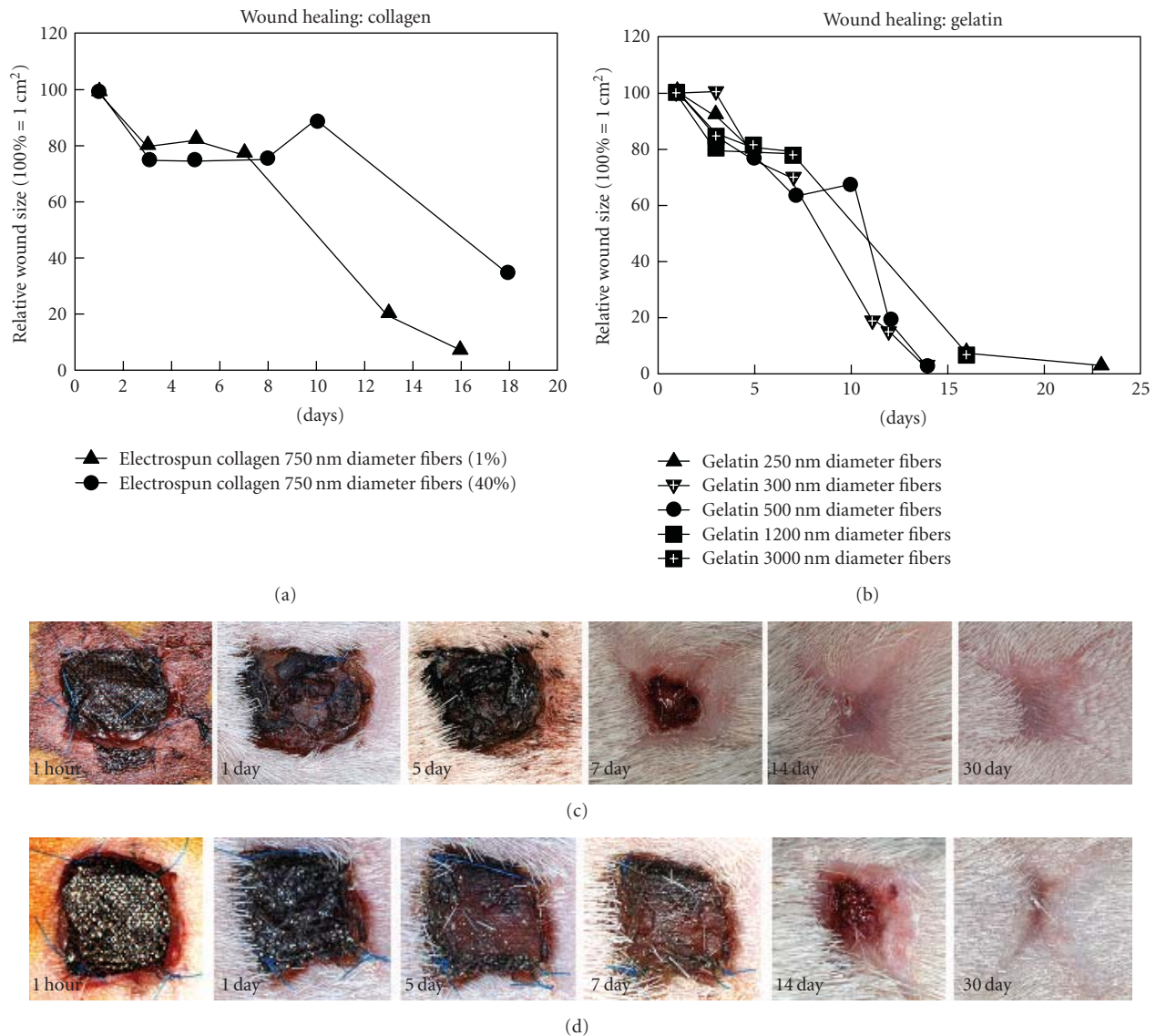


FIGURE 3: Dermal Reconstruction. Rates of wound closure in lesions treated with electrospun collagen (a) or electrospun gelatin (b). Note that increasing the extent of cross-linking has a modest effect on slowing wound closure and greatly increases total wound surface area in animals treated with electrospun collagen (a) and (c). Rates of wound closure were similar when injuries were treated with a wide variety of gelatin-based constructs (b) and (d). Panel (c) depicts the typical wound healing course for injuries treated with electrospun collagen in which approximately 70% of the available sites are cross-linked. Note the retention of wound surface area in this example. Panel (d) depicts the typical wound healing course for injuries treated with electrospun gelatin in which approximately 70% of the available sites are cross-linked. Note the classically X-shaped wound typical of a lesion that has undergone contraction.

a procedure routinely used to prepare collagen as a biomaterial and for use in the electrospinning process [1, 7]. Figure 7 illustrates an SDS gel depicting the α chain content of the acid soluble parent extract with respect to fractions that have been subjected to varying degrees of thermal denaturation.

Protein fractions were held at 4°C or heated to 50, 60, 70, 80, or 90°C for 1 hr. Detectable changes in the protein banding patterns present on the SDS gels were visible in all samples subjected to heating. Densitometric analysis of the separated protein fractions revealed that 50% of the collagen α chains were lost within 1 hr when soluble collagen was exposed to 70°C (Figure 7). Exposure to higher

temperatures accelerated the loss of the collagen α chains from the soluble fractions and resulted in progressively more α chain fragmentation and smearing in the gel lanes typical of a sample that has been broken down into a heterogeneous mixture of peptides. At temperatures of 80°C and greater, the protein bands corresponding to the individual α chains were completely lost after the 1 hr incubation interval. Commercially procured gelatin (collagen that has been heated and denatured during isolation) samples exhibited little or no protein banding associated with intact α chains on the SDS gels; these samples ran nearly exclusively as a continuous smear of proteins (not shown, see [7]).

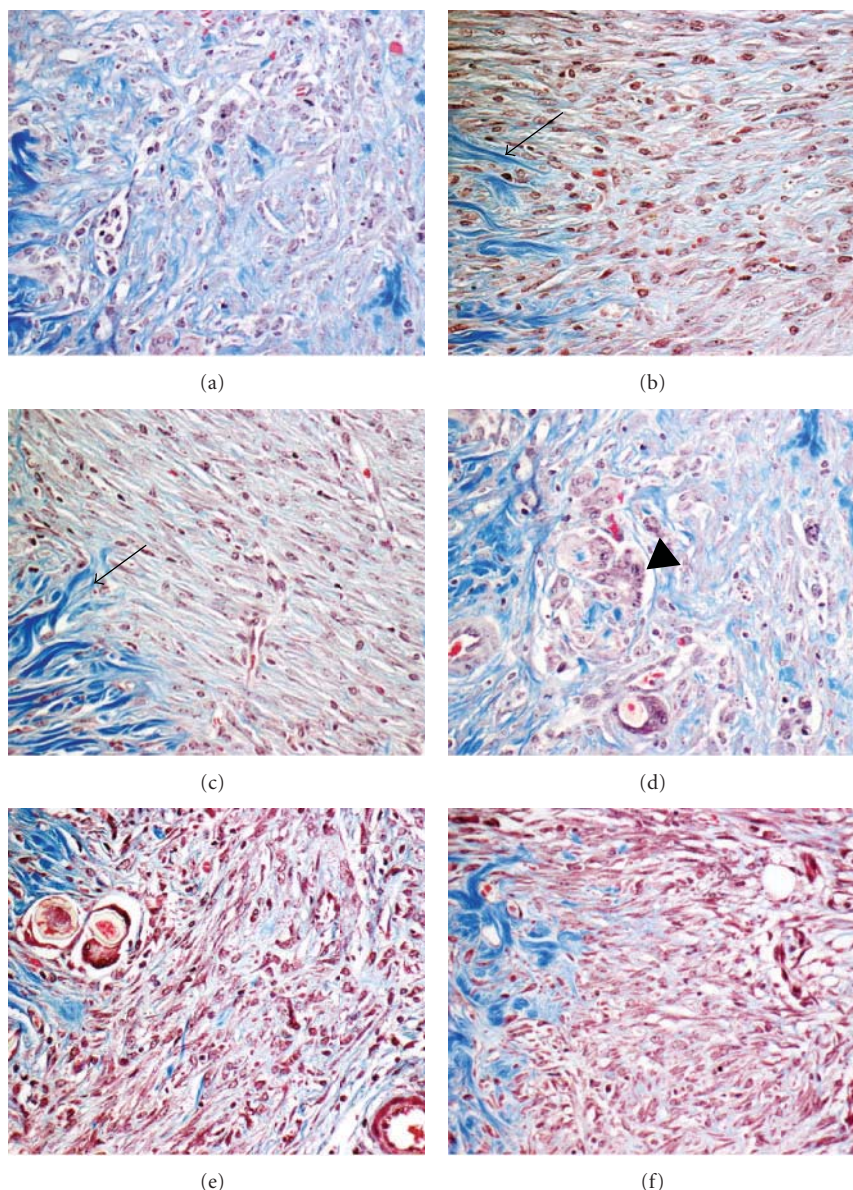


FIGURE 4: Dermal Reconstruction. Healing response to electrospun collagen (a)–(c) and electrospun gelatin (d)–(f) as a function of fiber diameter and pore dimension. Collagen-based implants exhibited a smooth continuum of cells at the interface of the lesion and the surrounding tissue. In each of the images depicted in this figure, native, uninjured tissue appears to the left of each data image (delineated by the large blue staining collagen bundles in the histological preparations, arrows (b) and (c)). Gelatin based-scaffolds were consistently less heavily infiltrated and exhibited evidence of an inflammatory response and accumulated foreign body giant cells (arrow head (d)). (a) and (d) average fiber diameter = 240–280 nm, average pore dimension = 1500–2000 nm², (b) and (e) average fiber diameter 500–600 nm, average pore dimension 3000–5000 nm², (c) and (f) average fiber diameter 800–1000 nm, average pore dimension 4000–5000 nm.

To examine how the electrospinning process (solvents, electric field, and the flash-lyophilization of proteins that occurs during fiber formation) might alter collagen α chain content, we next prepared scaffolds composed of electrospun Type I collagen or commercially sourced gelatin (conditions optimized to produce average fiber diameters = 1 μ m). As judged by scanning electron microscopy, these scaffolds were superficially identical. However, transmission electron microscopy reveals that scaffolds of electrospun

collagen exhibit the 67 nm banding pattern typical of the native fibril (Figures 8(a)–8(d)). In contrast, fibers of the electrospun gelatin lack this distinctive structure and are nearly homogenous in appearance.

For protein characterization of the electrospun scaffolds, we redissolved the collagen and gelatin-based scaffolds and separated the resulting extracts by SDS gel electrophoresis. The protein banding patterns on the gels and the specific complement of α chains in the electrospun collagen and

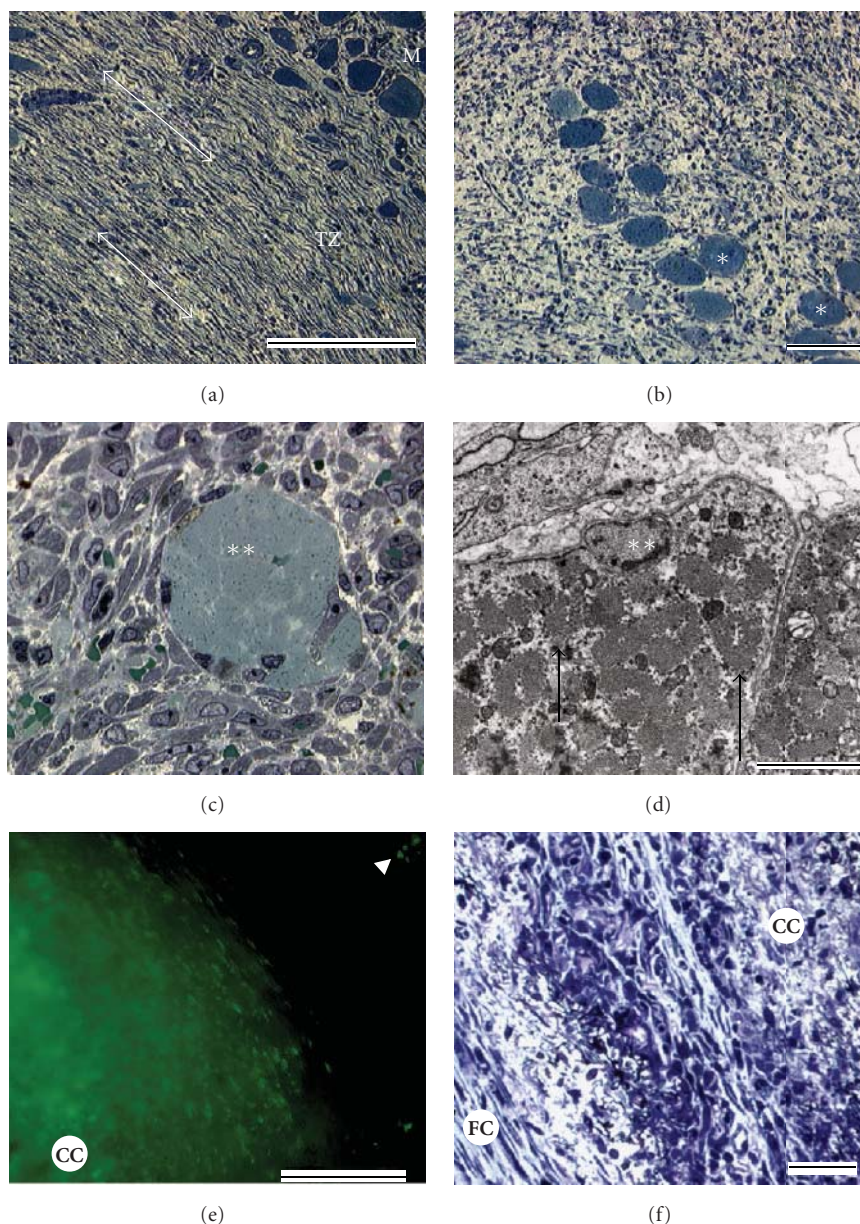


FIGURE 5: Muscle Fabrication: 3 Weeks. (a) Cross-section through the wall of cylindrical construct placed within the tissue of the rat vastus lateralis. M = endogenous host muscle tissue, TZ = transitional zone occupied by the wall of the electrospun construct. Note the lack of a fibrotic capsule. ((b), (c)) Sections taken from within the lumen of the tissue, dense cell populations are evident as are nascent myotubes (*). Scattered vascular elements are apparent and intermingle with the surrounding cell population. (d) TEM cross-section of developing myotube with forming myofibrillar elements (arrows). (e) Cell labeling experiments indicate that few cells migrate out of the implanted tissues (arrowhead). The bulk of the labeled cells are retained within the lumen of the electrospun constructs. (f) Tissue fabricated from gelatin undergoes necrosis and develops a fibrotic capsule (FC). CC = central core of implant.

the control starting material (Acid soluble Type I Collagen: Figure 7) were similar, but not identical. Samples of electrospun collagen exhibited subtle derangements in α chain content and, as judged by densitometric analysis, it was enriched in the $\alpha 2$ (I) content (see Figure 7) with respect to the other α chains. Protein separation analysis of the electrospun gelatin revealed, as expected, nearly complete α chain fragmentation (these samples displayed complete fragmentation even prior to the electrospinning process) and

was comparable to the calfskin collagen samples heated to 90°C for 1 hr (Figure 7).

3.2.2. Alpha Chain Functional Properties. Next we examined how thermal manipulation impacted the adhesion properties of acid-soluble collagen and its electrospun variants. In these experiments, we coated electrospun fibers of charged nylon with equal amounts of the various protein fractions described in Figure 7. This strategy made it possible to

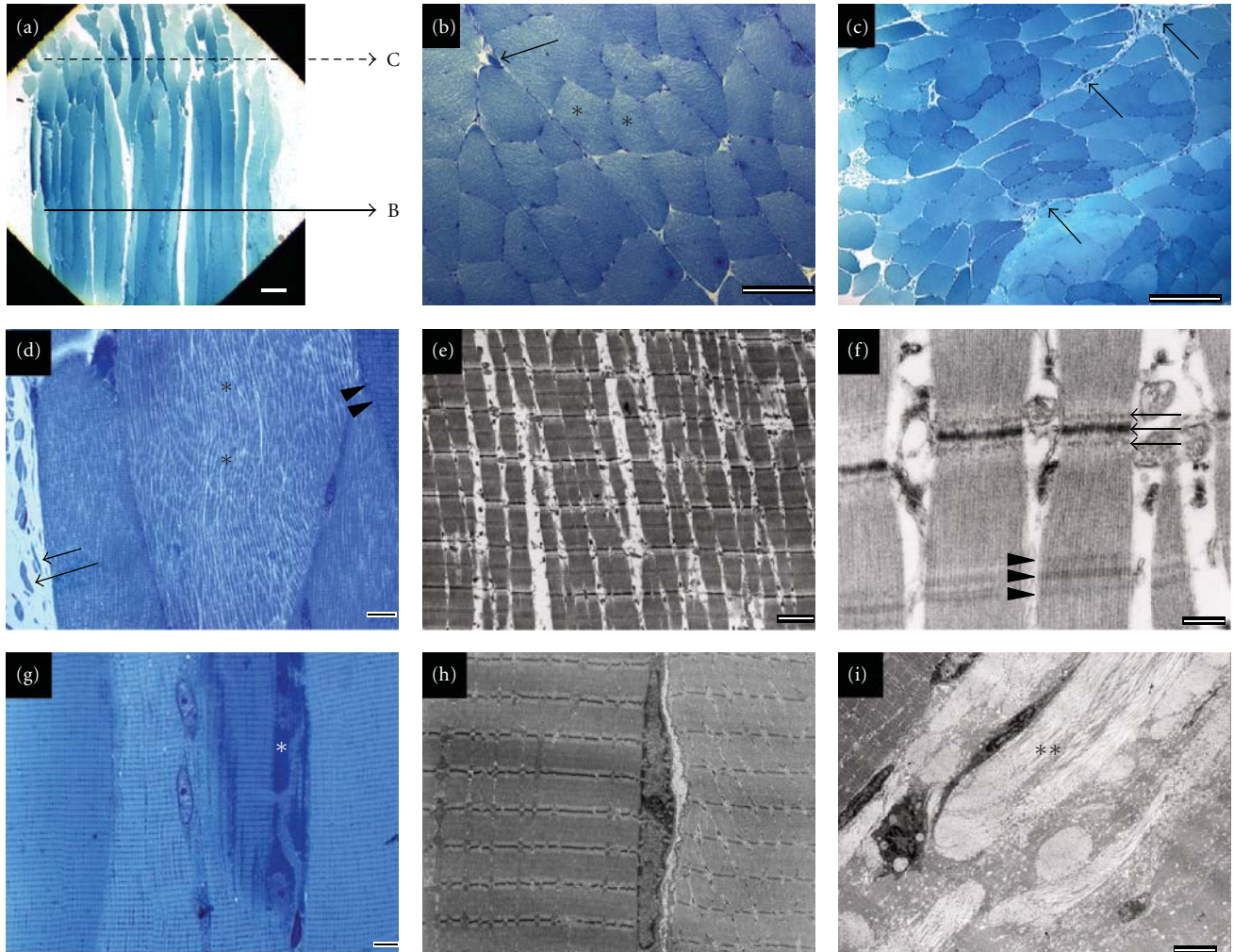


FIGURE 6: Muscle Fabrication: 8 Weeks. (a) Low magnification survey image depicting the terminal portions of muscle tissue engineered *in situ*. Images depicted in panels (b) and (c) were taken from the cross-sectional area denoted as “B” and “C”, respectively in panel (a). The tissue distal to the attachment sites exhibited stacked arrays of myotubes ((b), asterisks). Tissue alignment is disrupted to some degree at the distal attachment sites as a consequence of the sutures used to place the tissue ((c), arrows indicate functional blood vessels). Myofibril density is observed to vary within cells that are in close proximity to one another ((d), arrowheads and asterisk; also the myofibrillar density in (d) and (e) to (g) and (h)) and some subdomains of the tissue stain differentially at both the light (g) and EM levels (h) with stains designed to enhanced contrast. The tissue is highly biosynthetic as evidence by the accumulation of proteins in the vicinity of the nuclei and golgi (g, asterisk). A subset of engineered tissue exhibits sarcomeres (f) with unusual cytoarchitectural patterns at the Z bands (arrows) and H zones (arrowheads) characterized by accessory electron dense structures. At the ultrastructural level, the implants are surrounded by collagen fibrils ((i) asterisks).

separate the fiber-forming capacity of each fraction from the biological activity that it displayed while presenting each fraction in a “matrix” that exhibited identical architectural patterns (fiber size, pore properties, and material properties). Equal numbers of dermal fibroblasts were then plated onto protein-coated electrospun nylon fibers. Rates of adhesion to the parent collagen fraction were approximately 50% greater than rates of adhesion to BSA-coated surfaces (Figure 8(e)). With one exception, thermal manipulation of the acid-soluble collagen fractions did not dramatically impact functional performance in these assays. Samples heated to 70°C supported substantially higher rates of adhesion than the BSA-coated surfaces and all of the other collagen fractions

($P < .002$), the gelatin samples ($P < .001$), and the samples recovered from electrospun scaffolds ($P < .001$). Rates of adhesion to Type I collagen recovered after electrospinning were not statistically different from the parent controls and were qualitatively much higher than gelatin and the electrospun gelatin samples.

The denaturation of collagen α chains uncovers RGD binding sites [20, 21]. To test for the presence of these sites in the different samples, we challenged cells in the adhesion assays with increasing amounts of cyclic RGD peptide. The RGD peptide reduced adhesion in the control samples by about 20% and nearly 60% in collagen samples that been heated to 70°C. No inhibition was detected in the collagen

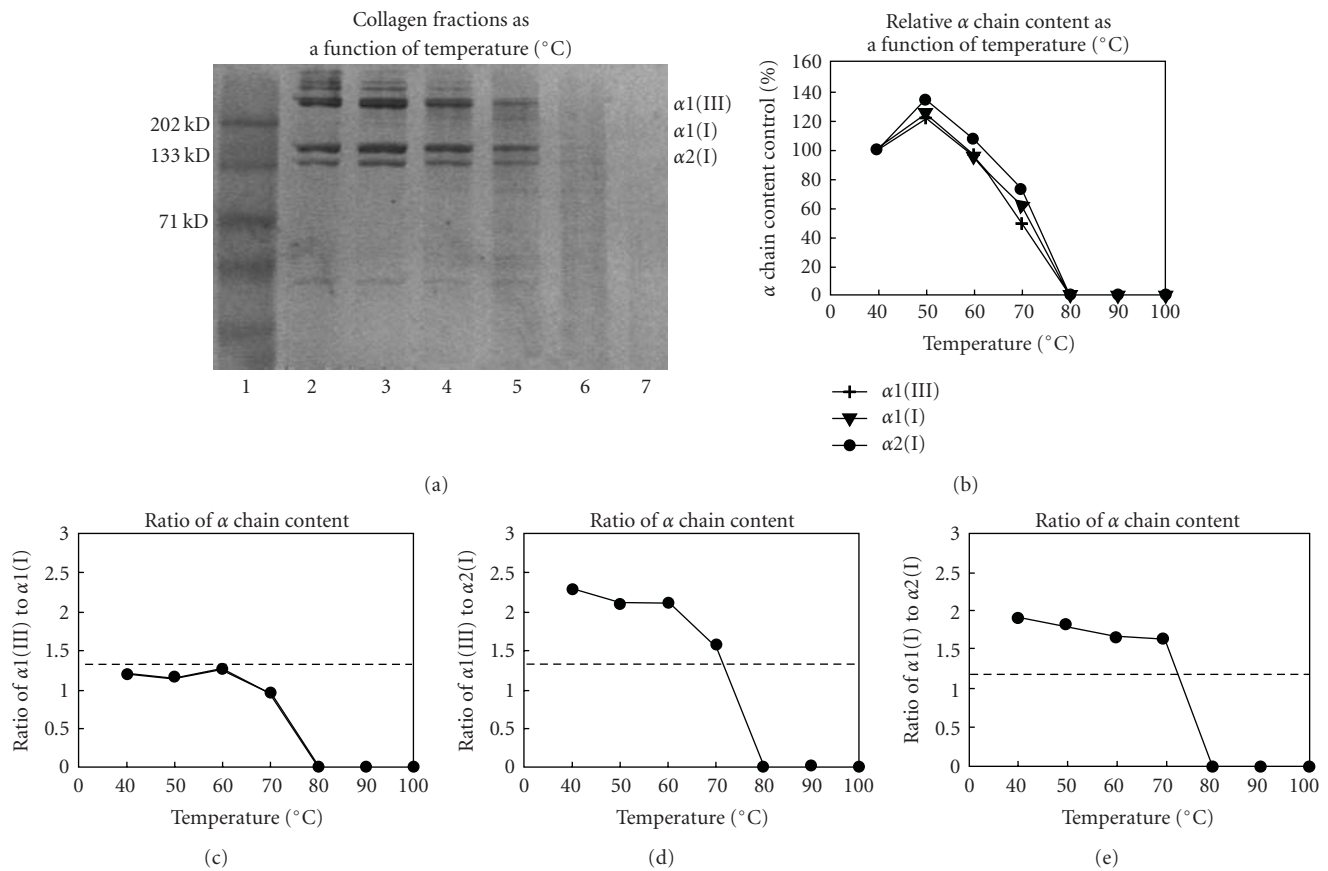


FIGURE 7: Analysis of Type I collagen α chain content. (a) Representative SDS gel depicting the affect of various degrees of heat denaturation on soluble collagen. Lane 1 = MW standards, 2 = control sample maintained and stored at 4°C, 3 = sample heated to 50°C for 1 hr, 4 = 60°C, 5 = 70°C, 6 = 80°C, and 7 = 90°C. (b) Densitometric analysis of α chain content from denaturation experiments. (c) Densitometric analysis (c) ratio of $\alpha 1(\text{III})$ to $\alpha 1(\text{I})$, (d) ratio of $\alpha 1(\text{III})$ to $\alpha 2(\text{I})$, (e) ratio of $\alpha 1(\text{I})$ to $\alpha 2(\text{I})$ as a function of thermal insult. Dotted lines in (c)–(e) depicts the actual ratio of the α chains present in collagen recovered immediately after electrospinning (no thermal insult).

recovered after electrospinning (Figure 8(f)). It is clear from the RGD-based competition assays that collagen recovered after electrospinning behaves very differently than denatured collagens or material recovered from a scaffold of electrospun gelatin. This observation is relevant when considering the functional properties of an electrospun collagen fiber that appears to lack the 67 nm repeat banding pattern. As long as the α chains are intact, even if they are not arrayed into a polymeric form that exhibits the 67 nm repeat banding pattern, these fibers can be expected to exhibit unique and potent biological properties. Together, our SDS gel assays and adhesion results indicate that electrospinning does not directly denature collagen α chains.

4. Discussion

In this study, through our functional assays, we explored the biological properties of electrospun collagen and electrospun gelatin. These two materials (collagen and gelatin) consistently exhibited very different functional profiles in all our assays. We note that endothelial cells began to penetrate into the fiber arrays of both electrospun collagen and electrospun

gelatin once a critical fiber/pore threshold was reached. However, subjectively cell growth appeared to be much more rapid on the collagen-based scaffolds. We conclude from these *in vitro* experiments, in the absence of an inflammatory cascade or other antigenic complications, that endothelial cell infiltration is not limited by scaffold composition. Rather, gross structural properties are more important in this type of setting. The composition of the scaffolds appeared to dictate more subtle functional characteristics that regulated cell growth.

Cell culture experiments conducted with osteoblasts indicate that fibrils of electrospun collagen appear to be sufficient to induce differentiation and promote the accumulation of hydroxyapatite crystals *in vitro*. We believe this rather unexpected result may be a reflection of an intrinsic structural motif that is uniquely present in electrospun collagen. We did not observe this same result when we plated cells onto a collagen gel, a form of collagen that normally self-assembles into fibrils that contain a repeating banding pattern that also mimics native collagen [22]. Since both electrospun collagen and the fibers present in a collagen gel can exhibit a banding pattern, it is unclear

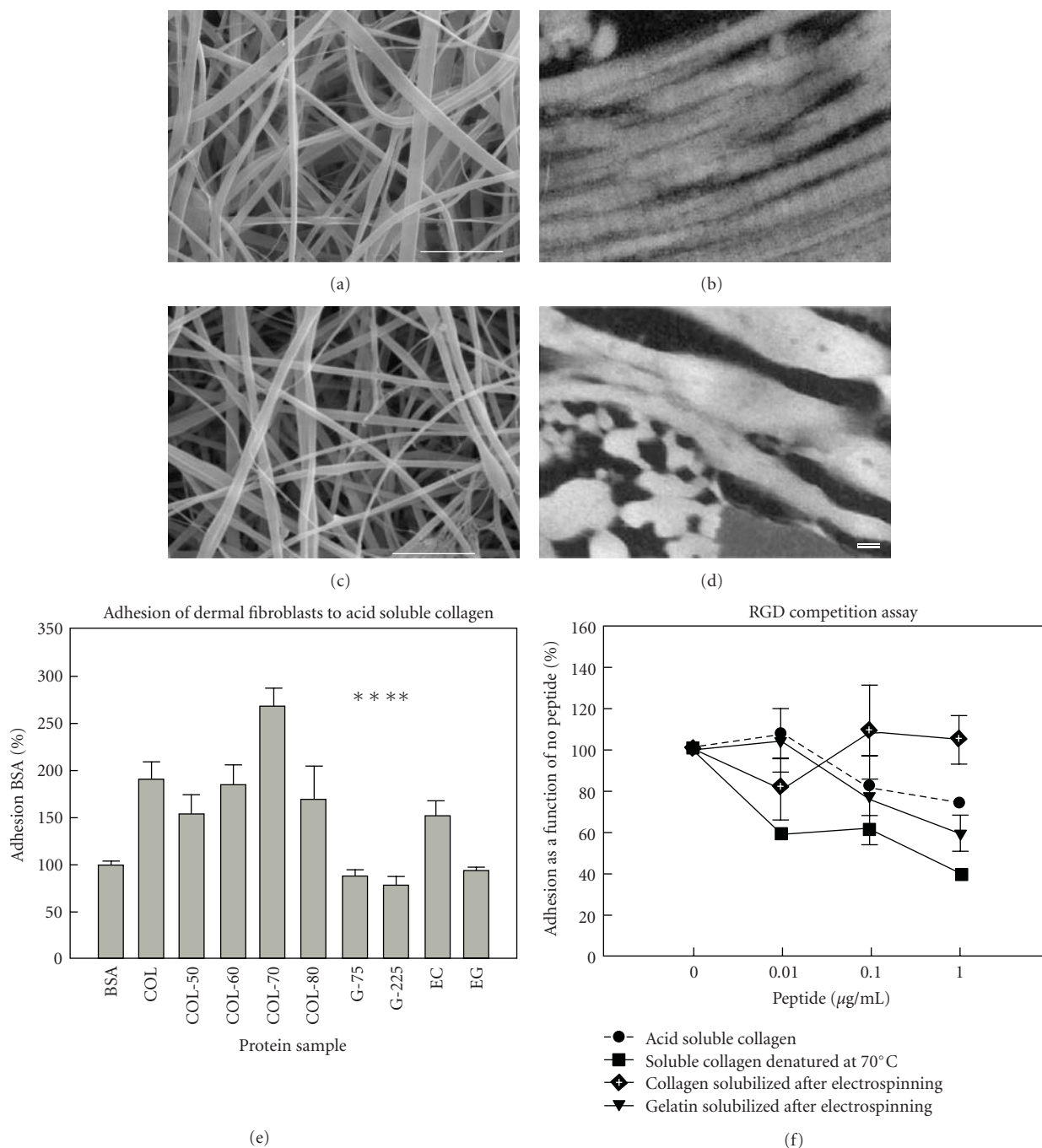


FIGURE 8: Ultrastructural and functional characteristics of collagen. Representative scanning electron and transmission electron micrographs of electrospun collagen ((a), (b)) and gelatin ((c), (d)). (e) Cell adhesion to various forms of collagen; maximal adhesion was observed in samples heated to 70°C. (F) RGD competition binding assay. Cyclic RGD peptides inhibited adhesion to denatured collagens in a concentration-dependent manner and had minor effects on control acid-soluble starting material and no effect on collagen recovered from electrospun scaffolds. Scale bars in (a) and (c) = 10 μm . Scale bar in (d) for (b) and (d) = 100 nm.

what drives these results. It is clear that these two types of fibers have subtle structural differences; fibers of electrospun collagen are not stable in an aqueous environment, unless they are cross-linked. In contrast, the fibers of a collagen gel are fully stable under these conditions and do not require such treatment. Fiber stability in a collagen gel is

linked to the exothermic reaction that occurs during fiber polymerization; this leads to the partial denaturation of the constituent α chains and results in a more stable fiber structure. In the electrospinning process, collagen alpha chains essentially undergo flash lyophilization. These inherent differences in the fiber formation process likely result in

the production of fibers exhibiting very different fine structures.

In dermal applications, wounds treated with electrospun collagen and electrospun gelatin underwent resolution over a similar time course. The nature of the tissue that resulted at the conclusion of wound closure was very different and varied as a function of fiber composition and the extent of cross-linking that was introduced in the scaffolds. Injuries treated with lightly cross-linked electrospun collagen and all samples of electrospun gelatin underwent varying degrees of wound contraction. Introducing additional cross-linking into the collagen-based materials likely stiffens the constructs and makes them less susceptible to wound contraction. All of the collagen-based scaffolds were infiltrated by fibroblasts and exhibited numerous functional blood vessels. In contrast, injuries treated with electrospun gelatin were consistently less densely populated and showed an accumulation of foreign body giant cells at the borders of the wound. This adverse response in the gelatin-based materials is undoubtedly related to the proinflammatory peptides present in highly denatured collagens [23].

The essential capacity of electrospun collagen to support rapid cell infiltration was readily apparent from the experiments in which we fabricated skeletal muscle *in situ*. The interconnected nature of the pores present in a scaffold of electrospun collagen appears to provide more than enough passive nutrient exchange to support the donor cell population. A nascent vascular supply developed in tandem with muscle differentiation to support the increased metabolic demand associated with this process. Consistent with this conclusion, we observed functional blood vessels traversing the external walls of the implanted tissue and penetrating into the internal aspects of the constructs. In contrast, once again, tissue fabricated with electrospun gelatin induced a marked inflammatory response, and by 3 weeks the tissue was largely necrotic.

To develop an understanding of the basis of biological properties of electrospun collagen, we compared and contrasted the structure and function of collagen α chains in samples subjected to varying degrees of thermal denaturation and electrospinning. Not surprisingly, α chain content is dramatically altered in response to heating. At 70°C for 1 hour, 50% of the α chains are lost; at 80°C there is essentially complete α chain fragmentation and specific bands corresponding to $\alpha 1(\text{III})$, $\alpha 1(\text{II})$, and $\alpha 2(\text{I})$ are no longer detectable. The α chain content of collagen subjected to electrospinning is subtly altered from the pattern observed in the starting materials (acid-soluble collagen). Based on our analysis, we have concluded that electrospun samples become enriched in $\alpha 2(\text{I})$ content. This conclusion is based on the observation that the ratio of $\alpha 1(\text{III})$: $\alpha 1(\text{I})$ is normal in the electrospun samples, $\alpha 1(\text{III})$: $\alpha 2(\text{I})$ is reduced and $\alpha 1(\text{I})$: $\alpha 2(\text{I})$ is reduced. Since the ratio of $\alpha 1(\text{III})$: $\alpha 1(\text{I})$ is unchanged we must assume that no change in $\alpha 1(\text{III})$ content has occurred as a consequence of the electrospinning process. Given this assumption and the observation that both $\alpha 1(\text{III})$: $\alpha 2(\text{I})$ and $\alpha 1(\text{I})$: $\alpha 2(\text{I})$ are depressed; the common factor is a change in $\alpha 2(\text{I})$ content; an increase in $\alpha 2(\text{I})$ is the simplest explanation for the observed results. As the denominator in

both ratios, any increase in $\alpha 2(\text{I})$ content results in a decrease in these ratios. It is unclear how this enrichment may occur; it is possible that differences in alpha chain solubility (or stability) in the electrospinning solutions may exist, leading to a preferential enrichment of the $\alpha 2(\text{I})$ chain. This result awaits further investigation.

Our baseline adhesion experiments failed to definitively identify a specific binding profile that might be used to evaluate the functional profile of the collagen α chains. A number of integrins ($\alpha 1\beta 1$, $\alpha 2\beta 1$, $\alpha 3\beta 1$) bind to Type I collagen in an RGD-independent manner and the $\alpha \nu \beta 3$ integrin binds with high affinity to *denatured* collagen in an RGD-dependent manner [21]. In competition binding assays, RGD challenge had little or no effect in control samples of collagen or collagen that had been recovered after electrospinning, suggesting that electrospinning in and of itself does not induce damage in a fashion that specifically uncovers cryptic RGD binding sites. We saw a dramatic decrease in adhesion when these same experiments were conducted with collagen fractions that had been heated to 70°C, these samples exhibited clear evidence of denaturation in our SDS gel studies.

5. Conclusions

Biophysical and structural evaluations demonstrate that electrospinning does not truly reconstitute the native structure of the collagen fibril [13]. Additionally, our data suggests that fibers of electrospun collagen become enriched in $\alpha 2(\text{I})$ content. However, our functional assays demonstrate that electrospun collagen has unique biological activity in a wide variety of tissue engineering applications. These data argue that it is not necessary to fully recapitulate the structure of the native fibril to generate a biologically relevant tissue engineering scaffold.

We believe that there are likely three critical variables that ultimately interact to determine the structural and functional properties of the electrospun collagen fibril. These include the quality of the starting material, the specific electrospinning conditions and, finally, the postprocessing manipulations that are used to prepare the material for use in a tissue engineering application. The first consideration is paramount; the starting material must not be denatured during any of the processes used to isolate and prepare the collagen for electrospinning (acid extraction, centrifugation steps, lyophilization and storage). The use of partially denatured collagen will obviously compromise the functional profile of the final product. Gelatin, a material that is composed of highly fragmented peptides readily spins into fibers but, it is highly proinflammatory in many settings.

Second, the role of fiber size in the formation of the ultrastructural organization of electrospun collagen has not been explored to any extent. The 67 nm banding pattern observed in electrospun samples appears to be most prominent in constructs composed of small diameter fibers. Some laboratories report that this banding pattern is confined to relatively small domains in an electrospun scaffold or that it is absent altogether [13]. We would argue that

the 67 nm repeat does not have to be present to impart potent functional properties onto the electrospun collagen fiber. Our cell adhesion experiments demonstrated that native and denatured collagen α chains have very distinctive biological properties, even when they are not assembled into fibrils. Given the dramatic differences in performance that distinguish electrospun collagen from electrospun gelatin in a broad spectrum of tissue engineering applications, it seems premature to discount the functional significance of this material [13].

Finally, during electrospinning collagen α chains are subjected to a very high strength electric field. This electric field must place these peptides in a high energy state as they traverse the charged electrospinning field; these protein subunits are then frozen and trapped in this high energy state by the flash lyophilization process that makes fiber formation possible. This residual energy may have direct role in determining the fine structure (banding) of the resulting fibers. Electrospun fibers of collagen that have been modestly cross-linked will undergo coiling when placed into an aqueous solution; this coiling is dramatically reduced as a function of increasing degrees of cross-linking [12]. At very high levels of cross-linking, fibers of electrospun collagen retain a nearly linear conformation when hydrated.

Modest cross-linking conditions appear to stabilize gross fiber structure (sufficient to keep the fibers from dissolving in an aqueous buffer); however, a modest degree of cross-linking does not appear to be sufficient to completely suppress α chain reorganization as these subunits return to a basal energy state. Upon hydration, the shedding of this excess energy appears to drive coiling. At high levels of cross-linking, fibril coiling is suppressed, suggesting the α chains are trapped in a very different tertiary configuration as compared to the fibers of more modestly cross-linked structures that can undergo molecular reorganization. The potential contribution of these variables in the formation of structure, and functional considerations in the electrospun collagen fibril, awaits further investigation. Given the potent biological activity of electrospun collagen, in a broad spectrum of applications, we can anticipate the development of unique tissue engineering scaffolds and the introduction of a new generation of tissue engineering products in the clinical market place.

Acknowledgments

This study is supported in part by NIH EB003087 (Simpson) and USAMRMC 9918006 (Simpson). Electron microscopy was conducted at the VCU Department of Neurobiology and Anatomy Microscopy Facility, supported in part by NIH-NCRR Shared Instrument Grant (1S10RR022495) and NIH-NINDS Center Core Grant (5P30NS04763).

References

- [1] J. A. Matthews, G. E. Wnek, D. G. Simpson, and G. L. Bowlin, "Electrospinning of collagen nanofibers," *Biomacromolecules*, vol. 3, no. 2, pp. 232–238, 2002.
- [2] C. P. Barnes, M. J. Smith, G. L. Bowlin et al., "Feasibility of electrospinning the globular proteins hemoglobin and myoglobin," *Journal of Engineered Fibers and Fabrics*, vol. 1, no. 2, pp. 16–28, 2006.
- [3] M. McManus, E. Boland, S. Sell et al., "Electrospun nanofibre fibrinogen for urinary tract tissue reconstruction," *Biomedical Materials*, vol. 2, no. 4, pp. 257–262, 2007.
- [4] S. W. Rothwell, E. Sawyer, J. Dorsey et al., "Wound healing and the immune response in swine treated with a hemostatic bandage composed of salmon thrombin and fibrinogen," *Journal of Materials Science*, vol. 20, no. 10, pp. 2155–2166, 2009.
- [5] E. D. Boland, B. D. Coleman, C. P. Barnes, D. G. Simpson, G. E. Wnek, and G. L. Bowlin, "Electrospinning polydioxanone for biomedical applications," *Acta Biomaterialia*, vol. 1, no. 1, pp. 115–123, 2005.
- [6] B. S. Jha, R. J. Colello, J. R. Bowman et al., "Two pole air gap electrospinning: fabrication of highly aligned, three-dimensional scaffolds for nerve reconstruction," *Acta Biomaterialia*, vol. 7, no. 1, pp. 203–215, 2011.
- [7] T. A. Telemeco, C. Ayres, G. L. Bowlin et al., "Regulation of cellular infiltration into tissue engineering scaffolds composed of submicron diameter fibrils produced by electrospinning," *Acta Biomaterialia*, vol. 1, no. 4, pp. 377–385, 2005.
- [8] S. A. Sell, M. J. McClure, C. P. Barnes et al., "Electrospun polydioxanone-elastin blends: potential for bioresorbable vascular grafts," *Biomedical Materials*, vol. 1, no. 2, pp. 72–80, 2006.
- [9] M. J. McClure, S. A. Sell, C. E. Ayres, D. G. Simpson, and G. L. Bowlin, "Electrospinning-aligned and random polydioxanone-polycaprolactone-silk fibroin-blended scaffolds: geometry for a vascular matrix," *Biomedical Materials*, vol. 4, no. 5, 2009.
- [10] C. Ayres, G. L. Bowlin, S. C. Henderson et al., "Modulation of anisotropy in electrospun tissue-engineering scaffolds: analysis of fiber alignment by the fast Fourier transform," *Biomaterials*, vol. 27, no. 32, pp. 5524–5534, 2006.
- [11] C. E. Ayres, G. L. Bowlin, R. Pizinger, L. T. Taylor, C. A. Keen, and D. G. Simpson, "Incremental changes in anisotropy induce incremental changes in the material properties of electrospun scaffolds," *Acta Biomaterialia*, vol. 3, no. 5, pp. 651–661, 2007.
- [12] D. Newton, R. Mahajan, C. Ayres, J. R. Bowman, G. L. Bowlin, and D. G. Simpson, "Regulation of material properties in electrospun scaffolds: role of cross-linking and fiber tertiary structure," *Acta Biomaterialia*, vol. 5, no. 1, pp. 518–529, 2009.
- [13] D. I. Zeugolis, S. T. Khew, E. S. Y. Yew et al., "Electro-spinning of pure collagen nano-fibres—just an expensive way to make gelatin?" *Biomaterials*, vol. 29, no. 15, pp. 2293–2305, 2008.
- [14] S. Heydarkhan-Hagvall, K. Schenke-Layland, A. P. Dhana-soon et al., "Three-dimensional electrospun ECM-based hybrid scaffolds for cardiovascular tissue engineering," *Biomaterials*, vol. 29, no. 19, pp. 2907–2914, 2008.
- [15] L. Yang, C. F. C. Fitié, K. O. van der Werf, M. L. Bennink, P. J. Dijkstra, and J. Feijen, "Mechanical properties of single electrospun collagen type I fibers," *Biomaterials*, vol. 29, no. 8, pp. 955–962, 2008.
- [16] D. G. Simpson, L. Terracio, M. Terracio, R. L. Price, D. C. Turner, and T. K. Borg, "Modulation of cardiac myocyte phenotype in vitro by the composition and orientation of the extracellular matrix," *Journal of Cellular Physiology*, vol. 161, no. 1, pp. 89–105, 1994.
- [17] A. E. Manis, J. R. Bowman, G. L. Bowlin, and D. G. Simpson, "Electrospun nitrocellulose and nylon: design and fabrication

- of novel high performance platforms for protein blotting applications,” *Journal of Biological Engineering*, vol. 1, article 2, 2007.
- [18] S. Weiner and W. Traub, “Organization of hydroxyapatite crystals within collagen fibrils,” *FEBS Letters*, vol. 206, no. 2, pp. 262–266, 1986.
- [19] I. V. Yannas, “Regeneration templates,” in *The Biomedical Engineering Handbook*, J. D. Bronzino, Ed., CRC press LLC, Fla, USA, 2000.
- [20] M. V. Agrez, R. C. Bates, A. W. Boyd, and G. F. Burns, “Arg-Gly-Asp-containing peptides expose novel collagen receptors on fibroblasts: implications for wound healing,” *Cell Regulation*, vol. 2, no. 12, pp. 1035–1044, 1991.
- [21] G. E. Davis, “Affinity of integrins for damaged extracellular matrix: Alpha v beta 3 binds to denatured collagen type I through RGD sites,” *Biochemical and Biophysical Research Communications*, vol. 182, no. 3, pp. 1025–1031, 1992.
- [22] D. A. Cisneros, C. Hung, C. M. Franz, and D. J. Muller, “Observing growth steps of collagen self-assembly by time-lapse high-resolution atomic force microscopy,” *Journal of Structural Biology*, vol. 154, no. 3, pp. 232–245, 2006.
- [23] K. R. Stevens, N. J. Einerson, J. A. Burmania, and W. J. Kao, “In vivo biocompatibility of gelatin-based hydrogels and interpenetrating networks,” *Journal of Biomaterials Science*, vol. 13, no. 12, pp. 1353–1366, 2002.

Research Article

Quantitatively Controlled Fabrication of Uniaxially Aligned Nanofibrous Scaffold for Cell Adhesion

Suk Hee Park,¹ Jung Woo Hong,¹ Jennifer Hyunjong Shin,^{1,2} and Dong-Yol Yang¹

¹ School of Mechanical Engineering and Aerospace System, Korea Advanced Institute of Science and Technology, Daejeon 305-701, Republic of Korea

² Bio and Brain Engineering, Korea Advanced Institute of Science and Technology, Daejeon 305-701, Republic of Korea

Correspondence should be addressed to Dong-Yol Yang, dyyang@kaist.ac.kr

Received 10 October 2010; Revised 27 January 2011; Accepted 21 March 2011

Academic Editor: Junping Wang

Copyright © 2011 Suk Hee Park et al. This is an open access article distributed under the Creative Commons Attribution License, which permits unrestricted use, distribution, and reproduction in any medium, provided the original work is properly cited.

In light of tissue engineering, development of a functional and controllable scaffold which can promote cell proliferation and differentiation is crucial. In this study, we introduce a controllable collection method of the electrospinning process for regularly-distributed and uniaxially oriented nanofiber scaffold and evaluate the effects of aligned nanofiber density on adhesion of dermal fibroblasts. The suggested spinning collector features an inclined void gap, which allows easy transfer of uniformly aligned fibers onto other surfaces. By undergoing multiple transfers, the density of the nanofibers can be quantitatively controlled. The resultant polycaprolactone (PCL) nanofibers had well-defined nanotopography in a 400–600 nm range. Human dermal fibroblasts were seeded on aligned nanofiber scaffolds of different densities achieved by varying the number of transfers. Cell morphology and actin stress fiber formation was accessed after seven days. The experimental results indicate that the contact guidance of the cells along the fiber alignment can be more activated with more than one guidance feature on a cell; that is, the high density of fiber is attained in so much that fiber spacing gets below the cell size.

1. Introduction

The importance of nanostructured topography in view of cell biology has been recognized as one of the key factors in tissue engineering applications. Nano- or micro-architectures that can mimic natural extracellular matrix (ECM) environments have been employed in fabrication of functionalized scaffolds to enhance cellular responses, such as adhesion, migration, proliferation, and locomotion [1–3]. The ECM-like structure, a complex structural network with various fibrillar constituents, has been simulated by a wide variety of fabrication techniques which include MEMS- (microelectromechanical system-) based lithography, electrospinning, and imprinting methods [4–6].

The electrospinning process, in particular, has advantages for fabricating cytocompatible scaffolds thanks to its high efficiency and simplicity in producing submicron to nanometer scale fibers from a wide range of biomaterials [7]. When a high electric potential is applied to the pendant drop of a polymer solution, the drop gets deformed into a cone shape, which is known as a Taylor cone. As a charged jet of

the polymer solution is launched from the tip of the cone and elongated into thinner fibers, it gradually solidifies forming a nanofibrous mesh on the grounded collector. In typical electrospinning process, the nanofibers from the elongated jet are randomly deposited on the collector due to jet bending and whipping caused by Columbic interaction between the jets [8]. Although these randomly assembled nonwoven nanofiber meshes have a wide range of bioapplications [9–13], the recent interest in the electrospun nanofibers has been focused on ordered forms of the fibers, especially uniaxially aligned fiber arrays in light of tissue engineering applications for anisotropic tissues such as tendons and muscles. Fiber configuration with uniaxial orientation can be dictated by collector geometry, which has been proposed in various ways including using a rotating cylinder [14, 15], a disk with a sharp edge [16], a spaced wire drum [17], and a parallel electrodes [18, 19].

The potential of applying these alignment techniques to scaffold fabrication is significant in that it can provide a defined architecture to guide cellular behavior as well as nanoscaled dimensions for the biomimetic ECM for a wide

range of cell lines such as fibroblasts, neuron cells, and muscle cells, and so forth [20–27]. Many studies on the guidance effect have been conducted using MEMS-based lithographic techniques to realize precise construction of ridge/groove patterns for cell guidance [22, 23]. However, in terms of utilization of biocompatible materials for scaffold fabrication and the fabrication itself, the electrospun nanofiber array is far more advantageous than MEMS-based processes. Based on the electrospinning technique, some efforts have been made to apply the fiber alignment technique with a rotating disk collector [26, 27]. Yet, due to the geometrical limitation of the disk edge, the employed technique makes it difficult to collect a wide area of fiber arrays.

We previously reported on the fabrication process of aligned electrospun nanofibers realized by the proposed inclined gap method [28], which provided regular distribution and high order alignment of the nanofibers over a relatively wide area. The intrinsic instability of fiber landing in the electrospinning process was mitigated by employing two separate strips that were configured horizontally and vertically with the inclined gap. In this study, aligned nanofibrous scaffolds with different densities were prepared by employing multiple transfers of the previously proposed process. Thanks to the favorable feature of void gap with suspended nanofibers, transfers of these fibers onto the other substrate can be easily accomplished. The repetitively overlapping transfer can provide quantitative control of the nanofiber densities in the scaffold in proportion to the number of transfers. Human dermal fibroblasts were cultured for seven days to observe the cell guidance effect and morphological changes on the scaffolds of different densities. Additionally, a smooth PDMS (polydimethylsiloxane) substrate and a number of randomly deposited nanofiber mesh on PDMS were tested to compare with the specimens of aligned nanofibers.

2. Materials and Methods

2.1. Materials. Polycaprolactone (PCL, average M_n ca. 80,000) was obtained by Aldrich (Milwaukee, Wis, USA). Methylene chloride (MC; Junsei Chemical) and N,N-dimethyl formamide (DMF; Junsei Chemical) were used as the solvents for the spinning solutions. PCL was dissolved in a mixture of MC and DMF (75/25 v/v). Cell culturing reagents, fibronectin (FN), Dulbecco's modified Eagle's medium (DMEM), Dulbecco's phosphate buffered saline (DPBS), penicillin-streptomycin, and fetal bovine serum (FBS) were all purchased from Gibco (Carlsbed, CA). Immuno-staining reagents Alexa Fluor 568 phalloidin and DAPI (4',6-diamidino-2-phenylindole, dilactate) were obtained from Invitrogen (Carlsbed, Calif, USA).

2.2. Scaffold Fabrication. The schematic of the electrospinning method is illustrated in Figure 1. Polymer solution was prepared by dissolving PCL in the mixture of MC and DMF at the concentration of 20 wt% defined as a proper condition in the previous work [28]. The higher concentration than that of the typical electrospinning could allow the successful suspension within the inclined void gap due to the sufficiency

of the fiber solidification. The PCL solution was electrospun from a 25-gauge needle connected to a power supply at an applied voltage of 14 kV. The infusion rate of solution through the needle was 0.6 mL/h. The randomly configured nanofiber mesh was obtained by simple electrospinning toward a thin PDMS membrane adhered to slide glass lying on the grounded metal plate. The spinning time was 2 min.

The collector for the formation of uniaxially aligned aluminum strips (0.2 mm thickness), which were fixed horizontally and vertically at upper and lower position, respectively. This height difference between the strips formed the void space and the electrospun nanofibers were suspended along the void gap. The spinning distance from the needle tip to the upper strip was determined as 160 mm. The suspended nanofibers with uniaxial alignment were transferred onto a surface of the PDMS membrane adhered to the slide glass and both ends of the fiber array were anchored with Permout (Fisher Scientific, Pittsburgh, Pa, USA).

2.3. Characterization of Electrospun Nanofibers. The resultant samples that were transferred with electrospun nanofibers were photographed using a scanning electron microscope (SEM; JSM-6300, JEOL) and an optical microscope (i-Camscope, Sometech Vision). The fiber alignment was quantified by employing the angles between the desired direction (perpendicular to the edge lines of two strips) and the longitudinal axes of the fibers. The angle distribution of each nanofiber was measured from the captured images by using ImageTool 3.0 (University of Texas Health Science Center in San Antonio, Tex, USA).

2.4. Cell Culture. Cell studies were performed using human dermal fibroblasts (6th and 10th passage) purchased from Lonza (Basel, Switzerland). The cells were cultured in Dulbecco's modified Eagle's medium (DMEM) (Lonza, Basel, Switzerland) containing 10% fetal bovine serum (FBS) supplemented with penicillin-streptomycin (Sigma, St. Louis, Mo, USA). Cultures were incubated in a humidified atmosphere of 5% CO₂ in air at 37°C. Prior to the cell seeding, all nanofiber scaffolds were sterilized in ethanol for 24 hours under ultraviolet irradiation, treated with O₂ plasma for 2 mins (Femto Science) and coated with fibronectin at 10 µg/mL for 1 hour at room temperature. Cells were harvested using trypsin/EDTA and resuspended in DMEM. Cells were then seeded onto the scaffolds at its density of 10⁴ cells per scaffold and incubated for 7 days in appropriate growth conditions. For mature binding of cells to the substrate, first media change was done after 36 hours of cell seeding and an additional media change was done on the 5th day for optimal growth. The process was carried out with extreme care to minimize any possible undesired simulation or dislodging of cells by mechanical agitation.

2.5. Immunofluorescence. After experiments, cells were washed with the warmed DPBS and fixed for 15 min in 3.7% formaldehyde. After DPBS washing, cells were permeabilized for 20 min in 2% Triton X-100 and blocked in 3% BSA (Invitrogen). Following three washes in DPBS, cells were

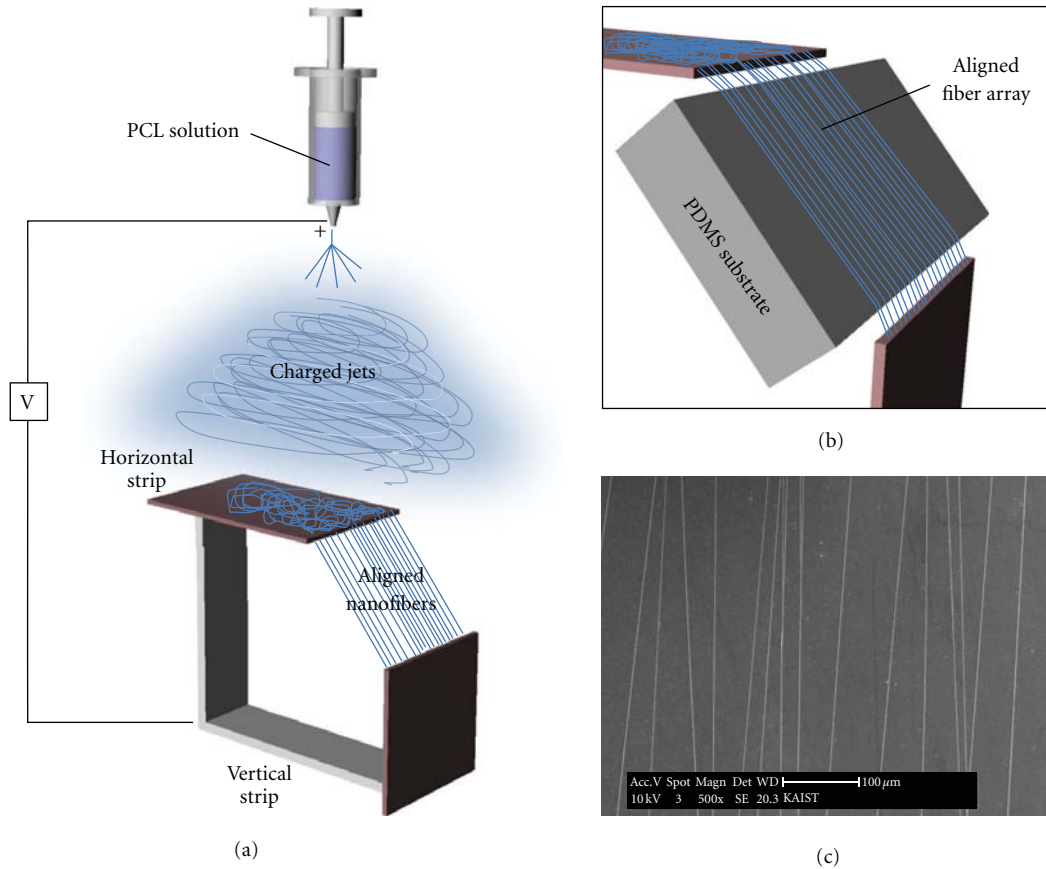


FIGURE 1: (a) Schematic diagram of the electrospinning setup for the inclined gap method. (b) The transfer of collected fibers onto PDMS substrate. (c) SEM image of the transferred nanofiber array.

stained for F-actin cytoskeleton with Alexa-568-phalloidin (Molecular Probes) at 1:50 dilution in blocking buffer. After rinsing, the nuclei of the cells were labeled with DAPI (300 nM, D1306, Molecular Probes), and then, they were finally mounted in a Vectashield (H-1000, Vector Laboratories) to minimize photobleaching. The cells were imaged using a Zeiss fluorescence microscope (Axiovert-200M, Zeiss) equipped with a CCD camera (Axiocam HSM, Zeiss) and image analysis software (Axiovision, Zeiss).

2.6. Cell Morphology. After 7 days of cell culture, the stained cells were observed under a light microscope (Carl Zeiss Axiovert 200 M) with phase contrast. 60 cells from each scaffold were randomly selected and the fluorescent images of actin and nuclei were analyzed using ImageTool 3.0 to measure the extent of cell alignment. The orientation angle of cell long axis was measured with respect to the reference, which is the desired direction of fiber alignment, that is, perpendicular axis to the collector edges. In addition, cell elongation factor E_f was calculated by [29]. The values of the elongation factor were calculated from 30 cells randomly selected from each scaffold. All statically analyses were performed using the Student's t -test. Mean values from different independent experiments were calculated and expressed as the mean \pm STD.

3. Results and Discussion

3.1. Uniformity of Nanofiber Array. In order to improve the uniformity of the aligned nanofiber array, the fiber collector was modified from a conventional design for the general gap method [28]. There have been several techniques developed to fabricate uniaxially oriented nanofibers [14–19]. Especially, the gap method, where two parallel electrodes are used as the collector, is considered to be effective in producing an aligned nanofiber array covering a wide area. When the two separate electrodes are placed at the position of the collector with a gap in between, the electric field lines are split into each edge of the electrodes. Because the electrospun jets tend to travel along the field lines, as-spun fibers are longitudinally stretched toward both edges of the electrodes and become uniaxially suspended across the gap [18, 19].

As reported previously [28], the modification of the configuration from a planar gap to an inclined gap allowed flexibility in time and space for improved alignment effect. As shown in Figures 2(a)–2(d) fiber collection from the inclined gap serves to create better conditions in both the alignment of fiber angle and the homogeneity in fiber distribution, whereas irregular distribution of nanofibers was observed in the case of the planar gap (marked by arrows in Figures 2(b), 2(g), and 2(h)). These irregularities would be accumulative

as the number of transfers increased, as shown in Figures 2(g), and 2(h). Thus, since multiple transfers were necessary to create a nanofiber array of higher density, the use of inclined gap configuration would be more advantageous in generating more homogenous scaffolds

3.2. Controlled Quantity of Nanofibers. Although the utilized electrospinning technique has the advantage of producing the relatively large area of fiber array, repulsion caused by the residual charges on the collected fibers creates an inherent difficulty in generating controlled nanofibrous scaffold containing a sufficient quantity of fibers. As shown in Figure 1(c), most of the intervals between the fibers appear to be several tens of micrometer which is larger than typical eukaryotic cells; for instance, the size of a fibroblast is about $10\ \mu\text{m}$ in length and $2\text{--}3\ \mu\text{m}$ in width [30]. Thus, a sub-ten-micrometer scale of fiber distance would be desired to ensure the interaction between the cell and the nanofibers. By employing multiple transfers on an inclined configuration, a reduction of fiber distance can be attained at approximately $2\ \mu\text{m}$ when 20 transfers were carried out (Figure 3(d)). As the quantity of nanofibers collected from single-step electrospinning was nearly invariable for the determined spinning time of 30 sec, the fiber quantity within the array would be proportional to the number of transfers. These results confirm the feasibility of the quantitative control of nanofibers using multitransfers of nanofibers using the inclined configuration of collector (Figures 2(a), 2(c), 2(e), and 2(f)).

3.3. Morphology of Nanofibers. While conventional electrospinning uses a simple electrically grounded collector without a gap, the collector used in our method comprises of two aluminum sheets separated by a gap. Because this collector configuration with a gap is designed such that as-spun fibers become suspended between both edges of the sheets, relatively rigid jets and fibers are preferred for stable suspension. When the initial concentration of the utilized solution is high, the whole jets and fibers throughout the spinning process exhibit more solid-like behavior. Thus, we increased the solution concentration to 20 wt% from the typical concentration of 10–12 wt%.

One concern about increasing the solution concentration for better mechanical stability is its consequence in the increased diameter of the nanofibers [31]. In our process, however, the fiber diameter can be achieved within the submicrometer scale despite the relatively high solution concentration. While the fiber deposited directly on the upper strip exhibited a thicker diameter (typically of the order of few micrometers as shown in Figure 4(b)), the nanofibers suspended between the edges of the upper and lower strips featured thinner diameters (typically ranging from 400 to 600 nm as shown in Figure 4(c)) suitable for tissue engineering applications.

3.4. Cell Morphology. In order to test how substratum topographies generated from the transferred nanofiber scaffolds influence cell morphology, several specimens of different densities of nanofibers were prepared by varying number of transfers from 1, 3, to 10. Fibroblasts were seeded

and cultured for seven days on each scaffold. As shown in Figure 5, the degree of cell alignment on the substrate transferred with nanofibers showed positive correlations with the density of fibers. Cells cultured on the scaffolds of 3 and 10 transfers show elongated morphology in the direction parallel to fiber alignment, whereas those on the scaffold of single transfer show little tendency of orientation.

To visualize the interaction between the nanofibers and the cultured cells better, cells were fluorescently stained for nuclei and cytoskeletal actin with DAPI and rhodamine phalloidin, respectively. As a control, a smooth PDMS substrate without nanofibers (Figure 6(a)) and the randomly-electrospun nanofiber scaffolds (Figure 6(b)) were used and compared with the aligned nanofiber substrates of different densities (Figures 6(c)–6(e)). All substrates were coated with fibronectin under the identified condition as described in Section 2. The superimposed stack of phase contrast and fluorescent images for nuclei and actin show intimate association of cells with nanofibers (Figures 6(b)–6(e)). The case of randomly oriented fibers shown in Figure 6(b) indicates cells' preference for the fibers to the smooth underlying surface. Often, cells stretch along the fiber length and are bounded by neighboring fibers. However, due to its randomness in orientation, neither of the cell alignment distribution nor the elongation morphology was any different from those cultured on the smooth PDMS surface without fibers.

On the scaffold with a single transfer (Figure 6(c)), the cell alignment (55% cells within $\pm 15^\circ$ of the reference direction) and elongation (the average value of 5.8) were achieved to some extent, but a significant fraction of cells was shown to be unaffected by nanofibers due to large fiber-fiber distance. On the other hand, cells on the scaffolds with 5 and 20 transfers, as shown in Figures 6(d) and 6(e), showed clear alignment and elongation along the fibers. For the scaffolds with 5 transfers, 67% of cells aligned within $\pm 15^\circ$ of the reference direction and the average elongation factor was 6.8, whereas the scaffolds with 20 transfers showed 95% alignment and the elongation factor of 11.6. Most of the aligned cells span over more than two fibers across its body width. It is noteworthy that the cell guidance appeared to be more effective when the fiber spacing in the scaffold was similar to or smaller than the cell size. In other words, cell contact with the multiple guide topographies may be crucial for contact guidance effect.

Figure 7 shows the formations of actin stress fibers of the cells cultured on the scaffolds with different number of nanofiber transfers. Cells making multiple contacts with the scaffold show strongly visible and densely distributed stress fibers as shown in Figures 7(c), and 7(d), compared to those forming a single contact with the scaffold shown in Figures 7(a), and 7(b). Because the actin stress fiber formation is one of the critical components in cellular functions such as migration and differentiation, the fiber density control would be an important parameter for the scaffold design for tissue engineering.

This study presents an initial effort to apply uniaxially aligned and uniformly distributed nanofibers to scaffold-based tissue engineering in a quantitatively controlled

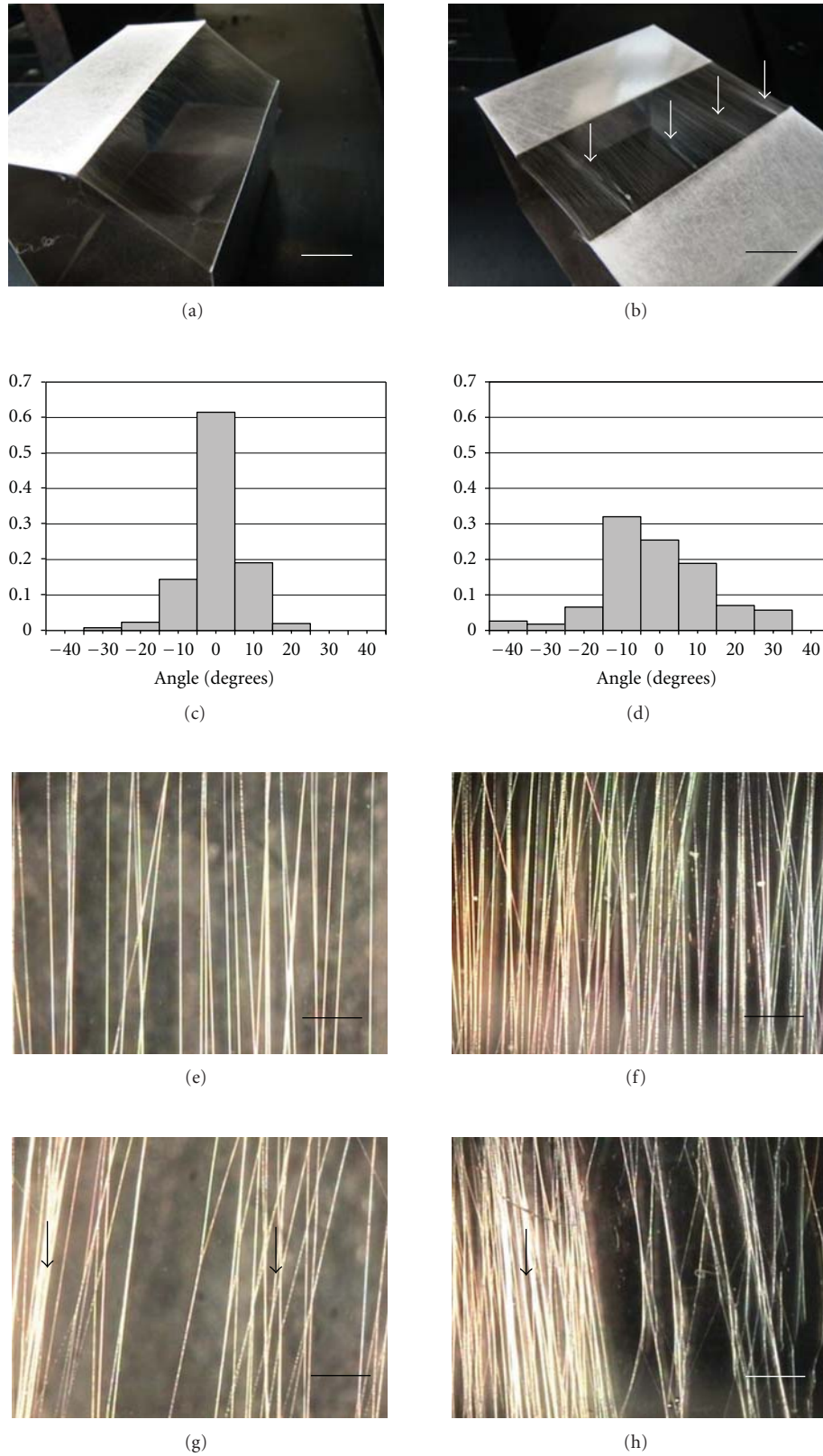


FIGURE 2: Comparison between results of the inclined and the planar gap collection: photographs of the fiber arrays suspended on (a) the inclined gap collector and (b) the planar gap collector. Histograms of angle distribution of fiber alignment in the arrays transferred from (c) the inclined gap collector and (d) the planar gap collector. Homogeneous fiber arrays collected from the inclined gap by (e) single transfer and (f) 3 transfers. Inhomogeneous fiber arrays collected from the planar gap by (g) single transfer and (h) 3 transfers. Arrows indicate the inhomogeneous conditions of the fiber distributions. The scale bars are 10 mm (a, b) and 100 μm (e)–(h), respectively.

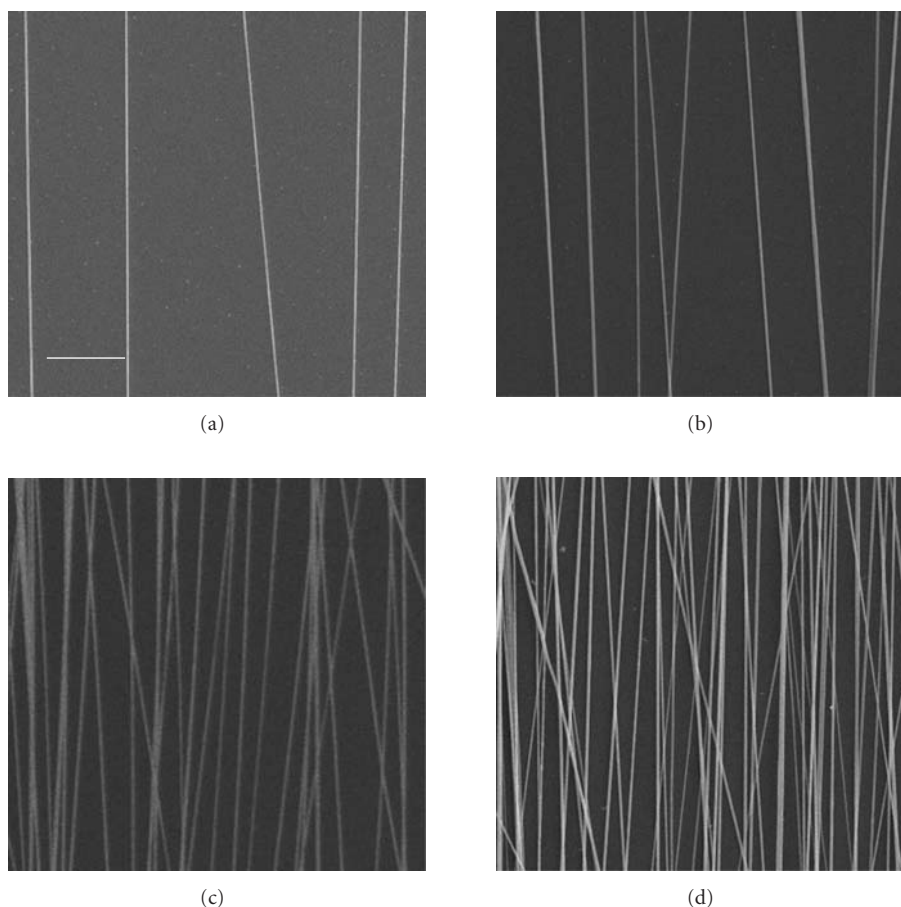


FIGURE 3: SEM images of the nanofiber arrays transferred repetitively: (a) 1 transfer, (b) 3 transfers, (c) 10 transfers, and (d) 20 transfers. The scale bar on (a) is $20\ \mu\text{m}$, and the other images are at the same magnification.

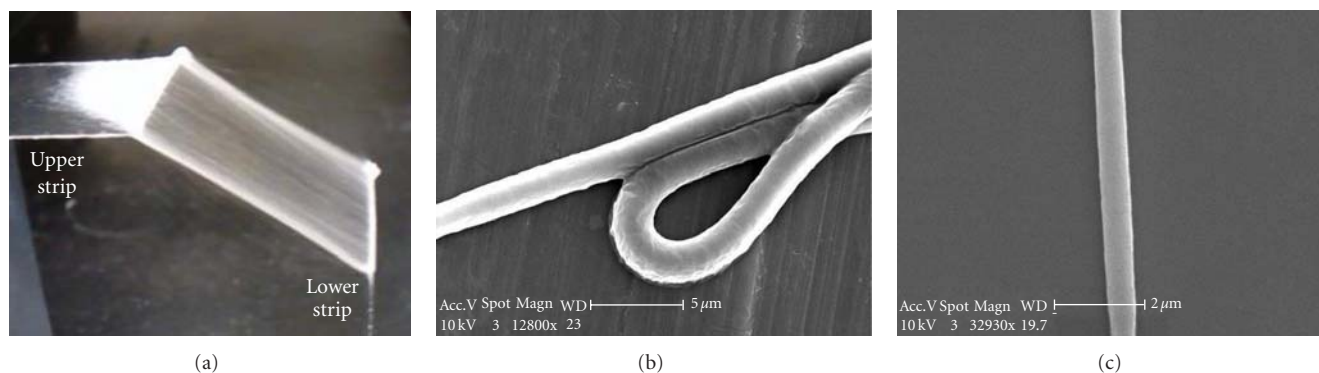


FIGURE 4: (a) Photograph of nanofibers collected on the upper strip and within the gap space. SEM images of (b) the microscale fibers deposited directly on the upper strip (the scale bar is $5\ \mu\text{m}$), and (c) the submicroscale fiber uniaxially suspended within the gap space (the scale bar is $2\ \mu\text{m}$).

manner and implies that a highly dense scaffold with nanofiber alignment would have functional significance. Besides as a dermal fibroblast used for wound healing strategy, the developed nanofiber scaffold could potentially contribute to other tissue engineering applications where tissue

anisotropy is a critical factor (e.g., blood vessels, muscles and nerves), and thus other cell types should be tested for efficacy of the scaffolds. In addition, because of the material universality of the electrospinning process, naturally occurring polymers such as collagens can be tested as scaffold materials.

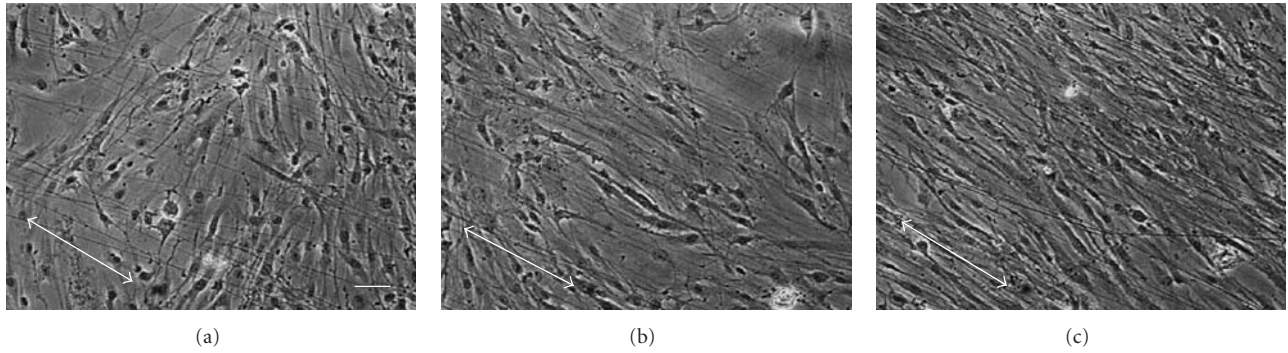


FIGURE 5: Phase contrast micrographs illustrating the cell alignment effect of different fiber arrays for (a) 1, (b) 3, and (c) 10 transfers. The scale bar on (a) is 100 μm ; the other images are at the same magnification. The arrows indicate the direction of the fiber orientation.

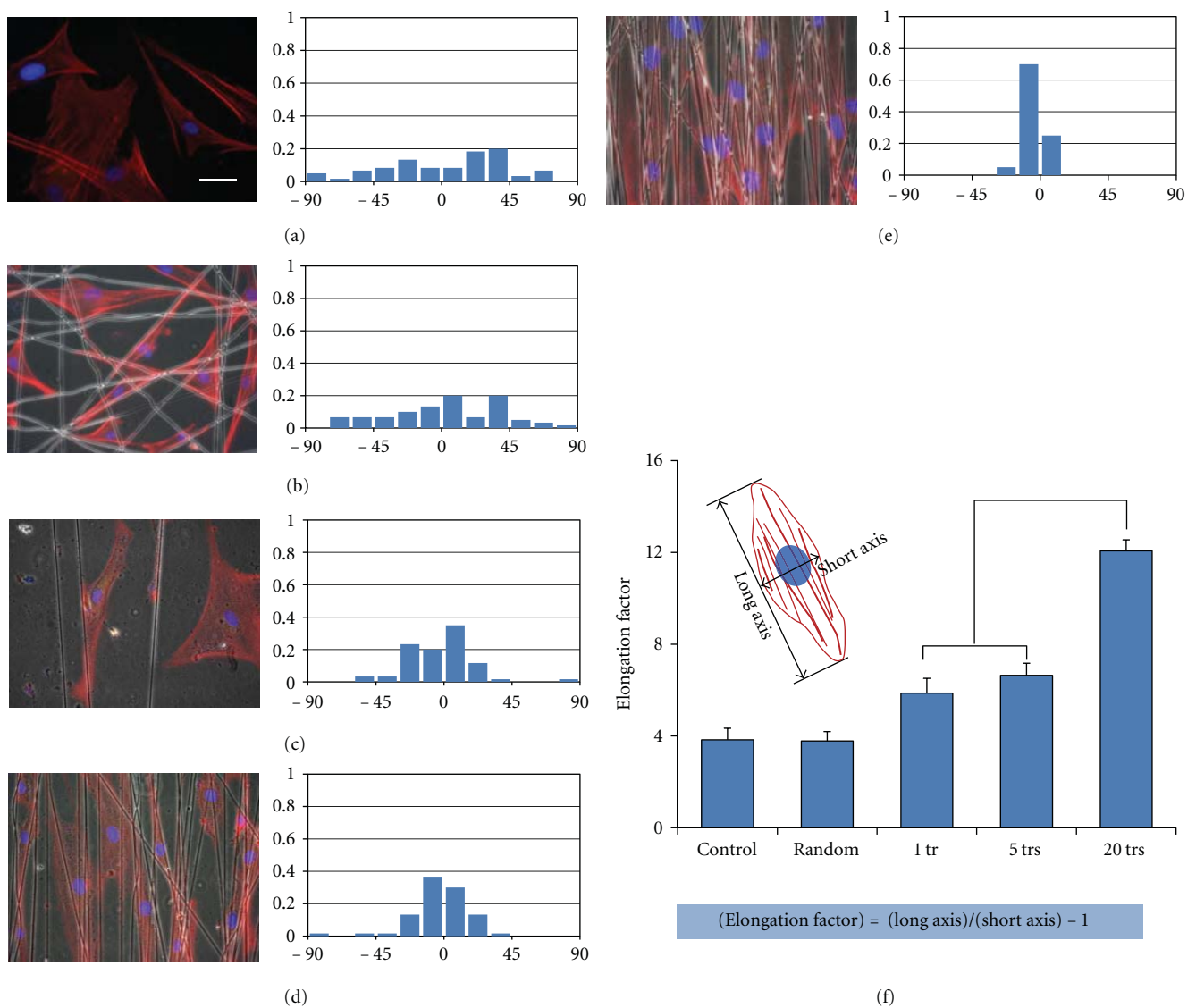


FIGURE 6: Immunofluorescent staining images of cell morphologies and quantitative assessments of cell alignments on (a) smooth PDMS substrate without fiber (control), (b) fiber mesh deposited randomly (random), (c) singly transferred substrate with aligned nanofibers (1 tr), and multiply transferred substrate with (d) 5 (5 trs) and (e) 20 transfers (20 trs). Red and blue correspond to actin and nucleus, respectively. The scale bar on (a) is 50 μm ; the other images are at the same magnification. (f) Elongation factor (E_f) of the each scaffold. Data shown as mean \pm standard error ($n = 30$ in each scaffold, *** $P < .001$).

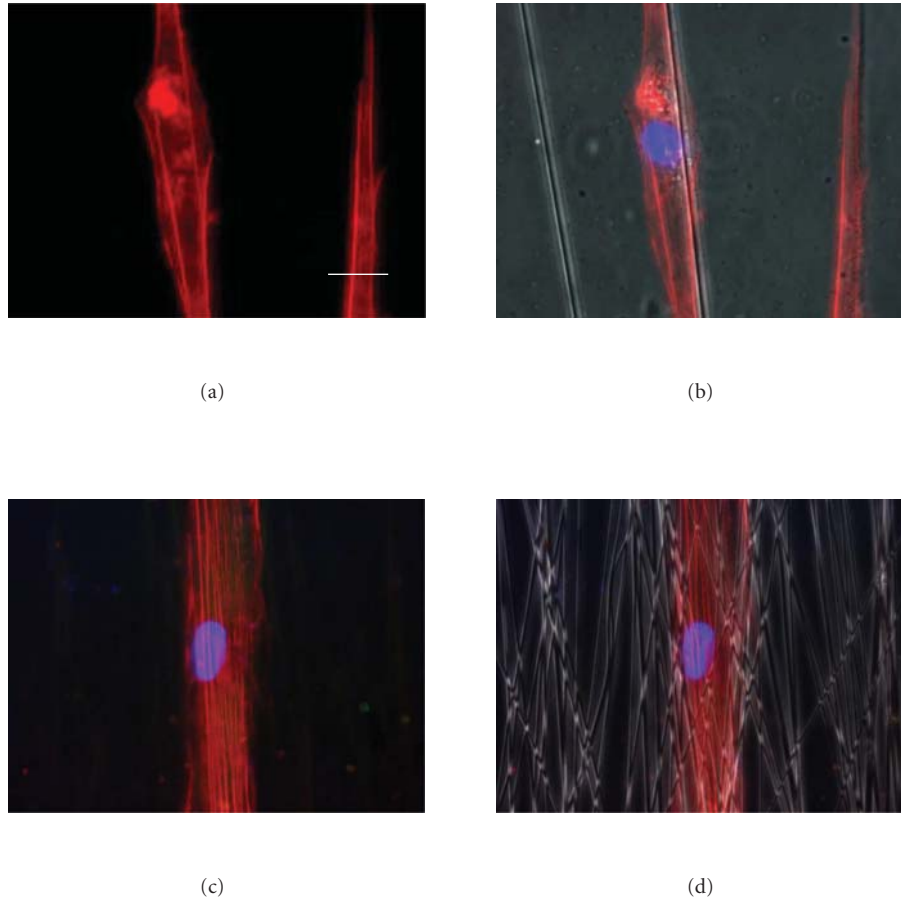


FIGURE 7: Immunofluorescent staining images to visualize the formation of actin stress fiber on the substrate (a, b) with single transfer and (c, d) with 20 transfers. The scale bar on (a) is $30\ \mu\text{m}$; the other images are at the same magnification.

4. Conclusions

In this study, uniaxially electrospun nanofiber arrays were constructed with quantitatively controlled density. As a single transfer of the nanofibers collected from the inclined gap provided a well-aligned and regularly distributed form, the developed nanofiber array could be applied to tissue scaffold by employing multiple transfers. The fiber density within a scaffold could be controlled in proportion to the number of transfers. Diameters of the nanofibers in the scaffold were in a submicrometer range, which means that the fibers were appropriate to utilize as nanotopographic features. In regard to the contact guidance along the aligned direction of the nanofibers, favorable interactions between the fibroblasts and the developed scaffold, especially in a highly dense scaffold with the fiber spacing reduced down to less than cell size, were revealed in observation of cell morphologies. The results regarding the aspect of the fiber density control are believed to help practical scaffold design with aligned configuration. Further studies with other cell types utilizing more quantitative biochemical assays are under way to evaluate the feasibility

of the developed scaffolds to tissue engineering applications.

References

- [1] C. S. Chen, M. Mrksich, S. Huang, G. M. Whitesides, and D. E. Ingber, "Geometric control of cell life and death," *Science*, vol. 276, no. 5317, pp. 1425–1428, 1997.
- [2] R. G. Flemming, C. J. Murphy, G. A. Abrams, S. L. Goodman, and P. F. Nealey, "Effects of synthetic micro- and nano-structured surfaces on cell behavior," *Biomaterials*, vol. 20, no. 6, pp. 573–588, 1999.
- [3] J. Y. Lim and H. J. Donahue, "Cell sensing and response to micro- and nanostructured surfaces produced by chemical and topographic patterning," *Tissue Engineering*, vol. 13, no. 8, pp. 1879–1891, 2007.
- [4] Y. Lu and S. C. Chen, "Micro and nano-fabrication of biodegradable polymers for drug delivery," *Advanced Drug Delivery Reviews*, vol. 56, no. 11, pp. 1621–1633, 2004.
- [5] A. Khademhosseini, R. Langer, J. Borenstein, and J. P. Vacanti, "Microscale technologies for tissue engineering and biology," *Proceedings of the National Academy of Sciences of the United States of America*, vol. 103, no. 8, pp. 2480–2487, 2006.

- [6] V. Mironov, V. Kasyanov, and R. R. Markwald, "Nanotechnology in vascular tissue engineering: from nanoscaffolding towards rapid vessel biofabrication," *Trends in Biotechnology*, vol. 26, no. 6, pp. 338–344, 2008.
- [7] Z. M. Huang, Y. Z. Zhang, M. Kotaki, and S. Ramakrishna, "A review on polymer nanofibers by electrospinning and their applications in nanocomposites," *Composites Science and Technology*, vol. 63, no. 15, pp. 2223–2253, 2003.
- [8] A. L. Yarin, S. Koombhongse, and D. H. Reneker, "Bending instability in electrospinning of nanofibers," *Journal of Applied Physics*, vol. 89, no. 5, pp. 3018–3026, 2001.
- [9] W. J. Li, C. T. Laurencin, E. J. Caterson, R. S. Tuan, and F. K. Ko, "Electrospun nanofibrous structure: a novel scaffold for tissue engineering," *Journal of Biomedical Materials Research*, vol. 60, no. 4, pp. 613–621, 2002.
- [10] C. Xu, R. Inai, M. Kotaki, and S. Ramakrishna, "Electrospun nanofiber fabrication as synthetic extracellular matrix and its potential for vascular tissue engineering," *Tissue Engineering*, vol. 10, no. 7–8, pp. 1160–1168, 2004.
- [11] L. S. Nair, S. Bhattacharyya, and C. T. Laurencin, "Development of novel tissue engineering scaffolds via electrospinning," *Expert Opinion on Biological Therapy*, vol. 4, no. 5, pp. 659–668, 2004.
- [12] S. Y. Chew, Y. Wen, Y. Dzenis, and K. W. Leong, "The role of electrospinning in the emerging field of nanomedicine," *Current Pharmaceutical Design*, vol. 12, no. 36, pp. 4751–4770, 2006.
- [13] S. G. Kumbar, R. James, S. P. Nukavarapu, and C. T. Laurencin, "Electrospun nanofiber scaffolds: engineering soft tissues," *Biomedical Materials*, vol. 3, no. 3, Article ID 034002, 15 pages, 2008.
- [14] E. D. Boland, G. E. Wnek, D. G. Simpson, K. J. Pawlowski, and G. L. Bowlin, "Tailoring tissue engineering scaffolds using electrostatic processing techniques: a study of poly(glycolic acid) electrospinning," *Journal of Macromolecular Science*, vol. 38, no. 12, pp. 1231–1243, 2001.
- [15] J. A. Matthews, G. E. Wnek, D. G. Simpson, and G. L. Bowlin, "Electrospinning of collagen nanofibers," *Biomacromolecules*, vol. 3, no. 2, pp. 232–238, 2002.
- [16] A. Theron, E. Zussman, and A. L. Yarin, "Electrostatic field-assisted alignment of electrospun nanofibres," *Nanotechnology*, vol. 12, no. 3, pp. 384–390, 2001.
- [17] P. Katta, M. Alessandro, R. D. Ramsier, and G. G. Chase, "Continuous electrospinning of aligned polymer nanofibers onto a wire drum collector," *Nano Letters*, vol. 4, no. 11, pp. 2215–2218, 2004.
- [18] D. Li, Y. Wang, and Y. Xia, "Electrospinning of polymeric and ceramic nanofibers as uniaxially aligned arrays," *Nano Letters*, vol. 3, no. 8, pp. 1167–1171, 2003.
- [19] D. Li, Y. Wang, and Y. Xia, "Electrospinning Nanofibers as Uniaxially Aligned Arrays and Layer-by-Layer Stacked Films," *Advanced Materials*, vol. 16, no. 4, pp. 361–366, 2004.
- [20] P. Weiss, "In vitro experiments on the factors determining the course of the outgrowing nerve fiber," *Journal of Experimental Zoology*, vol. 68, no. 3, pp. 393–448, 1934.
- [21] J. Sutherland, M. Denyer, and S. Britland, "Contact guidance in human dermal fibroblasts is modulated by population pressure," *Journal of Anatomy*, vol. 206, no. 6, pp. 581–587, 2005.
- [22] C. A. Mills, J. Escarré, E. Engel et al., "Micro- and nanostructuring of poly(ethylene-2,6-naphthalate) surfaces, for biomedical applications, using polymer replication techniques," *Nanotechnology*, vol. 16, no. 4, pp. 369–375, 2005.
- [23] A. I. Teixeira, G. A. Abrams, P. J. Bertics, C. J. Murphy, and P. F. Nealey, "Epithelial contact guidance on well-defined micro- and nanostructured substrates," *Journal of Cell Science*, vol. 116, no. 10, pp. 1881–1892, 2003.
- [24] G. A. Dunn and A. F. Brown, "Alignment of fibroblasts on grooved surfaces described by a simple geometric transformation," *Journal of Cell Science*, vol. 83, pp. 313–340, 1986.
- [25] P. Clark, P. Connolly, and G. R. Moores, "Cell guidance by micropatterned adhesiveness in vitro," *Journal of Cell Science*, vol. 103, no. 1, pp. 287–292, 1992.
- [26] C. Y. Xu, R. Inai, M. Kotaki, and S. Ramakrishna, "Aligned biodegradable nanofibrous structure: a potential scaffold for blood vessel engineering," *Biomaterials*, vol. 25, no. 5, pp. 877–886, 2004.
- [27] J. M. Corey, C. C. Gertz, B. S. Wang et al., "The design of electrospun PLLA nanofiber scaffolds compatible with serum-free growth of primary motor and sensory neurons," *Acta Biomaterialia*, vol. 4, no. 4, pp. 863–875, 2008.
- [28] S. H. Park and D. Y. Yang, "Fabrication of aligned electrospun nanofibers by inclined gap method," *Journal of Applied Polymer Science*, vol. 120, no. 3, pp. 1800–1807, 2011.
- [29] A. S. Crouch, D. Miller, K. J. Luebke, and W. Hu, "Correlation of anisotropic cell behaviors with topographic aspect ratio," *Biomaterials*, vol. 30, no. 8, pp. 1560–1567, 2009.
- [30] G. Khang, S. J. Lee, J. H. Lee, and H. B. Lee, "Interaction of Fibroblast Cells onto Fibers with Different Diameter," *Korea Polymer Journal*, vol. 7, no. 2, pp. 102–107, 1999.
- [31] C. A. Bashur, L. A. Dahlgren, and A. S. Goldstein, "Effect of fiber diameter and orientation on fibroblast morphology and proliferation on electrospun poly(D,L-lactic-co-glycolic acid) meshes," *Biomaterials*, vol. 27, no. 33, pp. 5681–5688, 2006.

Research Article

Electrospinning of Poly(ethylene-co-vinyl alcohol) Nanofibres Encapsulated with Ag Nanoparticles for Skin Wound Healing

Chao Xu,^{1,2} Feng Xu,^{1,3} Bin Wang,^{1,2} and TianJian Lu¹

¹ Biomedical Engineering and Biomechanics Center, School of Aerospace, Xi'an Jiaotong University, Xi'an 710049, China

² School of Engineering, University of Aberdeen, Aberdeen AB24 3UE, UK

³ Department of Medicine, HST-Center for Biomedical Engineering, Brigham and Women's Hospital, Harvard Medical School, Boston, MA 02115, USA

Correspondence should be addressed to Bin Wang, bin.wang@abdn.ac.uk

Received 2 November 2010; Revised 14 December 2010; Accepted 17 December 2010

Academic Editor: Zuwei Ma

Copyright © 2011 Chao Xu et al. This is an open access article distributed under the Creative Commons Attribution License, which permits unrestricted use, distribution, and reproduction in any medium, provided the original work is properly cited.

Skin wound healing is an urgent problem in clinics and military activities. Although significant advances have been made in its treatment, there are several challenges associated with traditional methods, for example, limited donor skin tissue for transplantation and inflammation during long-term healing time. To address these challenges, in this study we present a method to fabricate Poly(ethylene-co-vinyl alcohol) (EVOH) nanofibres encapsulated with Ag nanoparticle using electrospinning technique. The fibres were fabricated with controlled diameters (59 nm–3 μ m) by regulating three main parameters, that is, EVOH solution concentration, the electric voltage, and the distance between the injection needle tip (high-voltage point) and the fibre collector. Ag was added to the nanofibres to offer long-term anti-inflammation effect by slow release of Ag nanoparticles through gradual degradation of EVOH nanofibre. The method developed here could lead to new dressing materials for treatment of skin wounds.

1. Introduction

Skin wounds are a significant health problem, which negatively affect lives of millions of people worldwide inducing huge societal costs [1–3]. Every year in the USA, more than 1.25 million people have burns [4–6] and 6.5 million people have chronic skin ulcer caused by pressure, venous stasis, or diabetes mellitus [7]. Although skin wound healing has become an increasingly mature topic of study in clinics and academia [8, 9], there are only few breakthroughs in skin wound therapies, mainly due to limited capacities in mitigating body fluid loss and inflammation, particularly for damages of large skin areas.

Existing methods in skin wound treatment have shown steady progress, with increasing survival rate in large-scale burn injuries. There are broadly two types of treatment methods for skin wounds. The first is the medication method, in which coating medicines are applied onto wounded area and covered with bandages. Frequent dressing changes are required to clear body discharges and replace medicines. However, such frequent changes cause severe

pains and increase the rate of inflammation. The second method is skin transplantation, which is more effective in both improving healing and decreasing infections. However, this method is associated with several limitations such as the shortage of donor skin tissues and high cost [10]. As such, skin dressing is still the most widely used treatment in clinical practice and will remain so in the foreseeable future. There is an unmet need for novel materials for better functionality, availability, and effectiveness in skin wound dressing.

In this study, we explored new nanofibres-based dressing materials with better clinical properties to address the problems associated with existing woven and nonwoven materials currently used in skin wound treatment. The advantages of nanofibres network over the traditional dressing materials come from its large surface/volume ratio [11]. This helps to promote permeation of water molecules through the dressing to regulate the moisture level at the wound surface, an important factor to promote cell growth and reduce inflammation. The large surface/volume ratio system also allows drugs, for example, antibacterial drugs or cell growth promoters, to be retained within the structure to control

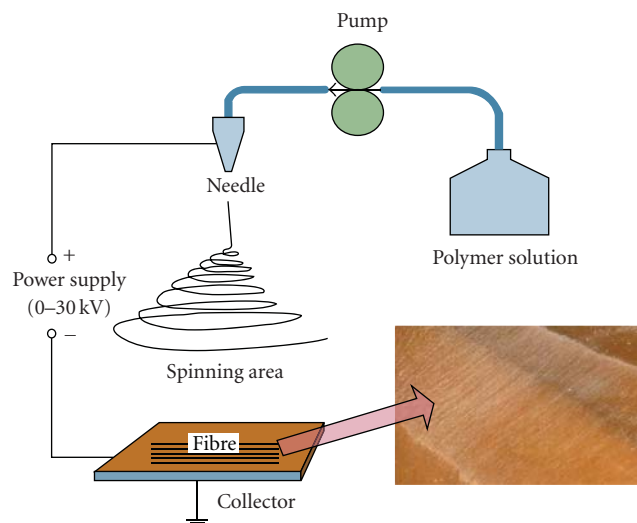


FIGURE 1: The electrospinning system. The electrospinning setup is composed of a syringe and blunt-end needle, a ground electrode as a collector, and a high-voltage supply with a low-current output (limited to a few mA) to generate a static electric field.

infections and facilitate new growths. In addition, materials of proven biocompatibility and biodecomposability such as Poly-L-lactide acid (PLLA), Polyorthoester (POE), and Poly (L-lactide-co-glycolide) (PLGA) [12, 13] can be selected for fabricating fibres encapsulated with drugs and controlling the release of the drugs. These advantages would lead to less frequency in dressing replacement and a better environment for wound healing.

Electrospinning phenomenon was firstly discovered in 1902 [14], where a high-voltage supply was used to stretch a polymer solution injected out of a fine needle. The phenomenon of Taylor Cone was discovered in 1969 by Sir Geoffrey Taylor. This phenomenon has been theoretically analysed, and it is shown that a conducting fluid can exist in equilibrium in the form of a cone under the action of electric field where a jet can be formed at the apex of the cone if a continuing supply of the liquid is provided [15]. In the past few years, significant advances have been achieved in this area, most noticeably in the manufacturing process of electrospun guidance nanofibres, the electrospinning of a bioceramic fibres process, and the technologies of coaxial electrospinning of producing nanotube fibres [16]. The fibre diameter has not been seen down to the size of a single nano, but diameters measured in tens of nanos are achievable (as in this study, we managed fibre diameter down to 50 nanos).

The fibre dries up or solidifies before being deposited onto the grounded collector. The setup used in this study is schematically shown in Figure 1. Note that due to the very low mass of the fibre, its spinning motion can be severely affected by even the smallest air flow in the “flight” space.

2. Material and Electrospinning Methods

2.1. Material. Poly(ethylene-co-vinyl alcohol) EVOH (Sigma-Aldrich, Batch number: 12822PE) was used to make

nanofibres in this study for its good mechanical properties, the biocompatibility, and biodecomposability [17]. The Ag contents in the fibres were obtained from 99.9995% pure AgNO_3 powders (Alfa Aesar, 7761-88-8) dissolved into the solution for electrospinning following standard protocol [18].

2.2. Preparation of EVOH Polymer Solution. Six different concentrations of EVOH solutions (2.5, 5.0, 7.5, 10.0, 12.5, and 15.0 wt%) were prepared, which can be readily electrospun at the room temperature. To prepare an EVOH polymer solution, we diluted EVOH powders in solvent of propan-2-ol, and water. A variety of proportions of propan-2-ol and water were tried, and it is found that the combination of polymer EVOH, 80% propan-2-ol and 20% water heated at 80°C with a reflux setup for 2 to 3 hours produces the solvent for an optimal output of nanofibres. Although solutions of other solvent proportions can be electrospun into fibres, such as EVOH dissolved in 70% 2-propanol/30% water, they appear to be hindrance to the formation of Ag particles in fibres when AgNO_3 was added, yielding in scattering Ag particle sizes and distributions.

2.3. Electrospinning Nanofibres. The system used to carry out the “spinning” is composed of a high power supply (Spellman CZE1000R, 0–30 kV,) with very low-current output (μA ranges), a peristaltic pump (Masterflex, 77120-52) with a feeding capacity in the range of 1.0–15.0 mL/h, a container (such as a syringe) with a fine needle, which is charged by the power supply, and a metal collector (can be in various shapes) which is normally grounded. The charged tip and grounded collector form a static electric field between them to provide the driving force to spin the fibre.

2.4. Encapsulation of Ag Nanoparticles in the Fibre. The suppressive effect of Ag to inflammation is well understood and utilized in clinical practice. To encapsulate Ag nanoparticles into fibres, AgNO_3 of various concentrations was first added into 7.5 wt% EVOH solution which was then electrospun into nanofibres. AgNO_3 in the fibres is deoxidized and forms into pure Ag nanoparticles when exposed to illumination. The speed of deoxidization can be accelerated by using UV lights. For fibres containing Ag, it was found that the collector is required to be changed from a plate shape to a stripe one without ground connection due to the increased conductivity of the fibre.

2.5. Characterization of the Fabricated Fibres. We fabricated nanofibres using different electrospinning parameters including the distance (15–35 cm) between the tip of the injecting needle and the collector, the voltage (8–20 kV) applied to generate the electric field, and the density (2.5–15.0 wt%) of the polymer solution. Scanning electron microscopy (JSM-6700 Cold FE SEM) was performed for fibre measurement. All fibre samples were mounted onto a copper stub and sputter coated with gold for energy spectrum analysis in SEM. Each sample was divided into 12 parts for diameter measurements. We used 12 uniform size

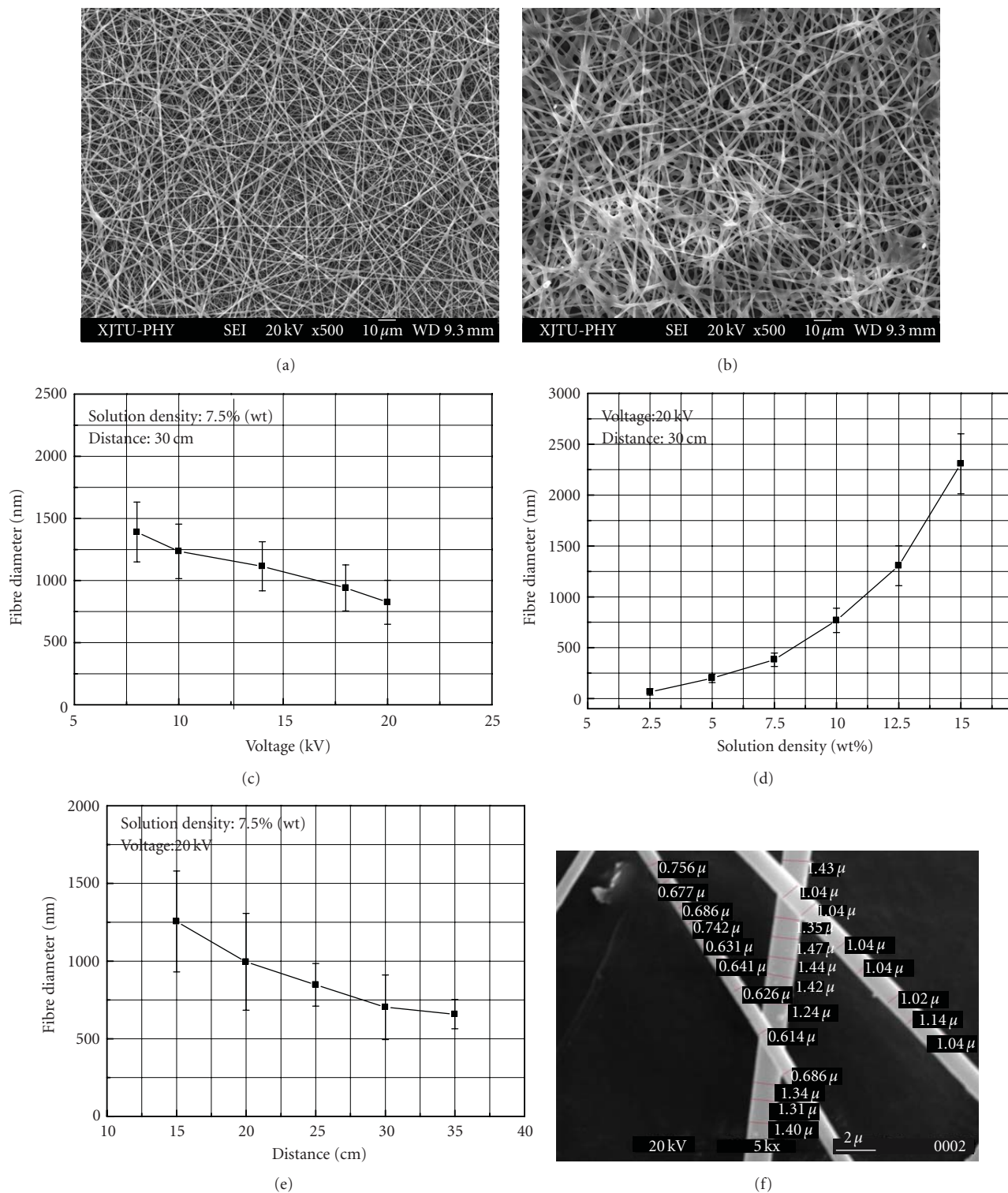


FIGURE 2: Nanofibres and fabrication parameters. (a) An SEM picture of EVOH nanofibres produced with a solution in a stabilized temperature; (b) an SEM picture of EVOH nanofibres with a solution in decreasing temperature; (c) effect of the voltage on fibre diameters when the solution density is 7.5% (wt) and needle tip-to-collector distance is 30 cm; (d) effect of the density on fibre diameters when the voltage is 20 kV and the tip-to-collector distance is 30 cm; (e) effect of the distance on fibre diameters when the solution density is 7.5% (wt) and the voltage is 20 kV; (f) an example of SEM measurement of fibre diameters.

conductive tapes ($3 \times 3 \text{ mm}^2$) to make 12 fibre samples from each experiment directly in different areas. All diameters of the 12 samples were measured under SEM (Figure 2(f)) long each fibre. Due to the variation of fibre diameters, around 1000 measurement were carried out in total for statistic evaluation. Figures 2(c)–2(e) show the average values. Based on the results, calculations were carried out for the 3 main control parameters, that is, the tip-to-collector distance, the field voltage, and the solution density.

In addition, another important parameter which controls the fibre formation is the injection rate of the EVOH solution. This is normally done through the feeding speed control of the micropump. However, our study shows that there is only a very narrow window of the speed which can be utilized to produce fibres. In other words, there is no much room to play with the injection speed. One either gets it right for clear fibres, or wrong for no fibres or poor fibre formations. Thus, the injection speed is not really a “controllable” parameter. In this study, the speed we used was 1.5 ml/h which allows us to obtain fibres in the diameter range from 100 to 1000 nanometers.

2.6. Bacteria Test. Bacteria test was performed to test the ability of restraining pathogens using the fabricated Ag-encapsulating nanofibres. *Staphylococcus aureus*, which is one of the main pathogenic bacterias found on animal/human burn surface, was used in this study. *Staphylococcus aureus* was diluted by LB culture fluid to OD600 value 1.1. 0.5 mL of the diluted fluid was used to fully cover the base of a culture dish. Four fibre samples with different concentrations of Ag nanoparticles were tiled into the culture dishes. The culture was then carried out in an incubator at shaking speed of 50 r/min for 6 hours at 37°C. To quantify the effectiveness of restraining pathogens, we measured the bacteriostatic loops at time intervals of 6 hours using a digital camera, and the diameters were measured by an electronic vernier caliper.

3. Results and Discussions

3.1. Fabrication Parameters. EVOH is thermally sensitive which may affect the electrospinning process. To check the effect of temperature, we used SEM to assess the morphology of the nanofibres fabricated with/without temperature control during the fabrication. The temperature of the solution was controlled either at 80°C constantly or allowed to cool down from 80°C to room temperature naturally during the spinning process, respectively. Comparison of Figures 2(a)–2(b) shows that the quality of fibres deteriorates when solution temperature is decreasing (Figure 2(b)), that is, fibres become sticky to form clusters with larger and uneven diameters. Figure 2(a) also shows larger interfibre space which is beneficiary for moisture regulation [19].

It is reported that the fibre diameter may influence the healing speed [20]. To evaluate the control of the fibre diameter, we quantified the relationship between the fibre diameter and the 3 parameters discussed, that is, the tip-to-collector distance, the voltage of the electric field, and the density of polymer solution. The findings are illustrated

in Figures 2(c)–2(e). Figure 2(c) shows the effect of voltage for the cases with a constant solution density at 7.5% and the tip-to-collector distance at 30 cm. We observed that the most suitable voltage range is from 10 to 20 kV. At lower voltages ($<10 \text{ kV}$), there is not enough power to drive the EVOH jet through the electric field to form nanofibres, while at a higher value ($>20 \text{ kV}$), the solution jet is broken by the too strong stretching force by the electrical field that no continuing fibres can be formed. Figure 2(d) shows results of 6 different values of solution density at 2.5, 5.0, 7.5, 10, 12.5, and 15.0 wt%, respectively. The voltage was kept at 20 kV and the tip-to-collector distance at 30 cm. It is clearly shown that the fibre diameter increases rapidly in increasing solution densities. The increased density leads to a higher viscosity which makes it more difficult to stretch the jet into finer fibres and also more prone to form “blockage” at the needle tip. We also noted that the fibre diameter can be influenced by the environmental temperature and humidity level. Higher temperature and low humidity are found to lead to finer fibre formation, though we were not able to quantify this. An effort to increase the temperature in the spinning space led to air circulation and yielded severe disturbance to fibre collection. Thus, all our results were obtained in ambient environmental conditions. Figure 2(e) shows results of 5 tip-to-collector distances of 15, 20, 25, 30 and 35 cm, respectively. 20 kV field voltage and 7.5 wt% solution density were used. We observed no significant effect of the distance on the fibre diameter. Nevertheless, the distance provided a space necessary for fibres to stretch and dry up before reaching the collector. Otherwise, fibres will stick together to form clusters. In our tests, this occurs when the distance was reduced to 10 cm. On the other hand, when the distance was increased to 40 cm, the fibres were not collectable due to too violent spinning.

3.2. Energy Spectrum Check of Encapsulated Ag Particles. The suppressive effect of Ag on inflammation is related to the purity Ag (simple substance) encapsulated. To check the content of the Ag particles obtained, the energy spectrum function of the SEM was used. Figures 3(e)–3(f) show the composition of the Ag particles and the image of the Ag particle in the fibres. It shows that the particles are simple substance Ag, where the elements C and O are from the EVOH polymer.

3.3. Bacteria Culture Tests. The main pathogens on the surface of skin burn is *Staphylococcus aureus* ($>80\%$) [21]. To assess the pathogen-restraining ability of the Ag-encapsulating nanofibres, we performed bacteria tests on EVOH fibres with different Ag concentrations (Figure 3(b)). We produced 4 samples of different Ag content, that is, 0.03 (Figure 3(b)-1), 0.07 (Figure 3(b)-2), 0.1 (Figure 3(b)-3), and 0.15 (Figure 3(b)-4) g, respectively, in 10 mL 7.5 wt% 80%/20% 2-propanol/water solution, respectively, and EVOH fibres without Ag (Figure 3(g)). Results of the bacteria tests are based on the measurements of bacteriostatic loop. The diameter of their bacteriostatic loops [22] was measured after culture (Figure 3(c)). A linearly increasing effectiveness

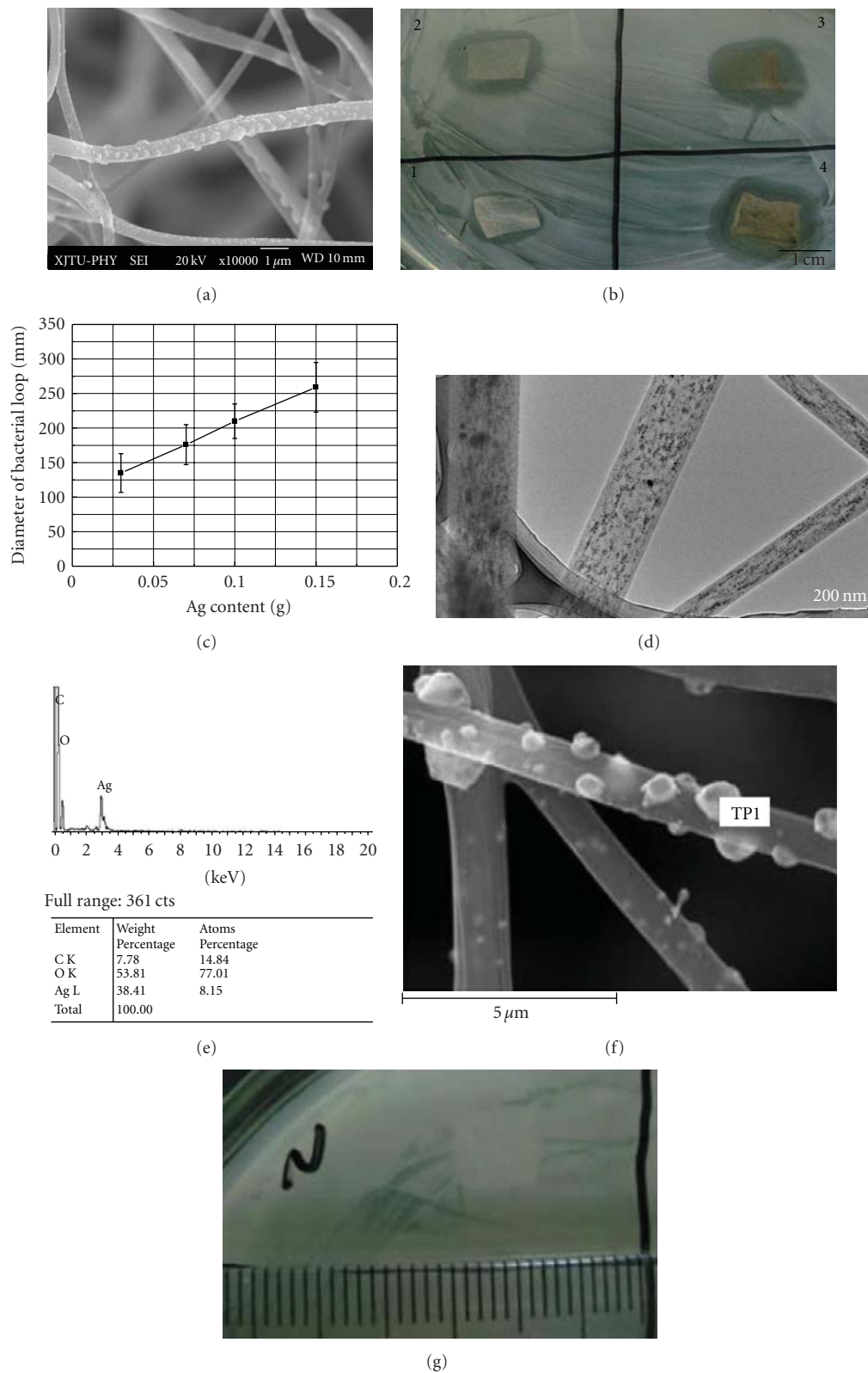


FIGURE 3: Fabrication Ag-encapsulated nanofibres and bacteria tests. (a) SEM image of nanofibre encapsulated with Ag nanoparticle (Tip-to-collector distance is 30 cm, voltage is 20 kV, and solution density is 7.5 wt%), (b) image of one set of culture test for bacteriostatic loop measurement, (c) averaged measurement of bacterial loop diameter versus Ag concentration (wt/10 mL), (d) a TEM image encapsulated with Ag nanoparticle (Tip-to-collector distance is 30 cm, voltage is 20 kV, and solution density is 7.5 wt %), (e) and (f) energy spectrum using SEM for encapsulated Ag particles, and (g) image of EVOH fibre without Ag particles in the bacteria test.

is found amongst the four concentrations used, with the highest Ag concentration yielding in the biggest loop for the same area of the fibre patches, clearly indicating a stronger pathogen-restraining effect. In contrast, no bacteriostatic loop was observed for pure EVOH fibres with Ag, indicating no pathogen restraining ability for fibres without Ag (Figure 3(g)).

In this study, no biodegradable tests were carried out on the nanofibres though this feature of the EVOH is well known [17]. The challenges remain in the simulation of the temperature, moisture, and importantly the PH value in a skin wound environment and their variations during the application of the fibres. However, this is a potentially important feature as it may determine the release speed of the Ag particles not on fibre surface and drugs which can be contained in the fibre. This remains a key test to be conducted in the following study.

4. Conclusions

Electrospinning is a straightforward approach to fabricate highly fibrous and porous EVOH materials for medical applications. In this study, we fabricated EVOH nanofibre encapsulated with Ag nanoparticles. The results of fibre characterization show that the nanofibre size can be controlled by regulating EVOH solution concentration, voltage, and distance of the electric field. Material characterization shows that 99% pure Ag particles can be formed in the fibre with AgNO₃ added to the solution. Adding high concentration of Ag might change the fibre morphology; however, only low concentrations of Ag were used in our experiments. Compared under SEM and TEM observations, the morphology of Ag particles fibres is of no significant difference with pure EVOH fibres. Results of bacteria tests show that pathogen-restraining ability of the Ag-encapsulated nanofibres is effective and proportional over a range of Ag concentration, indicating its inflammation control capacity and the potential for applications in skin wound treatment. To further evaluate the suitability and effectiveness of Ag-encapsulating nanofibres on skin wound healing, animal tests have been planned in the next stage of study.

Acknowledgment

The work was partially supported by the National Natural Science Foundation of China (nos. 10825210, 10872157, and 31050110125) and the National 111 Project of China (no. B06024).

References

- [1] F. Xu, P. F. Wang, M. Lin, T. J. Lu, and E. Y. K. Ng, "Quantification and the underlying mechanism of skin thermal damage: a review," *Journal of Mechanics in Medicine and Biology*, vol. 10, no. 3, pp. 373–400, 2010.
- [2] L. Zhou, Y. Hu, and M. Zhang, "Investigation on the psychological conditions of face or body burned patients," *Journal of North China Coal Medical College*, vol. 10, no. 4, pp. 503–504, 2008 (Chinese).
- [3] M. Choinière, R. Melzack, N. Girard, J. Rondeau, and M. J. Paquin, "Comparisons between patients' and nurses' assessment of pain and medication efficacy in severe burn injuries," *Pain*, vol. 40, no. 2, pp. 143–152, 1990.
- [4] P. A. Brigham and E. McLoughlin, "Burn incidence and medical care use in the United States: estimates, trends, and data sources," *Journal of Burn Care and Rehabilitation*, vol. 17, no. 2, pp. 95–107, 1996.
- [5] R. L. Sheridan, "Burn care: results of technical and organizational progress," *Journal of the American Medical Association*, vol. 290, no. 6, pp. 719–722, 2003.
- [6] B. H. Yu and J. E. Dimsdale, "Posttraumatic stress disorder in patients with burn injuries," *Journal of Burn Care and Rehabilitation*, vol. 20, no. 5, pp. 426–433, 1999.
- [7] I. Calif, "U.S. markets for wound management products," Medical Data International, 1997.
- [8] F. Xu, T. J. Lu, K. A. Seffen, and E. Y. K. Ng, "Mathematical modeling of skin bioheat transfer," *Applied Mechanics Reviews*, vol. 62, no. 5, Article ID 050801, 35 pages, 2009.
- [9] F. Xu and T. J. Lu, "Skin biothermomechanics: modeling and experimental characterization," in *Advances in Applied Mechanics*, E. van der Giessen and H. Aref, Eds., pp. 147–248, Academic Press, Burlington, Mass, USA, 2009.
- [10] B. Domres, D. Kistler, and J. Rutzynska, "Intermingled skin grafting: a valid transplantation method at low cost," *Annals of Burns and Fire Disasters*, vol. 20, no. 3, pp. 149–154, 2007.
- [11] C. R. Carlisle, C. Coulais, M. Namboothiry, D. L. Carroll, R. R. Hantgan, and M. Guthold, "The mechanical properties of individual, electrospun fibrinogen fibers," *Biomaterials*, vol. 30, no. 6, pp. 1205–1213, 2009.
- [12] L. E. Claes, "Mechanical characterization of biodegradable implants," *Clinical Materials*, vol. 10, no. 1–2, pp. 41–46, 1992.
- [13] A. A. Ignatius and L. E. Claes, "In vitro biocompatibility of bioresorbable polymers: poly(L, DL-lactide) and poly(L-lactide-co-glycolide)," *Biomaterials*, vol. 17, no. 8, pp. 831–839, 1996.
- [14] J. F. Cooley, "The process of electro-spinning," US patent, 1902.
- [15] G. Taylor, "Electrically driven jets," *Proceedings of the Royal Society of London. Series A*, vol. 313, no. 1515, pp. 453–475, 1969.
- [16] Y. Dzenis, "Spinning continuous fibers for nanotechnology," *Science*, vol. 304, no. 5679, pp. 1917–1919, 2004.
- [17] E. Kenawy, J. M. Layman, J. R. Watkins et al., "Electrospinning of poly(ethylene-co-vinyl alcohol) fibers," *Biomaterials*, vol. 24, no. 6, pp. 907–913, 2003.
- [18] P. Zhang, S. Phansiri, and J. Puonti-Kaerlas, "Improvement of cassava shoot organogenesis by the use of silver nitrate in vitro," *Plant Cell, Tissue and Organ Culture*, vol. 67, no. 1, pp. 47–54, 2001.
- [19] M. Zhang, Y. S. Huang, and Q. Zhang, "Protective effect of nitric oxide production on myocardium in severely scalded rats," *Chinese Journal of Burns*, vol. 23, no. 5, pp. 327–330, 2007.
- [20] C. B. D. J. Hinsey, "The recovery of diameter and impulse conduction in regenerating nerve fibers," *Annals of the New York Academy of Sciences*, vol. 47, no. 4, pp. 559–574, 1946.
- [21] A. S. Colsky, R. S. Kirsner, and F. A. Kerdel, "Analysis of antibiotic susceptibilities of skin wound flora in hospitalized dermatology patients: the crisis of antibiotic resistance has

come to the surface,” *Archives of Dermatology*, vol. 134, no. 8, pp. 1006–1009, 1998.

- [22] Q. Zheng, H. Wu, J. Du, S. Li, and Y. Yan, “The bacterial inhibitory ability and in vivo drug release pattern of a new drug delivery system: ciprofloxacin/tricalcium phosphate delivery capsule,” *Journal of Huazhong University of Science and Technology. Medical Sciences*, vol. 18, no. 3, p. 172176, 1998.

Research Article

Dependence of Spreading and Differentiation of Mesenchymal Stem Cells on Micropatterned Surface Area

Wei Song,^{1,2} Naoki Kawazoe,^{1,3} and Guoping Chen^{1,2,3}

¹ Biomaterials Center, National Institute for Materials Science, 1-1 Namiki, Tsukuba, Ibaraki 305-0044, Japan

² Graduate School of Pure and Applied Sciences, University of Tsukuba, 1-1-1 Tennodai, Tsukuba, Ibaraki 305-8571, Japan

³ International Center for Materials Nanoarchitectonics (MANA), National Institute for Materials Science, 1-1 Namiki, Tsukuba, Ibaraki 305-0044, Japan

Correspondence should be addressed to Guoping Chen, guoping.chen@nims.go.jp

Received 16 October 2010; Revised 6 January 2011; Accepted 5 February 2011

Academic Editor: Yanan Du

Copyright © 2011 Wei Song et al. This is an open access article distributed under the Creative Commons Attribution License, which permits unrestricted use, distribution, and reproduction in any medium, provided the original work is properly cited.

Micropatterning technology is a highly advantageous approach for directly assessing and comparing the effects of different factors on stem cell functions. In this study, poly(vinyl alcohol)- (PVA-) micropatterned polystyrene surfaces were prepared using photoreactive PVA and ultraviolet photolithography with a photomask. The micropatterned surface was suitable for single-cell array formation and long-term cell culture due to the nanometer thickness of nonadhesive PVA layer. Different degrees of cell spreading with the same cell shape were established by adjusting the sizes of circular, cell-adhesive polystyrene micropatterns. Cell spreading and differentiation of mesenchymal stem cells (MSCs) on the micropatterns were investigated at the single-cell level. The assembly and organization of the cytoskeleton were regulated by the degree of cell spreading. Individual MSCs on large circular micropatterns exhibited a more highly ordered arrangement of actin filaments than did those on the small circular micropatterns. Furthermore, the differentiation of MSCs was dependent on the degree of cell spreading. Increased cell spreading facilitated the osteogenic differentiation but suppressed the adipogenic differentiation of MSCs. This micropatterning method is valuable for stem cell research in tissue engineering and regenerative medicine.

1. Introduction

Stem cells, a reservoir of undifferentiated cells with the capacity for unlimited or prolonged self-renewal, have the potential to produce differentiated and specialized progenies [1]. They hold the key to a number of cellular processes, including development, tissue regeneration, and aging, and the promise of cures for many diseases and injuries. They are a versatile and promising cell source for tissue engineering and regenerative medicine [2].

The inherent plasticity and multilineage potential of stem cells have brought about the requirement for strictly controlling cell functions, such as growth, phenotypic expression, and differentiation [3–7]. Traditionally, the fate of stem cells has been regulated by biological factors, such as cytokines and growth factors [8–11]. Recently, more and more evidence has revealed that physical factors also contribute to the overall behaviors and functions of stem

cells [12–16]. The area of cell spreading is one such physical factor that has been demonstrated to affect cell behaviors and functions. Bhadriraju and Hansen [17] have reported that the stiffness of hepatocytes is affected by cell spreading. Cell stiffness increases with cell spreading but remains low in cells with round morphology. Szabo et al. [18] have demonstrated the high adipogenic potential of wild-type embryonic stem cells (ESCs) on non-adhesive substrata, where cell spreading is hindered. However, during routine cell culture, the process of cell spreading is often accompanied by a change in cell shape, the area of cell spreading is diverse among cells, and the heterogeneity within a cell population, such as cell-cell interaction, is complex. Therefore, a convenient method for strictly controlling the spreading area of a large number of individual cells with the same shape is extremely desirable for investigating the effect of cell spreading on cell functions.

Micropatterning technology [19] is particularly suitable for this purpose and is already used for investigating the

effects of physical parameters on cell behaviors, such as the orientation of the cell division axis [20], cell polarization [21, 22], proliferation [23], apoptosis [24], and differentiation [25]. However, one of the main obstacles in applying cell micropatterning technologies is that few of them are compatible with long-term cell culture. Extended culture time is normally required because many cell functions, such as differentiation, need a long time to respond to external stimuli.

In this study, we prepared poly(vinyl alcohol)- (PVA-) micropatterned polystyrene surfaces using ultraviolet photolithography with a photomask. This method is simple and reproducible. The micropatterned surfaces were used to culture mesenchymal stem cells (MSCs), form a stable cell array at the single-cell level for long-term cell culture, and compare the effect of cell spreading on the adipogenic and osteogenic differentiation of MSCs.

2. Materials and Methods

2.1. Synthesis of Azidophenyl-Derivatized Poly(vinyl alcohol). Azidophenyl-derivatized poly(vinyl alcohol) (AzPhPVA) was synthesized by coupling the hydroxyl groups of PVA to 4-azidobenzoic acid, as previously described [26, 27].

2.2. Micropatterning of Poly(vinyl alcohol). A polystyrene plate was cut from a polystyrene tissue culture flask (BD Falcon). The AzPhPVA solution (0.15 mL, 0.3 mg/mL) was placed on the polystyrene plate and air-dried in the dark at room temperature. The plate was covered with a photomask with UV blocking circular micropatterns of different areas and irradiated with UV light (Funa-UV-Linker FS-1500) at an energy of 0.2 J/cm² from a distance of 15 cm. After irradiation, the plate was immersed in MilliQ water and then ultrasonicated to completely remove any unreacted polymer from the unirradiated areas. After washing completely, the PVA-micropatterned surface was obtained.

2.3. Observation by Atomic Force Microscope (AFM). The surface topography of the PVA-micropatterned polystyrene plate was observed using an MFP-3D-BIO atomic force microscope (Asylum Research). A commercially available cantilever (spring constant: 0.06 N/m; oscillation frequency: 12–24 kHz; DNP, Veeco Probes) with a silicon nitride tip was used to measure the samples (90 × 90 μm²) in MilliQ water in contact mode. The diameter and thickness of the circular micropattern were measured by section analysis of the acquired image. Three randomly selected micropatterns were measured to calculate the means and standard deviations.

2.4. Cell Culture. Human bone marrow-derived mesenchymal stem cells (hMSCs) were obtained from Osiris Therapeutics (Columbia, MD) at passage 2. The cells were seeded in culture flasks using proliferation medium purchased from Lonza. The proliferation medium contained 440 mL of MSC basal medium, 50 mL of mesenchymal cell growth supplement, 10 mL of 200 mM L-glutamine, and 0.5 mL of a penicillin/streptomycin mixture. The cells were further

subcultured once after reaching confluence and used at passage 4. The cells were collected by treatment with trypsin/EDTA solution and suspended in control medium at a density of 1.5×10^4 cells/mL. The control medium was composed of Dulbecco's modified Eagle's medium (DMEM, Sigma) supplemented with 4500 mg/L glucose, 584 mg/L glutamine, 100 U/mL penicillin, 100 μg/mL streptomycin, 0.1 mM nonessential amino acids, 0.4 mM proline, 50 mg/L ascorbic acid, and 10% fetal bovine serum (FBS). The micropatterned polystyrene plates were placed in 6-well cell culture plates, and a glass ring (diameter: 15 mm; height: 10 mm) was placed over each PVA micropatterned polystyrene plate. Three milliliters of control medium were added to each well, and then the cell suspension solution (0.36 mL, 1.5×10^4 cells/mL) was placed inside the glass ring (seeding density: 3.0×10^3 cells/cm²). After 6 h, the glass rings were removed, and the control medium was replaced with adipogenic or osteogenic medium. The adipogenic medium consisted of DMEM supplemented with 4500 mg/L glucose, 584 mg/L glutamine, 100 U/mL penicillin, 100 μg/mL streptomycin, 0.1 mM nonessential amino acids, 0.4 mM proline, 50 mg/L ascorbic acid, 10% FBS, 1 M dexamethasone, 0.5 mM methylisobutylxanthine, 10 μg/mL insulin, and 100 μM indomethacin. The osteogenic medium consisted of DMEM supplemented with 1000 mg/L glucose, 584 mg/L glutamine, 100 U/mL penicillin, 100 μg/mL streptomycin, 0.1 mM nonessential amino acids, 50 mg/L ascorbic acid, 10% FBS, 100 nM dexamethasone, and 10 mM β-glycerophosphate disodium salt hydrate. The adipogenic and osteogenic media were changed every 3 days.

2.5. F-Actin Staining. After incubation for 6 h in control medium, the cultured cells were fixed with 4% paraformaldehyde, permeabilized with 0.2% Triton X-100, and blocked with 1% BSA solution. The F-actin and nuclei of cells were stained with Alexa Fluor 488 phalloidin (Invitrogen) and 4',6-diamidino-2-phenylindole (DAPI, Vector Laboratories, Inc.), respectively. Fluorescence photographs of the stained MSCs were captured by an Olympus BX51 microscope with a DP-70 CCD camera (Olympus, Tokyo, Japan).

2.6. Oil Red O Staining. After incubation in adipogenic induction medium for 7 days, the cultured cells were fixed with 4% paraformaldehyde, incubated in 60% isopropanol for 5 min, and then stained with fresh Oil Red O for 5 min. The Oil Red O solution was prepared by mixing three parts stock solution, 0.3% in isopropanol with two parts MilliQ water and filtering through a 0.2-μm filter. Photomicrographs were captured by an optical microscope with a DP-70 CCD camera (Olympus, Tokyo, Japan). The probability of MSC adipogenesis at different cell spreading areas was studied by calculating the percentage of MSCs that committed to an adipocyte lineage. MSCs containing lipid vacuoles positively stained by Oil Red O were considered to be adipocytes, and only single cells on each circular micropattern (as confirmed by nuclear staining) were counted. Three samples were used to calculate the means and standard deviations.

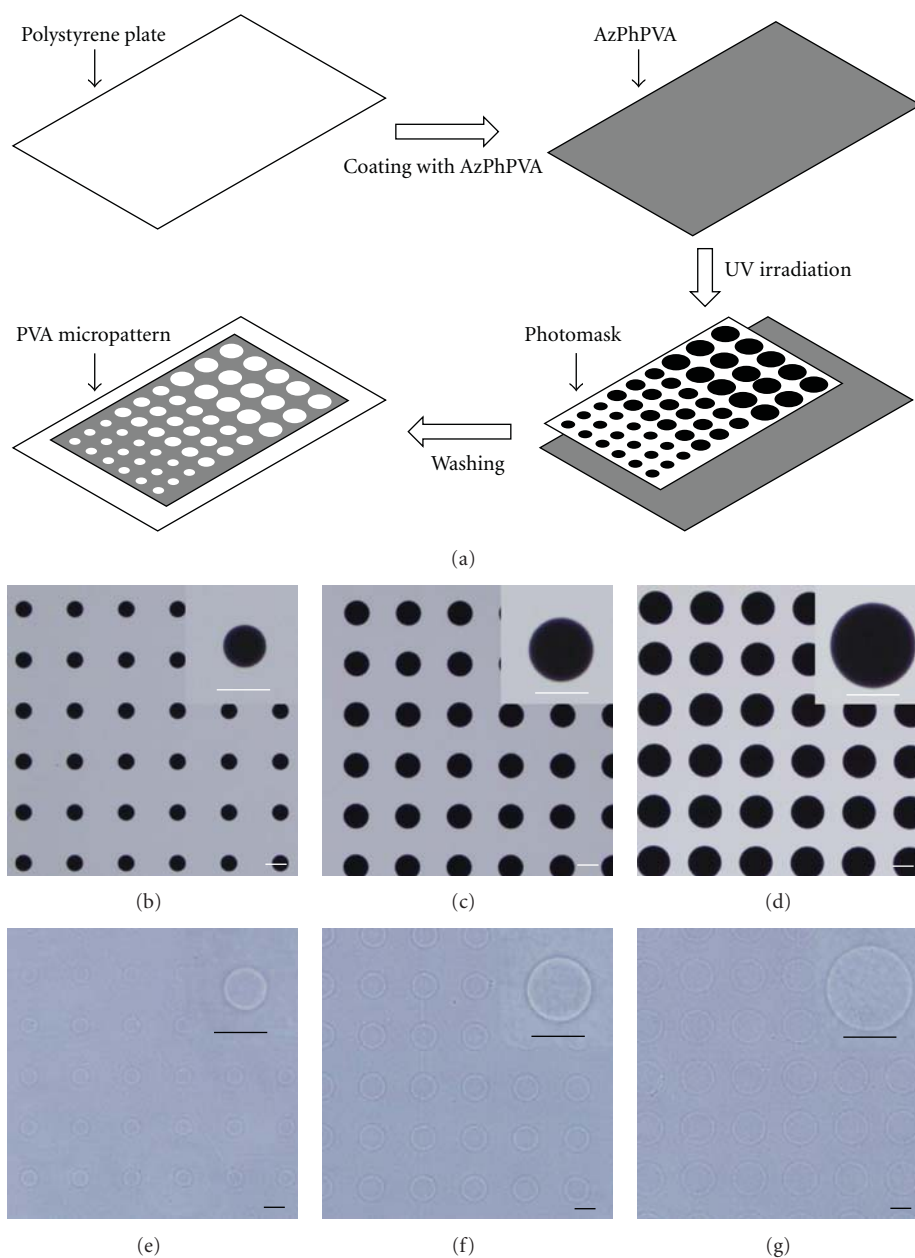


FIGURE 1: (a) Preparation scheme of the PVA-micropatterned surface. (b–d) Phase contrast micrographs of the photomask. (e–g) Phase contrast micrographs of the PVA-micropatterned polystyrene surface. Three types of circular polystyrene micropatterns with different diameters were formed and surrounded by PVA domains. Scale bars: 50 μm .

2.7. Alkaline Phosphatase (ALP) Staining. Cellular alkaline phosphatase (ALP) activity was assessed after culture for 7 and 21 days in osteogenic induction medium. The cultured cells were rinsed three times with phosphate-buffered saline (PBS) and fixed with 4% paraformaldehyde for 10 min at 4°C. The fixed cells were soaked in 0.1% naphthol AS-MX phosphate (Sigma) and 0.1% fast red violet LB salt (Sigma) in 56 mM 2-amino-2-methyl-1,3-propanediol (pH 9.9, Sigma) for 10 min at room temperature, washed with PBS, and then observed by an optical microscope with a DP-70 CCD camera (Olympus, Tokyo, Japan). The probability of MSC osteogenesis at different cell spreading

areas was studied by calculating the percentage of MSCs that committed to an osteoblast lineage. MSCs positively stained were considered to be osteoblasts, and only single cells on each circular micropattern (as confirmed by nuclear staining) were counted. Three samples were used to calculate the means and standard deviations.

2.8. Statistical Analysis. A one-way analysis of variance (ANOVA) with Tukey's *post hoc* test for multiple comparisons was used for statistical analysis. A value of $P < .05$ was considered to be a statistically significant difference.

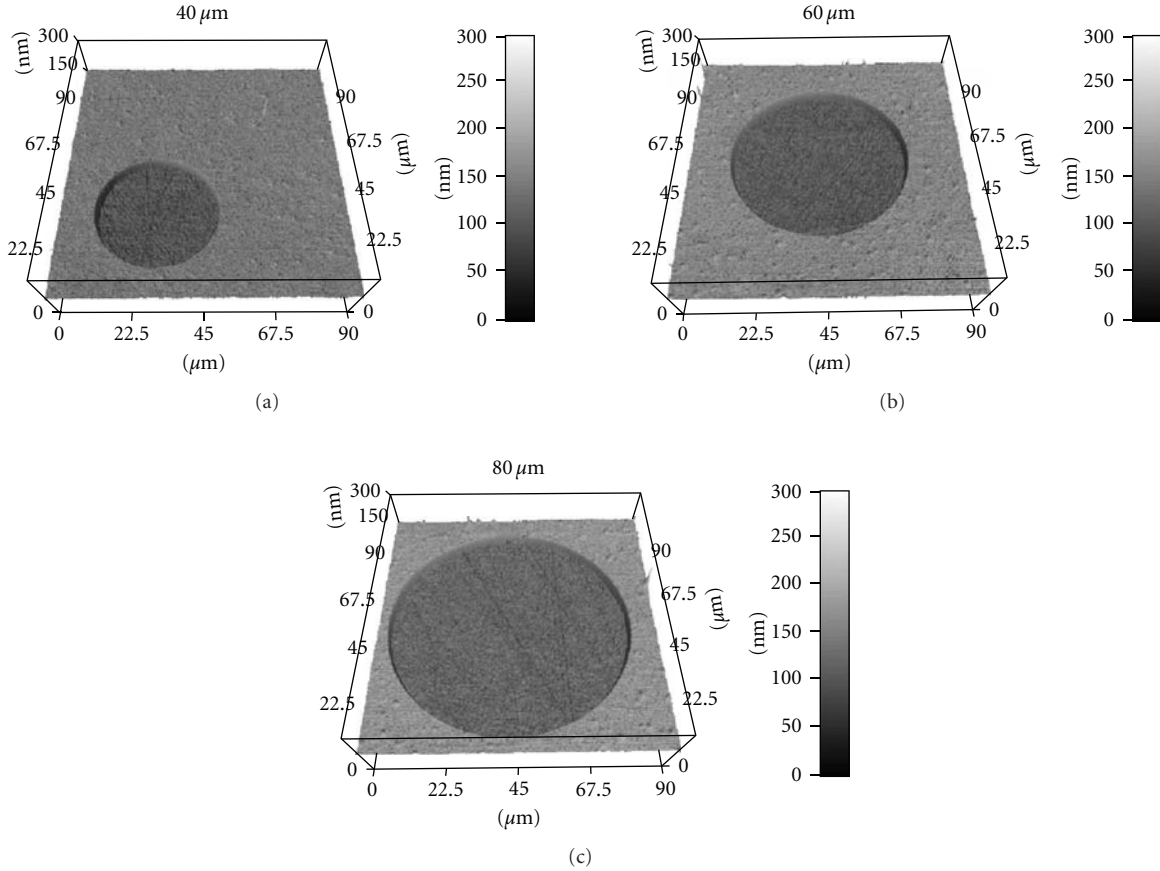


FIGURE 2: Three-dimensional AFM images of the three types of circular polystyrene micropatterns with different diameters measured in MilliQ water in contact mode.

3. Results

3.1. Preparation and Observation of PVA-Micropatterned Surfaces. The preparation scheme for the PVA-micropatterned polystyrene surface is illustrated in Figure 1(a). The AzPhPVA-coated plate was covered with a photomask and irradiated with UV light. The photomask had three different circular micropatterns with diameters of 40, 60, and 80 μm (Figures 1(b)–1(d)). These circular micropatterns were UV blocking, and the underlying AzPhPVA was protected from UV light, unreacted during UV irradiation, and washed away by MilliQ water after UV irradiation. However, the AzPhPVA under the surrounding UV transparent domains was exposed to UV light, inter- and intramolecularly crosslinked, and grafted to the polystyrene surface. Therefore, three different circular polystyrene micropatterns were formed and surrounded by PVA domains (Figures 1(e)–1(g)). The circular polystyrene micropatterns promoted cell adhesion, whereas the surrounding PVA domains inhibited cell adhesion.

To measure the diameter of each circular polystyrene micropattern, the PVA-micropatterned polystyrene surfaces were observed by AFM in MilliQ water in contact mode. The three-dimensional images of the three circular polystyrene micropatterns are shown in Figure 2. The diameter and

TABLE 1: The designed diameter of the circle on the photomask and the measured diameter and thickness of the prepared circular micropatterns, as determined by AFM section analysis. Data represent mean \pm SD ($n = 3$).

Designed diameter (μm)	Measured diameter (μm)	Measured thickness (nm)
40	39.2 ± 0.5	51.4 ± 1.9
60	59.9 ± 0.4	53.6 ± 2.8
80	79.8 ± 0.6	52.9 ± 3.0

thickness of the circle were analyzed by section analysis of the acquired images (Table 1). The diameters of the circular micropatterns formed from the 40-, 60-, and 80- μm -diameter photomask micropatterns were 39.2 ± 0.5 , 59.9 ± 0.4 , and 79.8 ± 0.6 μm , respectively. The circular polystyrene micropatterns had almost the same diameters as the designed photomask micropatterns. The thickness of the PVA layer was ranged from 51.4 to 53.6 nm. Therefore, circular polystyrene micropatterns with different diameters were formed, and their structures could be controlled by designing the micropatterns of a photomask.

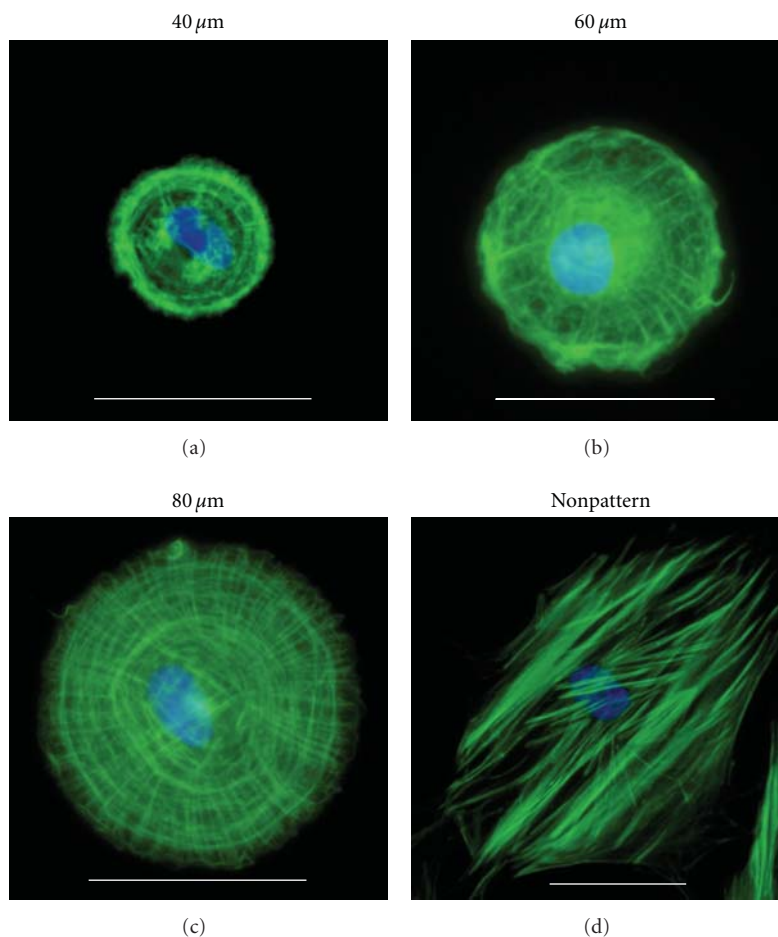


FIGURE 3: Fluorescence images of MSCs with different spreading areas stained for F-actin (green) and nuclei (blue) after culture in control medium for 6 h. “Nonpattern” indicates a bare polystyrene surface without micropatterning and grafting of PVA. Scale bars: 50 μm .

3.2. Cell Adhesion and Spreading. The micropatterned surfaces were used for the culture of MSCs in control medium. After 6 h of culture, MSCs only adhered to cell-adhesive circular polystyrene micropatterns, and MSCs on non-adhesive PVA regions were removed by a medium change. About 85% of circular micropatterns were occupied by a single cell, as confirmed by cell nuclear staining using DAPI. Therefore, the heterogeneity of the cell population in routine cell culture could be reduced, and the behaviors and functions of MSCs could be studied at a single-cell level.

As shown in Figure 3, F-actin staining revealed that the spreading of MSCs followed the underlying circular polystyrene micropatterns and was confined by the surrounding non-adhesive PVA domains, whereas MSCs spread freely on bare polystyrene surfaces (nonpatterned). Interestingly, the assembly and organization of the actin structure of the MSCs were affected by the degree of cell spreading. Circular MSCs with the largest degree of spreading (80 μm) mainly assembled actin in the radial and concentric directions of the circle. However, such organization of the actin structure weakened as the degree of cell spreading decreased. On the smallest circle (40 μm), MSCs predominately assembled actin along their edges, between the adhesive polystyrene

and non-adhesive PVA. The MSCs cultured on the bare polystyrene plate did not exhibit any regular organization.

3.3. Adipogenic Differentiation of MSCs with Different Cell Spreading Areas. MSCs were cultured on the micropatterns in adipogenic induction medium for 7 days. Some MSCs on micropatterns committed to adipocytes that contained lipid vacuoles. Lipid vacuoles were stained with Oil Red O, a specific marker for adipogenic differentiation. Representative optical photographs of positively stained cells with different cell spreading areas are shown in Figure 4(a). The probabilities that MSCs with different degrees of cell spreading committed to adipocytes were evaluated. The cells containing lipid vacuoles positively stained by Oil Red O were considered to be adipocytes, and only single cells on each circular micropattern were counted. The results show that the probability of MSC adipogenesis was dependent on the degree of cell spreading (Figure 4(b)). The percentages of MSCs undergoing adipogenic differentiation were $45.3 \pm 3.4\%$, $26.3 \pm 3.4\%$, and $14.7 \pm 4.2\%$ for 40- to 80- μm circles and $12.4 \pm 2.0\%$ for the bare polystyrene surface (nonpatterned). Therefore, the probability of adipogenic

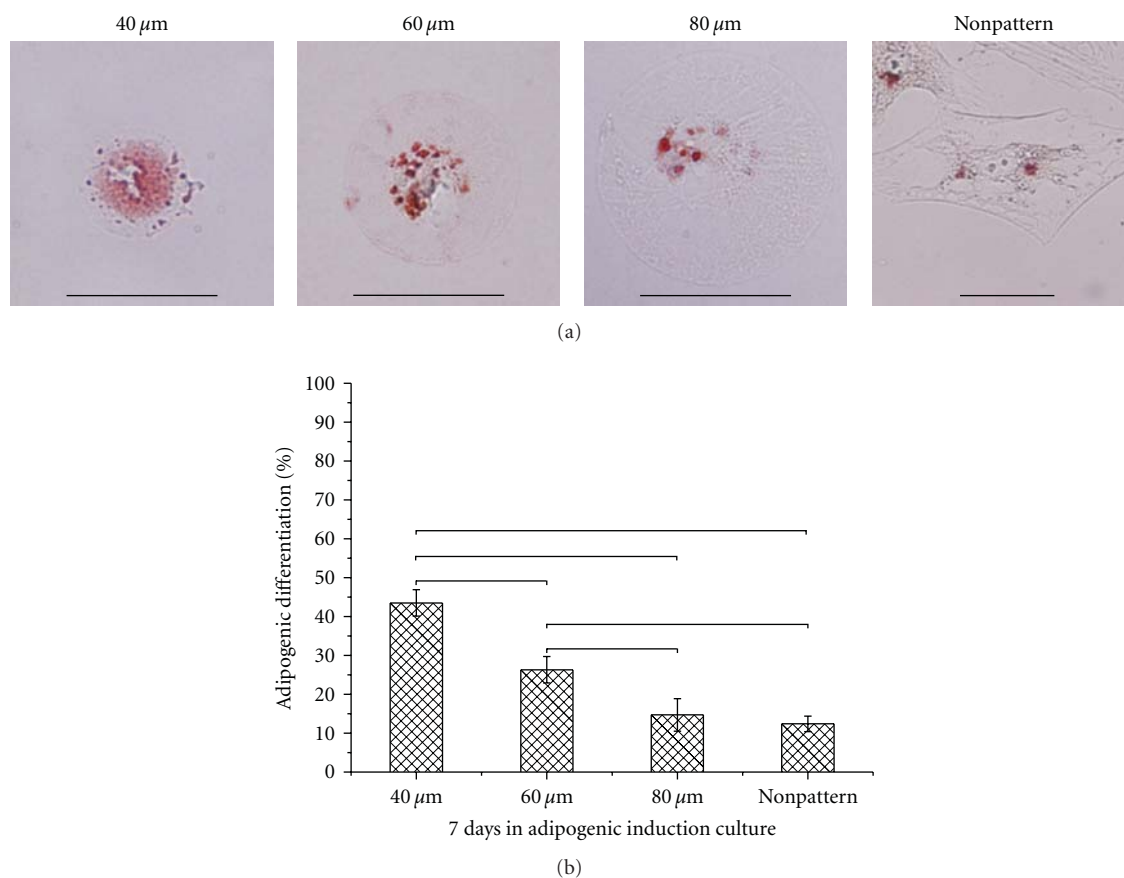


FIGURE 4: (a) Representative optical photographs of MSCs with different spreading areas stained by Oil Red O after culture in adipogenic induction medium for 7 days. (b) The percentage of adipogenic differentiation of MSCs with different spreading areas. Data represent mean \pm SD ($n = 3$). * $P < .05$, ** $P < .01$, and *** $P < .001$. Scale bars: 50 μ m.

differentiation of MSCs decreased as the degree of cell spreading increased.

3.4. Osteogenic Differentiation of MSCs with Different Cell Spreading Areas. MSCs were cultured on the micropatterns in osteogenic induction medium for 7 and 21 days. The cells that were constrained on the micropatterns did not spread out from the micropatterns, even after 21 days of culture, while a confluent cell layer already formed on the bare polystyrene surface (Figure 5(a)). This result indicates that the micropatterned surfaces were stable and useful for long-term cell culture and assessment. Osteogenic differentiation was evaluated by ALP staining, a marker for osteogenesis. Representative optical photographs of positively stained cells are shown in Figure 5(b). The probabilities that MSCs with different degrees of cell spreading committed to osteoblasts are shown in Figure 5(c). The percentages of MSCs undergoing osteogenic differentiation were $13.0 \pm 2.2\%$, $28.3 \pm 3.0\%$, and $41.2 \pm 1.9\%$ on micropatterns with 40- to 80- μ m circles and $54.6 \pm 4.2\%$ on the bare polystyrene surface (nonpatterned) after 7 days of osteogenic induction culture. The probability of osteogenic differentiation of MSCs increased as the degree of cell spreading was enhanced. After osteogenic induction culture for 21 days, the percentages

of MSCs undergoing osteogenic differentiation were $17.5 \pm 3.5\%$, $40.2 \pm 3.8\%$, and $53.9 \pm 5.4\%$ on the micropatterns with 40- to 80- μ m circles and $86.0 \pm 3.0\%$ on the bare polystyrene surface (nonpatterned). Although the trend of the probability of osteogenic differentiation at 21 days was similar to that at 7 days, more cells underwent osteogenic differentiation after long-term culture. These results indicate that cell spreading facilitated osteogenic differentiation of MSCs, and long-term cell culture on the micropatterned surfaces was realized.

4. Discussion

In this study, different degrees of cell spreading with the same cell shape were controlled using micropatterning technology, and the effect of differential cell spreading area on the differentiation of MSCs was investigated on a micropatterned surface at the single-cell level.

Although many methods have been adopted to construct micropatterned surfaces for cell culture [28], few of them would be compatible with long-term cell culture (especially longer than 2 weeks), mainly because of the unstable non-fouling layer. Here, photo-reactive PVA was micropatterned on cell-culture polystyrene surfaces using photolithography.

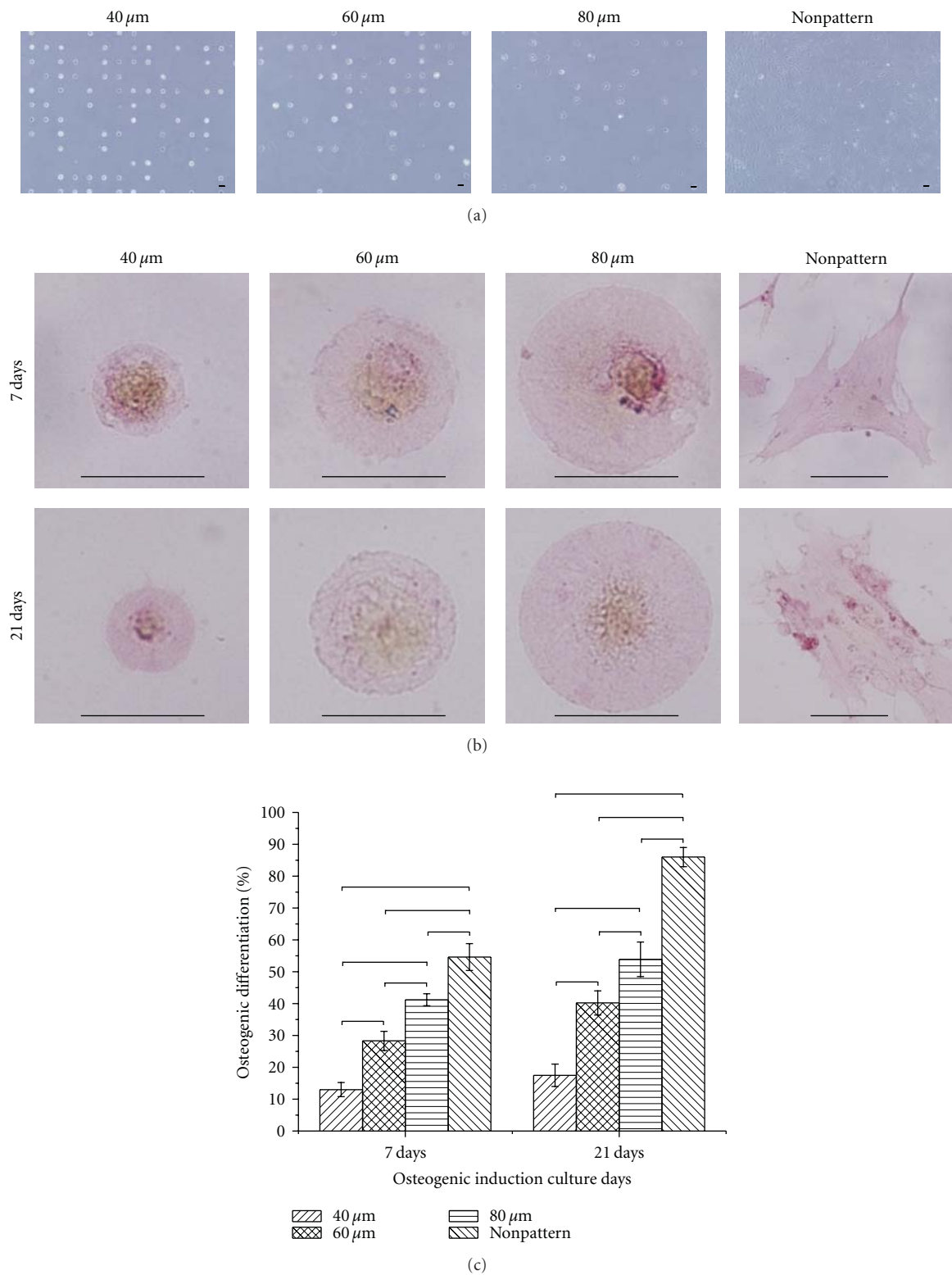


FIGURE 5: (a) Phase contrast photographs of MSCs after culture on micropatterned surfaces in osteogenic induction medium for 21 days. (b) Representative optical photographs of ALP staining of MSCs with different spreading areas after culture in osteogenic induction medium for 7 and 21 days. (c) The percentage of osteogenic differentiation of MSCs with different spreading areas after culture in osteogenic induction medium for 7 and 21 days. Data represent mean \pm SD ($n = 3$). * $P < .05$, ** $P < .01$, and *** $P < .001$. Scale bars: 50 μm .

Because PVA molecules were intra- and intermolecularly crosslinked and covalently grafted to the polystyrene surface, PVA micropattern on polystyrene surface was stable during long-term cell culture. The thickness of non-adhesive PVA layer within nanometer scale is important for preventing protein adsorption and cell adhesion and for trapping single cell in polystyrene circle. Arima et al. [29] have reported that highly hydrated PVA layer with the thickness around 53.3 nm effectively resists serum proteins adsorption. The thickness of our micropatterned PVA layer was from 51.4 to 53.6 nm, which protected cell spreading across the micropatterns. The PVA layer was controlled at nanometer scale to capture the single cell by means of different surface chemistry other than topography. Cell adhesion result showed that ~85% of circular polystyrene domain was occupied by single cell. However, the surface topography will affect cell behavior if the PVA layer increases to micrometer level which is similar to microwell structure. Multilayer cells are likely to be trapped in such PVA microwell. It has been reported that microwell structures were adopted to prepare multilayer cell spheroids [30, 31]. Therefore, nanometer-thick PVA micropattern on polystyrene surface is compatible with single-cell array formation and long-term cell culture.

With the advantage of micropatterns, cell adhesion, shape, and spreading were regulated at the single-cell level. Hence, the complexity of cell-cell interactions and the heterogeneity of the cell population during routine cell culture were significantly reduced [32]. The behaviors and functions of individual MSCs could be investigated and compared at specific conditions with a fixed shape but varied spreading areas. The actin structure of MSCs was affected by the degree of cell spreading. Well-organized stress fibers appeared in MSCs that adhered to the large circular micropatterns. In contrast, MSCs confined to small circular micropatterns assembled thicker actin filaments at the edge than in the interior, a phenomenon suggesting that cells were maximizing their spreading. It has been reported that actin structures play an important role in the differentiation of MSCs [33–35]. Thus, the different actin arrangements suggest a tight relationship among cell spreading, the cytoskeletal network, and stem cell functions.

The long-term effects of different degrees of cell spreading on the differentiation of isolated individual MSCs without direct cell-cell interactions were directly compared on the same PVA-micropatterned polystyrene surface. This way, uncertain factors arising from separate cell cultures and heterogeneity of cell population in common cell culture were greatly reduced. The differentiation of MSCs strongly depended on the degree of cell spreading. However, osteogenic and adipogenic differentiation of MSCs exhibited opposite correlations. Namely, cell spreading promoted osteogenic differentiation but suppressed adipogenic differentiation of MSCs. This result is consistent with other reports [14, 36], which also suggests that cell spreading favors osteogenic differentiation but inhibits adipogenic differentiation of MSCs. The reason may be that cytoskeletal contractility was enhanced with increased cell spreading [37, 38], and high contractility favors osteogenesis, whereas lower contractility enhanced the adipogenesis of MSCs [39, 40].

5. Conclusions

Different degrees of cell spreading with the same cell shape were established on PVA-micropatterned polystyrene surfaces. The assembly and organization of actin filaments depended on the degree of cell spreading. MSCs on larger circular micropatterns exhibited a more highly ordered actin structure, whereas MSCs on small circular micropatterns mainly aligned actin fibers along the edge between cell-adhesive polystyrene and non-adhesive PVA. The distinct degree of cell spreading also had an effect on the differentiation of MSCs. Osteogenic differentiation of MSCs increased with increased cell spreading. In contrast, adipogenic differentiation of MSCs decreased with increased cell spreading. This micropatterning technique provides a convenient method to directly compare stem cell functions for both short- and long-term cell culture.

Acknowledgment

This work was supported by World Premier International Research Center Initiative on Materials Nanoarchitectonics from the Ministry of Education, Culture, Sports, Science and Technology, Japan.

References

- [1] F. M. Watt and B. L. M. Hogan, "Out of eden: stem cells and their niches," *Science*, vol. 287, no. 5457, pp. 1427–1430, 2000.
- [2] M. P. Lutolf, P. M. Gilbert, and H. M. Blau, "Designing materials to direct stem-cell fate," *Nature*, vol. 462, no. 7272, pp. 433–441, 2009.
- [3] F. Guilak, D. M. Cohen, B. T. Estes, J. M. Gimble, W. Liedtke, and C. S. Chen, "Control of stem cell fate by physical interactions with the extracellular matrix," *Cell Stem Cell*, vol. 5, no. 1, pp. 17–26, 2009.
- [4] T. Hoshiba, N. Kawazoe, T. Tateishi, and G. Chen, "Development of stepwise osteogenesis-mimicking matrices for the regulation of mesenchymal stem cell functions," *Journal of Biological Chemistry*, vol. 284, no. 45, pp. 31164–31173, 2009.
- [5] T. Hoshiba, N. Kawazoe, T. Tateishi, and G. Chen, "Development of extracellular matrices mimicking stepwise adipogenesis of mesenchymal stem cells," *Advanced Materials*, vol. 22, no. 28, pp. 3042–3047, 2010.
- [6] L. Guo, N. Kawazoe, Y. Fan et al., "Chondrogenic differentiation of human mesenchymal stem cells on photoreactive polymer-modified surfaces," *Biomaterials*, vol. 29, no. 1, pp. 23–32, 2008.
- [7] L. Guo, N. Kawazoe, T. Hoshiba, T. Tateishi, G. Chen, and X. Zhang, "Osteogenic differentiation of human mesenchymal stem cells on chargeable polymer-modified surfaces," *Journal of Biomedical Materials Research. Part A*, vol. 87, no. 4, pp. 903–912, 2008.
- [8] N. Jaiswal, S. E. Haynesworth, A. I. Caplan, and S. P. Bruder, "Osteogenic differentiation of purified, culture-expanded human mesenchymal stem cells in vitro," *Journal of Cellular Biochemistry*, vol. 64, no. 2, pp. 295–312, 1997.
- [9] M. F. Pittenger, A. M. Mackay, S. C. Beck et al., "Multilineage potential of adult human mesenchymal stem cells," *Science*, vol. 284, no. 5411, pp. 143–147, 1999.

- [10] K. Alberti, R. E. Davey, K. Onishi et al., "Functional immobilization of signaling proteins enables control of stem cell fate," *Nature Methods*, vol. 5, no. 7, pp. 645–650, 2008.
- [11] M. R. Doran, B. D. Markway, I. A. Aird et al., "Surface-bound stem cell factor and the promotion of hematopoietic cell expansion," *Biomaterials*, vol. 30, no. 25, pp. 4047–4052, 2009.
- [12] A. J. Engler, S. Sen, H. L. Sweeney, and D. E. Discher, "Matrix elasticity directs stem cell lineage specification," *Cell*, vol. 126, no. 4, pp. 677–689, 2006.
- [13] M. J. Dalby, N. Gadegaard, R. Tare et al., "The control of human mesenchymal cell differentiation using nanoscale symmetry and disorder," *Nature Materials*, vol. 6, no. 12, pp. 997–1003, 2007.
- [14] R. McBeath, D. M. Pirone, C. M. Nelson, K. Bhadriraju, and C. S. Chen, "Cell shape, cytoskeletal tension, and RhoA regulate stem cell lineage commitment," *Developmental Cell*, vol. 6, no. 4, pp. 483–495, 2004.
- [15] R. Peerani, B. M. Rao, C. Bauwens et al., "Niche-mediated control of human embryonic stem cell self-renewal and differentiation," *EMBO Journal*, vol. 26, no. 22, pp. 4744–4755, 2007.
- [16] J. T. Connelly, J. E. Gautrot, B. Trappmann et al., "Actin and serum response factor transduce physical cues from the microenvironment to regulate epidermal stem cell fate decisions," *Nature Cell Biology*, vol. 12, no. 7, pp. 711–718, 2010.
- [17] K. Bhadriraju and L. K. Hansen, "Extracellular matrix- and cytoskeleton-dependent changes in cell shape and stiffness," *Experimental Cell Research*, vol. 278, no. 1, pp. 92–100, 2002.
- [18] E. Szabo, T. Feng, E. Dziak, and M. Opas, "Cell adhesion and spreading affect adipogenesis from embryonic stem cells: the role of calreticulin," *Stem Cells*, vol. 27, no. 9, pp. 2092–2102, 2009.
- [19] G. Chen, N. Kawazoe, Y. Fan, Y. Ito, and T. Tateishi, "Grid pattern of nanothick microgel network," *Langmuir*, vol. 23, no. 11, pp. 5864–5867, 2007.
- [20] M. Théry, V. Racine, A. Pépin et al., "The extracellular matrix guides the orientation of the cell division axis," *Nature Cell Biology*, vol. 7, no. 10, pp. 947–953, 2005.
- [21] M. Théry, V. Racine, M. Piel et al., "Anisotropy of cell adhesive microenvironment governs cell internal organization and orientation of polarity," *Proceedings of the National Academy of Sciences of the United States of America*, vol. 103, no. 52, pp. 19771–19776, 2006.
- [22] J. E. Gautrot, B. Trappmann, F. Ocegüera-Yanez et al., "Exploiting the superior protein resistance of polymer brushes to control single cell adhesion and polarisation at the micron scale," *Biomaterials*, vol. 31, no. 18, pp. 5030–5041, 2010.
- [23] R. G. Thakar, Q. Cheng, S. Patel et al., "Cell-shape regulation of smooth muscle cell proliferation," *Biophysical Journal*, vol. 96, no. 8, pp. 3423–3432, 2009.
- [24] C. S. Chen, M. Mrksich, S. Huang, G. M. Whitesides, and D. E. Ingber, "Geometric control of cell life and death," *Science*, vol. 276, no. 5317, pp. 1425–1428, 1997.
- [25] L. Q. Wan, S. M. Kang, G. Eng et al., "Geometric control of human stem cell morphology and differentiation," *Integrative Biology*, vol. 2, no. 7–8, pp. 346–353, 2010.
- [26] N. Kawazoe, L. Guo, M. J. Wozniak et al., "Adipogenic differentiation of mesenchymal stem cells on micropatterned polyelectrolyte surfaces," *Journal of Nanoscience and Nanotechnology*, vol. 9, no. 1, pp. 230–239, 2009.
- [27] H. Lu, L. Guo, M. J. Wozniak et al., "Effect of cell density on adipogenic differentiation of mesenchymal stem cells," *Biochemical and Biophysical Research Communications*, vol. 381, no. 3, pp. 322–327, 2009.
- [28] D. Falconnet, G. Csucs, H. Michelle Grandin, and M. Textor, "Surface engineering approaches to micropattern surfaces for cell-based assays," *Biomaterials*, vol. 27, no. 16, pp. 3044–3063, 2006.
- [29] Y. Arima, M. Kawagoe, M. Furuta, M. Toda, and H. Iwata, "Effect of swelling of poly(vinyl alcohol) layers on complement activation," *Biomaterials*, vol. 31, pp. 6926–6933, 2010.
- [30] J. Y. Karp, J. Yeh, G. Eng et al., "Controlling size, shape and homogeneity of embryoid bodies using poly(ethylene glycol) microwells," *Lab on a Chip*, vol. 7, pp. 786–794, 2007.
- [31] Y. Y. Choi, B. G. Chung, D. H. Lee, A. Khademhosseini, J. H. Kim, and S. H. Lee, "Controlled-size embryoid body formation in concave microwell arrays," *Biomaterials*, vol. 31, pp. 4296–4303, 2010.
- [32] R. Singhvi, A. Kumar, G. P. Lopez et al., "Engineering cell shape and function," *Science*, vol. 264, no. 5159, pp. 696–698, 1994.
- [33] C. Y. Tay, H. Yu, M. Pal et al., "Micropatterned matrix directs differentiation of human mesenchymal stem cells towards myocardial lineage," *Experimental Cell Research*, vol. 316, no. 7, pp. 1159–1168, 2010.
- [34] J. P. Rodríguez, M. González, S. Ríos, and V. Cambiazo, "Cytoskeletal organization of human mesenchymal stem cells (MSC) changes during their osteogenic differentiation," *Journal of Cellular Biochemistry*, vol. 93, no. 4, pp. 721–731, 2004.
- [35] G. Yourek, M. A. Hussain, and J. J. Mao, "Cytoskeletal changes of mesenchymal stem cells during differentiation," *ASAIO Journal*, vol. 53, no. 2, pp. 219–228, 2007.
- [36] M. Guvendiren and J. A. Burdick, "The control of stem cell morphology and differentiation by hydrogel surface wrinkles," *Biomaterials*, vol. 31, no. 25, pp. 6511–6518, 2010.
- [37] P. Roca-Cusachs, J. Alcaraz, R. Sunyer, J. Samitier, R. Farré, and D. Navajas, "Micropatterning of single endothelial cell shape reveals a tight coupling between nuclear volume in G1 and proliferation," *Biophysical Journal*, vol. 94, no. 12, pp. 4984–4995, 2008.
- [38] M. Théry, A. Pépin, E. Dressaire, Y. Chen, and M. Bornens, "Cell distribution of stress fibres in response to the geometry of the adhesive environment," *Cell Motility and the Cytoskeleton*, vol. 63, no. 6, pp. 341–355, 2006.
- [39] K. A. Kilian, B. Bugarija, B. T. Lahn, and M. Mrksich, "Geometric cues for directing the differentiation of mesenchymal stem cells," *Proceedings of the National Academy of Sciences of the United States of America*, vol. 107, no. 11, pp. 4872–4877, 2010.
- [40] S. A. Ruiz and C. S. Chen, "Emergence of patterned stem cell differentiation within multicellular structures," *Stem Cells*, vol. 26, no. 11, pp. 2921–2927, 2008.

Research Article

Surface Modification of Titanium with Heparin-Chitosan Multilayers via Layer-by-Layer Self-Assembly Technique

Yao Shu,¹ Guomin Ou,² Li Wang,³ Jingcai Zou,¹ and Quanli Li⁴

¹ Department of Stomatology, Affiliated Hospital Academy of Military, Medical Sciences of Chinese PLA, Beijing 100071, China

² West China College of Stomatology, Sichuan University, Chengdu 610041, China

³ Stomatology Department, Xuzhou Medical College, Xuzhou 221000, China

⁴ College of Stomatology, Anhui Medical University, Hefei 230032, China

Correspondence should be addressed to Quanli Li, ql-li@126.com

Received 4 June 2010; Revised 8 August 2010; Accepted 24 September 2010

Academic Editor: Xiaojun Yu

Copyright © 2011 Yao Shu et al. This is an open access article distributed under the Creative Commons Attribution License, which permits unrestricted use, distribution, and reproduction in any medium, provided the original work is properly cited.

Extracellular matrix (ECM), like biomimetic surface modification of titanium implants, is a promising method for improving its biocompatibility. In this paper chitosan (Chi) and heparin (Hep) multilayer was coated on pure titanium using a layer-by-layer (LbL) self-assembly technique. The Hep-Chi multilayer growth was carried out by first depositing a single layer of positively charged poly-L-lysine (PLL) on the NaOH-treated titanium substrate (negatively charged surface), followed by alternate deposition of negatively charged Hep and positively charged Chi, and terminated by an outermost layer of Chi. The multilayer was characterized by DR-FTIR, SEM, and AFM, and osteoblasts were cocultured with the modified titanium and untreated titanium surfaces, respectively, to evaluate their cytocompatibility *in vitro*. The results confirmed that Hep-Chi multilayer was fabricated gradually on the titanium surface. The Hep-Chi multilayer-coated titanium improved the adhesion, proliferation and differentiation of osteoblasts. Thus, the approach described here may provide a basis for the preparation of modified titanium surfaces for use in dental or orthopedic implants.

1. Introduction

Titanium (Ti) metal and its alloys have been widely used as orthopedic and dental implants. However, Ti is a bioinert material, so that it passively integrated with bone when implanted, and the process of osseointegration between bone and Ti surface needs a long time [1]. Considerable research has been carried out to improve the biocompatibility of titanium implants. Recently, works on the immobilization of biologically active molecules on titanium surfaces and extracellular matrix- (ECM-) like biomimetic surface modification have generated great interest in the dental and orthopedic fields [2–4]. The approach includes passive adsorption, silicate coupling, self-assembled monolayers (SAMs), Langmuir-Blodgett (LB) membranes, and layer-by-layer (LbL) self-assembly methods [3, 5–9]. The LbL deposition process was discovered and developed in the 1990s by Decher and coworkers [10]. This technique is based on the consecutive adsorption of polyanions and polycations

via electrostatic interactions. LbL allows for the deposition of homogeneous films with layer thickness controlled on the nanometer scale and with controlled surface structure and charge. Compared with the classic chemical immobilization method, the LbL technique has the least demand for reactive chemical bonds and efficiently keeps molecular activity [8]. Thus, The LbL self-assembly has already been applied extensively in biomaterial fields [11, 12]. In 1995, Cai et al. [8] built a multilayer with chitosan and gelatin (gelatin as the outmost layer) on titanium surface via LbL technique, which was proved to improve titanium biocompatibility. Later reports [13, 14] showed that, if chitosan was the outmost layer, the coating would have similar effect, and would be stable for more than 3 weeks immersed into PBS solution in room temperature. Hu et al. [15] demonstrated that Chi/pGB (plasmid DNA) LbL-modified titanium films were beneficial for sustained *in situ* inducing osteoprogenitor cells to differentiate into mature osteoblasts over a long time.

Glycosaminoglycan (GAG) is an important component of the extracellular matrix (ECM) and has the specific affinity with growth factors and adherence proteins [16, 17]. Heparin (Hep) is an anionic polysaccharide, and can interact with many growth factors to benefit osseointegration indirectly. Heparin-binding growth factors (HBGFs), such as transforming growth factor- β (TGF- β) and bone morphogenetic proteins (BMPs), modulate bone formation and bone resorption by acting as autocrine or paracrine effectors on bone cell proliferation and differentiation [18–20]. Heparan-like molecules, like heparin or heparan sulfates, are able to induce bone regeneration of skull defects and possibly mediated by potentiation of endogenous growth factor activities and/or by neutralization of proteolytic activities [21]. Chitosan (Chi) is a cationic natural biopolymer produced by alkaline N-deacetylation of chitin, with an analogous structure to GAG, and has been extensively used in medicine due to its good biocompatibility, biodegradability, low toxicity, and low cost [22, 23]. Thus, in this study, Chi and Hep were used for an LbL self-assembly system to “build” the bioactive coating on titanium substrate. To our knowledge, little has been studied up to now that Chi and Hep are immobilized on titanium surface via the LbL technique to enhance titanium biocompatibility.

Titanium carries net negative charge at a physiological pH [24] and can be used as substrates for LbL assembly. Furthermore, surface properties and structure of titanium play an essential role in protein adsorption. The increase of hydroxyl groups, surface energy, and submicrometer morphology of titanium surface would enhance the reactivity of titanium with the protein and reduce the release of the biomacromolecules [25, 26]. Titanium treated with alkali solution has the surface property with large hydroxyl groups, higher surface energy, hydrophilicity, and submicrometer porous morphology [27]. Thus, we chose NaOH-treated titanium as the substrate surface to build a multilayer coating composed of chitosan and heparin. We expect that this Hep-Chi multilayer coating can improve Ti biocompatibility.

2. Materials and Methods

2.1. Materials. Commercial pure titanium was purchased from Baoji Non-ferrous Metal Co. Ltd. (Shanxi Province, China). Chitosan (degree of deacetylation 96.5%; viscosity 55 mPa.s) was from Yuhuan Ocean Biochemical Co. Ltd. (Zhejiang province, China). Heparin was from Suolaibao Biochemical Co. Ltd. (Shanghai, China). Dulbecco's modified Eagle's medium (DMEM), trypsin and fetal bovine serum (FBS) were from GIBCO Life Technologies (Grand Island, NY, USA). Poly-L-lysine (PLL, 15–30 kDa), MTT (3-(4,5-dimethylthiazol-2-yl)-2,5-diphenyltetrazolium bromide), dimethyl sulfoxide (DMSO) were from Sigma-Aldrich Inc. (USA). the ALP activity kit was from Nanjing Jiancheng Bioengineering Institute (Nanjing, China). Other chemical reagents (A. R.) were from Changzheng Chemical Agent Company (Chengdu, China).

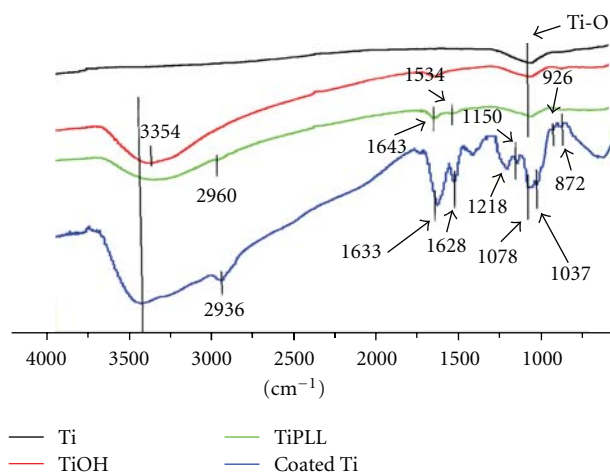


FIGURE 1: DR-FTIR spectra of untreated titanium (Ti), NaOH-treated titanium (TiOH), PLL-coated titanium (TiPLL), and Ti/PLL/(Hep/Chi)₁₈(coated Ti).

2.2. Preparation of Titanium Surface with NaOH. Titanium (Non-ferrous Metal Co. Ltd., Baoji, China) disks (10 mm in diameter and 2 mm thick) were polished to a reflective mirror-like finish. Firstly the specimens were ultrasonically cleaned in a detergent solution, then in acetone, ethanol, and de-ionized water, and finally dried at 60°C. These original titanium samples would be used as the control ones in the later cell experiments. The cleaned specimens were soaked in 5 M NaOH solution at 60°C for 24 hours and followed by de-ionized water at 80°C for 24 hours, then were cleaned with de-ionized water, and at last dried at 60°C.

2.3. Fabrication of Multilayers of Heparin-Chitosan. Chitosan (Chi, a polycation) was dissolved in 1% (V/V) acetic acid with a concentration of 5 mg/mL, and its pH value was adjusted to about 4 with 1% (V/V) acetic solution and 0.1 M NaOH. Heparin (Hep, a polyanion) was dissolved in de-ionized water with concentration of 5 mg/mL, and its pH value was also adjusted to about 4. Poly-L-lysine solution of 2.5 mg/mL was dissolved in a phosphate buffer solution (PBS, pH = 7.4).

The NaOH-treated samples were immersed in PLL solution for 30 minutes, thus, obtaining a precursor layer with the stable positive charge to initiate the LbL assembly process. The multilayers were fabricated by alternately and successively immersing the titanium samples in the heparin and chitosan solution, followed by 10 minutes of adsorption and subsequently rinsing two times with de-ionized water for 1 minute every cycle. The cycle was repeated n times to obtain the desired film, terminated with a layer of Chi—denoted as Ti/PLL/(Hep/Chi) _{n} —and dried at ambient environment. The surface-modified titanium samples with eighteen-layer films, Ti/PLL/(Hep/Chi)₁₈, were achieved by such alternative deposition for the further cell experiments.

2.4. Analysis of the Morphology and Chemical Character of the Surfaces. The morphology of all the specimen surfaces

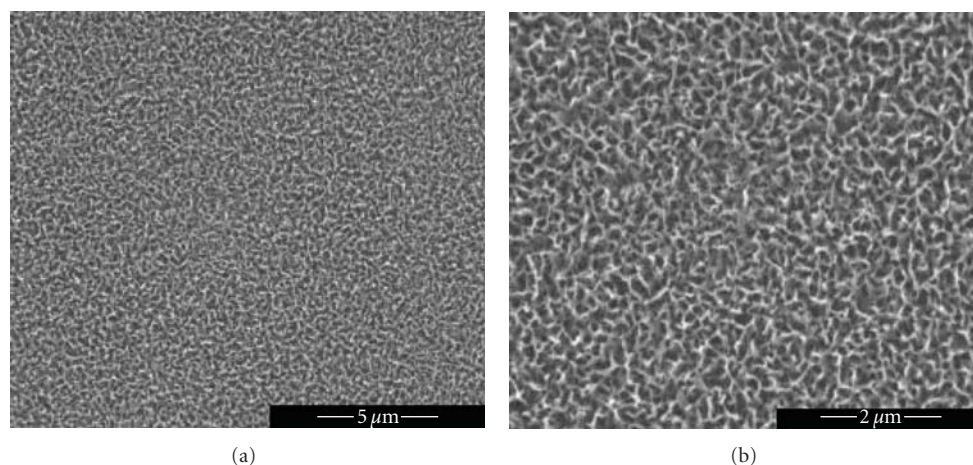


FIGURE 2: SEM images of sample surfaces: NaOH treated titanium.

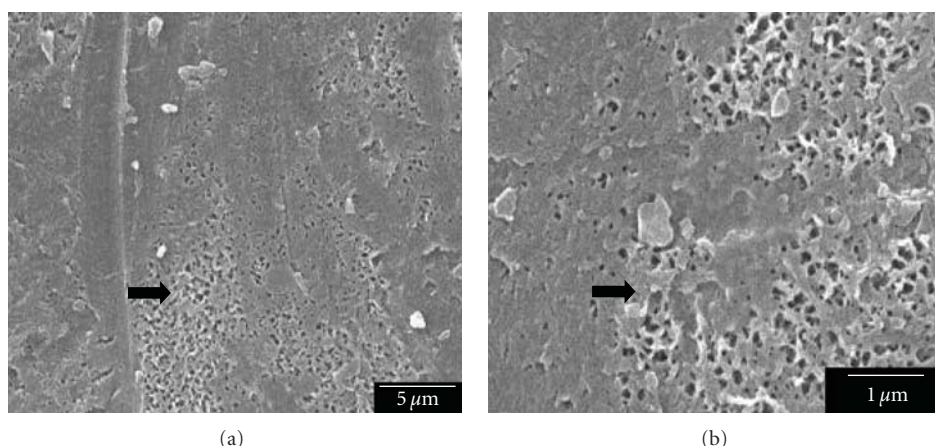


FIGURE 3: SEM images of sample surfaces: Ti/PLL/(Hep/Chi)₁₀.

was characterized by scanning electron microscopy (SEM; QUANTA 200, FTI, Holland) at the accelerating voltage of 20 KV and atomic force microscopy (AFM; SPI3800N Seiko, Japan) with tapping mode and standard Si tips. The chemical character of the surfaces was studied by diffuse reflectance Fourier transform infrared spectroscopy (DR-FTIR; agna-IR 550, Nicolet, Madison, Am) at the resolution of 4 cm^{-1} .

2.5. Cell Culture. Osteoblasts were isolated via sequential collagenase digestions of neonatal rat calvaria according to the established protocol [28]. They were cultured in 25 mL culture bottles containing 5 mL DMEM 10% FBS, and incubated at a humidified 5% CO₂ atmosphere at 37°C. The medium was changed every third day and for sub-culture. Osteoblasts at passage no. 2-3 were used in the following experiments.

2.6. Cell Adhesion. At passage no. 2 cells were seeded onto the original titanium samples and LbL-modified titanium samples at a density of 5×10^4 cells/cm² in a 24-well plate.

The samples were sterilized with ethylene oxide in West China Hospital affiliated to Sichuan University.

After being cultured on the samples for 4 hours and 24 hours, respectively, the cells adhered to the samples were gently washed with PBS 3 times, fixed with 2.5% glutaraldehyde solution for 2 hours at 4°C, dehydrated through a series of graded ethanol solution, critical point dried, and then sputter gold coated in vacuum. The two-group samples were observed by SEM (Philips, FEI inspect F, Holland) for the morphologic change of cell attachment and spreading.

2.7. Cell Proliferation. Proliferation of the cells was studied by the MTT assay. Yellow MTT reagent can be converted to a dark blueformazan by mitochondrial succinate dehydrogenase of viable cells [29]. Therefore, the production of formazan may reflect the number of viable cells or cell viability.

Osteoblasts were seeded at a density of 8×10^4 cells/cm² in a 24-well plate containing the original titanium samples and LbL-modified titanium samples. The culture medium in

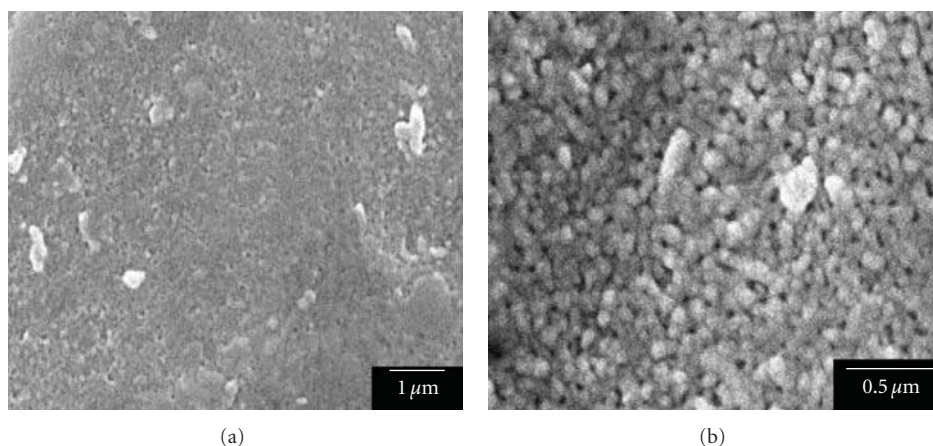


FIGURE 4: SEM images of sample surfaces: Ti/PLL/(Hep/Chi)₁₆.

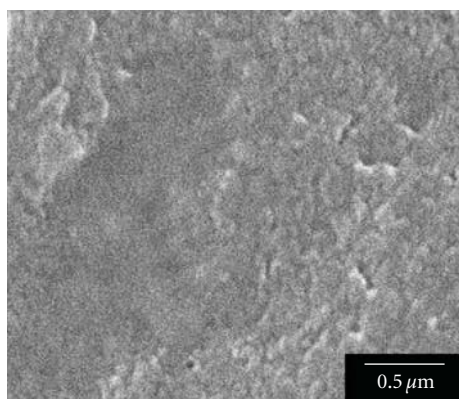


FIGURE 5: SEM images of sample surfaces: Ti/PLL/(Hep/Chi)₁₈.

wells was refreshed every 3 days. After 1, 4, and 7 days of the culture, respectively, 40 μ L MTT (5 mg/mL) was added to each well containing 1 mL culture medium and incubated for 4 hours at 37°C. Then, the blue formazan reaction product was dissolved by adding 420 μ L DMSO and transferred to a 96-well plate (200 μ L every well). The absorbance was measured at 570 nm using a Bio Assay Reader (HTS7000 plus, PERKIN ELMER, USA). Four replicates were read for each sample, and the mean value was used as the final result.

2.8. Cell Differentiation. Alkaline phosphatase (ALP) activity is one of the most widely used early osteodifferentiation markers for osteoblasts [30]. ALP can convert the substrate p-nitrophenyl phosphate into yellow p-nitrophenol and phosphate.

Osteoblasts (2×10^5 cells/cm²) were seeded onto the LbL-modified titanium samples and control ones in two 6-well plates and cultured for 7 days. Cells were removed off the samples by trypsinization and centrifuged (1000 r/min, 8 minutes). We moved away the supernatant, added 5 mL PBS solution to be a suspension, and counted the cell number

and adjusted to the same concentration between the control and experimental groups. Then, aliquot of cell suspension was centrifuged (1000 r/min, 8 minutes) again, resuspended in 120 μ L PBS solution, and maintained at -20°C . These suspensions were experienced three freeze-thaw cycles, and used for determining the ALP activity with p-nitrophenyl phosphates substrate as the kit instruction. The absorbance at 405 nm was measured by a Bio Assay Reader (HTS7000 plus, PERKIN ELMER, USA).

2.9. Statistical Analysis. All data were expressed as means \pm standard deviation (S) for $n = 4$. Single factor analysis of variance (ANOVA) technique was used to assess the statistical significance of the results between the two groups. The statistical assessment was done by the software SPSS 15.0 at a confidence level of 95%.

3. Results and Discussion

3.1. DR-FTIR. In the FTIR spectrum of the NaOH-treated titanium (Figure 1), the broad peak at 3354 cm^{-1} suggested that the surface was rich in hydroxyl groups.

In Figure 1 of PLL-coated sample (Ti/PLL), the distinctive $-\text{NH}_2(\text{C}=\text{O})$ symmetric vibrational I and II bands were centered at about 1643 cm^{-1} , 1543 cm^{-1} ; the peak at 2956 cm^{-1} was attributed to alkyl vibrational band. These indicated that PLL was coated onto the NaOH-treated titanium.

A comparison of the DR-FTIR spectra of untreated titanium (Ti), NaOH-treated titanium (TiOH), and the coated titanium (TiPLL, Ti/PLL/(Hep/Chi)₁₈) (Figure 1) confirmed that Hep-Chi were coated on the titanium surface; that is, the distinctive peaks of chitosan at 1150 cm^{-1} and 926 cm^{-1} , sulphonic acid group peaks of heparin at 1218 cm^{-1} and 872 cm^{-1} existed in spectra (Figure 1 blue line).

3.2. SEM. The SEM photos (Figure 2) showed that the surface of NaOH-treated titanium was characterized by uniform submicron pores and a mesh-like morphology.

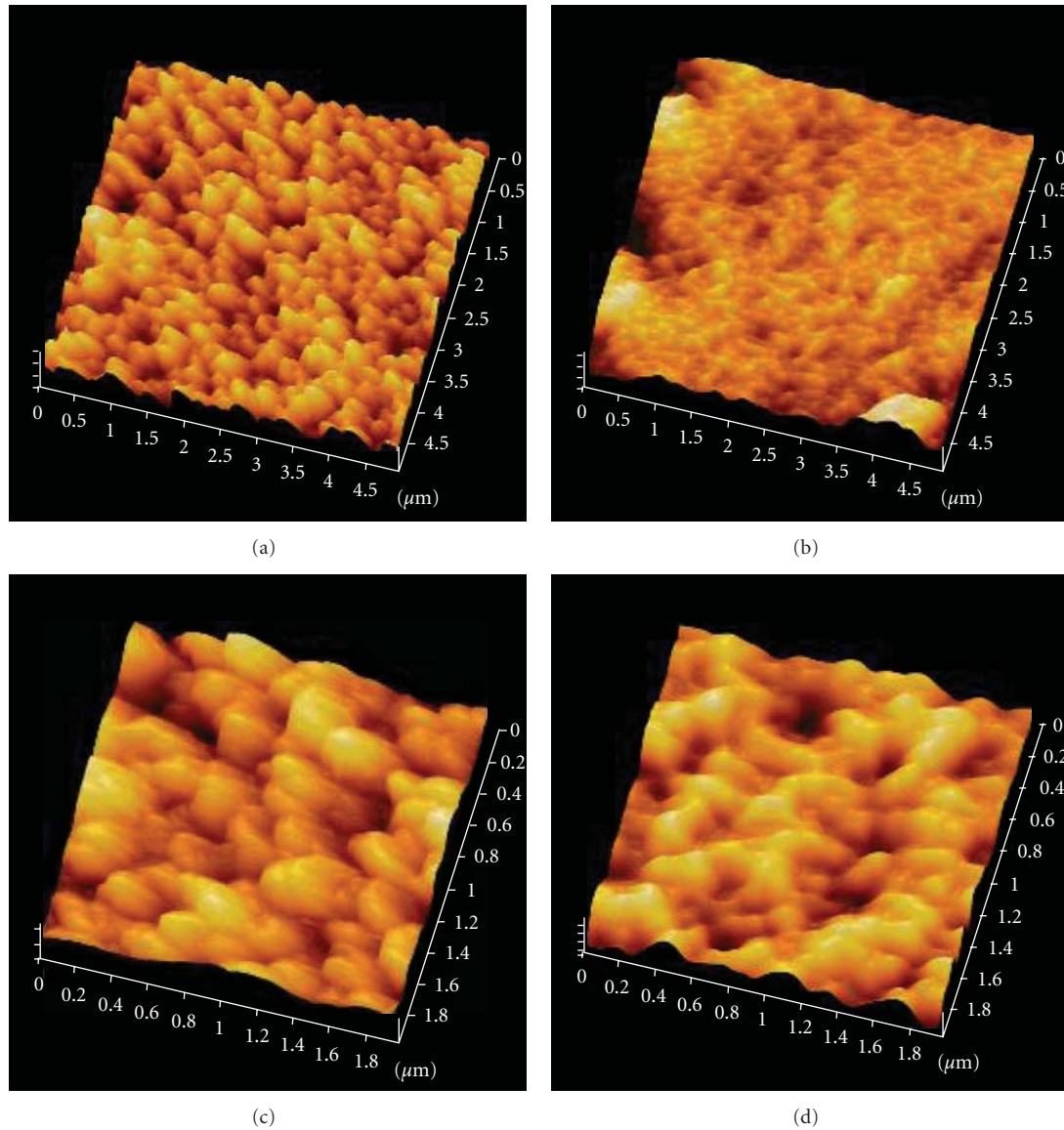


FIGURE 6: AFM images of sample surfaces: NaOH-treated titanium (Ti-OH) ((a), (c)) and coated titanium (Ti/PLL/(Hep/Chi)₁₈) ((b), (d)). The image size is 5 μm × 5 μm ((a), (b)) and 2 μm × 2 μm ((c), (d)).

The SEM images of the multilayers are shown in Figures 3–5. In the increasing of cycles of multilayers, the net structures have disappeared gradually, and submicron pores have changed by Hep and Chi deposition. As the arrow showed in Figure 3, some mesh-like structures were still found in the surface of Ti/PLL/(Hep/Chi)₁₀ samples because of the incomplete coverage of coating. But after 16 times cycles of the preparation (Ti/PLL/(Hep/Chi)₁₆), displayed in Figure 4, the mesh-like structure could not be seen, replaced by tightly deposited polysaccharides chitosan granules (Figure 4(b)). Up to 18 times cycles (Ti/PLL/(Hep/Chi)₁₈), more polysaccharides granules deposited, the coating became denser and smoother, and obvious granules could not be seen via SEM on partial surface (Figure 5).

3.3. AFM. The surface morphology of the multilayers was further confirmed by AFM (Figure 6). AFM photos of NaOH-treated Ti (Figures 6(a) and 6(c)) showed that the mesh-like morphology in SEM images was formed of many taper-pointed granules, in which “topography” was like valleys and peaks. Ra (Arithmetic Average Roughness) was about 65.7 nm. For the multilayer-coated samples (Ti/PLL/(Hep/Chi)₁₈) (Figures 6(b) and 6(d)), ball or oval granules deposited on the substrate surface, and Ra became about 47.5 nm. The surface was smoother than NaOH-treated Ti, with the similar images observed by SEM.

3.4. Cell Adhesion. The cellular initial behavior on a biomaterial is an important factor for evaluation of its

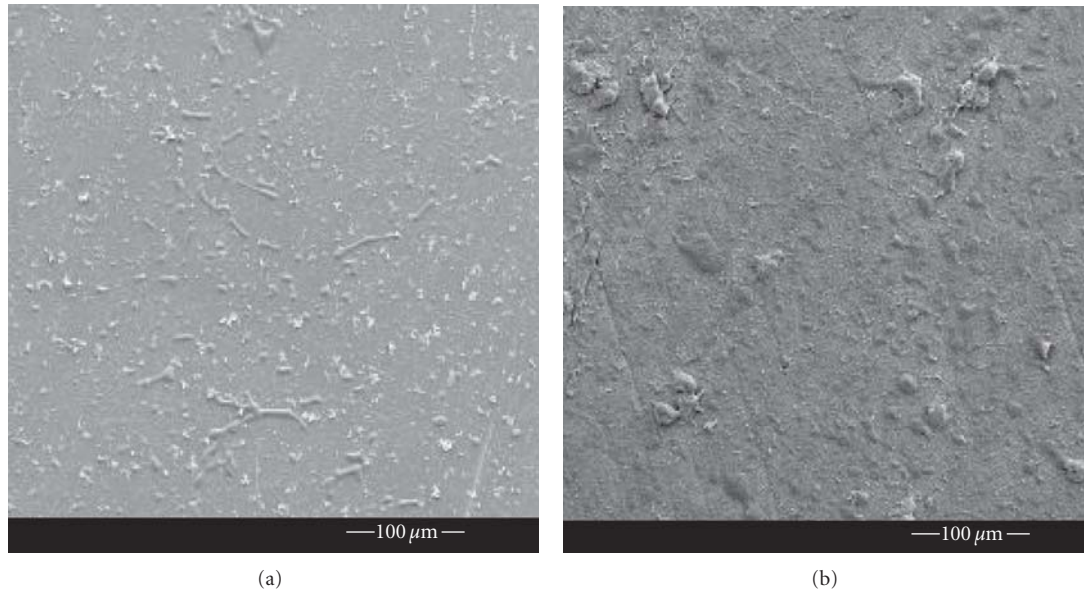


FIGURE 7: SEM images of osteoblasts adhered to original titanium (a) and LbL-modified titanium (Ti/PLL/(Hep/Chi)₁₈) (b) after seeding 4 hours.

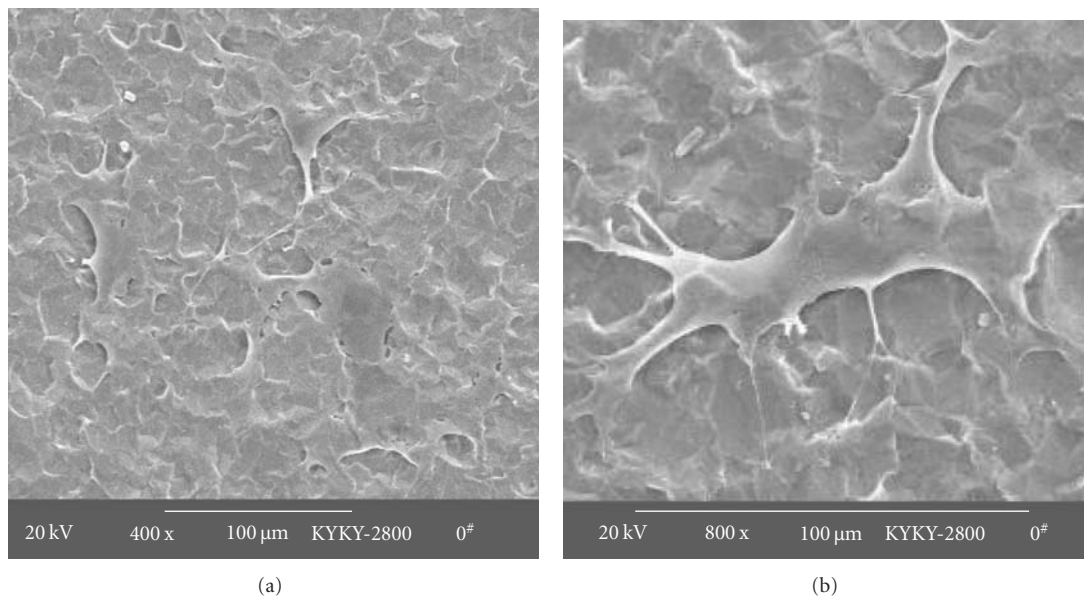


FIGURE 8: SEM images of osteoblasts adhered to original titanium (a) and LbL-modified titanium (Ti/PLL/(Hep/Chi)₁₈) (b) after seeding for 24 hours.

biocompatibility. Cell adhesion, spreading, and migration on materials are the first sequential reactions when contacting with a material surface, which is important for cell survival [8].

Figure 7 showed, after seeding for 4 hours, that cells randomly adhered and spread on both LbL-modified titanium surfaces and control ones. The number of adhered cells on modified titanium surfaces were greater than on original ones. Many adhered cells on modified titanium extended

their pseudopods and showed a tendency to spread, whereas the cells on original titanium still retained a flat shape.

Compared with that of control ones, osteoblasts adhered to LbL-modified titanium surface fully spread after seeding for 24 hours, as shown in Figure 8, and developed more cellular processes to facilitate cell-substrate and cell-cell interactions [31]. Strong interactions between the cells and modified titanium surfaces would promote cell adhesion and tend to be helpful for cell proliferation. These indicated that

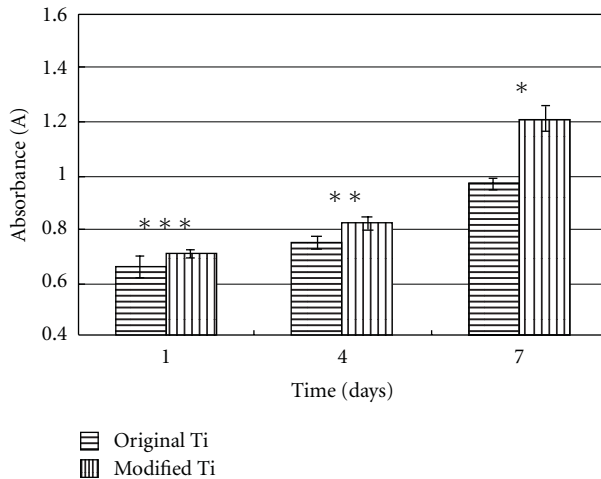


FIGURE 9: Proliferation of osteoblasts cultured on original titanium and LbL-modified titanium evaluated by MTT test at 1, 4, and 7 days. Error bars represent means \pm S for $n = 4$; * $P < .01$; ** $P < .05$; *** $P > .05$ (compared with the control).

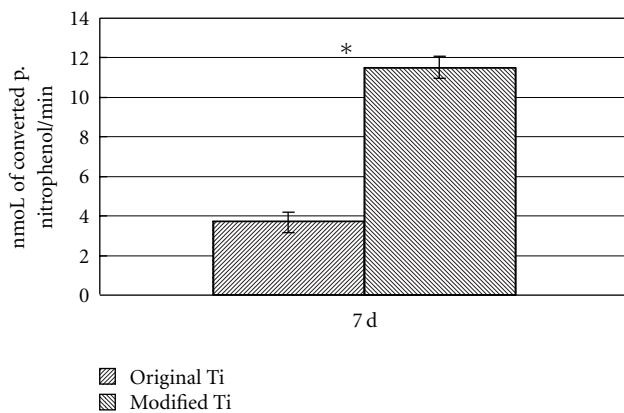


FIGURE 10: ALP activity of osteoblasts cultured on original titanium and LbL-modified titanium after 7 days of incubation. Error bars represent means \pm S for $n = 4$; * $P < .01$ (compared with the control).

the LbL-modified titanium was more favorable for the cell adhesion than the control.

3.5. Cell Proliferation. Figure 9 showed that the absorbance of formazan produced by viable cells adhered to LbL-modified titanium and the control ones at 1 day, 4 days, and 7 days of culture, respectively. MTT test results showed that the number of the cell proliferation had no significant difference between the two groups at 1 day ($P > .05$), the cells cultured on modified titanium surfaces proliferated faster than those on original ones at 4 days and 7 days, and the differences had statistical significance ($P < .05$).

Osteoblasts cultured on LbL-modified titanium showed higher proliferation viability compared with those on original titanium. Tryoen-Tóth et al. [11] revealed that the terminating layer in polyelectrolyte multilayer films influenced the cell adhesion and cell viability. Our study also indicated

that Chi as the outmost layer of polyelectrolyte multilayers was biocompatible with osteoblasts.

3.6. Cell Differentiation. When cultured up to 7 days, osteoblasts grow into maturation and osteo-differentiation stage and express a large number of ALP. The ability of cell differentiation could be estimated by ALP activity assay. Figure 10 showed a statistically significant difference of ALP activity between the two groups ($P < .01$). The osteoblasts cultured on the modified group displayed much higher ALP expression than those on the control group, and they owned the stronger ability of cell differentiation. As demonstrated in a previous study, ALP was significant in bone matrix mineralization [32]. Thus, the modification with heparin-chitosan multilayers on titanium surface via LbL technique is promising to improve the osseointegration of the titanium-based implants.

The results in this study regarding osteoblast proliferation and differentiation are consistent with previous studies and indicate that LbL modification of titanium is helpful for the osteoblast growth [8, 13–15]. These results also suggest that the biological responses such as cell adhesion, cell proliferation, as well as cell differentiation depend markedly on the surface properties of the substrates. Chitosan was confirmed as a good candidate to improve the biocompatibility of the titanium substrate [33].

4. Conclusion

Polyelectrolyte multilayer of chitosan and heparin was successfully coated on titanium substrate using a layer-by-layer self-assembly technique. The multilayer can promote the adhesion, proliferation, and differentiation of osteoblasts *in vitro*. We suggest that heparin-chitosan multilayer on titanium surfaces via LbL method is beneficial to osteoblast biocompatibility.

Acknowledgments

This work was financially supported by Key Program of the Natural Science Foundation of the Higher Education Institutions of Anhui province of China (Grant no. KJ2009A169) and Science and Technology Program of Anhui Province of China (Grant no. 08010302196).

References

- [1] T. Albrektsson and M. Jacobsson, "Bone-metal interface in osseointegration," *Journal of Prosthetic Dentistry*, vol. 57, no. 5, pp. 597–607, 1987.
- [2] D. A. Puleo and A. Nanci, "Understanding and controlling the bone-implant interface," *Biomaterials*, vol. 20, no. 23-24, pp. 2311–2321, 1999.
- [3] M. Tirrell, E. Kokkoli, and M. Biesalski, "The role of surface science in bioengineered materials," *Surface Science*, vol. 500, no. 1–3, pp. 61–83, 2002.
- [4] C. M. Stanford, "Surface modifications of implants," *Oral and Maxillofacial Surgery Clinics of North America*, vol. 14, no. 1, pp. 39–51, 2002.

- [5] Q. Liu, J. Ding, F. K. Mante, S. L. Wunder, and G. R. Baran, "The role of surface functional groups in calcium phosphate nucleation on titanium foil: a self-assembled monolayer technique," *Biomaterials*, vol. 23, no. 15, pp. 3103–3111, 2002.
- [6] A. Nanci, J. D. Wuest, L. Peru et al., "Chemical modification of titanium surfaces for covalent attachment of biological molecules," *Journal of Biomedical Materials Research*, vol. 40, no. 2, pp. 324–335, 1998.
- [7] T. Salditt and U. S. Schubert, "Layer-by-layer self-assembly of supramolecular and biomolecular films," *Reviews in Molecular Biotechnology*, vol. 90, no. 1, pp. 55–70, 2002.
- [8] K. Cai, A. Rechtenbach, J. Hao, J. Bossert, and K. D. Jandt, "Polysaccharide-protein surface modification of titanium via a layer-by-layer technique: characterization and cell behaviour aspects," *Biomaterials*, vol. 26, no. 30, pp. 5960–5971, 2005.
- [9] G. G. S. Grant, D. S. Koktysh, B. Yun, R. L. Matts, and N. A. Kotov, "Layer-by-layer assembly of collagen thin films: controlled thickness and biocompatibility," *Biomedical Microdevices*, vol. 3, no. 4, pp. 301–306, 2001.
- [10] G. Decher, "Fuzzy nanoassemblies: toward layered polymeric multicomposites," *Science*, vol. 277, no. 5330, pp. 1232–1237, 1997.
- [11] P. Tryoen-Tóth, D. Vautier, Y. Haikel et al., "Viability, adhesion, and bone phenotype of osteoblast-like cells on polyelectrolyte multilayer films," *Journal of Biomedical Materials Research*, vol. 60, no. 4, pp. 657–667, 2002.
- [12] L. Richert, P. Lavalle, E. Payan et al., "Layer by layer buildup of polysaccharide films: physical chemistry and cellular adhesion aspects," *Langmuir*, vol. 20, no. 2, pp. 448–458, 2004.
- [13] K. Cai, Y. Hu, K. D. Jandt, and Y. Wang, "Surface modification of titanium thin film with chitosan via electrostatic self-assembly technique and its influence on osteoblast growth behavior," *Journal of Materials Science: Materials in Medicine*, vol. 19, no. 2, pp. 499–506, 2008.
- [14] K. Cai, Y. Hu, and K. D. Jandt, "Surface engineering of titanium thin films with silk fibroin via layer-by-layer technique and its effects on osteoblast growth behavior," *Journal of Biomedical Materials Research A*, vol. 82, no. 4, pp. 927–935, 2007.
- [15] Y. Hu, K. Cai, Z. Luo et al., "Surface mediated in situ differentiation of mesenchymal stem cells on gene-functionalized titanium films fabricated by layer-by-layer technique," *Biomaterials*, vol. 30, no. 21, pp. 3626–3635, 2009.
- [16] J. K. Suh and H. W. Matthew, "Application of chitosan-based polysaccharide biomaterials in cartilage tissue engineering: a review," *Biomaterials*, vol. 21, no. 24, pp. 2589–2598, 2000.
- [17] T. Albrektsson and H. A. Hansson, "An ultrastructural characterization of the interface between bone and sputtered titanium or stainless steel surfaces," *Biomaterials*, vol. 7, no. 3, pp. 201–205, 1986.
- [18] S. Mohan and D. J. Baylink, "Bone growth factors," *Clinical Orthopaedics and Related Research*, no. 263, pp. 30–48, 1991.
- [19] L. S. Beck, E. P. Amento, Y. Xu et al., "TGF- β 1 induces bone closure of skull defects: temporal dynamics of bone formation in defects exposed to rhTGF- β 1," *Journal of Bone and Mineral Research*, vol. 8, no. 6, pp. 753–761, 1993.
- [20] B. Zhao, T. Katagiri, H. Toyoda et al., "Heparin potentiates the in vivo ectopic bone formation induced by bone morphogenetic protein-2," *Journal of Biological Chemistry*, vol. 281, no. 32, pp. 23246–23253, 2006.
- [21] F. Blankaert, J. L. Saffar, M. L. Colombier, G. Carpentier, D. Barritault, and J. P. Caruelle, "Heparan-like molecules induce the repair of skull defects," *Bone*, vol. 17, no. 6, pp. 499–506, 1995.
- [22] E. Khor and L. Y. Lim, "Implantable applications of chitin and chitosan," *Biomaterials*, vol. 24, no. 13, pp. 2339–2349, 2003.
- [23] J. Berger, M. Reist, J. M. Mayer, O. Felt, and R. Gurny, "Structure and interactions in chitosan hydrogels formed by complexation or aggregation for biomedical applications," *European Journal of Pharmaceutics and Biopharmaceutics*, vol. 57, no. 1, pp. 35–52, 2004.
- [24] D. T. Wassell and G. Embery, "Adsorption of bovine serum albumin on to titanium powder," *Biomaterials*, vol. 17, no. 9, pp. 859–864, 1996.
- [25] B. Feng, J. Weng, B. C. Yang et al., "Surface characterization of titanium and adsorption of bovine serum albumin," *Materials Characterization*, vol. 49, no. 2, pp. 129–137, 2002.
- [26] E. Jansson and P. Tengvall, "Adsorption of albumin and IgG to porous and smooth titanium," *Colloids and Surfaces B: Biointerfaces*, vol. 35, no. 1, pp. 45–51, 2004.
- [27] H. M. Kim, F. Miyaji, T. Kokubo, and T. Nakamura, "Effect of heat treatment on apatite-forming ability of Ti metal induced by alkali treatment," *Journal of Materials Science: Materials in Medicine*, vol. 8, no. 6, pp. 341–347, 1997.
- [28] K. Cai, K. Yao, S. Lin et al., "Poly(D,L-lactic acid) surfaces modified by silk fibroin: effects on the culture of osteoblast in vitro," *Biomaterials*, vol. 23, no. 4, pp. 1153–1160, 2002.
- [29] M. C. Serrano, R. Pagani, M. Vallet-Regí et al., "In vitro biocompatibility assessment of poly(ϵ -caprolactone) films using L929 mouse fibroblasts," *Biomaterials*, vol. 25, no. 25, pp. 5603–5611, 2004.
- [30] P. Sibilla, A. Sereni, G. Aguiari et al., "Effects of a hydroxyapatite-based biomaterial on gene expression in osteoblast-like cells," *Journal of Dental Research*, vol. 85, no. 4, pp. 354–358, 2006.
- [31] L. Lu, L. Kam, M. Hasenbein et al., "Retinal pigment epithelial cell function on substrates with chemically micropatterned surfaces," *Biomaterials*, vol. 20, no. 23–24, pp. 2351–2361, 1999.
- [32] Y. Takagishi, T. Kawakami, Y. Hara, M. Shinkai, T. Takezawa, and T. Nagamune, "Bone-like tissue formation by three-dimensional culture of MG63 osteosarcoma cells in gelatin hydrogels using calcium-enriched medium," *Tissue Engineering*, vol. 12, no. 4, pp. 927–937, 2006.
- [33] J. D. Bumgardner, R. Wiser, P. D. Gerard et al., "Chitosan: potential use as a bioactive coating for orthopaedic and craniofacial/dental implants," *Journal of Biomaterials Science, Polymer Edition*, vol. 14, no. 5, pp. 423–438, 2003.

Research Article

Particle Size Control of $\text{Y}_2\text{O}_3:\text{Eu}^{3+}$ Prepared via a Coconut Water-Assisted Sol-Gel Method

Maria de Andrade Gomes, Mário Ernesto Giroldo Valerio, and Zélia Soares Macedo

Laboratory of Advanced Ceramic Materials, Physics Department, Federal University of Sergipe,
49100-000 São Cristóvão, SE, Brazil

Correspondence should be addressed to Zélia Soares Macedo, zelia.macedo@gmail.com

Received 2 October 2010; Revised 24 November 2010; Accepted 23 December 2010

Academic Editor: Yanan Du

Copyright © 2011 Maria de Andrade Gomes et al. This is an open access article distributed under the Creative Commons Attribution License, which permits unrestricted use, distribution, and reproduction in any medium, provided the original work is properly cited.

Eu^{3+} -doped Y_2O_3 nanoparticles were produced through proteic sol-gel technique, and the adjustment of pH was tested in order to control the particle size of the powders. A strong correlation between the initial pH and the temperature of crystallization was observed, allowing the production of particles with controlled diameter from 4 nm to 50 nm. The samples were characterized by X-ray diffraction, high-resolution transmission electron microscopy, optical microscopy and photoluminescence spectroscopy in both absorption and emission modes. A blue shift of the excitation peak corresponding to energy transfer from $\text{Y}_2\text{O}_3:\text{Eu}^{3+}$ host to Eu^{3+} ions was observed, as the particle size was reduced from 50 to 4 nm. The suppression of a charge transfer band also resulted from the reduction of the particle size. The emission spectrum of the Y_2O_3 with particles of 50 nm was found to be similar to that of bulk material whereas 4 nm particles presented broadened emission peaks with lower intensities.

1. Introduction

There is currently a great deal of interest on the development of luminescent nanoparticles for biomedical applications. Compared to traditional organic dyes and fluorescent proteins, inorganic phosphors can offer several advantages such as tunable emission from visible to infrared wavelengths, large absorption coefficient across a wide spectral range, high quantum yield and stability against photobleaching [1]. In the past few years, luminescent quantum dots (QDs) have been investigated aiming their application as labels in biosensing and imaging [2–6]. However, one of the major concerns in the medical applications of QDs is their inherent toxicity, since the most widely used QDs probes, like CdSe, CdTe, CdS, PbSe and ZnSe, are heavy metal-based materials. A number of mechanisms, such as free radical formation of heavy metal, interaction of QDs with intracellular components and surface oxidation, have been postulated to be responsible for QDs cytotoxicity [5, 6]. Considering these limitations, the production of heavy metal-free luminescent nanoparticles becomes a matter of the highest importance and rare earth-doped nanocrystals

are pointed out as the best candidates to substitute QDs luminescent probes [7–10].

Amongst a variety of luminescent rare earth-doped systems, Eu^{3+} -doped Y_2O_3 shows the highest quantum efficiency (almost 100%), and it is widely investigated for applications in fluorescent lamps, display panels and luminescent inks [11–13]. Different methods have been employed to produce nanocrystalline $\text{Y}_2\text{O}_3:\text{Eu}^{3+}$ [14–16]. In this work, a coconut water-based sol-gel synthesis, also known as proteic sol-gel route, was investigated. The advantages of this new method are the simplicity and low environmental impact, since it employs the protein chains of coconut water and metal salts in substitution of alcoxide precursors [17].

As it is widely known, the reactivity of the particles increases as their size decreases. This high reactivity leads to the agglomeration of these small particles and can result in undesirable coalescence [18] during thermal treatments for the crystallization of the samples. On the other hand, there are reports on the influence of pH on the agglomeration degree and particle size of the materials produced by wet chemistry and combustion synthesis [19–21]. In a previous work, the proteic sol-gel route was used, without

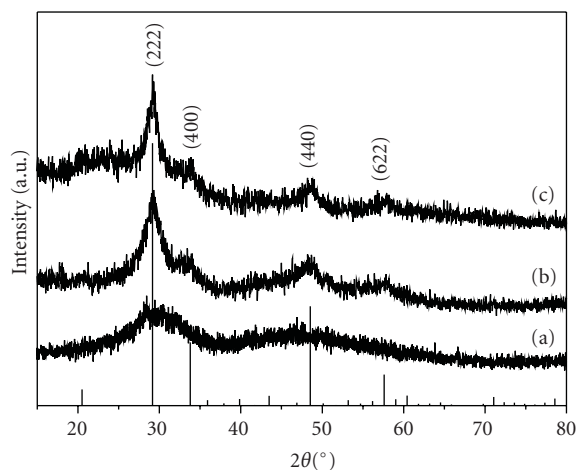


FIGURE 1: X-ray diffraction patterns of $\text{Y}_2\text{O}_3:\text{Eu}^{3+}$ produced by sol-gel with pH control: (a) amorphous phase (xerogel), (b) pH = 7.0, crystallised at 350°C and (c) pH = 9.0, crystallised at 400°C.

pH control, to produce Y_2O_3 [22]. The smallest particles obtained by this method sized 50 nm. In the present work, the adjustment of the pH during the synthesis was tested in order to produce even smaller particles, establishing a direct relationship between the initial pH and the final granulometry of the powders. The influence of the particle size on the luminescent properties of these phosphors are also presented and discussed.

2. Experimental

The $\text{Y}_2\text{O}_3:\text{Eu}^{3+}$ nanopowders were prepared via proteic sol-gel [17] using the salts $\text{Y}(\text{NO}_3)_3$ and $\text{Eu}(\text{NO}_3)_3$ (Alfa Aesar, grade purity 99.99%) as precursor materials. These reactants were mixed with processed coconut water, according to the formula $(\text{Y}_{0.98}\text{Eu}_{0.02})_2\text{O}_3$, and homogenized by stirring at room temperature. In this route, the metal ions are believed to bind to the polymeric chains present in coconut water, forming a colloidal suspension (sol). To adjust pH, ammonium hydroxide, NH_4OH (Vetec, P.A.) was added drop by drop into the sol, while it was stirred, and the pH values of the sol were monitored using a Lutron 206 pH meter. It has been reported that the pH of the solution can modify the size of nanoparticles [19–21]. The pH values investigated in this work were 5.0, 7.0, and 9.0. A sample without pH control was also produced and used as reference. After stirring for 10 minutes, the sol was polymerized and formed a gel, which was dried at 100°C/24 hours. The dried material (aerogel) was homogenized and calcined to reach the crystalline phase. Several calcination temperatures were tested from 300°C up to 850°C. After the calcinations, the samples were washed in distilled water to eliminate residual KCl phase, which is an ionic salt present in coconut water.

The crystalline phase of the powders was inspected by X-ray diffraction (XRD-Rigaku RINT 2000/PC) in continuous scanning mode using $\text{Cu K}\alpha$ radiation. The average crystallite size of the samples was obtained from the full width at

half maximum (FWHM) of the diffraction peaks, with instrumental correction using LaB_6 standard powder [20, 23]. Transmission electron microscopy (TEM) images were obtained with a Tecnai 20 microscope and they were used to analyse morphology and size of the produced nanoparticles. Micrographs of the samples illuminated with ultraviolet (UV) light were obtained with an optical microscope. For both electron and optical microscopy, the powders were dispersed in isopropyl alcohol with the aid of an ultrasonic bath.

The optical properties of the Eu^{3+} -doped Y_2O_3 samples were inspected via photoluminescence technique in emission and excitation modes. These optical spectra were acquired at room temperature in an ISS PC1TM spectrofluorometer that uses a 300 W Xenon lamp as excitation source. The emission spectra were measured with excitation fixed at 245 nm whereas the excitation spectra were measured by monitoring the intensity of luminescence at 614 nm ($^5\text{D}_0 \rightarrow ^7\text{F}_2$ transition of Eu^{3+}).

3. Results and Discussion

Figure 1 presents the X-ray diffraction patterns of 2% Eu^{3+} -doped Y_2O_3 nanocrystals produced at pH = 7.0 and pH = 9.0. For all the samples studied, the obtained XRD patterns were consistent with the cubic phase of Y_2O_3 with spatial group Ia3 (JCPDS No 79-1257). The most intense peaks correspond to the crystal planes (222), (400), (440), and (622). These peaks are broadened due to the small size of the nanoparticles. From the diffraction patterns, one can observe that the sample produced at pH = 7.0 was crystallised after calcination at 350°C. At this temperature, all the other samples were amorphous. For the sample synthesized at pH = 9.0, the lowest crystallization temperature was 400°C and the other samples only presented crystalline structure after calcinations at 450°C.

The crystallite size could be estimated from the FWHM of the diffraction peaks using Scherrer's equation $d = K\lambda/(\beta \cdot \cos \theta_B)$, where K is the shape coefficient for the reciprocal lattice point (in this work $K = 0.89$), λ is the wavelength of the X-rays ($\lambda = 0.15405$ nm), θ_B is the peak position, and $\beta = \sqrt{B^2 - b^2}$ is the width of specimen's peak (B) corrected by a instrumental broad factor (in this work, $b = 0.005192$ rad). The results are presented in Table 1, where it can be observed that the biggest crystallite size were obtained for the sample calcined at 850°C, departing from the sol without pH control. The smallest crystallites were produced at pH = 7.0 and $T = 350^\circ\text{C}$. As expected, the samples calcined at lower temperatures presented smaller crystallites. One can also observe that the particles produced at pH = 7.0 present a pronounced growth at 500°C, reaching the average size of 18 nm whereas the samples produced at lower pH values remain smaller than 10 nm at this temperature.

The reduction of the surface energy is the driving force for both nucleation and particle growth. This thermodynamic parameter depends on the surface tension of curved interfaces and also on the net surface area of the particles [24]. Nanoparticles have high surface energy due

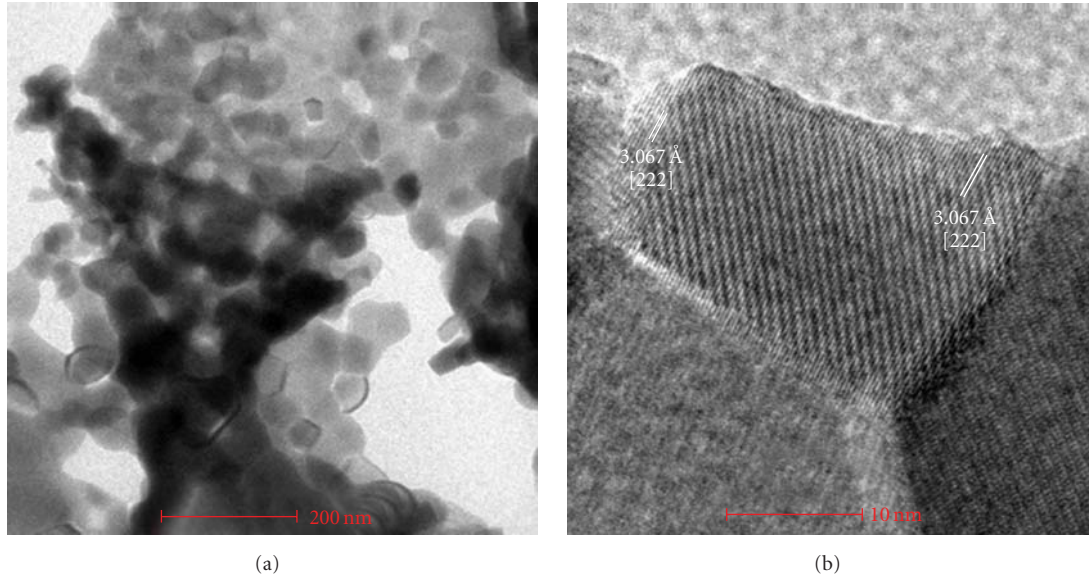


FIGURE 2: Micrographs of powder produced at pH = 7.0 and calcined at 500°C. (a) TEM image showing spherical-like produced particles. (b) HRTEM image indicating that each particle contains only one crystallite.

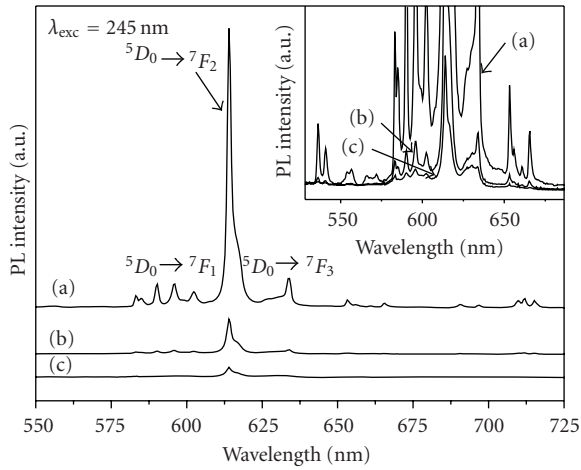


FIGURE 3: Emission spectra of $\text{Y}_2\text{O}_3:\text{Eu}^{3+}$ nanocrystals with particle sizes of 50 nm (curve a), 7 nm (curve b), and 4 nm (curve c).

to the small curvature radius and large surface area, so the system spontaneously tends to decrease the interface solid solution, and particles tend to grow in order to minimize the surface energy. On the other hand, the surface tension (and, consequently, the surface energy) of particles in suspension can be decreased by adsorption of the amine groups from the ammonium hydroxide [25], which promote both electrostatic and steric stabilization of nanoparticles. This stabilization prevents the grown of the particles, so the acidity of the medium of synthesis strongly influences the particle size [26]. Besides that, as temperature can also influence surface energy [26], lowering the synthesis

TABLE 1: Crystallite size of the $\text{Y}_2\text{O}_3:\text{Eu}^{3+}$ -particles produced by proteic sol-gel as a function of pH and temperature (n.d. stands for not determined).

	Without pH control	pH = 5.0	pH = 7.0	pH = 9.0
$T = 350^\circ\text{C}$	amorphous	amorphous	3 nm	amorphous
$T = 400^\circ\text{C}$	amorphous	amorphous	4 nm	6 nm
$T = 450^\circ\text{C}$	7 nm	7 nm	5 nm	7 nm
$T = 500^\circ\text{C}$	9 nm	9 nm	18 nm	n.d.
$T = 850^\circ\text{C}$	50 nm	n.d.	n.d.	n.d.

temperature results in a wider size distribution with an increased amount of small particles.

Figure 2 presents TEM images of the powder prepared at pH = 7.0 and treated at 500°C. In Figure 2(a), one can observe spherical-like particles with reduced agglomeration degree when compared with the results from other synthesis methods [11]. For the samples shown in Figure 2, the average particle size observed in the micrographs was 20 nm, which agrees with the crystallite size determined from the X-ray diffraction patterns (see Table 1). Figure 2(b) presents the high-resolution (HRTEM) image of the same sample, where one can observe the lattice planes indicating that each particle contains only one crystallite. Consequently, the crystallite sizes presented in Table 1 can be interpreted as the average particle size of the samples. In Figure 2(b), the distance between [222] family planes is 3.067 Å, which is consistent with the value of 3.066 Å obtained from crystallographic database [27].

One important step on the development of alternative nontoxic nanocrystals for biomedical imaging is the

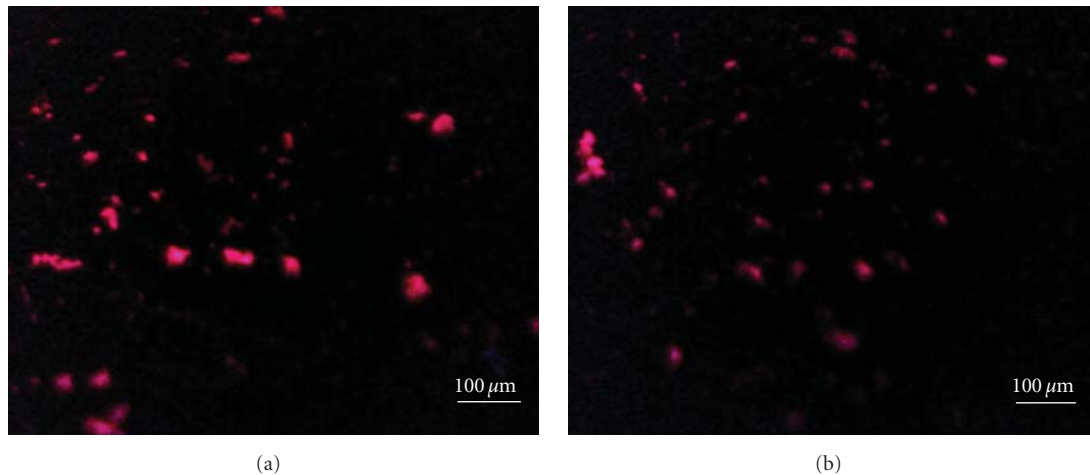


FIGURE 4: Micrographs of $\text{Y}_2\text{O}_3:\text{Eu}^{3+}$ produced by proteic sol-gel: (a) without pH control and calcined at 850°C and (b) at $\text{pH} = 7.0$ and calcined at 350°C . The images were registered during illumination with UV light.

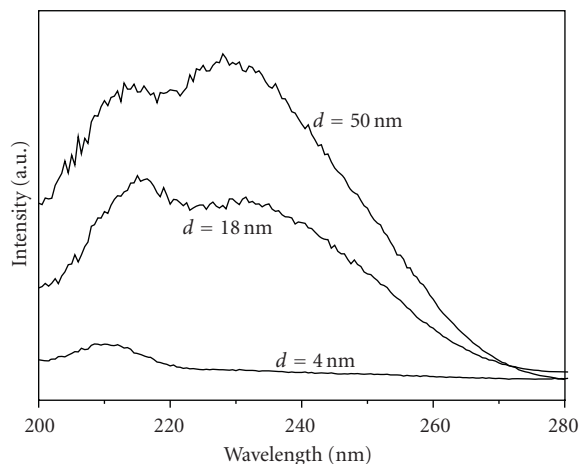


FIGURE 5: Excitation spectra of $\text{Y}_2\text{O}_3:\text{Eu}^{3+}$ nanocrystals with average particle size of 4, 18, and 50 nm, monitored for $^5D_0 \rightarrow ^7F_2$ (614 nm) emission.

investigation of their luminescence properties. In this work, the emission and excitation spectra of doped $\text{Y}_2\text{O}_3:\text{Eu}^{3+}$ produced by proteic sol-gel were measured for samples with different particle sizes. Figure 3 presents the emission spectra for samples with particle sizes of 50 nm (curve a), 7 nm (curve b), and 4 nm (curve c), under excitation of 245 nm. In these spectra, the intensity was normalized by the excitation intensity (I_0), so the luminescent intensities are comparable. For particle sizes of 50 nm, the features of the emission spectrum are similar to those of the bulk material [28]. The main peak at 614 nm originates from $^5D_0 \rightarrow ^7F_2$ forced electric-dipole transition of Eu^{3+} ; the one centered at 633 nm corresponds to $^5D_0 \rightarrow ^7F_3$ transition and the peaks around 595 nm correspond to $^5D_0 \rightarrow ^7F_1$ transition, which is a magnetic-dipole transition [29]. For the samples with average diameter of 7 and 4 nm, the emission peaks are at the same positions, indicating

the same electronic transitions, but they are significantly broadened due to local disorder surrounding the Eu^{3+} ions. The intensity of luminescence also depends on the particle size and this dependence should be taken into account for the application of these nanoparticles as biological labels. At 614 nm, the intensity of the 4 nm particles is 3.3% of that observed for the 50 nm particles. On the other hand, the dimensional similarity of the smaller particles with some biological macromolecules such as nucleic acids and proteins would allow a better integration of these nanoparticles with biological systems, with possible applications in medical diagnostics and targeted therapeutics. Figure 4 presents the images obtained with optical microscope (magnification of 400x) of the powder samples with particle diameter of 50 nm (Figure 4(a)) and 4 nm particles (Figure 4(b)), under UV excitation. Due to the low magnification, it is not possible to distinguish isolated particles, but from these images, it can be concluded that the luminescence of the smaller particles is still strong enough to be detected by fluorescence microscopy techniques.

The excitation spectra for the $^5D_0 \rightarrow ^7F_2$ transition of Eu^{3+} is presented in Figure 5 for the samples with particle sizes of 50 nm, 18 nm and 4 nm. For smaller particles, it is observed a lower overall intensity of the spectra, compared to the 50 nm sample. An excitation band near 214 nm was observed for all the samples and was assigned to the energy transfer excitation from the Y_2O_3 host to Eu^{3+} [30]. This band is slightly blue shifted to 209 nm for the 4 nm sample. For the particles with average size of 50 nm and 18 nm, it is also observed a band at around 210 nm, which is associated with a charge transfer (CT) from O^{2-} to Eu^{3+} . Electrons from the 2p orbital of oxygen are transferred to the 5D_0 excited level of Eu^{3+} , and the red light is emitted when the decay $^5D_0 \rightarrow ^7F_2$ occurs [31]. As the CT band is especially sensitive to the local order surrounding O^{2-} , its intensity is reduced for the particles with 18 nm and suppressed for the particles with 4 nm. Similar behaviour was ascribed by other authors to $\text{Y}_2\text{O}_3:\text{Eu}^{3+}$ particles smaller than 10 nm [30].

4. Conclusions

Size-controlled $\text{Y}_2\text{O}_3\text{:Eu}^{3+}$ nanoparticles were successfully obtained via proteic sol-gel with pH adjustment at the initial stage of the synthesis. The average particle size was tunable from 4 to 50 nm by the control of the pH and calcination temperature of the samples. The advantages of this synthesis route are the simplicity, low environmental impact, and low cost of production, since it employs a natural resource (coconut water) instead of the conventional metallic alkoxides. The temperature of 350°C, used for the production of particles with average diameter of 4 nm, is at least 500°C lower than those reported in the literature for the crystallization of this material [22]. The luminescent characterization of the samples has shown a dependence of the quantum yield on the particle size, probably related to the suppression of the charge transfer from the oxygen to the excited level of Eu^{3+} . Nevertheless, the particles with diameter of 4 nm still presented strong red emission, suggesting that they are suitable to be used in conjugation with biological systems. These conjugation tests are currently being performed in our research group.

Acknowledgments

The authors wish to acknowledge CETENE for the use of microscopy facilities and the financial agencies CNPq, CAPES, FINEP, and FAPITEC/SE.

References

- [1] X. Gao, L. Yang, J. A. Petros, F. F. Marshall, J. W. Simons, and S. Nie, "In vivo molecular and cellular imaging with quantum dots," *Current Opinion in Biotechnology*, vol. 16, no. 1, pp. 63–72, 2005.
- [2] R. Dey, S. Mazumder, M. K. Mitra, S. Mukherjee, and G. C. Das, "Review: biofunctionalized quantum dots in biology and medicine," *Journal of Nanomaterials*, vol. 2009, Article ID 815734, 17 pages, 2009.
- [3] W. Zhong, "Nanomaterials in fluorescence-based biosensing," *Analytical and Bioanalytical Chemistry*, vol. 394, no. 1, pp. 47–59, 2009.
- [4] A. M. Smith, G. Ruan, M. N. Rhyner, and S. Nie, "Engineering luminescent quantum dots for in vivo molecular and cellular imaging," *Annals of Biomedical Engineering*, vol. 34, no. 1, pp. 3–14, 2006.
- [5] A. P. Alivisatos, W. Gu, and C. Larabell, "Quantum dots as cellular probes," *Annual Review of Biomedical Engineering*, vol. 7, pp. 55–76, 2005.
- [6] T. Jamieson, R. Bakhshi, D. Petrova, R. Pocock, M. Imani, and A. M. Seifalian, "Biological applications of quantum dots," *Biomaterials*, vol. 28, no. 31, pp. 4717–4732, 2007.
- [7] W. Cai, A. R. Hsu, Z. B. Li, and X. Chen, "Are quantum dots ready for in vivo imaging in human subjects?" *Nanoscale Research Letters*, vol. 2, no. 6, pp. 265–281, 2007.
- [8] J. Yuan and G. Wang, "Lanthanide-based luminescence probes and time-resolved luminescence bioassays," *Trends in Analytical Chemistry*, vol. 25, no. 5, pp. 490–500, 2006.
- [9] N. Pradhan, D. M. Battaglia, Y. Liu, and X. Peng, "Efficient, stable, small, and water-soluble doped ZnSe nanocrystal emitters as non-cadmium biomedical labels," *Nano Letters*, vol. 7, no. 2, pp. 312–317, 2007.
- [10] K. Manzoor, S. Johnny, D. Thomas, S. Setua, D. Menon, and S. Nair, "Bio-conjugated luminescent quantum dots of doped ZnS: a cyto-friendly system for targeted cancer imaging," *Nanotechnology*, vol. 20, no. 6, p. 113, 2009.
- [11] Z. Wei-Wei, X. Mei, Z. Wei-Ping et al., "Site-selective spectra and time-resolved spectra of nanocrystalline $\text{Y}_2\text{O}_3\text{:Eu}$," *Chemical Physics Letters*, vol. 376, no. 3–4, pp. 318–323, 2003.
- [12] M. Abdullah, . Astuti, and . Khairurrijal, "Synthesis of luminescent ink from europium-doped Y_2O_3 dispersed in polyvinyl alcohol solution," *Advances in OptoElectronics*, vol. 2009, Article ID 918351, 8 pages, 2009.
- [13] P. Psuja, D. Hreniak, and W. Strek, "Rare-earth doped nanocrystalline phosphors for field emission displays," *Journal of Nanomaterials*, vol. 2007, Article ID 81350, 7 pages, 2007.
- [14] B. Bihari, H. Eilers, and B. M. Tissue, "Spectra and dynamics of monoclinic Y_2O_3 and Eu^{3+} : Y_2O_3 nanocrystals," *Journal of Luminescence*, vol. 75, no. 1, pp. 1–10, 1997.
- [15] A. Konrad, U. Herr, R. Tidecks, F. Kummer, and K. Samwer, "Luminescence of bulk and nanocrystalline cubic yttria," *Journal of Applied Physics*, vol. 90, no. 7, pp. 3516–3523, 2001.
- [16] D. Dosev, B. Guo, and I. M. Kennedy, "Photoluminescence of Eu^{3+} : Y_2O_3 as an indication of crystal structure and particle size in nanoparticles synthesized by flame spray pyrolysis," *Journal of Aerosol Science*, vol. 37, no. 3, pp. 402–412, 2006.
- [17] M. A. Macêdo and J. M. Sasaki, "Processo de fabricação de pós nanoparticulados," Patent Pending 0203876-5/BR.
- [18] H. Eilers, "Synthesis and characterization of nanophase yttria co-doped with erbium and ytterbium," *Materials Letters*, vol. 60, no. 2, pp. 214–217, 2006.
- [19] F. A. Andrade de Jesus, R. S. Silva, A. C. Hernandez, and Z. S. Macedo, "Effect of pH on the production of dispersed $\text{Bi}_4\text{Ge}_3\text{O}_{12}$ nanoparticles by combustion synthesis," *Journal of the European Ceramic Society*, vol. 29, no. 1, pp. 125–130, 2009.
- [20] C. T. Meneses, W. H. Flores, F. Garcia, and J. M. Sasaki, "A simple route to the synthesis of high-quality NiO nanoparticles," *Journal of Nanoparticle Research*, vol. 9, no. 3, pp. 501–505, 2007.
- [21] W. Luan and L. Gao, "Influence of pH value on properties of nanocrystalline BaTiO_3 powder," *Ceramics International*, vol. 27, no. 6, pp. 645–648, 2001.
- [22] P. J. R. Montes, M. E. G. Valerio, M. A. Macêdo, F. Cunha, and J. M. Sasaki, "Yttria thin films doped with rare earth for applications in radiation detectors and thermoluminescent dosimeters," *Microelectronics Journal*, vol. 34, no. 5–8, pp. 557–559, 2003.
- [23] B. D. Cullity and S. R. Stock, *Elements of X-ray Diffraction*, Prentice Hall, Upper Saddle River, NJ, USA, 3rd edition, 2001.
- [24] A. I. Rusanov, "Surface thermodynamics revisited," *Surface Science Reports*, vol. 58, no. 5–8, pp. 111–239, 2005.
- [25] J. P. Jolivet, S. Cassaignon, C. Chanéac, D. Chiche, O. Durupthy, and D. Portehault, "Design of metal oxide nanoparticles: control of size, shape, crystalline structure and functionalization by aqueous chemistry," *Comptes Rendus Chimie*, vol. 13, no. 1–2, pp. 40–51, 2010.
- [26] G. Cao, *Nanostructures & Nanomaterials—Synthesis, Properties & Applications*, Imperial College Press, London, UK, 2004.
- [27] G. Baldinozzi, J. F. Béar, and G. Calvarin, "Rietveld refinement of two-phase Zr-doped Y_2O_3 ," *Materials Science Forum*, vol. 278–281, no. 2, pp. 680–685, 1998.

- [28] Z. Fu, S. Zhou, T. Pan, and S. Zhang, "Preparation and luminescent properties of cubic $\text{Eu}^{3+}:\text{Y}_2\text{O}_3$ nanocrystals and comparison to bulk $\text{Eu}^{3+}:\text{Y}_2\text{O}_3$," *Journal of Luminescence*, vol. 124, no. 2, pp. 213–216, 2007.
- [29] S. Setua, D. Menon, A. Asok, S. Nair, and M. Koyakutty, "Folate receptor targeted, rare-earth oxide nanocrystals for bi-modal fluorescence and magnetic imaging of cancer cells," *Biomaterials*, vol. 31, no. 4, pp. 714–729, 2010.
- [30] J. W. Wang, Y. M. Chang, H. C. Chang et al., "Local structure dependence of the charge transfer band in nanocrystalline $\text{Y}_2\text{O}_3:\text{Eu}^{3+}$," *Chemical Physics Letters*, vol. 405, no. 4–6, pp. 314–317, 2005.
- [31] S. J. Dhoble, I. M. Nagpure, J. G. Mahakhode, S. V. Godbole, M. K. Bhide, and S. V. Moharil, "Photoluminescence and XEL in $\text{Y}_2\text{O}_3:\text{Eu}^{3+}$ phosphor," *Nuclear Instruments and Methods in Physics Research. Section B*, vol. 266, no. 15, pp. 3437–3442, 2008.

Research Article

BN Nanoparticles/Si₃N₄ Wave-Transparent Composites with High Strength and Low Dielectric Constant

Dongliang Zhao, Yujun Zhang, Hongyu Gong, Baoxin Zhu, and Xiaoyu Zhang

Key Laboratory for Liquid-Solid Structural Evolution and Processing of Materials, Ministry of Education and Shandong University, Jinan 250061, China

Correspondence should be addressed to Yujun Zhang, yujunzhang1956@126.com

Received 9 November 2010; Revised 20 January 2011; Accepted 7 March 2011

Academic Editor: Wei He

Copyright © 2011 Dongliang Zhao et al. This is an open access article distributed under the Creative Commons Attribution License, which permits unrestricted use, distribution, and reproduction in any medium, provided the original work is properly cited.

Si₃N₄ wave-transparent composites with different volume content of BN nanoparticles (BN_{np}/Si₃N₄) were prepared by gas pressure sintering at 1800°C in N₂ atmosphere. The effects of BN nanoparticles on the dielectric and mechanical properties of BN_{np}/Si₃N₄ composites were investigated. The results showed that the addition of the BN nanoparticles improved the dielectric properties of BN_{np}/Si₃N₄ composites effectively and decreased the mechanical properties. When the volume content of BN nanoparticles was 10%, the dielectric constant and dielectric loss tangent were 4.31 and 0.006, respectively, and the bending strength and fracture toughness still reached 198.9 MPa and 3.36 MPa·m^{1/2}. The high mechanical properties of BN_{np}/Si₃N₄ composites with 10% BN nanoparticles were attributed to homogeneously dispersed BN nanoparticles which were embedded in the pores formed by the rod-like β-Si₃N₄.

1. Introduction

Silicon nitride (Si₃N₄) was one of the most promising ceramic materials for the applications of microwave transparent materials which protected the spacecraft from the influences of harsh environment [1, 2], due to its high mechanical strength, good thermal shock resistance, and excellent rain erosion resistance [3–5]. However, its relatively high dielectric constant and dielectric loss tangent at room and elevated temperatures limited the wider applications as the advanced vehicles [6, 7]. To solve this problem, Xia et al. [8] prepared porous Si₃N₄ ceramics with a porosity of 30–55% for decreasing the dielectric constant, and Zhang et al. [9] prepared BN/Si₃N₄ composites by adding the BN particles with low dielectric constant. All of those methods could effectively decrease the dielectric constant and dielectric loss tangent, yet unfortunately, a drastic degradation of strength occurred unbearably.

It was well known that the addition of nanoparticles to a ceramic matrix could improve the mechanical properties of ceramic nanocomposites [10, 11]. BN/Si₃N₄ nanocomposite with superior mechanical properties, prepared by Gao et

al. alleviated the shortcoming of low strength encountered in conventional BN/Si₃N₄ composite [12]. In this paper, BN nanoparticles were introduced into the Si₃N₄ matrix to fabricate BN_{np}/Si₃N₄ composites by gas pressure sintering. The dielectric and mechanical properties of BN_{np}/Si₃N₄ composites with different volume content of BN nanoparticles were investigated.

2. Experimental Procedure

α-Si₃N₄ powders (α-Si₃N₄ > 93%, D₅₀ < 0.5 μm; UNIS-CERA, Beijing, China) and BN nanoparticles (purity > 99.5 wt.%, D₅₀ < 100 nm; NNT Co., Ltd., Taiwan, China) were used as the starting materials. Figure 1 showed the XRD pattern of Si₃N₄ raw powders, and the principal crystal phase was α-Si₃N₄. The dry gel of yttrium aluminum garnet (YAG), which prepared from yttrium chloride and polyaluminium chloride by sol-gel method, were used as sintering aids [13]. The XRD patterns of dry gel of YAG before and after sintering at current temperature were shown in Figure 2, which indicated that the dry gel of YAG transformed to YAG after sintering.

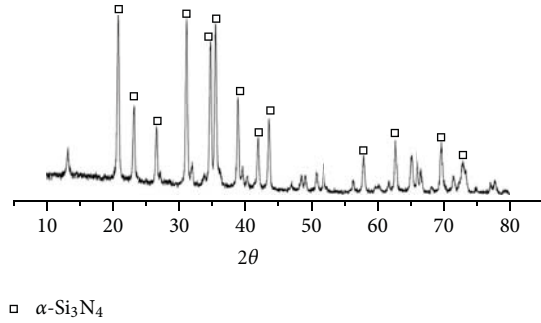


FIGURE 1: XRD pattern of Si_3N_4 raw powders.

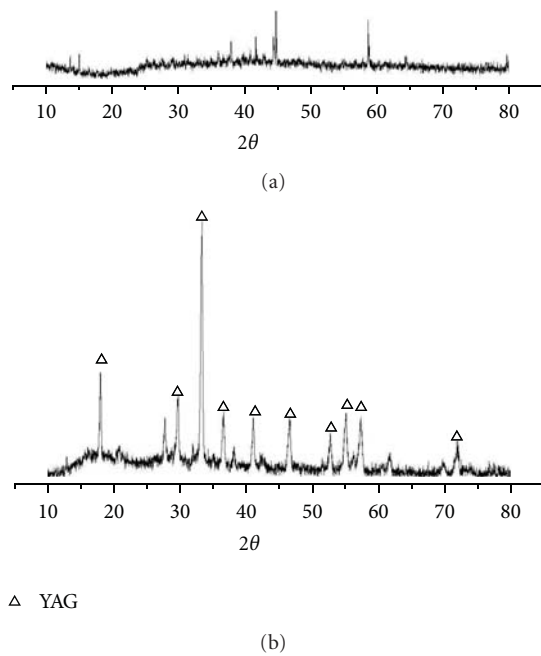


FIGURE 2: The XRD patterns of the dry gel of YAG before and after sintering. (a) dry gel of YAG; (b) dry gel of YAG after sintering.

The Si_3N_4 , BN nanoparticles and 4 vol% dry gel of YAG were ball milled for 24 h in anhydrous ethanol, followed by drying at 70°C for 24 h under vacuum. The mixture was then molded by isostatic pressing method under 120 MPa. The green body was sintered at 1800°C for 120 minutes under the pressure of 6–8 MPa in N_2 atmosphere.

The apparent porosity and density were determined by Archimedes' displacement method. The bending strength was measured by the three-point bending test and the fracture toughness was determined by the single-edge-precracked beam (SEPB) method. The samples were machined into $22.76 \times 10.06 \times 5$ mm to measure the dielectric properties by the method of completely filled short circuited waveguide technique at a frequency of 9.36 GHz. The phase composition and microstructure was investigated by the XRD (PANalytical X'Pert Alpha-1) and SEM (ZEISS).

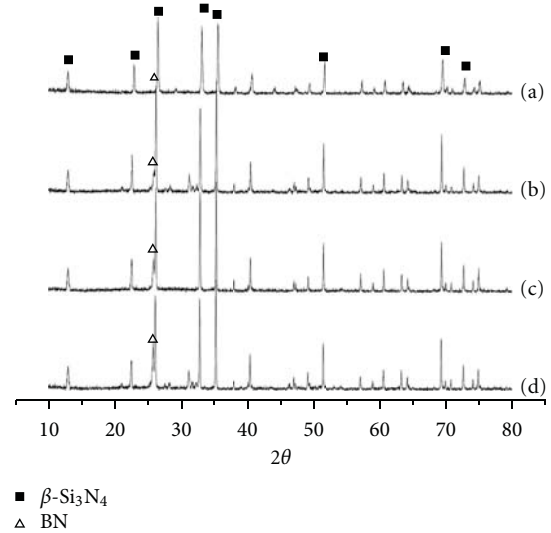


FIGURE 3: XRD patterns of $\text{BN}_{\text{np}}/\text{Si}_3\text{N}_4$ composites with different contents of BN nanoparticles. (a) 5 vol %; (b) 10 vol %; (c) 15 vol %; (d) 20 vol %.

3. Results and Discussion

Figure 3 shows the XRD patterns of $\text{BN}_{\text{np}}/\text{Si}_3\text{N}_4$ composites with different volume content of BN nanoparticles. As can be seen, the principal crystal phase in all the four samples is $\beta\text{-Si}_3\text{N}_4$, which indicates that the $\alpha\text{-Si}_3\text{N}_4$ raw powders transform to β phase during sintering process. But the random diffraction peaks can be seen in sample (b) and (d) near 31° (2θ), which indicates that trace $\alpha\text{-Si}_3\text{N}_4$ does not transform to β phase. Distinct reflections of h-BN are observed in the XRD pattern at 26.7° (2θ), and the diffraction peak intensities of the h-BN increase with the increasing of BN nanoparticles. However, YAG phase is not detected in XRD patterns due to the amount being too small to be detected. Because the dielectric constant and dielectric loss tangent of YAG were higher than BN and Si_3N_4 , the composites using fewer amounts of YAG as sintering aids could possess lower dielectric constant and dielectric loss tangent.

Figure 4 shows the SEM images of $\text{BN}_{\text{np}}/\text{Si}_3\text{N}_4$ composites. The fracture surfaces of the composites with 10 vol % and 20 vol % BN nanoparticles were shown in Figures 4(a), and 4(b), and the surfaces that were polished and chemically etched in molten NaOH were shown in Figures 4(c), and 4(d). From the SEM graphs, the massive rod-like $\beta\text{-Si}_3\text{N}_4$ can be observed, that is consistent with the result of XRD patterns shown in Figure 3. The dense packing rod-like $\beta\text{-Si}_3\text{N}_4$ grains form tough interlocking microstructure, which could absorb more energy during the fracture process. For the dielectric properties, a large amount of rod-like grains accumulate together to form a lot of pores with the size of $0.5\text{--}1\text{ }\mu\text{m}$, which may decrease the dielectric constant of $\text{BN}_{\text{np}}/\text{Si}_3\text{N}_4$ composites effectively. Furthermore, as can be seen in Figures 4(a), and 4(c), the homogeneously dispersed BN nanoparticles, which embed in the submicron pores formed by rod-like $\beta\text{-Si}_3\text{N}_4$ grains, may prevent the crack

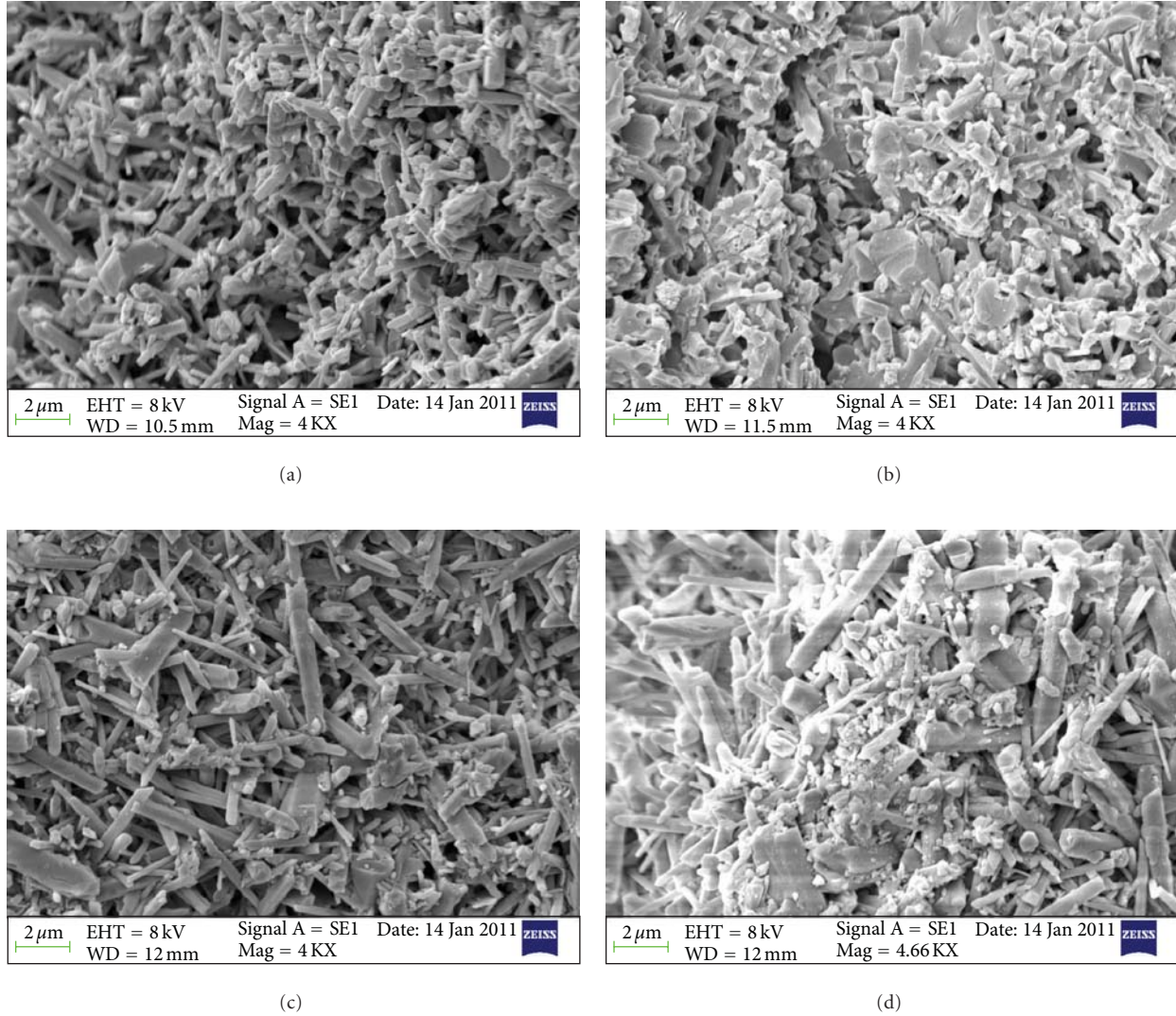


FIGURE 4: The SEM images of the $\text{BN}_{\text{np}}/\text{Si}_3\text{N}_4$ composites. (a) 10 vol% fracture surface; (b) 20 vol% fracture surface; (c) 10 vol% polished and etched surface; (d) 20 vol% polished and etched surface.

propagating along the submicron pores or prolong the crack propagation path. So $\text{BN}_{\text{np}}/\text{Si}_3\text{N}_4$ composites with 10% BN nanoparticles maintained relatively good mechanical properties. But when the content of BN nanoparticles increases to a high level in Figures 4(b), and 4(d), agglomerate structure of BN nanoparticles could cause a drastic loss of strength inevitably.

Figures 5 and 6 show the apparent porosity and dielectric properties of $\text{BN}_{\text{np}}/\text{Si}_3\text{N}_4$ composites with different volume content of BN nanoparticles. It can be seen that the dielectric constant and dielectric loss tangent of $\text{BN}_{\text{np}}/\text{Si}_3\text{N}_4$ composites decreases obviously with the increasing of BN nanoparticles and the apparent porosity increases. When the volume content of BN nanoparticles is 10%, the dielectric constant and dielectric loss tangent are 4.31 and 0.006, respectively. Because, for the well-distributed two-phase composites, the addition of the BN nanoparticles with lower dielectric constant could decrease the dielectric constant

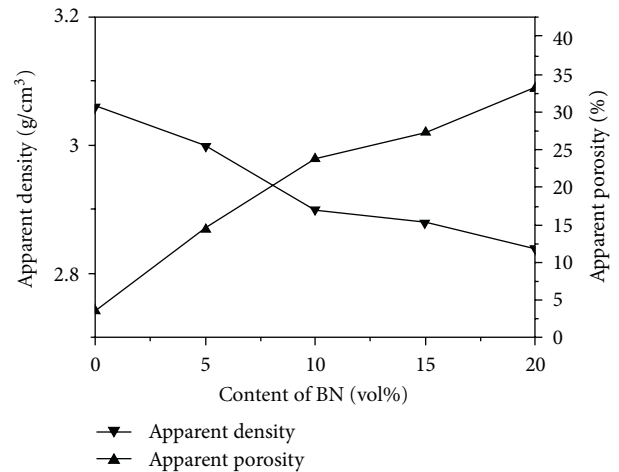


FIGURE 5: The apparent porosity and density of $\text{BN}_{\text{np}}/\text{Si}_3\text{N}_4$ composites.

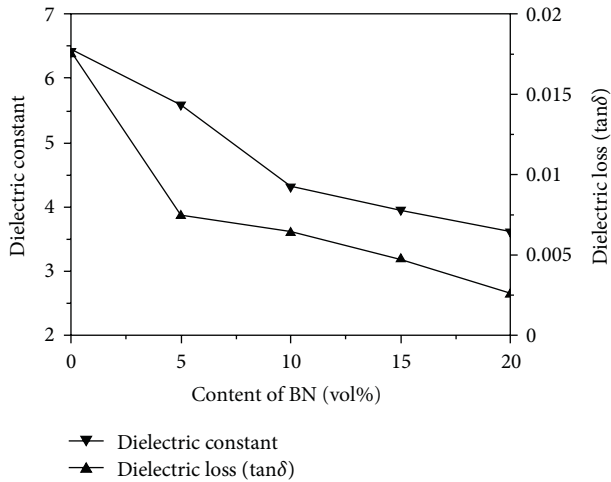


FIGURE 6: The dielectric constant and dielectric loss tangent of $\text{BN}_{\text{np}}/\text{Si}_3\text{N}_4$ composites.

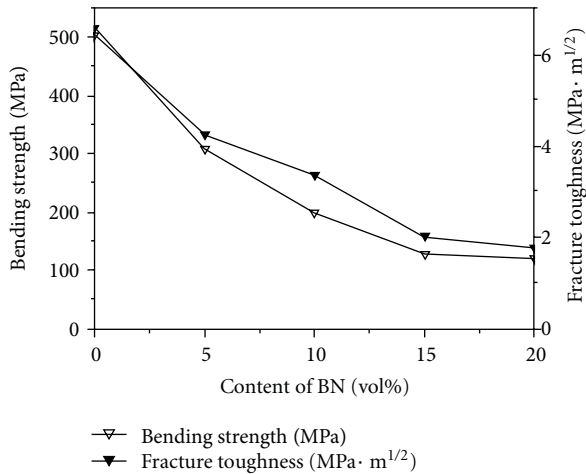


FIGURE 7: The bending strength and fracture toughness of $\text{BN}_{\text{np}}/\text{Si}_3\text{N}_4$ composites.

and dielectric loss tangent of the composites according to Lichtencker's logarithmic equation [14]. Furthermore, the apparent porosity increases with the addition of BN nanoparticles, and the increasing of apparent porosity could also decrease the dielectric constant and dielectric loss tangent of the composites [7, 8].

Figure 7 shows the bending strength and fracture toughness of $\text{BN}_{\text{np}}/\text{Si}_3\text{N}_4$ composites. As can be seen, the bending strength and fracture toughness of the composites decrease monotonously with the increasing of BN nanoparticles. It is attributed to not only the increase of apparent porosity but also the weaker bonds between BN and Si_3N_4 [15]. When the content of BN nanoparticles increases to a high level, a drastic loss of strength occurs inevitably for the agglomeration of BN nanoparticles. However, the bending strength and fracture toughness of $\text{BN}_{\text{np}}/\text{Si}_3\text{N}_4$ composites with 10% BN nanoparticles still reach 198.9 MPa and $3.36 \text{ MPa} \cdot \text{m}^{1/2}$. The

homogeneous distribution of BN nanoparticles should be responsible for the high strength of $\text{BN}_{\text{np}}/\text{Si}_3\text{N}_4$ composites.

4. Conclusion

The $\text{BN}_{\text{np}}/\text{Si}_3\text{N}_4$ composites with low dielectric constant and excellent mechanical properties were prepared. The dielectric constant and dielectric loss tangent of $\text{BN}_{\text{np}}/\text{Si}_3\text{N}_4$ composites decreased obviously with the addition of the BN nanoparticles, and the bending strength and fracture toughness decreased. When the volume content of BN nanoparticles was 10%, the dielectric constant and dielectric loss tangent were 4.31 and 0.006, respectively, and the bending strength and fracture toughness still reached 198.9 MPa and $3.36 \text{ MPa} \cdot \text{m}^{1/2}$. Distinct reflections of h-BN were observed in the XRD pattern, along with the reflections of β - Si_3N_4 . The homogeneously dispersed BN nanoparticles may improve the mechanical properties of the $\text{BN}_{\text{np}}/\text{Si}_3\text{N}_4$ composites.

Acknowledgments

This work is supported by the National Nature Science Foundation of China (no. 51072099) and the Key Technology R&D Program of Shandong Province (2010GGX10308).

References

- [1] S. Ding, Y. P. Zeng, and D. Jiang, "Oxidation bonding of porous silicon nitride ceramics with high strength and low dielectric constant," *Materials Letters*, vol. 61, no. 11-12, pp. 2277–2280, 2007.
- [2] G. Qi, C. Zhang, and H. Hu, "High strength three-dimensional silica fiber reinforced silicon nitride-based composites via polyhydromethylsilazane pyrolysis," *Ceramics International*, vol. 33, no. 5, pp. 891–894, 2007.
- [3] J. Barta, M. Manela, and R. Fischer, " Si_3N_4 and $\text{Si}_2\text{N}_2\text{O}$ for high performance radomes," *Materials Science and Engineering*, vol. 71, pp. 265–272, 1985.
- [4] F. L. Riley, "Silicon nitride and related materials," *Journal of the American Ceramic Society*, vol. 83, no. 2, pp. 245–265, 2000.
- [5] A. Ziegler, J. C. Idrobo, M. K. Cinibulk, C. Kisielowski, N. D. Browning, and R. O. Ritchie, "Interface structure and atomic bonding characteristics in silicon nitride ceramics," *Science*, vol. 306, no. 5702, pp. 1768–1770, 2004.
- [6] Y. Liu, L. Cheng, L. Zhang, Y. Xu, and Y. Liu, "Fabrication and characterization of $\text{SiO}_2(\text{f})/\text{Si}_3\text{N}_4$ composites," *Journal of University of Science and Technology Beijing*, vol. 14, no. 5, pp. 454–459, 2007.
- [7] X. Li, X. Yin, L. Zhang, L. Cheng, and Y. Qi, "Mechanical and dielectric properties of porous Si_3N_4 - SiO_2 composite ceramics," *Materials Science and Engineering A*, vol. 500, no. 1-2, pp. 63–69, 2009.
- [8] Y. Xia, Y. P. Zeng, and D. Jiang, "Dielectric and mechanical properties of porous Si_3N_4 ceramics prepared via low temperature sintering," *Ceramics International*, vol. 35, no. 4, pp. 1699–1703, 2009.
- [9] W. R. Zhang, C. H. Wang, J. Liu et al., "Study on high properties and microwave transmitting Si_3N_4 -BN based ceramic composites," *Bulletin of the Chinese Ceramic Society*, no. 3, pp. 3–6, 2003.

- [10] R. G. Wang, W. Pan, M. N. Jiang, J. Chen, and Y. Luo, "Investigation of the physical and mechanical properties of hot-pressed machinable $\text{Si}_3\text{N}_4/\text{h-BN}$ composites and FGM," *Materials Science and Engineering B*, vol. 90, no. 3, pp. 261–268, 2002.
- [11] P. Rendtel, A. Rendtel, and H. Hübner, "Mechanical properties of gas pressure sintered $\text{Si}_3\text{N}_4/\text{SiC}$ nanocomposites," *Journal of the European Ceramic Society*, vol. 22, no. 12, pp. 2061–2070, 2002.
- [12] L. Gao, X. Jin, J. Li, Y. Li, and J. Sun, "BN/ Si_3N_4 nanocomposite with high strength and good machinability," *Materials Science and Engineering A*, vol. 415, no. 1-2, pp. 145–148, 2006.
- [13] D. L. Zhao, Y. J. Zhang, H. Y. Gong et al., "Effects of sintering aids on the mechanical and dielectric properties of Si_3N_4 ceramics," *Materials Research Innovations*, vol. 14, no. 4, pp. 338–341, 2010.
- [14] W. D. Kingery, H. K. Bowen, and D. R. Uhlmann, *Introduction to Ceramics*, John Wiley & Sons, New York, NY, USA, 1976.
- [15] Y. Sun, Q. Meng, D. Jia, and C. Guan, "Effect of hexagonal BN on the microstructure and mechanical properties of Si_3N_4 ceramics," *Journal of Materials Processing Technology*, vol. 182, no. 1–3, pp. 134–138, 2007.

Research Article

Analysis of Carbon Nanotubes on the Mechanical Properties at Atomic Scale

Xiaowen Lei,¹ Toshiaki Natsuki,² Jinxing Shi,¹ and Qing-Qing Ni^{2,3}

¹Interdisciplinary Graduate School of Science and Technology, Shinshu University, 3-15-1 Tokida, Ueda, Nagano 386-8567, Japan

²Department of Functional Machinery and Mechanics, Shinshu University, 3-15-1 Tokida, Ueda, Nagano 386-8567, Japan

³Institute of Road and Bridge Engineering, Dalian Maritime University, 1 Linghai Road, Ganjingzi, Dalian 116026, China

Correspondence should be addressed to Toshiaki Natsuki, natsuki@shinshu-u.ac.jp

Received 14 June 2010; Accepted 23 August 2010

Academic Editor: Junping Wang

Copyright © 2011 Xiaowen Lei et al. This is an open access article distributed under the Creative Commons Attribution License, which permits unrestricted use, distribution, and reproduction in any medium, provided the original work is properly cited.

This paper aims at developing a mathematic model to characterize the mechanical properties of single-walled carbon nanotubes (SWCNTs). The carbon-carbon (C-C) bonds between two adjacent atoms are modeled as Euler beams. According to the relationship of Tersoff-Brenner force theory and potential energy acting on C-C bonds, material constants of beam element are determined at the atomic scale. Based on the elastic deformation energy and mechanical equilibrium of a unit in graphite sheet, simply form ED equations of calculating Young's modulus of armchair and zigzag graphite sheets are derived. Following with the geometrical relationship of SWCNTs in cylindrical coordinates and the structure mechanics approach, Young's modulus and Poisson's ratio of armchair and zigzag SWCNTs are also investigated. The results show that the approach to research mechanical properties of SWCNTs is a concise and valid method. We consider that it will be useful technique to progress on this type of investigation.

1. Introduction

Since the discovery by Iijima in 1991 [1], carbon nanotubes (CNTs) have generated huge activities in most areas of science and engineering due to their unprecedented mechanical, electrical, and thermal properties [2–13]. Especially in mechanical field, experimental measurements have determined that CNTs possess excellent mechanical properties [14–21]. Therefore, an effective method to analyze the basic characteristics of nanosized CNTs is essential.

In the past, researchers used experimental method to measure mechanical properties of CNTs. Treacy et al. [14] firstly measured the amplitude of intrinsic thermal vibrations observed in transmission electron microscopy (TEM). The average value of Young's modulus of CNTs derived from this experimental technique is 1.8 TPa by 11 tubes, in which the lowest value and the highest value are 0.40 TPa and 4.15 TPa, respectively. Later, Poncharal et al. [18] obtained Young's modulus of CNTs which is between 0.7 and 1.3 TPa by electromechanical resonant vibrations. In addition, based on an atomic force microscope (AFM), Wong et al. [20] in 1997 firstly directly measured the stiffness constant of armchair

MWCNTs pinned at one end, from which the value of Young's modulus of CNTs is 1.28 TPa. Salvétat et al. [21] used the AFM for experiment of bending an armchair (multi-walled carbon nanotubes) MWCNT pinned at each end over a hole and obtained an average modulus value of CNTs of 0.81 TPa. These experiments all promote the research of mechanical properties of CNTs. However, in description of nanoscale structures, the results are with experimental errors.

Meanwhile, for researching mechanical properties of CNTs, a number of researchers solved the difficulties in nanosized experiments in terms of computer simulation. For the analysis of nanostructural materials, atomic simulation methods such as first-principle quantum-mechanical methods [22], molecular dynamics (MD) [23, 24], and Monte Carlo [25] simulations have been routinely adopted. As early as 1993, Overney et al. [26] calculated Young's modulus of rigid short SWCNTs which is 1.5 TPa, approximately equal to that of graphite. This was followed by a range of papers predicting that Young's modulus of CNTs is close to 1 TPa independent of type and diameter [27]. Yakobson et al. [28] fitted these results by MD simulations of the continuum shell

model. Unlike the previous work that assumed a thickness of 0.34 nm, both the thickness and Young's modulus were taken as the fitting parameters, yielding a thickness of 0.066 nm and Young's modulus of 5.5 TPa. The MD approach was also used by Lu [27, 29] who reported that Young's modulus is 1 TPa and claimed that chirality and the number of walls have little effect on the value of Young's modulus. A different potential model was used by Yao and Lordi [16] who obtained Young's modulus of CNTs as 1 TPa. Although MD method has been widely used in simulating the properties of nanostructural materials, it is complex and time consuming, especially for large amount atomic systems. Therefore, the continuum mechanics seems to be a better way to investigate the properties of CNTs. However, for the case of nanoreinforced adhesives, these models cannot accurately describe the influence of the relationship between carbon atoms upon the mechanical properties and their interactions in the composite systems because they lack the appropriate constitutive relations that govern material behavior at this scale [30]. Another modeling approach is the atomic-based continuum technique, which has the unique advantage of describing atomic structured properties in a continuum framework for reducing the computational demand while employing the appropriated atomic constitutive relations.

Therefore, there is a demand of developing a modeling technique that could analyze the mechanical properties of CNTs at the atomic scale. Considering CNTs as a rolled cylindrical graphite sheet, we step from Young's modulus of the C-C bonds counted as Euler beam at atomic scale and extend the theory of classical structural mechanics into the modeling of carbon graphite sheet. The effects of tube curvature on the mechanical properties of SWCNTs are considered in closed-form solutions. The mechanical properties of SWCNTs, including Young's modulus, Poisson's ratio, the length of C-C bonds and the angle between the adjacent C-C bonds are discussed as functions of nanosized structure.

2. The Structure of CNTs

CNTs can be considered as graphite sheets rolled into cylindrical shape. The one-atom-thick graphite sheet looks like chicken wire which is made of a single-carbon-atom thickness. The structure of CNTs as shown in Figure 1 is conveniently explained in terms of the chiral vector integers (n, m) and the chiral angle θ [31]:

$$\theta = \tan^{-1} \left(\frac{\sqrt{3}n}{2m+n} \right). \quad (1)$$

CNTs are classified into three categories named as zigzag ($n, 0$): $\theta_z = 0^\circ$; armchair (n, n): $\theta_a = 30^\circ$; and chiral (n, m): ($m \neq n \neq 0$). The relationship between radius r_{cnt} and integers (n, m) is expressed as

$$r_{\text{cnt}} = \frac{\sqrt{3}L_{\text{CC}}}{2\pi} \sqrt{n^2 + m^2 + mn}, \quad (2)$$

where L_{CC} is the length of C-C bonds, 0.142 nm, for SWCNTs.

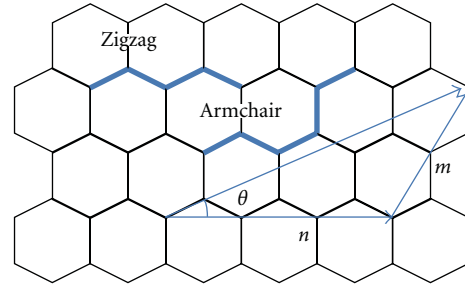


FIGURE 1: Schematic diagram of hexagonal graphite sheet.

3. Mechanics Model of Graphite Sheet

From the viewpoint of molecular mechanics, CNTs are treated as a large array of molecules consisting of carbon atoms. According to the Tersoff-Brenner force field theory [3, 32], the total molecular potential energy of the force field for nanostructured material can be defined as the sum of bonding and nonbonding energies:

$$V = \sum V_r + \sum V_\theta + \sum V_\phi + \sum V_\omega + \sum V_{\text{vdw}} + \sum V_{\text{el}}, \quad (3)$$

where V_r is the energy induced by bond stretch interaction, V_θ is the energy by the bond angle bending, V_ϕ is the energy by the dihedral angle torsion, V_ω is the energy by improper torsion, V_{vdw} is the energy by the nonbonding van der Waals (vdW) interaction, and V_{el} is the energy by the electrostatic interaction. As the axial loading, improper torsion and nonbonding interactions subjected to CNTs are very small [33], for covalent systems, the main contributions to the total molecular potential energy come from the first four terms of (3). Simplified system potential energy of CNTs with C-C bonds is given as

$$\begin{aligned} V_r &= \frac{1}{2}k_r(r - r_0)^2 = \frac{1}{2}k_r(\Delta r)^2, \\ V_\theta &= \frac{1}{2}k_\theta(\theta - \theta_0)^2 = \frac{1}{2}k_\theta(\Delta\theta)^2, \\ V_\tau &= V_\phi + V_\omega = \frac{1}{2}k_\tau(\Delta\phi)^2, \end{aligned} \quad (4)$$

where k_r , k_θ , and k_τ are the bond stretching, bond bending, and torsional resistance constants, respectively, while Δr , $\Delta\theta$, and $\Delta\phi$ represent the bond stretching increment, the bond angle change, and the angle change of bond twisting, respectively.

According to classical structural mechanics, the strain energy of a uniform beam in graphite sheet is expressed as

$$\begin{aligned} U_l &= \frac{EA}{2L_{\text{CC}}}(\Delta l)^2, \\ U_\theta &= \frac{EI}{2L_{\text{CC}}}(\Delta\theta)^2, \\ U_\theta &= \frac{GJ}{2L_{\text{CC}}}(\Delta\phi)^2, \end{aligned} \quad (5)$$

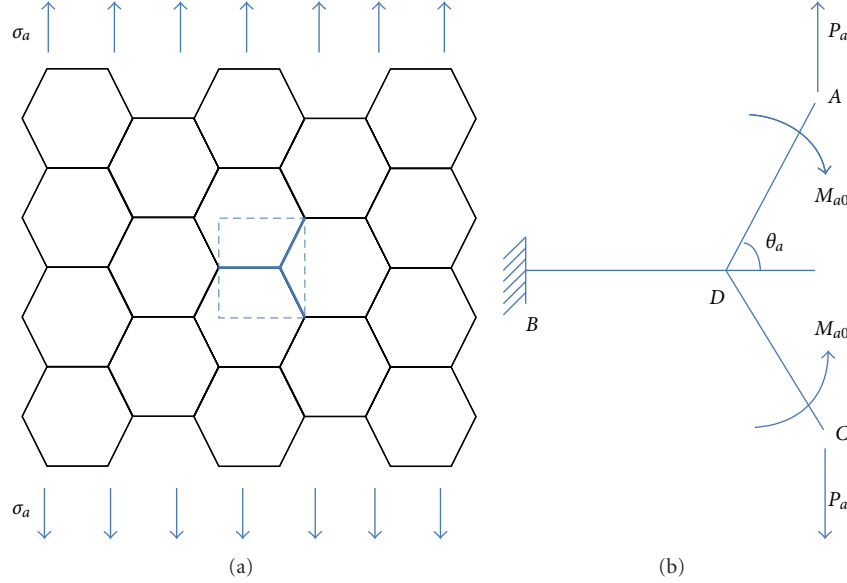


FIGURE 2: Force analysis of armchair graphite sheet unit subjected to axial tension loading.

where EA is the tensile resistance of beam (C–C bonds), EI is the flexural rigidity, GJ is the torsional stiffness, and Δl , $\Delta\theta$, and $\Delta\phi$ are the axial stretching deformation, the rotational angle at the end of the beam, and the relative rotation between the ends of the beam, respectively.

Based on energy conservation law, a linkage between the force constants in molecular mechanics and the sectional stiffness parameters in structural mechanics is established. Equations (4) and (5) are equal to each others in one-to-one corresponding directions. The direct relationship between the structural mechanics parameters and the molecular mechanics parameters is deduced as follows:

$$EA = L_{CC}k_r, \quad EI = L_{CC}k_\theta, \quad GJ = L_{CC}k_\tau. \quad (6)$$

As long as the force constants k_r , k_θ , and k_τ are known, the sectional stiffness parameters EA , EI , and GJ can be determined, then the deformation and elastic behavior of CNTs at atomic scale can be modeled. By further analysis of (4) and (5), three more constants of C–C bonds D (diameter of C–C bonds), E , and G depend on k_r , k_θ , and k_τ :

$$D = 4\sqrt{\frac{k_\theta}{k_r}}, \quad E = \frac{k_r^2 L_{CC}}{4\pi k_\theta}, \quad G = \frac{k_r^2 k_\tau L_{CC}}{8\pi k_\theta^2}. \quad (7)$$

3.1. Young's Modulus for Armchair Graphite Sheet. Knowledge of Young's modulus (E) is the first step towards the material using as a structural element for various applications. SWCNTs can be regarded as a two-dimensional continuum shell which is composed of discrete molecular structures linked by C–C bonds. The unrolled graphite sheet of armchair SWCNTs is shown in Figure 2. Figure 2(b) plots the smallest unit of armchair graphite sheet, in which the force P_a and moment M_{a0} are displayed. The unit of armchair graphite sheet can be analyzed based on solid mechanics, and the unit along BD bond is symmetry of both structure and

force. Therefore, in terms of the elastic deformation energy, the energy of an armchair unit is written as

$$W_a = \frac{(P_a \sin \theta_a)^2 \times l_a}{2EA} + \int_0^{l_a} \frac{(P_a x \cos \theta_a - M_{a0})^2}{2EI} dx, \quad (8)$$

where E is Young's modulus of beam and l_a is the C–C bonds of armchair graphite sheet. When the relationship between force P_a and moment M_{a0} is determined, the strain of the unit can be resolved by using energy W_a .

According to Castigliano's Law, the rotation angel on point C is zero due to symmetry of structure and force that is shown in

$$\theta_{ac} = \frac{\partial W_a}{\partial M_{a0}} = 0. \quad (9)$$

Substituting (8) into (9), the relationship between force P_a and moment M_{a0} is obtained:

$$M_{a0} = \frac{P_a l_a}{2} \cos \theta_a. \quad (10)$$

Meanwhile, the elastic deformation energy W_a is rewritten as follows:

$$W_a = \frac{P_a^2 l_a \sin^2 \theta_a}{2EA} + \frac{P_a^2 l_a^3 \cos^2 \theta_a}{24EI}. \quad (11)$$

Based on Castigliano's law, the displacement of the unit is defined by the elastic deformation energy differential

$$\delta_a = \frac{\partial W_a}{\partial P_a} = \frac{P_a l_a \sin^2 \theta_a}{EA} + \frac{P_a l_a^3 \cos^2 \theta_a}{12EI}, \quad (12)$$

and the strain of armchair graphite sheet is defined as follows:

$$\varepsilon_a = \frac{\delta_a}{l_a \sin \theta_a}. \quad (13)$$

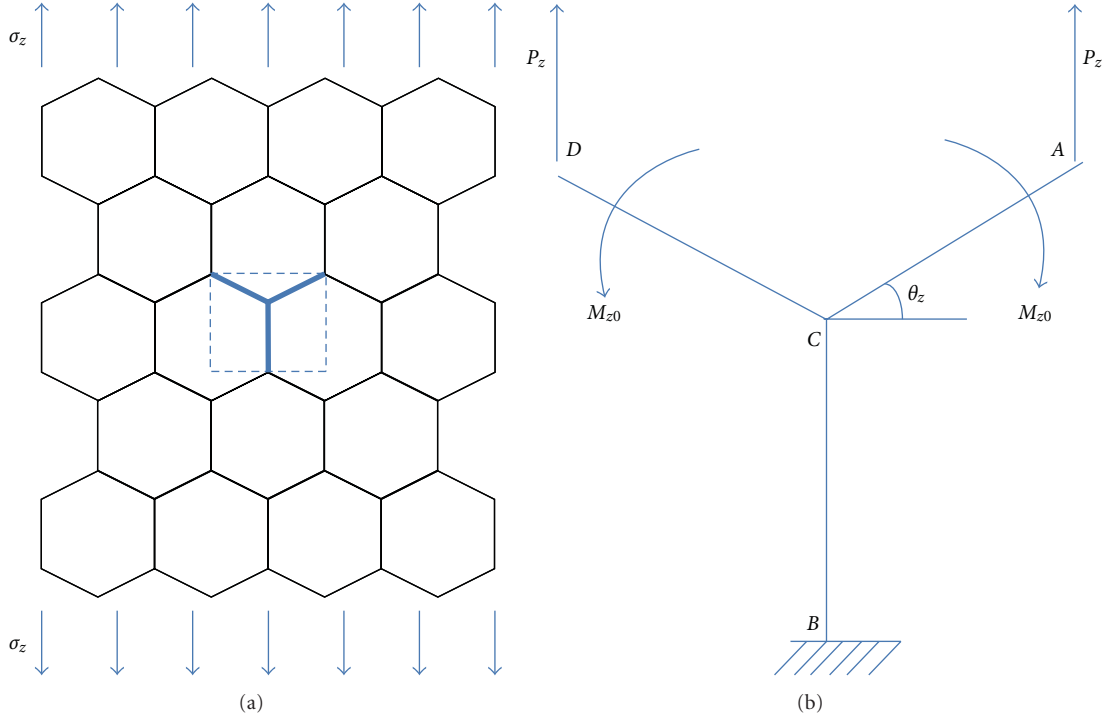


FIGURE 3: Force analysis of zigzag graphite sheet unit subjected to axial tension loading.

For an armchair graphite sheet being subjected to the tension stress σ_a , the equation of static equilibrium of the unit is expressed as

$$\sigma_a t l_a (1 + \cos \theta_a) = P_a. \quad (14)$$

Based on Hooke's law, the relationship of the tension stress and the strain is

$$\sigma_a = E_a \varepsilon_a. \quad (15)$$

When $\theta_a = 60^\circ$, Young's modulus of armchair graphite sheet E_a yields

$$E_a = \frac{\sqrt{3}E}{t} \left(\frac{9l_a}{4A} + \frac{l_a^3}{16I} \right)^{-1}, \quad (16)$$

where t is the thickness of the graphite sheet.

3.2. Young's Modulus for the Zigzag Graphite Sheet. For a zigzag graphite sheet, the analytical approach is similar to that of the armchair graphite sheet. The unit of a zigzag graphite sheet is drawn in Figure 3, and the energy of the unit is drawn in

$$W_z = \frac{P_z^2 l_z}{EA} (\sin^2 \theta_z + 2) + \frac{P_z^2 l_z^3 \cos^2 \theta_z}{12EI}, \quad (17)$$

where l_a is the C-C bonds of the zigzag graphite sheet. The displacement of the zigzag unit is defined as

$$\delta_z = \frac{P_z l_z}{EA} (\sin^2 \theta_z + 2) + \frac{P_z l_z^3 \cos^2 \theta_z}{12EI}. \quad (18)$$

Then the strain of per unit length is obtained as follows:

$$\varepsilon_z = \frac{\delta_z}{l_z (\sin \theta_z + 1)}. \quad (19)$$

For a zigzag graphite sheet being subjected to the tension stress σ_z , the force acting on the unit can be written as

$$\sigma_z t d \cos \theta_z = P_z. \quad (20)$$

When $\theta_z = 30^\circ$, we can obtain Young's modulus E_z of zigzag graphite sheet:

$$E_z = \frac{\sqrt{3}E}{t} \left(\frac{9l_z}{4A} + \frac{l_z^3}{16I} \right)^{-1}. \quad (21)$$

4. Molecular Mechanics Model of SWCNTs

SWCNTs can be ideally constructed starting from a graphite sheet. According to the chiral vector, there are three kinds of structure, as shown in Figure 4. After the two-dimensional sheets are rolled into a three-dimensional tube, intrinsic properties of the structure will be changed, such as mechanical and physical characteristics.

4.1. Angle Measurement for SWCNTs. Figure 4(a) shows an armchair SWCNT. According to (2) the radius of armchair SWCNTs is $r_{\text{acnt}} = 3n \cdot L_{\text{CC}} / 2\pi$. Meanwhile, by geometric

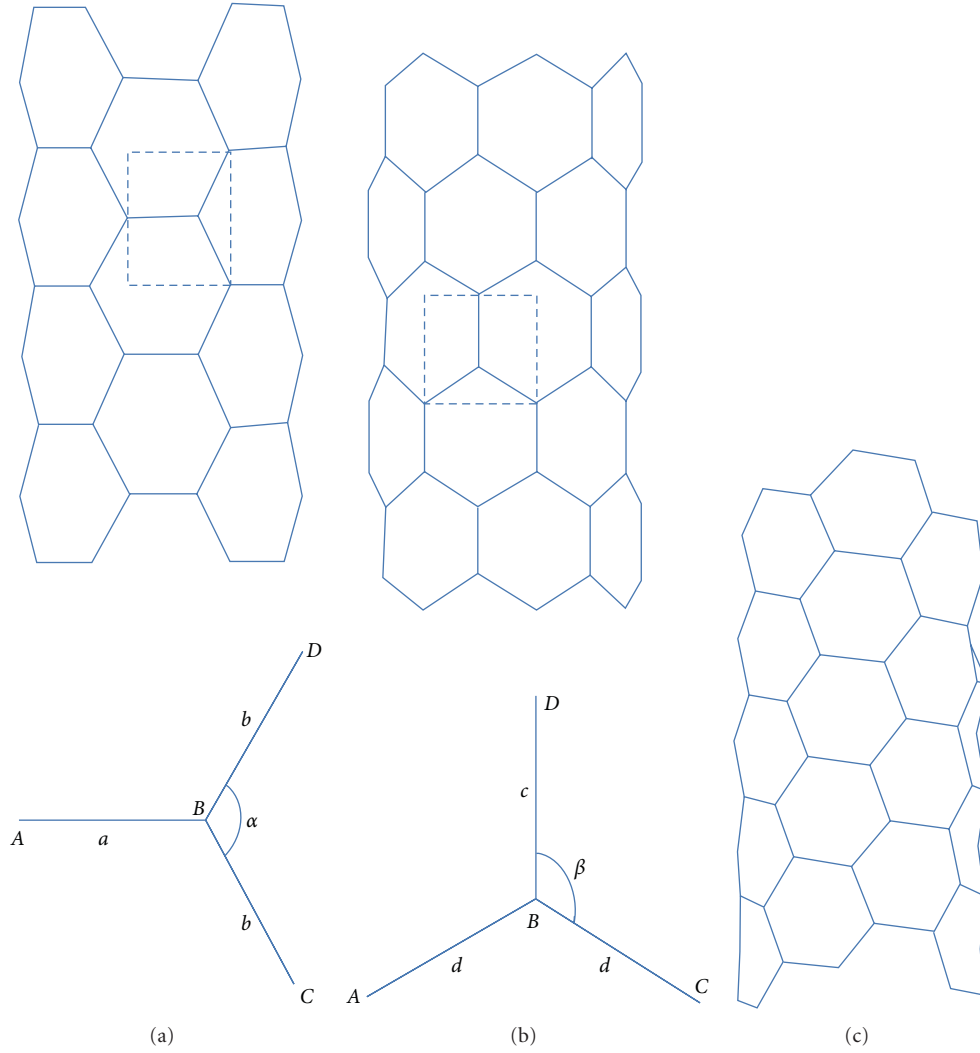


FIGURE 4: Classification of SWCNTs by chiral vector and chiral angle (a) armchair SWCNT, (b) zigzag SWCNT, and (c) chiral SWCNT.

relationships in cylindrical coordinates shown in Figure 4(a), we obtain the coordinates of carbon atoms:

$$\begin{aligned}
 A &= (r_{\text{acnt}}, 0, 0), \\
 B &= \left(r_{\text{acnt}} \cos \frac{2\pi}{3n}, r_{\text{acnt}} \sin \frac{2\pi}{3n}, 0 \right), \\
 C &= \left(r_{\text{acnt}} \cos \frac{\pi}{n}, r_{\text{acnt}} \sin \frac{\pi}{n}, -\frac{\sqrt{3}}{2} L_{\text{CC}} \right), \\
 D &= \left(r_{\text{acnt}} \cos \frac{\pi}{n}, r_{\text{acnt}} \sin \frac{\pi}{n}, \frac{\sqrt{3}}{2} L_{\text{CC}} \right).
 \end{aligned} \quad (22)$$

Because of the effect of curvature, the lengths of the bonds between carbon atoms in vector space are shorter than those in plane and characterized in different numerical

values, which are displayed in Figure 4(a) and given as follows:

$$\begin{aligned}
 a &= |\vec{BA}| = \frac{3n}{2\pi} \sqrt{2 - 2 \cos \frac{2\pi}{3n}} L_{\text{CC}}, \\
 b &= |\vec{BD}| = |\vec{BC}| = \frac{3n}{2\pi} \sqrt{2 - 2 \cos \frac{\pi}{3n} + \frac{\pi^2}{3n^2}} L_{\text{CC}}.
 \end{aligned} \quad (23)$$

In cylindrical coordinates, on account of the curvature, the included angles between the adjacent bonds in a carbon cycle of SWCNTs are different from those of graphite sheets. In accordance with geometrical relationships, the included angle between the adjacent bonds for an arbitrary unit of armchair SWCNTs plotted in Figure 4(a) relates with coordinate figures of carbon atoms in the unit:

$$\cos \alpha = \frac{\vec{BD} \cdot \vec{BC}}{|\vec{BD}| |\vec{BC}|}. \quad (24)$$

Substituting (23) into (24), we obtain the included angle of armchair SWCNTs

$$\alpha = \cos^{-1} \left(\frac{6n^2(1 - \cos \pi/3n) - \pi^2}{6n^2(1 - \cos \pi/3n) + \pi^2} \right). \quad (25)$$

Figure 4(b) shows a zigzag SWCNT. According to (2) the radius of zigzag SWCNTs is $r_{\text{zcnt}} = \sqrt{3}n \cdot L_{\text{CC}}/2\pi$. Considering geometric relationships in cylindrical coordinates, the coordinate figures are described as

$$\begin{aligned} A &= (r_{\text{zcnt}}, 0, 0), \\ B &= \left(r_{\text{zcnt}} \cos \frac{\pi}{n}, r_{\text{zcnt}} \sin \frac{\pi}{n}, \frac{1}{2}L_{\text{CC}} \right), \\ C &= \left(r_{\text{zcnt}} \cos \frac{2\pi}{n}, r_{\text{zcnt}} \sin \frac{2\pi}{n}, 0 \right), \\ D &= \left(r_{\text{zcnt}} \cos \frac{\pi}{n}, r_{\text{zcnt}} \sin \frac{\pi}{n}, \frac{3}{2}L_{\text{CC}} \right). \end{aligned} \quad (26)$$

The distances of the bonds in vector space are as follows:

$$\begin{aligned} c &= \left| \vec{BD} \right| = L_{\text{CC}}, \\ d &= \left| \vec{BA} \right| = \left| \vec{BC} \right| = \frac{\sqrt{3}n}{2\pi} \sqrt{2 - 2 \cos \frac{\pi}{n} + \frac{\pi^2}{3n^2} L_{\text{CC}}}. \end{aligned} \quad (27)$$

For zigzag SWCNTs, the analysis method resembles armchair SWCNTs; we calculate the included angle for zigzag SWCNTs as follows:

$$\beta = \cos^{-1} \left(\frac{-\pi}{\sqrt{6n^2(1 - \cos \pi/n) + \pi^2}} \right). \quad (28)$$

4.2. Elastic Properties for SWCNTs. Considering space curvature, Young's modulus of SWCNTs in cylindrical coordinates depends on bond length and included angle between two bonds. The method for calculating Young's modulus of armchair SWCNTs in three-dimensions resembles that in two dimensions. Affecting factors in three dimensional coordinates of Young's modulus of armchair SWCNTs are mentioned in (23) and (25); Young's modulus of armchair SWCNTs is expressed in

$$E_{\text{acnt}} = \xi \lambda_a \left(k_{a1} \frac{1}{A} + k_{a2} \frac{1}{12I} \right)^{-1}, \quad (29)$$

where $\xi = (E/t)$, $\lambda_a = \sin(\alpha/2)/a + b \cos(\alpha/2)$, $k_{a1} = \sin^2 \alpha/2$, and $k_{a2} = b^2 \cos^2 \alpha/2$.

We obtain Young's modulus of zigzag SWCNTs given in the following in the same way

$$E_{\text{zcnt}} = \xi \lambda_z \left(k_{z1} \frac{1}{A} + k_{z2} \frac{1}{12I} \right)^{-1}, \quad (30)$$

where $\lambda_z = (d \sin(\beta - (\pi/2)) + c)/(d \cos(\beta - (\pi/2)))$, $k_{z1} = d \sin^2(\beta - (\pi/2)) + 2c$, and $k_{z2} = \cos^2(\beta - (\pi/2))d^3$.

4.3. Poisson's Ratio for SWCNTs. For armchair SWCNTs, the stretch deformations of the bonds caused by concentrated force and bending moment are schematically signed in Figure 5(a) to analyze Poisson's ratio. The equilibrium of force P_a and bending moment M_a can be computed from Figure 5(a)

$$2M_a = P_a b \sin \frac{\alpha}{2}. \quad (31)$$

According to geometric properties and elastic theory, taking the included angle between two bonds in three dimensions into consideration, we obtain the equilibrium equations about extension variation of the C-C bonds

$$\begin{aligned} \delta_a^{P1} &= \frac{P_a \sin \alpha/2}{EA}, \\ \delta_a^{P2} &= \frac{P_a b^3 \cos \alpha/2}{3EI}, \\ \delta_a^M &= -\frac{M_a b^2 \cos \alpha/2}{2EI}, \end{aligned} \quad (32)$$

where EA and EI are the tensile resistance and the flexural rigidity of beam, and δ_a^{P1} , δ_a^{P2} , and δ_a^M are the deformations of beam caused by force P_a and bending moment M_a , respectively. The strains in axial direction and circumferential direction are defined as follows, respectively:

$$\begin{aligned} \epsilon_{a1} &= \frac{\delta_a^{P1} \cos(\alpha/2) - (\delta_a^{P2} + \delta_a^M) \sin \alpha/2}{a + b \cos \alpha/2}, \\ \epsilon_{a2} &= \frac{\delta_a^{P1} \sin(\alpha/2) + (\delta_a^{P2} + \delta_a^M) \cos \alpha/2}{b \sin \alpha/2}. \end{aligned} \quad (33)$$

Poisson's ratio of armchair SWCNTs can be defined as the ratio between circumferential strain, and axial strain, substituting (31) and (32) into (33) we can get Poisson's ratio of armchair SWCNTs

$$\nu_a = \frac{\epsilon_{a1}}{\epsilon_{a2}} = -\frac{(12I - Ab^3) \sin^2(\alpha/2) \cos(\alpha/2)}{(12I \sin^2(\alpha/2) + Ab^3 \cos^2 \alpha/2)((a/b) + \cos \alpha/2)}. \quad (34)$$

For zigzag SWCNTs, the analysis step is similar to that for armchair SWCNTs. To analyze Poisson's ratio of zigzag SWCNTs, Figure 5(b) schematically signs the stretch deformations of the bonds caused by force P_z and bending moment M_z ; the relationship of force and bending moment is given in

$$2M_z = P_z b \sin \frac{\alpha}{2}. \quad (35)$$

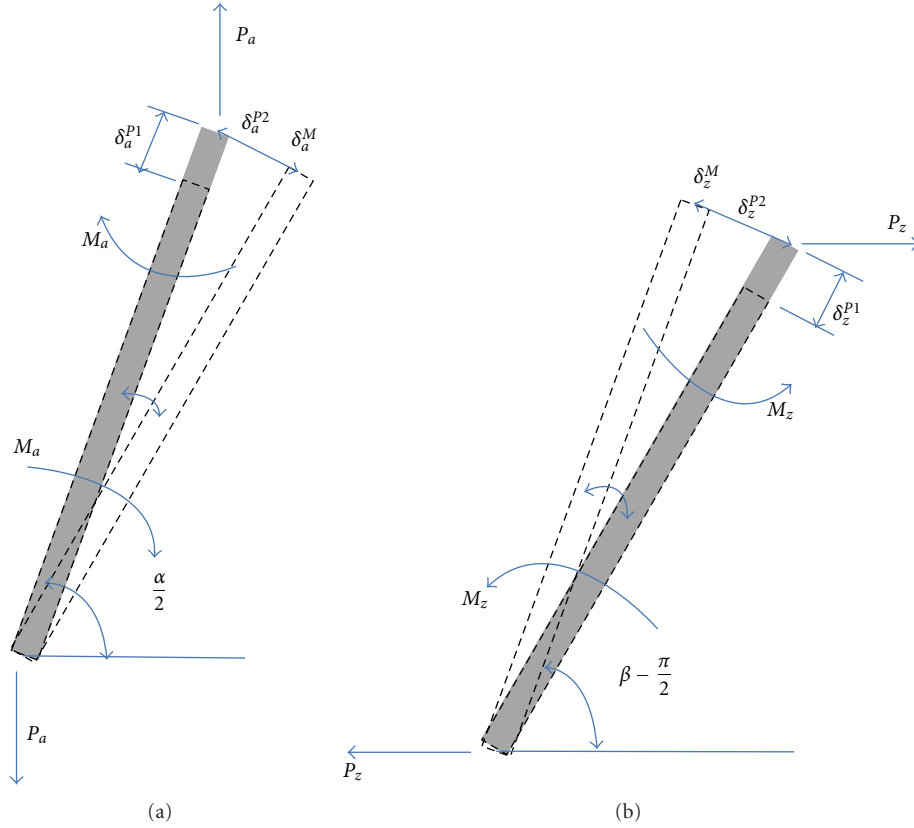


FIGURE 5: Analysis of axial deformation and angular displacement of armchair and zigzag SWCNTs.

The equilibrium equations about extension variation of the bond are described as

$$\begin{aligned}
 \delta_z^{P1} &= \frac{P_z \sin(\beta - (\pi/2))}{EA}, \\
 \delta_z^{P2} &= \frac{P_z d^3 \cos(\beta - (\pi/2))}{3EI}, \\
 \delta_z^{P3} &= \frac{2P_z \sin(\beta - (\pi/2))}{EA}, \\
 \delta_z^M &= -\frac{M_z d^2 \cos(\beta - (\pi/2))}{2EI}.
 \end{aligned} \quad (36)$$

The strains in axial direction and circumferential direction are defined as follows, respectively:

$$\begin{aligned}
 \varepsilon_{z1} &= \frac{\delta_z^{P1} \cos(\beta - (\pi/2)) - (\delta_z^{P2} + \delta_z^M) \sin(\beta - (\pi/2))}{d \cos(\pi - \beta)}, \\
 \varepsilon_{z2} &= \frac{\delta_z^{P1} \sin(\beta - (\pi/2)) + (\delta_z^{P2} + \delta_z^M) \cos(\beta - (\pi/2)) + \delta_z^{P3}}{c + d \sin(\pi - \beta)}.
 \end{aligned} \quad (37)$$

Poisson's ratio of armchair SWCNTs can be defined as the ratio between circumferential strain and axial strain; then we obtain

$$\begin{aligned}
 \nu_z &= \frac{\varepsilon_{z1}}{\varepsilon_{z2}} \\
 &= \frac{(12I - Ab^3)((c/d) + \sin(\beta - (\pi/2))) \sin(\beta - (\pi/2))}{(12I \sin^2(\beta - (\pi/2)) + Ad^3 \cos^2(\beta - (\pi/2)) + 24A)}.
 \end{aligned} \quad (38)$$

5. Results and Discussions

The atomic-based continuum mechanic approach described in the previous section was implemented for studying the effective elastic properties of graphite sheets and SWCNTs. In this section, the mechanical characteristics of graphite sheet and SWCNTs are examined.

5.1. Mechanics Model of Graphite Sheet. In the present simulation, $k_r/2 = 46\,900$ kcal/mole/nm², $k_\theta/2 = 63$ kcal/mole/rad² and $k_t/2 = 20$ kcal/mole/rad², are taken [34]. L_{CC} and t are 0.142 nm and 0.34 nm, respectively. According to (6) and (7), the constants of beam are obtained and summarized in Table 1. Comparing the evaluated elastic moduli of graphite sheets with the literature results, Tserpes [8] and Kalamkarov [9] reported $E = 5.49$ TPa and

TABLE 1: Geometrical and material properties of C–C bonds.

Beam element	Abbreviation	Value	Unit
Diameter	D	0.146	nm
Cross-section area	A	1.678×10^{-2}	nm^2
Moment of inertia	I	2.241×10^{-5}	nm^4
Young's modulus	E	5.530	TPa
Shear elastic modulus	G	0.871	TPa

$G = 0.871$ TPa, $E = 5.488$ TPa and $G = 0.8711$ TPa of C–C bonds, respectively.

Comparing (16) to (21), Young's moduli of the armchair graphite sheet and the zigzag graphite sheet have the same expression form except for l_a and l_z . Because the carbon cycle is a regular hexagon, graphite sheets have $l_a = l_z = L_{CC}$. We obtain Young's moduli of both armchair and zigzag graphite sheets as 1.0424 TPa, which is close to the value of 1.033 TPa calculated by Li and Chou [31] and the value of 1.04 TPa computed by Shokrieh and Rafiee [11]. It can be seen that the predicted values obtained from the model at the atomic scale agree well with those reported in the literatures.

5.2. Molecular Mechanics Model of SWCNTs. Since SWCNTs are defined as rolled graphite sheets, the lengths of bonds in vector space are changed owing to the effect of curvature. For armchair SWCNTs rolled by armchair graphite sheets, all of the lengths of C–C bonds become shorter because of the connection with curvature in circumferential direction, while, for zigzag SWCNTs rolled by zigzag graphite sheet, the length c is only in vertical direction equal to the C–C bonds length of graphite sheets. According to (23) and (27), the variation of C–C bonds lengths with radius are shown in Figure 6. With increasing radius of SWCNTs, the bond lengths a , b , and d approach to the length $c = 0.142$ nm which is the bond length of graphite itself, owing to the curvature approaching to zero in infinite radius.

When graphite sheets are rolled into SWCNTs, the lengths and spatial relations of C–C bonds change obviously. Figure 7 shows the variation of included angles of two adjacent C–C bonds with radius according to (25) and (28). It expresses that the included angles are quite sensitive to SWCNTs in small radius. The included angle of zigzag SWCNTs is a little larger than that of armchair SWCNTs in the same radius. As being larger than 1.1 nm, the radius makes less influence on the included angles of both armchair and zigzag SWCNTs, and the two lines show a tendency to be 120 degree which is close to that of graphite sheets, due to the SWCNTs being regarded as graphite sheet when radius is infinite.

Comparing (29) to (30), Young's moduli of armchair and zigzag SWCNTs have the same expression form except for coefficients λ_a , k_{a1} , k_{a2} and λ_z , k_{z1} , k_{z2} . As the two Young's moduli shown in Figure 8, Young's moduli predicted by the present theory decrease monotonically with the increase of radius. Young's modulus of armchair SWCNTs is slightly higher than that of zigzag SWCNTs with the same smaller

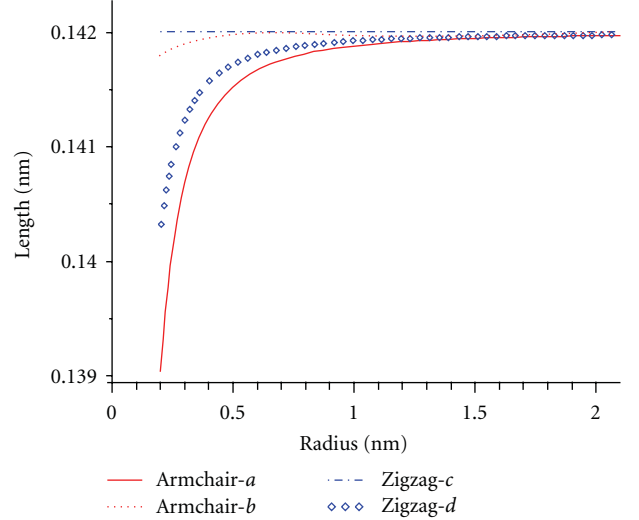


FIGURE 6: C–C bonds lengths of armchair SWCNTs and zigzag SWCNTs.

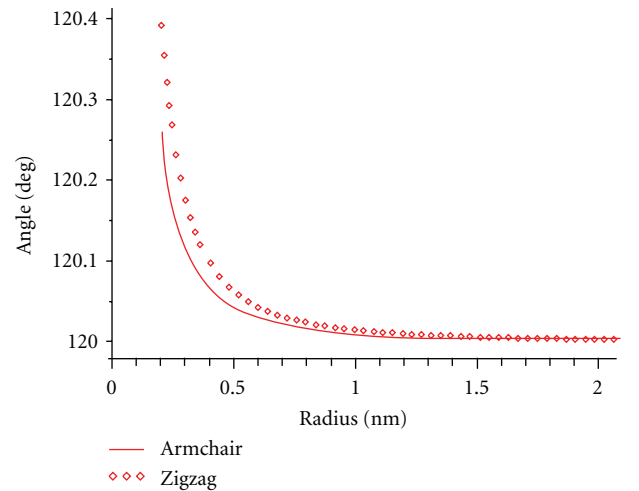


FIGURE 7: Included angles of adjacent C–C bonds in armchair SWCNTs and zigzag SWCNTs.

radius. When the radius is larger, the two declining curves gradually develop into horizontal lines, which tend to be a constant of 1.0424 TPa. The value is Young's modulus of graphite sheet.

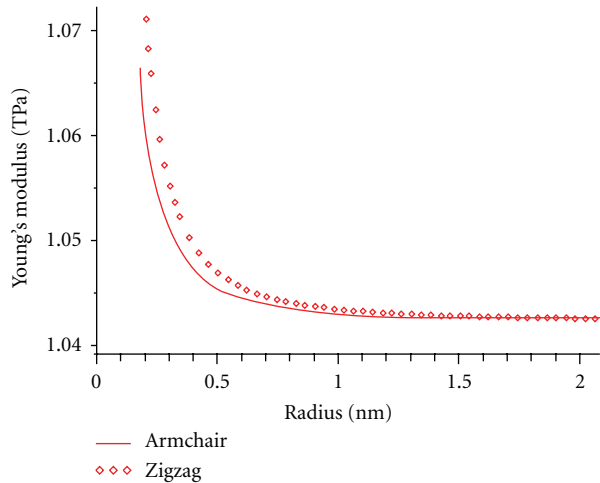


FIGURE 8: Young's modulus of armchair SWCNTs and zigzag SWCNTs.

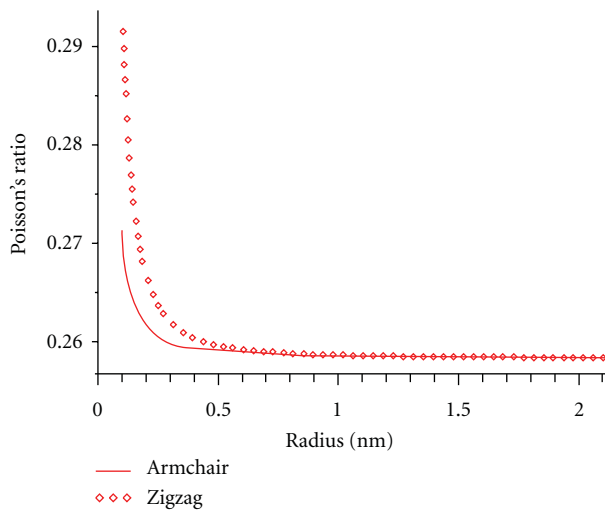


FIGURE 9: Poisson's ratio of armchair SWCNTs and zigzag SWCNTs.

Considering the variations of length and included angles of two adjacent C–C bonds, from graphite sheets into SWCNTs, Figure 9 shows the variations of Poisson's ratio of the armchair and zigzag SWCNTs as a function of nanotube radius. It is found that, in general, Poisson's ratio of armchair SWCNTs is slightly higher than that of zigzag SWCNTs. Poisson's ratios of armchair and zigzag SWCNTs show a smoothly monotonic decreasing versus increasing radius. When the radius of SWCNTs is larger, the two curves tend to be a straight line which means that Poisson's ratios approach to be a steady value of 0.26, which makes a great agreement with those reported in the literatures [6, 33].

6. Conclusions

The mechanical properties of both armchair and zigzag SWCNTs are characterized by using continuum mechanics

in the atomic scale. In terms of the conjunction of Tersoff-Brenner force field method and energy conservation law, the graphite sheet is of isotropic property and Young's modulus of graphite sheet is obtained to be 1.04 TPa. Furthermore, considering the variations of the length and the included angle of two adjacent C–C bonds rolled from graphite sheets into SWCNTs, Young's modulus and Poisson's ratio of SWCNTs with armchair and zigzag structures are investigated as a function of SWCNT radius. We predict that Young's modulus and Poisson's ratio of SWCNTs are influenced obviously by relatively smaller radius while being little affected by larger radius. We are confident that this model provides a useful method to analyze mechanical properties of CNTs and other nanosized structures at the atomic scale.

Acknowledgment

This work was supported by Grant-in-Aid for Global COE Program by the Ministry of Education, Culture, Sports, Science and Technology.

References

- [1] S. Iijima, "Helical microtubules of graphitic carbon," *Nature*, vol. 354, no. 6348, pp. 56–58, 1991.
- [2] F. Li, H. M. Cheng, S. Bai, G. Su, and M. S. Dresselhaus, "Tensile strength of single-walled carbon nanotubes directly measured from their macroscopic ropes," *Applied Physics Letters*, vol. 77, no. 20, pp. 3161–3163, 2000.
- [3] W. H. Chen, H. C. Cheng, and Y. L. Liu, "Radial mechanical properties of single-walled carbon nanotubes using modified molecular structure mechanics," *Computational Materials Science*, vol. 47, pp. 985–993, 2010.
- [4] Z. Spitalskya, D. Tasisb, K. Papagelisb, and C. Galiotis, "Carbon nanotube—polymer composites: chemistry, processing, mechanical and electrical properties," *Progress in Polymer Science*, vol. 35, pp. 357–401, 2010.
- [5] M. A. L. Manchado, L. Valentini, J. Biagiotti, and J. M. Kenny, "Thermal and mechanical properties of single-walled carbon nanotubes-polypropylene composites prepared by melt processing," *Carbon*, vol. 43, no. 7, pp. 1499–1505, 2005.
- [6] T. Natsuki, K. Tantrakarn, and M. Endo, "Effects of carbon nanotube structures on mechanical properties," *Applied Physics A*, vol. 79, no. 1, pp. 117–124, 2004.
- [7] M. R. Falvo, G. J. Clary, R. M. Taylor II et al., "Bending and buckling of carbon nanotubes under large strain," *Nature*, vol. 389, no. 6651, pp. 582–584, 1997.
- [8] K. I. Tserpes and P. Papanikos, "Finite element modeling of single-walled carbon nanotubes," *Composites Part B*, vol. 36, no. 5, pp. 468–477, 2005.
- [9] A. L. Kalamkarov, A. V. Georgiades, S. K. Rokkam, V. P. Veedu, and M. N. Ghasemi-Nejhad, "Analytical and numerical techniques to predict carbon nanotubes properties," *International Journal of Solids and Structures*, vol. 43, no. 22–23, pp. 6832–6854, 2006.
- [10] O. L. Blakslee, D. G. Proctor, E. J. Seldin, G. B. Spence, and T. Weng, "Elastic constants of compression-annealed pyrolytic graphite," *Journal of Applied Physics*, vol. 41, no. 8, pp. 3373–3382, 1970.

- [11] M. M. Shokrieh and R. Rafiee, "Prediction of Young's modulus of graphene sheets and carbon nanotubes using nanoscale continuum mechanics approach," *Materials and Design*, vol. 31, no. 2, pp. 790–795, 2010.
- [12] K. N. Kudin, G. E. Scuseria, and B. I. Yakobson, " C_2F , BN, and C nanoshell elasticity from *ab initio* computations," *Physical Review B*, vol. 64, no. 23, Article ID 235406, 10 pages, 2001.
- [13] O. Lourie and H. D. Wagner, "Evaluation of Young's modulus of carbon nanotubes by micro-Raman spectroscopy," *Journal of Materials Research*, vol. 13, no. 9, pp. 2418–2422, 1998.
- [14] M. M. J. Treacy, T. W. Ebbesen, and J. M. Gibson, "Exceptionally high Young's modulus observed for individual carbon nanotubes," *Nature*, vol. 381, no. 6584, pp. 678–680, 1996.
- [15] J.-P. Salvetat, J.-M. Bonard, N. B. Thomson et al., "Mechanical properties of carbon nanotubes," *Applied Physics A*, vol. 69, no. 3, pp. 255–260, 1999.
- [16] N. Yao and V. Lordi, "Young's modulus of single-walled carbon nanotubes," *Journal of Applied Physics*, vol. 84, no. 4, pp. 1939–1943, 1998.
- [17] P. M. Ajayan, O. Stephan, C. Colliex, and D. Trauth, "Aligned carbon nanotube arrays formed by cutting a polymer resin-nanotube composite," *Science*, vol. 265, no. 5176, pp. 1212–1214, 1994.
- [18] P. Poncharal, Z. L. Wang, D. Ugarte, and W. A. de Heer, "Electrostatic deflections and electromechanical resonances of carbon nanotubes," *Science*, vol. 283, no. 5407, pp. 1513–1516, 1999.
- [19] M. R. Falvo, G. J. Clary, R. M. Taylor II et al., "Bending and buckling of carbon nanotubes under large strain," *Nature*, vol. 389, no. 6651, pp. 582–584, 1997.
- [20] E. W. Wong, P. E. Sheehan, and C. M. Lieber, "Nanobeam mechanics: elasticity, strength, and toughness of nanorods and nanotubes," *Science*, vol. 277, no. 5334, pp. 1971–1975, 1997.
- [21] J.-P. Salvetat, A. J. Kulik, J.-M. Bonard et al., "Elastic modulus of ordered and disordered multiwalled carbon nanotubes," *Advanced Materials*, vol. 11, no. 2, pp. 161–165, 1999.
- [22] F. Ding, "Theoretical study of the stability of defects in single-walled carbon nanotubes as a function of their distance from the nanotube end," *Physical Review B*, vol. 72, Article ID 245409, 7 pages, 2005.
- [23] K. M. Liew, C. H. Wong, X. Q. He, M. J. Tan, and S. A. Meguid, "Nanomechanics of single and multiwalled carbon nanotubes," *Physical Review B*, vol. 69, no. 11, Article ID 115429, 8 pages, 2004.
- [24] V. U. Unnikrishnan, D. Banerjee, and J. N. Reddy, "Atomistic-mesoscale interfacial resistance based thermal analysis of carbon nanotube systems," *International Journal of Thermal Sciences*, vol. 47, no. 12, pp. 1602–1609, 2008.
- [25] Y. Zhou, M. A. Baseer, H. Mahfuz, and S. Jeelani, "Monte Carlo simulation on tensile failure process of unidirectional carbon fiber reinforced nano-phased epoxy," *Materials Science and Engineering A*, vol. 420, no. 1-2, pp. 63–71, 2006.
- [26] G. Overney, W. Zhong, and D. Tománek, "Structural rigidity and low frequency vibrational modes of long carbon tubules," *Zeitschrift für Physik D*, vol. 27, no. 1, pp. 93–96, 1993.
- [27] J. P. Lu, "Elastic properties of single and multilayered nanotubes," *Journal of Physics and Chemistry of Solids*, vol. 58, no. 11, pp. 1649–1652, 1997.
- [28] B. I. Yakobson, C. J. Brabec, and J. Bernholc, "Nanomechanics of carbon tubes: instabilities beyond linear response," *Physical Review Letters*, vol. 76, pp. 2511–2514, 1996.
- [29] J. P. Lu, "Elastic properties of carbon nanotubes and nanoropes," *Physical Review Letters*, vol. 79, no. 7, pp. 1297–1300, 1997.
- [30] S. A. Meguid, J. M. Wernik, and Z. Q. Cheng, "Atomistic-based continuum representation of the effective properties of nano-reinforced epoxies," *The International Journal of Solids and Structures*, vol. 47, pp. 1723–1736, 2010.
- [31] C. Li and T.-W. Chou, "A structural mechanics approach for the analysis of carbon nanotubes," *The International Journal of Solids and Structures*, vol. 40, no. 10, pp. 2487–2499, 2003.
- [32] J.-L. Tsai, S.-H. Tzeng, and Y.-T. Chiu, "Characterizing elastic properties of carbon nanotubes/polyimide nanocomposites using multi-scale simulation," *Composites Part B*, vol. 41, pp. 106–115, 2009.
- [33] T. Natsuki, K. Tantrakarn, and M. Endo, "Prediction of elastic properties for single-walled carbon nanotubes," *Carbon*, vol. 42, no. 1, pp. 39–45, 2004.
- [34] W. D. Cornell, P. Cieplak, C. I. Bayly et al., "A second generation force field for the simulation of proteins, nucleic acids, and organic molecules," *Journal of the American Chemical Society*, vol. 117, no. 19, pp. 5179–5197, 1995.

Research Article

Some Observations on Carbon Nanotubes Susceptibility to Cell Phagocytosis

Aneta Fraczek-Szczypta,¹ Elzbieta Menaszek,^{1,2} and Stanislaw Blazewicz¹

¹ Department of Biomaterials, Faculty of Materials Science and Ceramics, AGH-University of Science and Technology, al Mickiewicza 30, 30-059 Krakow, Poland

² Department of Cytobiology, Collegium Medicum, Jagiellonian University, Medyczna 9, 30-068 Krakow, Poland

Correspondence should be addressed to Aneta Fraczek-Szczypta, afraczek@agh.edu.pl

Received 30 September 2010; Accepted 30 December 2010

Academic Editor: Xiaojun Yu

Copyright © 2011 Aneta Fraczek-Szczypta et al. This is an open access article distributed under the Creative Commons Attribution License, which permits unrestricted use, distribution, and reproduction in any medium, provided the original work is properly cited.

The aim of this study was to assess the influence of different types of carbon nanotubes (CNTs) on cell phagocytosis. Three kinds of carbon nanotubes: single-walled carbon nanohorns (SWCNHs), multiwalled carbon nanotubes (MWCNTs), and ultra-long single-walled carbon nanotubes (ULSWCNTs) before and after additional chemical functionalization were seeded with macrophage cell culture. Prior to biological testing, the CNTs were subjected to dispersion process with the use of phosphate buffered solution (PBS) and PBS containing surfactant (Tween 20) or dimethyl sulfoxide (DMSO). The results indicate that the cells interaction with an individual nanotube is entirely different as compared to CNTs in the form of aggregate. The presence of the surfactant favors the CNTs dispersion in culture media and facilitates phagocytosis process, while it has disadvantageous influence on cells morphology. The cells phagocytosis is a more effective for MWCNTs and SWCNHs after their chemical functionalization. Moreover, these nanotubes were well dispersed in culture media without using DMSO or surfactant. The functionalized carbon nanotubes were easily dispersed in pure PBS and seeded with cells.

1. Introduction

Carbon nanotubes (CNTs) are being produced in increasingly large quantities for many technical and medical applications due to their novel properties, such as enhanced thermal, electronic, mechanical, and biological properties. In biological systems, they have been investigated as drug delivery vehicles, targeted cancer therapies, tissue scaffolds, and biosensors [1–3]. CNTs due to their relative large length-to-diameter aspect ratio, with a very large specific surface are suitable for highly sensitive molecular detection and recognition. Consequently, a large fraction of the CNT surface can be modified with functional groups of various complexities, which would modulate its *in vivo* and *in vitro* behaviour [4].

However, opinions about the biocompatibility of CNTs *in vitro* and *in vivo* environments are not unequivocal. Some authors indicate that CNTs are biocompatible in contact with cells and tissue, that is, they stimulate osteoblast and

nerve cells to grow and proliferate and induce muscle and blood vessels to regenerate [5–7]. Contrary to these outcomes, many critical results point to the cytotoxicity of CNTs. The toxicity of CNTs is a prime concern, and several groups point to their similarity to asbestos fibres [8]. Other scientists indicate that CNTs may lead to dermal toxicity due to accelerated oxidative stress in the skin and pulmonary toxicity through induced lung lesions characterized by the presence of granulomas [9, 10].

The question arises why the opinions about the biocompatibility of carbon nanotubes are so different?

Many scientists explain that CNTs toxicity in both *in vivo* and *in vitro* studies has been attributed to various factors, for instance, length, type of functionalization, their concentration, duration and method of exposure, catalyst impurity, agglomeration, and even the dispersants used to dissolve the nanotubes [4, 11–16]. However, most aspects of CNT toxicity remain still not properly recognized. One of the important aspects is the transport of CNTs across the

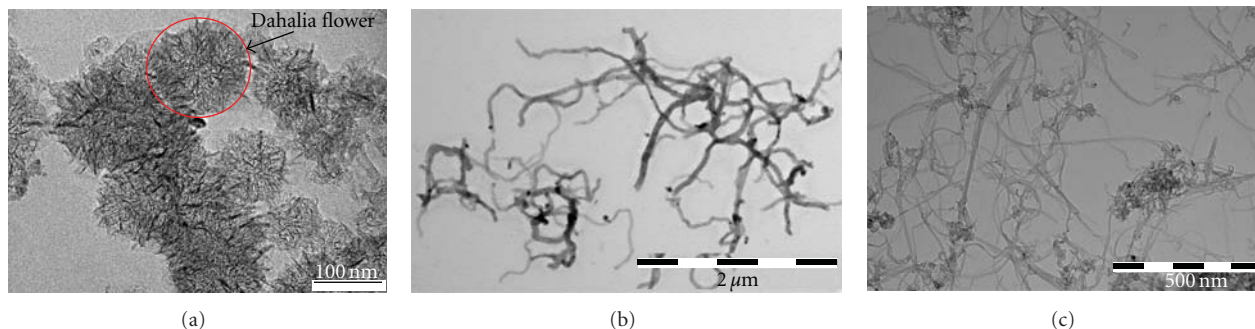


FIGURE 1: TEM microphotography of SWCNH (a), MWCNT (b), and ULSWCNT (c) before chemical functionalization.

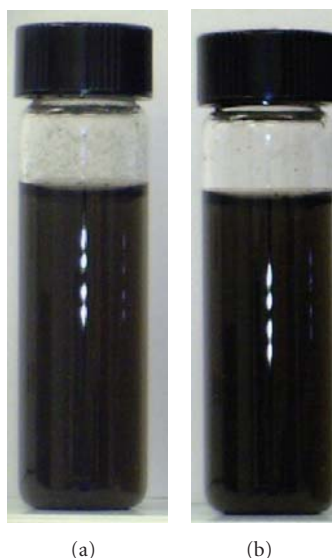


FIGURE 2: MWCNT in 10% DMSO just after dispersion (a) and 48 h later (b).

cell membrane. Two potential transport mechanisms of CNT have been considered: endocytosis/phagocytosis and energy-independent passive process [4, 17, 18].

The aim of this study is to examine the effect of dispersion degree of CNTs on cell phagocytosis process. The CNTs dispersion depends upon a number of factors, such as the type of CNTs, their geometry, the presence of surface chemical state as well as the type of surfactants. These factors are qualitatively analyzed in view of differently prepared CNTs to their susceptibility to cells response.

2. Materials and Methods

Five kinds of pristine and functionalized carbon nanotubes (CNTs) were used in this work. The pristine CNTs were provided by NanoAmor USA and NanoCraft Inc USA. The pristine carbon nanotubes used in this experiment were denoted, as follows (Figure 1):

- (i) SWCNH—single wall carbon nanohorns,
- (ii) MWCNT—multi wall carbon nanotubes,

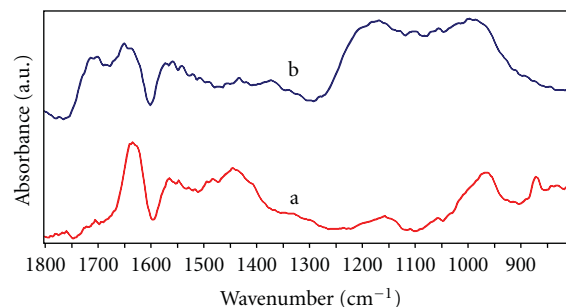


FIGURE 3: IR spectra of MWCNT (a) and MWCNT-F (b).

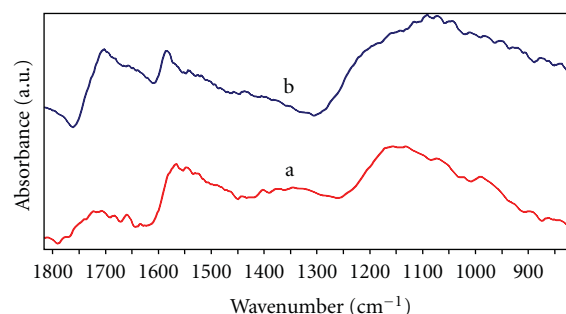


FIGURE 4: IR spectra of SWCNH (a) and SWCNH-F (b).

- (iii) ULSWCNT—ultra-long-single-wall carbon nanotubes.

The diameters of SWCNHs ranged from 2 to 3 nm and length from 30 to 50 nm, with a 19° closed-end called carbon nanohorns. Carbon nanohorns belong to the carbon nanotubes family. The tip of this tube is closed by a conical cap with a cone angle of 19°. The individual carbon nanohorns have a tendency to aggregate together and form dahlia-flower-like structured particles (Figure 1(a)). SWCNH aggregates have been regarded as potentially good drug carriers, which possess some advantages over other drug carriers [2, 19].

MWCNTs had diameters in the range of 10–30 nm and were 1–2 μm long, whereas ULSWCNTs had diameters from 0.7 to 2 nm and length from 15–30 μm.

TABLE 1: Purity of carbon nanotubes before and after chemical oxidative treatment.

Chemical oxidation	Samples	Concentration (wt.%)			
		Fe	Co	Al	Ni
Before	SWCNH	1.8	0.007	0.5	0.2
After	SWCNH-F	0.05	0.0001	0.04	0.003
Before	MWCNT	0.3	0.006	0.06	1.2
After	MWCNT-F	0.01	0.001	0.01	0.1
Before	ULSWCNT	0.003	0.8	0.02	0.002
After	ULSWCNT-F	0.0001	0.08	0.006	0.0003

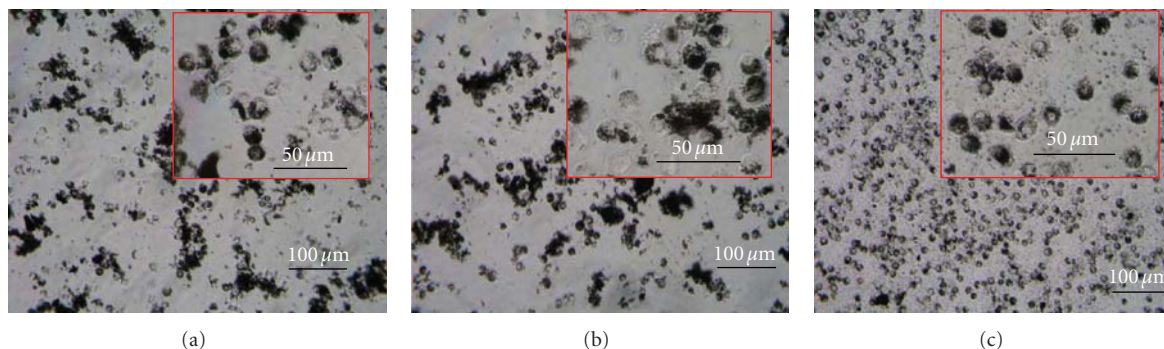


FIGURE 5: Macrophages in contact with SWCNH dispersed in PBS (a), in PBS + 1% DMSO (b), and in PBS + 1% Tween 20 (c).

A mixture of concentrated H_2SO_4 and HNO_3 with volume ratio of 3 : 1 was made for functionalization of the CNTs. They were immersed into this mixture and kept four hours at temperatures between 60°C and 70°C . The main aim of this process was the removal of metallic catalysts and chemical modification by introducing of carboxyl acid groups on the CNT surface. In this way, two types of samples were prepared

- (i) SWCNH-F—SWCNHs after chemical purification in concentrated acid,
- (ii) MWCNT-F—MWCNTs after chemical purification in concentrated acid.

CNTs were sterilized by the UV method for 0.5 h. Before incubation with cells, each type of carbon nanotubes was sonicated for 1 min using a tip sonicator (PALMER INSTRUMENTS, Model: CP 130 PB) in three different solutions:

- (i) PBS—phosphate buffered solution,
- (ii) PBS + 1% DMSO (DMSO—dimethyl sulfoxide),
- (iii) PBS + 1% Tween 20,

with a concentration of CNT $38 \mu\text{g/mL}$ (a safe concentration level of CNTs is to be around $40 \mu\text{g/mL}$) [20]. Dimethyl sulfoxide (DMSO) used in our experiments is an appropriate polar aprotic solvent that dissolves both polar and nonpolar compounds, miscible in a wide range of organic solvents as well as in water. In medicine, DMSO is predominantly used as a topical analgesic, a vehicle for topical application of pharmaceuticals, as an anti-inflammatory agent and as an antioxidant. Because DMSO enhances the rate of absorption

of some compounds through organic tissues including skin, it can be used as a drug delivery system. This solvent has acceptable biological properties, and the suspensions prepared with the dispersed CNTs perform a long-lasting stability (Figure 2).

Tween 20 is a stable and a relative nontoxic detergent and emulsifier used in a number of pharmacological applications. It was used as a dispersion agent of carbon nanotubes in previous works [21, 22]. After sonication, all kinds of CNTs were observed in contact with RAW 264.7 for 24 h.

The morphology of CNTs before functionalization was analyzed using transmission electron microscopy (TEM) (Tecnai G2 F20 (200 kV) and Joel). The degree of purification of CNTs was determined using inductively coupled plasma optical emission spectrometry (ICP-OES) (Multiwave 3000, Perkin Elmer Co.). Evaluation of the functionalization of carbon nanotubes was done using Fourier transform infrared spectroscopy (FTIR) (Bio-Rad FTS60V spectrometer). The transmission of FTIR spectra was registered in the range of $800\text{--}1800 \text{ cm}^{-1}$ using KBr pellets. The phagocytosis of nanotubes by RAW 264.7 macrophages was observed using inverted microscope (Olympus CKX41, Germany).

The murine macrophage RAW 264.7 cell line (ATCC, GB) was used in this study. The cells were cultured in 75-cm^2 tissue culture flasks (Nunc, Denmark) in Dulbecco's modified Eagle's medium (DMEM; PAA, Austria) supplemented with antibiotics (penicillin G 100 U/mL, streptomycin $10 \mu\text{g/mL}$ (Sigma-Aldrich, Germany)) and 10% fetal bovine serum (PAA, Austria). The flasks of cultured cells were incubated at 37°C in humidified 95% air and 5% CO_2 . Cells were routinely passaged by harvesting using a cell scraper and replated in tissue culture flasks at a ratio of 1 : 5

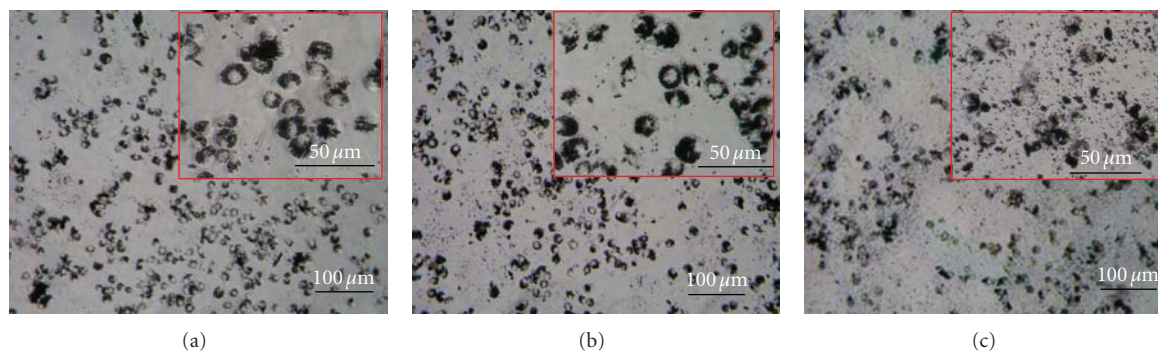


FIGURE 6: Macrophages in contact with SWCNH-F dispersed in PBS (a), in PBS + 1% DMSO (b), and in PBS + 1% Tween 20 (c).

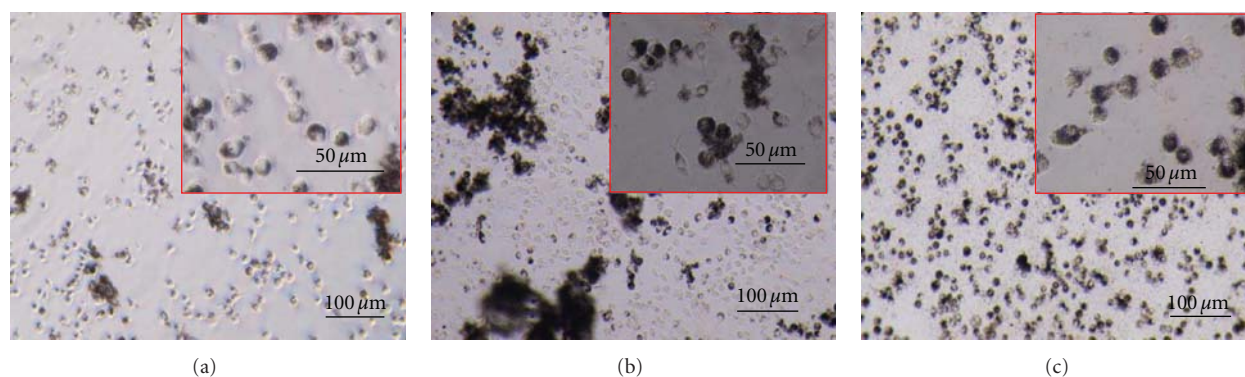


FIGURE 7: Macrophages in contact with MWCNT dispersed in PBS (a), in PBS + 1% DMSO (b), and in PBS + 1% Tween 20 (c).

for subculturing. Cells were passaged no more than 10 times before an experiment. In our experiment, cells were placed into 24-well dishes (Nunc, Denmark) at a population density of 5×10^4 cells/mL/well and allowed to adhere for 2 h. Next, 10 μ L of nanotubes dispersed in different media were added to cell culture. After 24 h, the supernatant from above cells was collected for cytotoxic assay and cells in culture dishes were observed with inverted optical microscope.

3. Results and Discussion

Purity of carbon nanotubes was determined using ICP-OES. The results are gathered in Table 1.

ICP-OES analysis of the as-prepared SWCNH indicated mainly the presence of iron (Fe) catalyst (1.8 wt.%) in this sample. In the case of the pristine MWCNT and ULSWCNT, the ICP-OES analysis showed mainly the presence of nickel (Ni) (1.2 wt.%) and cobalt (Co) (0.8 wt.%), respectively. Using this method, the effectiveness of metal catalysts removal from CNTs after the oxidation process in acid ($\text{H}_2\text{SO}_4:\text{HNO}_3$) was determined. The acid treatment of CNTs allowed to remove the metal catalyst residues in CNT samples, to open the end caps of the CNTs, and to leave them terminated with carboxylic groups [23–26]. The concentration of metal catalysts significantly decreases for all types of carbon nanotubes after chemical oxidation (Table 1). The conclusion drawn from this analysis is that the chemical oxidation method was useful for the purification of CNTs.

To clarify the influence of the acid mixture on the surface chemistry of MWCNT and SWCNH after the functionalization process, the FTIR investigation was carried out and the corresponding results are shown in Figures 3 and 4. The spectrum of the as-prepared CNTs shows the C–C stretching bonds in the range of $1580\text{--}1650\text{ cm}^{-1}$ characteristic to the expected nanotube phonon modes [26]. The spectrum of the CNTs after oxidation presents two characteristic bands at 1710 cm^{-1} (for MWCNT-F) and at 1704 cm^{-1} (for SWCNH-F) and a broad band in the range from 900 to 1220 cm^{-1} assigned to $\nu_{\text{C=O}}$ and $\nu_{\text{C-O}}$ carbonyl and carboxyl groups. These bands were not observed in the spectra of CNTs before the treatment. This implies that the oxygen-containing functional groups are introduced on the MWCNT and SWCNH surfaces during their oxidative treatment. These functional groups are usually found to be attached to the ends of the nanotubes or defects along their wall, due to the enhanced reactivity of these sites [26]. The characteristic bands of FTIR spectrum of other samples are gathered in Table 2. The presence of the chemical group on CNTs surface confirms the effectiveness of functionalization methods.

In order to identify the phagocytosis process, both pristine and functionalized CNTs were analyzed using macrophage cell line (RAW 264.7). The proper application of carbon nanotubes in a biological environment is directly connected with overcoming the agglomeration problem. Due to van der Waals interactions, carbon nanotubes have a strong tendency to orient themselves parallel to each other.

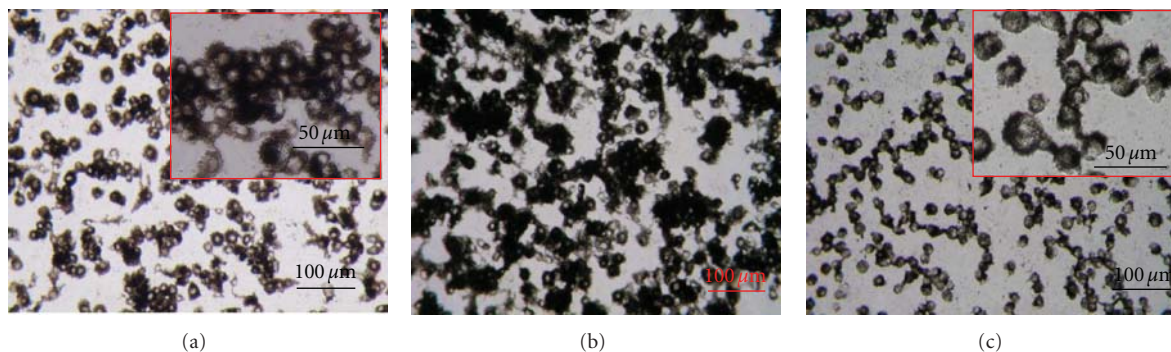


FIGURE 8: Macrophages in contact with MWCNT-F dispersed in PBS (a), in PBS + 1% DMSO (b), and in PBS + 1% Tween 20 (c).

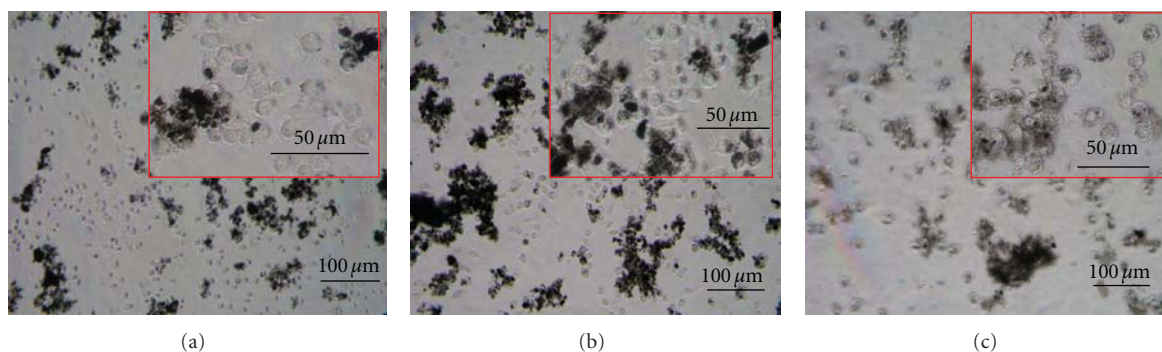


FIGURE 9: Macrophages in contact with ULWCNT dispersed in PBS (a), in PBS + 1% DMSO (b), and in PBS + 1% Tween 20 (c).

TABLE 2: Results from FTIR spectroscopy of MWCNT and SWCNH after functionalization in acids.

MWCNT-F	SWCNH-F	Chemical bond
Wavenumber (cm^{-1})		
1710	1704	C=O and C–O
900–1220	900–1220	

During such an interaction, the CNTs create agglomerates in the form of ropes and bundles with the binding energy accompanying this mechanism several hundreds of $\text{meV}/\mu\text{m}$ [27]. The properties of agglomerated carbon nanotubes are different than those observed for their single, separated forms [14–16]. Hence, the preliminary step before *in vitro* testing is their good dispersion in a medical environment. All kinds of CNTs were dispersed in the pure PBS or PBS containing 1% of DMSO or Tween 20, at the concentration of $38 \mu\text{g}/\text{mL}$ and then introduced to DMEM. The dispersion was monitored using a digital camera (Camedia C5050Z, Olympus, Germany) after 24 h. The sets of suspensions containing various CNTs prepared in different way are visualized in Figure 11.

The aggregates of all types of CNTs were dispersed using ultrasounds (results not shown). However, a part of carbon nanotubes after dispersion had a tendency to secondary aggregation (Figure 11). A complete sedimentation was observed for pristine CNTs in PBS solution and PBS with DMSO only (Figure 11(A, B, G, H, M, and N)). The Tween

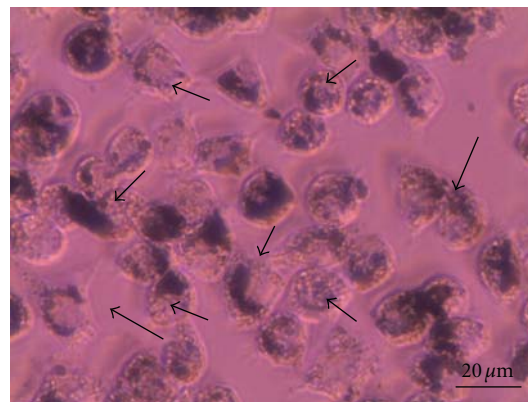


FIGURE 10: The macrophage cells after incubation with nanotubes dispersed in Tween 20.

20 added to PBS improves the dispersity and stability of SWCNH and MWCNT in culture media (Figure 11(C and I)). A different situation was observed in the case of ULWCNT, namely, the presence of Tween 20 did not inhibit the sedimentation process (Figure 11(O)). The hydrophobic nature of the pristine CNTs has a decisive influence on the agglomeration process of CNT in PBS solution. Moreover, the presence of culture media ingredients (e.g., protein, hormones, vitamins, etc.) may have an impact on the sedimentation process. Due to nature of the Tween 20 surfactant, its presence in the PBS solution improves dispersion of

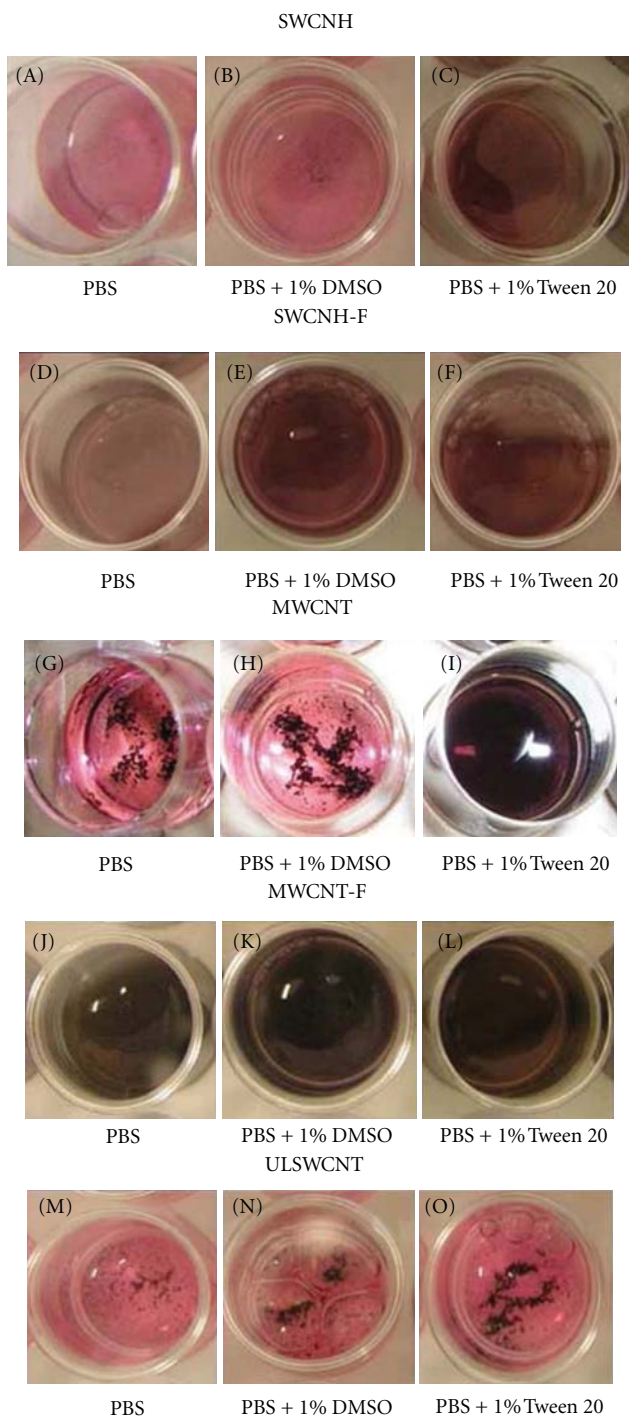


FIGURE 11: Photographs of CNTs suspensions using three different liquids 24 h after dispersion.

MWCNT and SWCNH. It is well known that the surfactants decrease the surface energy of a liquid, allowing easier spreading, and lowering the interfacial tension between two liquids, or between a liquid and a solid. The positive impact of Tween 20 surfactant was observed during dispersion of MWCNTs and SWCNHs, while in the case of ULSWCNTs, the agglomeration was comparable with samples containing

pure PBS and PBS with DMSO (Figure 11(O)). The probable reason could be the length of ULSWCNT, which limits their appropriate dispersion in a solvent. The ULSWCNTs tend to entangle and bundle, which makes their dispersion process and assessment of the surfactant's impact difficult.

A different situation was observed for MWCNT and SWCNH after functionalization in a mixture of acids. Both SWCNH-F and MWCNT-F were well dispersed in all prepared suspensions and maintained their stability up to 24 h (Figure 11(D, E, F, J, K, and L)). The most effective process was observed for MWCNT-F (Figure 11(J, K, and L)). The reason for good dispersion of CNTs in pure PBS and PBS with additives was the surface chemistry of these materials. The presence of carboxylic groups on carbon nanotubes changes their wettability from hydrophobic to hydrophilic.

The phagocytosis of CNTs by RAW 264.7 macrophages and its features was qualitatively analysed on the basis of the series of microphotographs gathered in Figures 5, 6, 7, 8, and 9.

As it results from analyse of these images, the macrophages phagocytose all kinds of CNT with different intensity. The most intensive phagocytosis process was observed for the samples after chemical modification (Figures 6 and 8). The presence of chemical groups on CNTs surface improves their dispersity in solutions. The well-separated carbon nanotubes in a suspension are easier “devoured” by cells. Such images are particularly observed for MWCNT-F (Figure 8), where the cells, regardless of types of solvent, were entirely filled with those CNTs. A similar situation was noticed for SWCNH and MWCNT dispersed in PBS containing Tween 20 (Figures 5(c) and 7(c)). In order to compare the phagocytoses effectiveness between MWCNT-F dispersed in different solvent with MWCNT (Figures 8(a), 8(b), and 8(c)) dispersed in PBS containing Tween 20 (Figure 7(c)), the following relationship may be proposed: Figure 8(a) = Figure 8(b) = Figure 8(c) ≥ Figure 7(c). Comparable or higher phagocytosis effectiveness observed for MWCNT-F (Figures 8(a), 8(b), and 8(c)) in comparison with MWCNT (Figure 7(c)) can be explained by the presence of shorter carbon nanotubes after their oxidation in an acidic medium.

In the case of samples containing higher size agglomerates, the phagocytosis was distinctly inhibited (Figures 5(a), 5(b), 7(a), 7(b), and 9). Such a case was noticed particularly for the cultures contacted with ULSWCNT where the highest number of cells without carbon nanotubes can be seen (Figure 9). Additionally, the hampered phagocytosis of ULSWCNT by RAW 264.7 could come out of a high length of this form (15–30 μm). The influence of the length of CNTs on cell phagocytosis could be confirmed by differentiation between the phagocytosis of SWCNHs (length from 30 to 50 nm) or MWCNTs (length between 1–2 μm) and ULSWCNTs. The influence of the length of the CNTs has already been confirmed in the literature [13]. In spite of the existing agglomerates in SWCNHs and MWCNTs-based suspensions, phagocytosis was easier in comparison to ULSWCNTs-based suspension (Figures 5(a), 5(b), 7(a), 7(b), 9(a), and 9(b)).

The results indicate that the surfactant (Tween 20) has an advantageous influence on the dispersion process of carbon nanotubes in culture media and facilitates phagocytosis by macrophages. The drawback of the application of Tween 20 is its disadvantageous impact on cell morphology (Figure 10). The cell membrane was heterogeneous with numerous vacuoles in cytoplasm (black arrows). The similar results were also observed by Monteiro-Riviere [22]. On the contrary, this phenomenon was not observed for cells harvested with PBS and PBS + 1% DMSO additions.

4. Conclusion

Five kinds of pristine and chemically modified carbon nanotubes were contacted with macrophages to verify their influence on cell phagocytosis. The appropriate dispersion of CNTs in culture media is one of the crucial issues which has a strong impact for interaction cell-CNT. There were used three types of dispersion agents (PBS, PBS + DMSO and PBS + Tween 20). PBS + Tween 20 was the most effective dispersion agent for CNTs, although this surfactant is probably partially toxic for cells, which limits its further application. The use of both pure PBS and PBS with DMSO did not reveal any influence on the good dispersion process of CNT in culture media. The best dispersity was observed for carbon nanotubes after chemical functionalization in an oxidative treatment, irrespective of dispersing agents. Simultaneously, for these kinds of CNTs the highest phagocytosis was observed. The results show that the interaction between CNTs and cells strongly depends on an average agglomerates size and the length of CNTs.

These results provided preliminary information about the influence of different types of CNTs and their degree of dispersity on the phagocytosis processed by macrophage cells. Further investigations are, however, required for better understanding of the mechanism of phagocytosis and the influence of CNTs on the fundamental biological interaction with cells.

Acknowledgment

This work has been supported by the Marie Curie Actions—Industry-Academia Partnerships and Pathways (IAPP), FP7-PEOPLE-IAPP-2008, project number 230766.

References

- [1] A. M. Schrand, L. Dai, J. J. Schlager, S. M. Hussain, and E. Osawa, "Differential biocompatibility of carbon nanotubes and nanodiamonds," *Diamond and Related Materials*, vol. 16, no. 12, pp. 2118–2123, 2007.
- [2] J. Xu, M. Yudasaka, S. Kouraba, M. Sekido, Y. Yamamoto, and S. Iijima, "Single wall carbon nanohorn as a drug carrier for controlled release," *Chemical Physics Letters*, vol. 461, no. 4–6, pp. 189–192, 2008.
- [3] B. S. Harrison and A. Atala, "Carbon nanotube applications for tissue engineering," *Biomaterials*, vol. 28, no. 2, pp. 344–353, 2007.
- [4] C. P. Firme and P. R. Bandaru, "Toxicity issues in the application of carbon nanotubes to biological systems," *Nanomedicine: Nanotechnology, Biology, and Medicine*, vol. 6, no. 2, pp. 245–256, 2010.
- [5] X. Shi, B. Sitharaman, Q. P. Pham et al., "Fabrication of porous ultra-short single-walled carbon nanotube nanocomposite scaffolds for bone tissue engineering," *Biomaterials*, vol. 28, no. 28, pp. 4078–4090, 2007.
- [6] K. Matsumoto, C. Sato, Y. Naka, A. Kitazawa, R. L. D. Whitby, and N. Shimizu, "Neurite outgrowths of neurons with neurotrophin-coated carbon nanotubes," *Journal of Bioscience and Bioengineering*, vol. 103, no. 3, pp. 216–220, 2007.
- [7] A. Fraczek, E. Menaszek, C. Paluszkiwicz, and M. Blazewicz, "Comparative in vivo biocompatibility study of single- and multi-wall carbon nanotubes," *Acta Biomaterialia*, vol. 4, no. 6, pp. 1593–1602, 2008.
- [8] C. A. Poland, R. Duffin, I. Kinloch et al., "Carbon nanotubes introduced into the abdominal cavity of mice show asbestos-like pathogenicity in a pilot study," *Nature Nanotechnology*, vol. 3, no. 7, pp. 423–428, 2008.
- [9] A. A. Shvedova, V. Castranova, E. R. Kisin et al., "Exposure to carbon nanotube material: assessment of nanotube cytotoxicity using human keratinocyte cells," *Journal of Toxicology and Environmental Health Part A*, vol. 66, no. 20, pp. 1909–1926, 2003.
- [10] D. B. Warheit, B. R. Laurence, K. L. Reed, D. H. Roach, G. A. M. Reynolds, and T. R. Webb, "Comparative pulmonary toxicity assessment of single-wall carbon nanotubes in rats," *Toxicological Sciences*, vol. 77, no. 1, pp. 117–125, 2004.
- [11] V. E. Kagan, H. Bayir, and A. A. Shvedova, "Nanomedicine and nanotoxicology: two sides of the same coin," *Nanomedicine: Nanotechnology, Biology, and Medicine*, vol. 1, no. 4, pp. 313–316, 2005.
- [12] A. Bianco, K. Kostarelos, C. D. Partidos, and M. Prato, "Biomedical applications of functionalised carbon nanotubes," *Chemical Communications*, no. 5, pp. 571–577, 2005.
- [13] Y. Sato, A. Yokoyama, K. I. Shibata et al., "Influence of length on cytotoxicity of multi-walled carbon nanotubes against human acute monocytic leukemia cell line THP-1 in vitro and subcutaneous tissue of rats in vivo," *Molecular BioSystems*, vol. 1, no. 2, pp. 176–182, 2005.
- [14] P. Wick, P. Manser, L. K. Limbach et al., "The degree and kind of agglomeration affect carbon nanotube cytotoxicity," *Toxicology Letters*, vol. 168, no. 2, pp. 121–131, 2007.
- [15] K. L. Aillon, Y. Xie, N. El-Gendy, C. J. Berkland, and M. L. Forrest, "Effects of nanomaterial physicochemical properties on in vivo toxicity," *Advanced Drug Delivery Reviews*, vol. 61, no. 6, pp. 457–466, 2009.
- [16] P. M. V. Raja, J. Connolly, G. P. Ganesan et al., "Impact of carbon nanotube exposure, dosage and aggregation on smooth muscle cells," *Toxicology Letters*, vol. 169, no. 1, pp. 51–63, 2007.
- [17] P. Cherukuri, S. M. Bachilo, S. H. Litovsky, and R. B. Weisman, "Near-infrared fluorescence microscopy of single-walled carbon nanotubes in phagocytic cells," *Journal of the American Chemical Society*, vol. 126, no. 48, pp. 15638–15639, 2004.
- [18] R. Singh, D. Pantarotto, D. McCarthy et al., "Binding and condensation of plasmid DNA onto functionalized carbon nanotubes: toward the construction of nanotube-based gene delivery vectors," *Journal of the American Chemical Society*, vol. 127, no. 12, pp. 4388–4396, 2005.

- [19] K. Ajima, M. Yudasaka, T. Murakami, A. Maigné, K. Shiba, and S. Iijima, "Carbon nanohorns as anticancer drug carriers," *Molecular Pharmaceutics*, vol. 2, no. 6, pp. 475–480, 2005.
- [20] M. Bottini, S. Bruckner, K. Nika et al., "Multi-walled carbon nanotubes induce T lymphocyte apoptosis," *Toxicology Letters*, vol. 160, no. 2, pp. 121–126, 2006.
- [21] R. Rastogi, R. Kaushal, S. K. Tripathi, A. L. Sharma, I. Kaur, and L. M. Bharadwaj, "Comparative study of carbon nanotube dispersion using surfactants," *Journal of Colloid and Interface Science*, vol. 328, no. 2, pp. 421–428, 2008.
- [22] N. A. Monteiro-Riviere, A. O. Inman, Y. Y. Wang, and R. J. Nemanich, "Surfactant effects on carbon nanotube interactions with human keratinocytes," *Nanomedicine: Nanotechnology, Biology, and Medicine*, vol. 1, no. 4, pp. 293–299, 2005.
- [23] S. H. Su, W. T. Chiang, C. C. Lin, and M. Yokoyama, "Multi-wall carbon nanotubes: purification, morphology and field emission performance," *Physica E*, vol. 40, no. 7, pp. 2322–2326, 2008.
- [24] V. Datsyuk, M. Kalyva, K. Papagelis et al., "Chemical oxidation of multiwalled carbon nanotubes," *Carbon*, vol. 46, no. 6, pp. 833–840, 2008.
- [25] J. Liu, A. G. Rinzler, H. Dai et al., "Fullerene pipes," *Science*, vol. 280, no. 5367, pp. 1253–1256, 1998.
- [26] E. B. Barros, A. G. S. Filho, V. Lemos et al., "Charge transfer effects in acid treated single-wall carbon nanotubes," *Carbon*, vol. 43, no. 12, pp. 2495–2500, 2005.
- [27] R. Tucknott and S. N. Yaliraki, "Aggregation properties of carbon nanotubes at interfaces," *Chemical Physics*, vol. 281, no. 2-3, pp. 455–463, 2002.

Research Article

Enhanced Photocatalytic Activity for Degradation of Methyl Orange over Silica-Titania

Yaping Guo,¹ Shaogui Yang,² Xuefei Zhou,³ Chunmian Lin,¹ Yajun Wang,¹ and Weifeng Zhang¹

¹ College of Biological and Environmental Engineering, Zhejiang University of Technology, Hangzhou 310014, China

² State Key Laboratory of Pollution Control and Resources Reuse, Nanjing University, Nanjing 210093, China

³ State Key Laboratory of Pollution Control and Resources Reuse, Tongji University, Shanghai 200092, China

Correspondence should be addressed to Shaogui Yang, yangdlut@126.com

Received 1 November 2010; Accepted 2 March 2011

Academic Editor: Junping Wang

Copyright © 2011 Yaping Guo et al. This is an open access article distributed under the Creative Commons Attribution License, which permits unrestricted use, distribution, and reproduction in any medium, provided the original work is properly cited.

Silica-modified titania (SMT) powders with different atomic ratios of silica to titanium (Rx) were successfully synthesized by a simple ultrasonic irradiation technique. The prepared samples were characterized by X-ray diffraction (XRD), FT-IR spectroscopy, transmission electron microscopy (TEM), X-ray photoelectron spectroscopy (XPS), and ultraviolet visible spectroscopy. The specific surface area was measured according to BET theory. Results indicate that the addition of silica to titania can suppress the crystalline size growth and the transformation of anatase phase to rutile phase of titania, enlarge specific surface area of the titania particles, and result in a blue shift of absorption edge compared to pure titania. The photocatalytic activity of the SMT samples was evaluated by decolorizing methyl orange aqueous solutions under UV-visible light irradiation. It was found in our study that this activity was affected by silica content, calcination temperature, H₂SO₄, and oxidants such as KIO₄, (NH₄)₂S₂O₈ and H₂O₂. The results reveal that the photocatalytic activity of 0.1-SMT catalyst is the best among all samples calcined at 550°C for 1 h and it is 1.56 times higher than that of Degussa P-25 titania, which is a widely used commercial TiO₂ made by Germany Degussa company and has been most widely used in industry as photocatalyst, antiultraviolet product, and thermal stabilizer. The optimal calcination temperature for preparation was 550°C. The photocatalytic activity of SMT samples is significantly enhanced by H₂SO₄ solution treatment and oxidants.

1. Introduction

As a cost-effective, nontoxic, effective photocatalyst, nanosize TiO₂ has received much attention during the past three decades. In its practical application, it is very important to improve the efficiency of titania-based photocatalysts because titania usually has a small surface area and pore volume, which leads to its low adsorption of organic pollutants. Therefore, the enlargement of specific surface area and adsorption capability is desirable for titania photocatalyst.

Generally speaking, two strategies have been developed to solve the problem. One is the synthesis of malodorous titania with high specific surface area resulting in high adsorbability and photocatalytic activity [1], the other is the combination of titania materials with adsorbent [2]. For the former strategy, titania mostly exists in an amorphous or

semicrystalline phase so it has low photocatalytic activity. It has been proven that the later method is relatively easy to prepare. As an adsorbent and stabilizer, silica is the best candidate as it not only possesses a large specific surface area, but also has no absorption in UV region. Titania-silica mixed oxide has attracted considerable attention as attractive materials for photocatalytic applications because of the synergetic function of the photocatalytic activity, adsorbability, and stability. This may be partially the intimate interaction of titanium dioxide and silica, the new different structural characteristics and physicochemical/reactivity properties of titania-silica complex, such as quantum-sized crystalline, large surface area, high thermal stability, high adsorbability of reactant, or high acidity [3, 4]. Most of studies for titania-silica were concentrated on the structure type of titania supported on silica or titanium

silicate series [5–8], the application of waste air purification [9] and wastewater treatment [10]. However, few studies on wastewater treatment with titania-silica have been reported.

The purpose of the paper is to explore SMT with high photoactivity for purifying the water. Methyl orange was chosen as a probe for its relatively high reactivity and high stability. We also found that the photocatalytic activity of the prepared SMT could be greatly improved by H_2SO_4 solution treatment. Explanations are provided based on the influence of sulfuric acid treatment on photocatalytic activity.

2. Materials and Methods

2.1. Materials. Tetraethylorthosilicate (TEOS), tetrabutylorthotitanate (TBOT), methyl orange, sulfuric acid, KIO_4 , $(\text{NH}_4)_2\text{S}_2\text{O}_8$, and H_2O_2 were from Shanghai Chemical Company at analytic purity.

2.2. Methods

2.2.1. Preparation of Silica-Modified Titania (SMT) and Surface Acid Treatment. Nanocrystalline Titania powders were prepared by hydrolysis under ultrasonic irradiation [11, 12]. Tetrabutylorthotitanate (TBOT) was used as a titanium source. Tetraethylorthosilicate (TEOS) was used as a precursor of the dopant. The mixture of TBOT (0.1125 mol) and TEOS was directly added dropwise to distilled water (900 mL) under vigorous stirring at room temperature. The atomic ratios of silica to titanium, which hereafter was designated as Rx, were 0, 0.05, 0.1, and 0.2, respectively. The samples were then irradiated with an ultrasonic cleaning bath (KQ3200E, 40 kHz, 150 W) for 1 h, followed by aging in a closed beaker at room temperature for 24 h. After aging, these samples were dried at 100°C for about 8 h in air in order to vaporize water in the gels and then ground to fine powders to obtain dry gel samples. The dried gel samples were calcined at different temperature in air for 1 h.

To enhance the photocatalytic activity of the powders, we dipped the SMT in $1\text{ mol}\cdot\text{L}^{-1}$ H_2SO_4 aqueous solutions at room temperature. After 20 mins, the samples were withdrawn from the H_2SO_4 solutions. They were carefully rinsed with deionized water and dried at 100°C for 2 h in an oven in air.

2.2.2. Characterization. XRD patterns were made using a X'TRA diffractometer (made in ARL Company in Swiss) with $\text{Cu K}\alpha$ radiation over the scan range $20\text{--}60^\circ\text{C}$ for wide angle XRD. The average crystalline size of powders was estimated by the Scherrer formula [13]: $D = 0.89\lambda/\beta\cos\theta$ (where D is the crystallite size, λ is the wavelength of the X-ray radiation ($\text{Cu K}\alpha = 0.15418\text{ nm}$), K is usually taken as 0.89, and β is the line width at half-maximum height, after subtraction of equipment broadening). The FT-IR spectra were recorded by a NEXUS 870 FT-IR, made in U.S. NICOLET Company in a wavenumber range of $4000\text{--}400\text{ cm}^{-1}$. UV-V is spectroscopic analysis that was

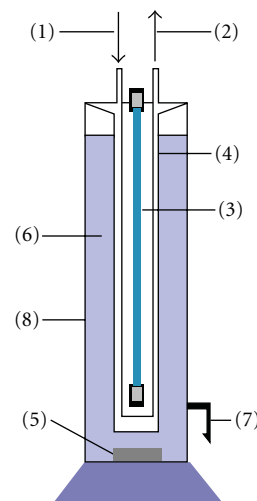


FIGURE 1: Photoreactor system for methyl orange degradation. (1) Cooling water input, (2) water outflow, (3) UV lamp, (4) Quartz sleeve, (5) Stirrer bar, (6) reactant solution, (7) exhaust, and (8) glass reactor.

performed by using a spectrophotometer (SHIMADZU UV-2401). X-ray photoelectron spectroscopy (XPS) measurements were done with an ESC ALB MK-II XPS System with a monochromatic Al KR source and a charge neutralizer. Measurement of BET (BET aims to explain the physical adsorption of gas molecules on a solid surface and serves as the basis for an important analysis technique for the measurement of the specific surface area of a material. In 1938, Stephen Brunauer, Paul Hugh Emmett, and Edward Teller published an article about the BET theory in a journal for the first time; “BET” consists of the first initials of their family names [12], surface area was performed using N_2 adsorption/desorption isotherms on a Micromeritics ASAP 2020.

2.2.3. Photocatalytic Activity of Silica-Modified Titania (SMT). The photocatalytic activity of prepared SMT powders for decomposition of methyl orange was investigated as shown in Figure 1. The photocatalytic reactor has an effective volume of 150 mL. The experiment was performed in the following condition: UV irradiation (a 400 W high-pressure mercury lamp from factory of Beijing light with a maximum wavelength of 365 nm, $I_0 = 1.50\text{ mW}/\text{cm}^2$), vigorous stirring, no airflow. The initial concentration of methyl orange was $20\text{ mg}\cdot\text{L}^{-1}$ and Rx-SMT powders were kept 1.0 g/L in all cases.

Degussa P25 titania particles ($50\text{ m}^2/\text{g}$) with crystalline structure of ca. 20% rutile and 80% anatase and primary particle size of ca. 21 nm was taken as a reference to test the photoactivity of the Rx-SMT powders towards the degradation of methyl orange.

The concentration of methyl orange was determined using UV-1600 spectroscopy at wavelength $\lambda = 440\text{ nm}$ quantitatively. Total organic carbon (TOC) was determined with Shimadzu TOC-5000 analyzer.

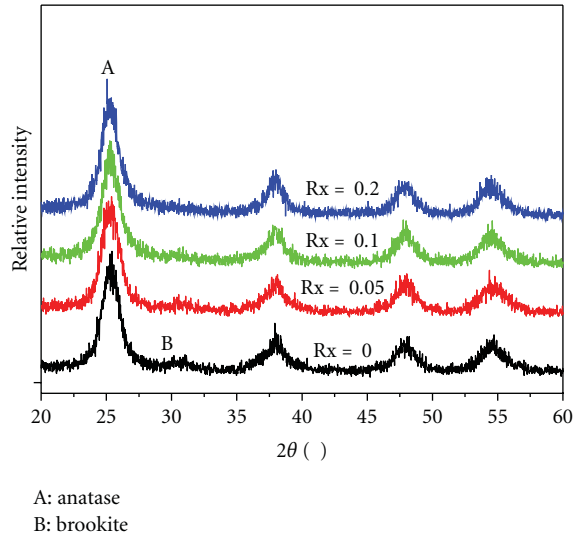


FIGURE 2: XRD patterns of the Rx-SMT xerogel powders ($R_x = 0, 0.05, 0.1$, and 0.2) and dried at 100°C for 8 h.

3. Results and Discussion

3.1. Crystal Structure and TEM Photomicrography. XRD was used to investigate the changes of crystalline phase of the SMT gel powders before and after heat treatment. Figure 2 shows the effects of silica on phase structures of the TiO_2 powders dried at 100°C for 8 h. The anatase phase is dominant in the as-prepared TiO_2 sample, but there is a small amount of brookite in it. The weak peak at $2\theta = 30.7^\circ$ corresponds to the brookite phase of titania. When $R_x > 0.1$, the intensities of brookite peaks steadily become weaker and finally disappear. This is probably due to the fact that silica suppresses the crystallization of brookite by adsorbing onto the surfaces of TiO_2 particles. Similar result has been observed with F ion doping [14].

Figure 3 shows the effects of silica content on the phase structures of Rx-SMT powders calcined at 550°C . For pure titania ($R_x = 0$), significant peaks of rutile phase are observed obviously. The dominant phase of titania ($R_x > 0$) is anatase when some portion of silica is embedded into titania particles. Apart from the diffraction peaks corresponding to anatase, there are no other diffraction peaks from $2\theta = 20$ – 60 degree for all SMT samples (except for pure titania) as shown in Figure 3, indicating that silica exists in an amorphous phase. The average size of anatase titania from Scherrer formula was presented in Table 1. The result shows that the crystallite size decreased sharply with increasing the doping silica content up to 0.05. When the silica content was over 0.05, there was no significant change in the crystallite size of SMT particles. This result confirms that the embedding of some portion of silica into titania particle inhibits the growth of anatase crystal of titania particles [15].

Figure 4 shows the effects of calcination temperature on phase structures of 0.1-SMT powders. It can be seen that the peak intensities of anatase increase and the width of the (101) plane diffraction peak of anatase ($2\theta = 25.4^\circ$) becomes

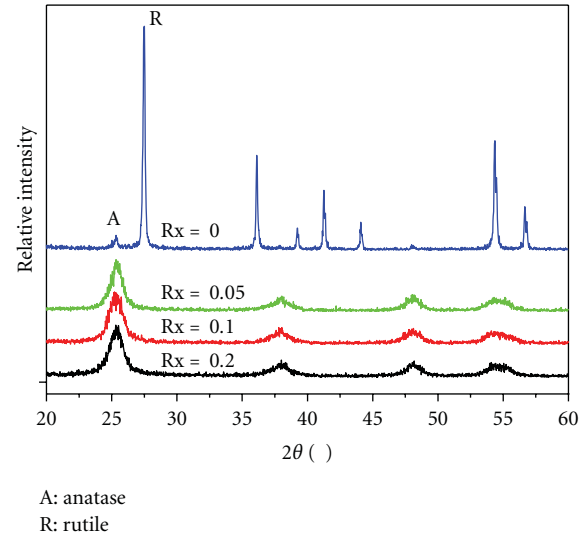


FIGURE 3: XRD patterns of Rx-SMT powders ($R_x = 0, 0.05, 0.1$, and 0.2) calcined at 550°C for 1 h.

TABLE 1: Textural properties of the Rx-SMT powders prepared at 550°C for 1 h.

Samples	Si/Ti molecular ratio by XPS	Surface area ($\text{m}^2 \cdot \text{g}^{-1}$)	Average size (nm)
0-SMT	0	20	50.5
0.05-SMT	0.053	160	8.9
0.1-SMT	0.094	196	7.2
0.1-SMT treated by H_2SO_4 solution	0.093	195	7.2
0.2-Silica titania	0.206	208	6.9

narrower with increasing calcination temperature (from 100 to 750°C). It has been reported that anatase-type TiO_2 changes to rutile-type structure by heat treatment above 635°C from the results of a kinetic study on the anatase-to-rutile phase transformation [13]. At 750°C , anatase is a main phase and a small amount of rutile phase is detected, while the phase of pure titania calcined at 550°C was dominant rutile phase. The resulting SMT powders contain only anatase phase in the calcination temperature range of 100 – 650°C . Accordingly, SMT samples show high thermal stability and the presence of silica seems to be critical for the stabilization of the anatase phase. The presence of silicon atoms in the anatase matrix retards the change of face-centered cubic arrangement of oxide ion in anatase into hexagonal packing in rutile because this change is associated with the cleavage of a part of Ti-O bonds [9]. The decrease of the surface energy caused by substitution of the surface OH groups with oxide ions also contributes to the thermal stability of the present products [15]. The average sizes at different temperatures were calculated, which corresponded to 1.4, 4.6, 10.1, and 28.8 nm for 100, 450, 650, and 750°C , respectively. At temperatures lower than 650°C , anatase phases are present in relatively small grain sizes. However,

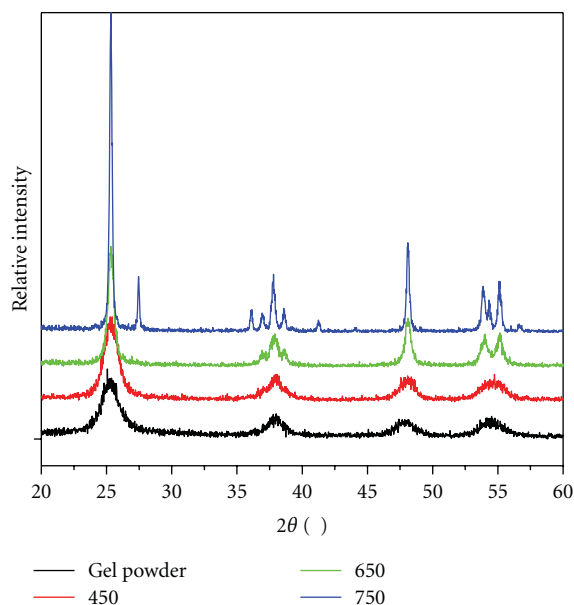


FIGURE 4: XRD patterns of 0.1-SMT powders calcined at (a) 100, (b) 450, (c) 650, and (d) 700°C for 1 h.

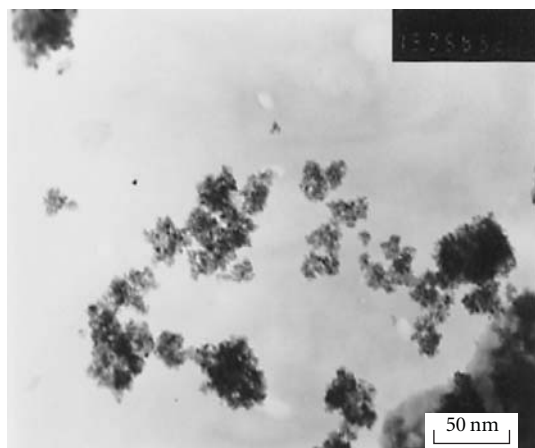


FIGURE 5: TEM image of 0.1-SMT prepared by ultrasonic irradiation hydrolysis and calcined at 550°C.

at 750°C ($R_x = 0.1$), anatase and rutile phases are both present and the grains of various phases grow dramatically. This is attributable to the fact that the phase transitions accelerate the process of grain growth by providing the heat of phase transformation [16]. The XRD results revealed that the heat treatment induced the increase of crystalline size and phase transformation.

Figure 5 shows TEM photographs of 0.1-SMT powders calcined at 550°C for 1 h. It can be seen that the dispersion property of the sample is good. Table 1 indicates that specific surface area of the samples increase with the increase of the silica content. This result confirms that the suitable addition of silica into titania matrix helps to suppress the reduction of surface area at high calcination temperature. It is well noted that the specific surface areas of 0.1-SMT ($196 \text{ m}^2/\text{g}$) and

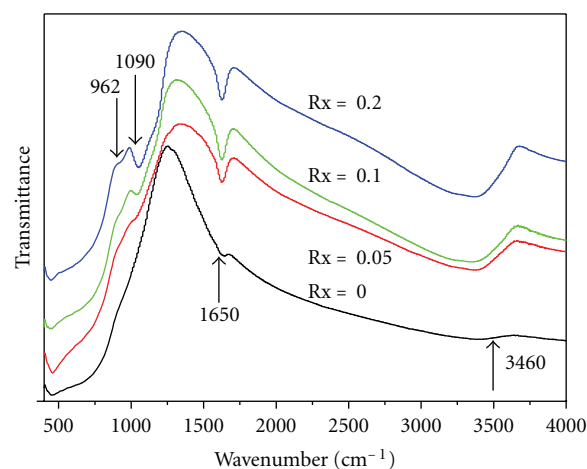


FIGURE 6: FT-IR spectra of Rx-SMT powders calcined at 550°C for 1 h.

0.1-SMT after H_2SO_4 solution treatment ($195 \text{ m}^2/\text{g}$) are not significantly different.

3.2. FT-IR Spectroscopy. FT-IR spectra of Rx-SMT calcined at 550°C for 1 h are presented in Figure 6. The peak around 1090 cm^{-1} attributed to the asymmetric stretching vibrations of Si–O–Si band [17], and the Ti–O–Si linkage stretching band appears at about 962 cm^{-1} [18]. When the ratio of silicon to titanium was over 0.1, the distinct band for Ti–O–Si vibration (962 cm^{-1}) was observed. The existence of Si–O–Ti bond in FT-IR analysis may be attributed to the existence of covalent bond between amorphous SiO_2 and crystalline TiO_2 . The band for the asymmetric Si–O–Si stretching vibration was observed for all composite samples, and its intensity was increased with increasing the silicon content. The presence of Si–O–Si bond in FT-IR is caused by the formation of SiO_2 in the samples, which is in agreement with the reported result [19]. Besides, Ti–O–Ti bond may be present in the range of 400 to 600 cm^{-1} [20] for all samples. From these results of FT-IR, it is clear that the silica exists as segregated amorphous phase in the anatase titania powders and some metal–O–metal bonding of Ti–O–Si, which result from formation of a new ternary amorphous $\text{Si}_x\text{Ti}_y\text{O}_z$ phase as there is no match in the XRD analysis and/or existence of covalent bond between amorphous SiO_2 and crystalline TiO_2 .

The peak around 1650 cm^{-1} is due to the bending vibration of O–H bond, which is assigned to the chemisorbed water, and the peak around 3460 cm^{-1} is assigned to the stretching mode of O–H bond and related to free water [21]. This water band was increased with increasing the ratio of silica to titanium. This is due to the fact that silica has the capability to absorb water in air [22]. In addition, when titania was embedded with silica, crystallite growth was suppressed and the surface area was kept larger (as shown in Table 1), and in this case, the capability to hold absorbed water became larger.

FT-IR spectra of Rx-SMT after H_2SO_4 treatment were presented in Figure 7. The peak corresponding to 1244 cm^{-1}

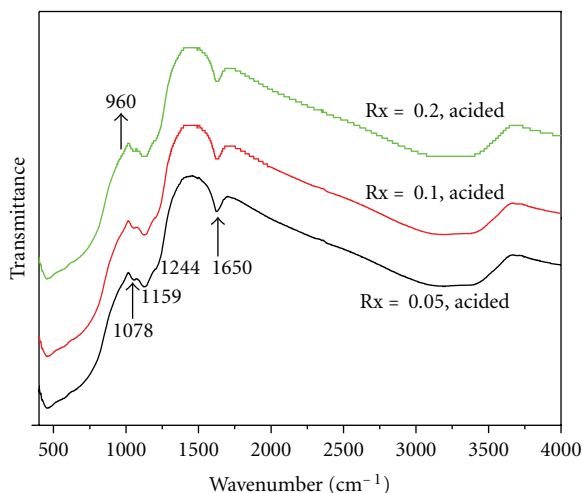


FIGURE 7: FTIR spectra of Rx-SMT powders treated by 1M H_2SO_4 solution. Rx = 0.05, 0.1, and 0.2.

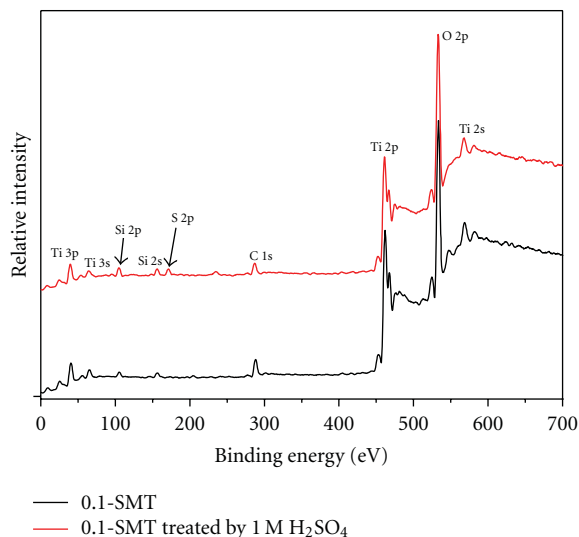


FIGURE 8: XPS spectra of 0.1-SMT calcined at 550°C for 1 h and 0.1-SMT treated by H_2SO_4 solution.

is the stretching frequency of $\text{S}=\text{O}$, and the peaks corresponding to 1159 and 1078 cm^{-1} are the characteristic frequencies of SO_4^{2-} , which indicated the chelatometric coordinated adsorption of SO_4^{2-} on SMT. The sulfate ion, both in surface and bulk, creates high surface acidity to improve the photocatalytic activity [23].

3.3. XPS Studies. Figure 8 shows the XPS spectrum of 0.1-SMT powders heat-treated at 550°C for 1 h and 0.1-SMT treated by 1M H_2SO_4 solution. XPS peaks show that the 0.1-SMT powders contain only Ti, O, Si, and a trace amount of carbon. The following binding energies are used in our quantitative measurements: Ti 2p at 460.10 eV, O 1s at 531.35 eV, Si 2p at 103.8 eV, and C 1s at 286.20 eV. The atomic ratio of Ti:O:Si is about 1:2.13:0.13, which is higher than the nominal atomic composition of TiO_2 ,

indicating that silica atoms are partially concentrated on the surface region of the titania particles [7]. The C element is ascribed to the residual carbon from precursor solution and the adventitious hydrocarbon from the XPS instrument itself. It is easily observed that 0.1-SMT treated by 1M H_2SO_4 solution contains Ti, O, Si, S, and a trace amount of carbon. The binding energies of Ti 2p, O 1s, Si, S, and C 1s are 460.70, 531.9, 105, 171.1, and 286.45 eV, respectively. It is easily noted from the figure that the binding energy of Ti 2p in 0.1-SMT after H_2SO_4 treatment is higher than that of 0.1-SMT before H_2SO_4 treatment; the higher binding energy is helpful to improve its photocatalytic activity.

3.4. UV-Vis Spectra. As a photocatalyst, the wavelength distribution of the absorbed light is one of the important properties regardless of the quantum yield. Figure 9 shows the UV-Vis diffuse reflectance spectra (UV/Vis DRS) of prepared powders with the different silica content. Absorption edge of rutile (Rx = 0) is found to be at the shorter wavelength than that of anatase. Compared Rx-SMT samples with pure titania sample, the absorption spectrum of the Rx-SMT samples show a stronger absorption in the UV-visible range and a blue shift in the band gap absorption edge was observed in all SMT samples. The blue shift of absorption of a photocatalyst means that the photocatalyst has a greater oxidation-reduction potential and enhance the absorption, which will improve its photocatalytic activity [24].

The energy band gap of prepared samples could be estimated from a plot of $(\alpha h\nu)^{1/2}$ versus photon energy ($h\nu$). The intercept of the tangent to the plot will give a good estimation of the band gap energy for indirect band gap materials such as TiO_2 [25, 26]. The absorption coefficient α can be calculated from the measured absorbance (A) using the following equation:

$$\alpha = \frac{2.303\rho 10^3}{lcM} A, \quad (1)$$

where the density $\rho = 3.9\text{ g cm}^{-3}$, molecular weight $M = 79.9\text{ g mol}^{-1}$, c is the molar concentration of TiO_2 , and l is the optical path length.

The calculated band gap energies of all silica-modified samples with different Rx values (0, 0.05, 0.1, and 0.2) are about 2.97 eV, 3.29, 3.31, and 3.34 eV, respectively. The above results imply that the absorption edge was clearly shifted toward shorter wavelengths for all SMT samples.

3.5. Photocatalytic Activity. As the photocatalytic mechanism suggests, both photocatalysts and a light source are necessary for the photo-oxidation reaction to occur [6]. A control experiment was conducted on three different conditions: (i) in the dark in presence of 0.1-SMT, (ii) only UV irradiation without photocatalyst, and (iii) under UV illumination in presence of 0.1-SMT. In all above conditions, the initial concentration of Methyl orange is 20 mg/L. In Figure 1, the concentration of MO is plotted as a function of reaction time.

As can be seen in Figure 10, in the dark, 0.9% of the initial substrate disappeared after 1 h of continuous stirring due to the adsorption phenomena. Over this time, abatement

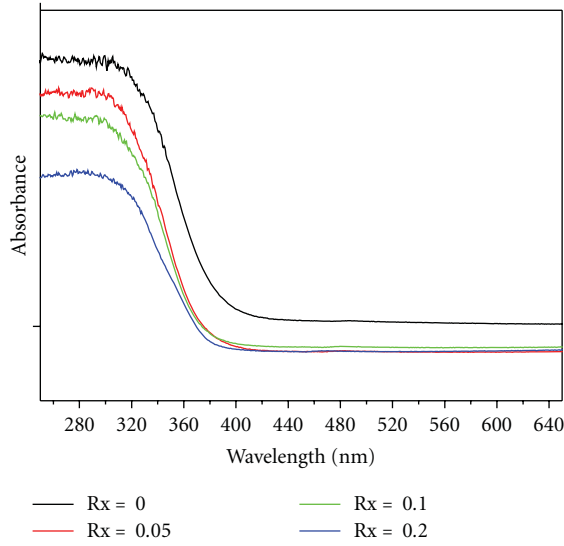


FIGURE 9: UV-Vis spectra of Rx-SMT with different Si/Ti ratios. Rx = 0, 0.05, 0.1, and 0.2.

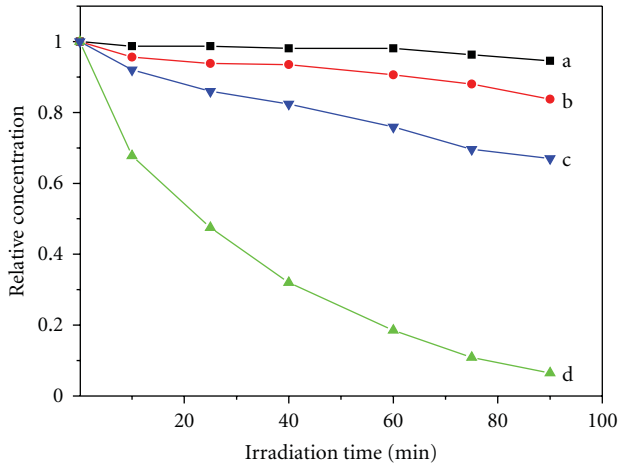


FIGURE 10: The variation of MO and TOC concentrations by photocatalytic technology with 0.1-SMT; (a) MO-dark experiment; (b) MO-direct photolysis; (c) TOC-photocatalysis; (d) MO-photocatalysis.

of 5.4% after 1.5 h was detected. In direct photolysis, about 8% disappearing efficiency was observed during the 1 h irradiation; and 17% of the initial methyl orange disappeared after 1.5 h. When aqueous 0.1-SMT suspension was exposed to UV light, the concentration of MO decrease markedly. About 68–82% of methyl orange was bleached within 40–60 mins of time experiment, respectively. It can be clearly seen from Figure 10 that 93.5% of methyl orange in aqueous solution was photocatalytically degraded, and its corresponding mineralization efficiency was only 33%. It indicated that the complete mineralization of Methyl orange took more time than degradation.

TABLE 2: The kinetics constants and regression coefficients of methyl orange photocatalysis on Rx-SMT and Degussa P-25 titania.

Photocatalyst	Kinetic constant (min ⁻¹)	r^2	Ratio of K to K_{P25}
Rx = 0	$K_0 = 0.0015$	0.9398	0.0789
Rx = 0.05	$K_1 = 0.0234$	0.9949	1.2316
Rx = 0.1	$K_2 = 0.0296$	0.9952	1.5579
Rx = 0.2	$K_3 = 0.0149$	0.9956	0.7842
Degussa P-25 titania	$K_{P25} = 0.019$	0.9977	1

The photocatalytic activity of Rx-SMT powders is affected by various factors, such as the doping silica content, calcined temperature, and sulfuric acid treatment.

3.6. Doping Silica Content. The photocatalytic activity of the prepared SMT powders for the decomposition of methyl orange was investigated as a function of silica content. The photocatalytic degradation follows pseudo first-order kinetics. The results are presented in Figure 11 and Table 2. It is clearly seen that the photocatalytic degradation rate of methyl orange firstly increased with increasing the silica content when the range of silica content was from 0 to 0.1, it may be due to the decrease of average sizes as shown in the XRD analysis in Figure 3 and the increase of surface hydroxyl group as shown in the analysis of FT-IR in Figure 4. However, higher silica content (>0.1) did not favor the further enhancement of the photoactivity of SMT powders because the crystallinity of anatase decreased in spite of the larger specific surface area (Table 2), and SiO_2 did not exhibit photocatalytic activity. It should be noted that the photocatalytic activity of 0.1-SMT is the best among all the samples and it was about 1.56 times of that of Degussa P25 titania, which is recognized as an excellent photocatalyst [27]. The difference in both of specific surface area and anatase crystallites is responsible for this discrepancy of Rx-SMT photoactivity and the surface area of Rx-SMT samples were presented in Table 1. Moreover, another reason on enhancement of SMT is ultrasonic irradiation in the preparation of samples; ultrasonic irradiation enhances hydrolysis of titanium and silicon alkoxide, and crystallization of the gel, because ultrasonic cavitation creates a unique environment for hydrolysis of titanium and silicon alkoxide. The similar result has been observed in formaldehyde degradation in silica titania system, which was reported [9].

It can be seen from Figure 11 and Table 2 that pure titania (Rx = 0) shows very poor photocatalytic activity, compared to other samples. This can be easily explained that the sample was mainly composed of rutile phase with poor photocatalytic activity and has low specific surface area.

3.7. Calcined Temperature. It is well known that calcination is a common treatment that can be used to enhance the photoactivity of nanosized photocatalysts [27]. The photocatalytic activity of the prepared 0.1-SMT powders for the decomposition of methyl orange was investigated

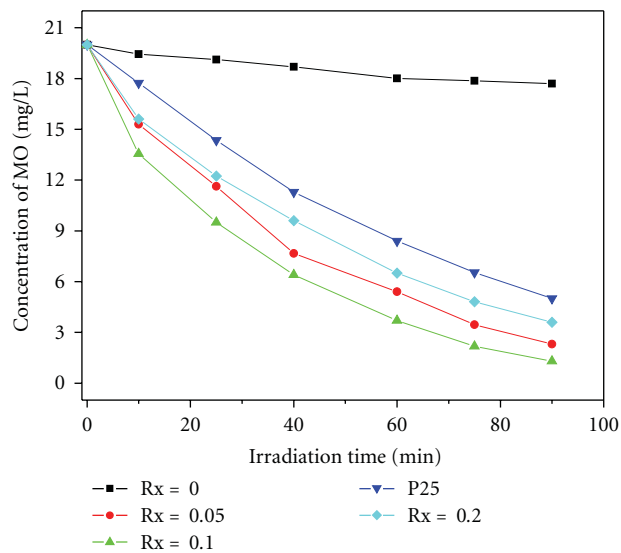


FIGURE 11: Concentration changes of methyl orange versus UV irradiation time with Rx-SMT photocatalysts calcined at 550°C for 1 h.

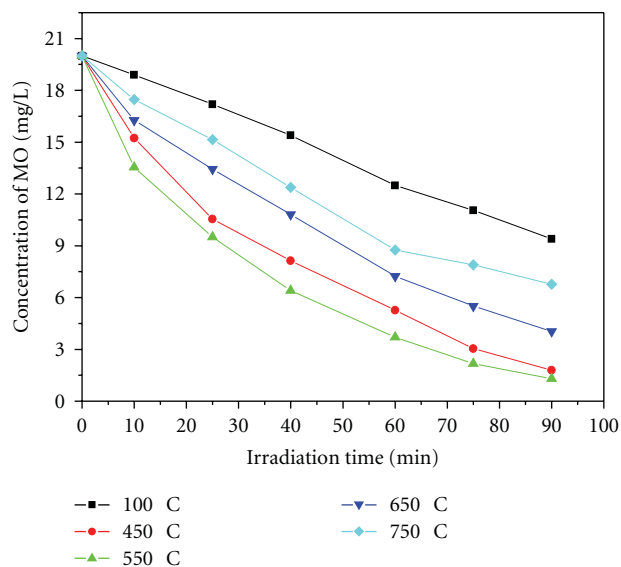


FIGURE 12: Concentration changes of methyl orange versus UV irradiation time with 0.1-SMT powders calcined at 100, 450, 550, 650, and 750°C.

as a function of calcination temperature and the result was shown in Figure 12. The 0.1-SMT sample calcined at 100°C shows good photocatalytic activity with a reaction rate constant of $7.9 \times 10^{-3} \text{ min}^{-1}$. The reaction rate constant increases with increasing calcination temperature. Enhancing the photocatalytic activity at elevated temperatures can be ascribed to an obvious improvement in the crystallinity of anatase (as shown in Figure 4). At 550°C, the reaction rate constant k reaches the highest value of $2.96 \times 10^{-2} \text{ min}^{-1}$ and it is obviously higher than that of Degussa P-25 titania ($k = 1.9 \times 10^{-2} \text{ min}^{-1}$). The high photocatalytic activity of

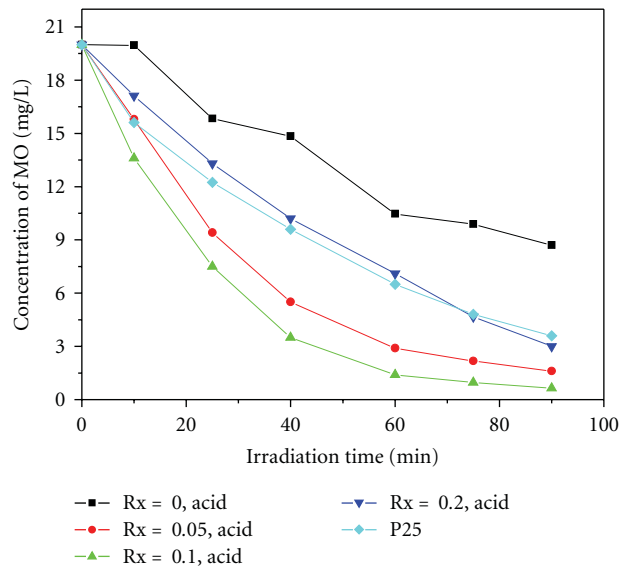


FIGURE 13: Concentration changes of methyl orange versus UV irradiation time with different photocatalysts.

TABLE 3: The kinetics constants and regression coefficients of methyl orange photocatalysis on Rx-SMT treated by H_2SO_4 solution.

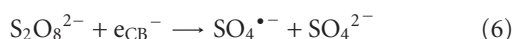
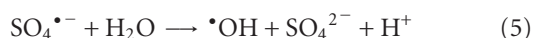
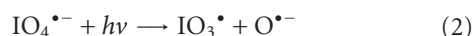
Photocatalyst	Kinetic constant (min^{-1})	r^2	Ratio of K to K_{P25}
Rx = 0, acid	0.0094	0.9627	0.4947
Rx = 0.05, acid	0.0295	0.9763	1.5526
Rx = 0.1, acid	0.0405	0.9876	2.0558
Rx = 0.2, acid	0.0194	0.9873	1.0210

the sample calcined 550°C is partially due to its large surface area and small crystallite size. Moreover, both of the intense absorption in the UV-visible range and a blue shift in the band gap transition of the SMT samples indicate that more powerful photogenerated holes and electrons can participate in the photocatalytic reactions. Calcination temperatures well above 550°C are not desirable. Samples calcined at 750°C display relatively poor photocatalytic activity.

3.8. H_2SO_4 Treatment. The photocatalytic activity of the prepared Rx-SMT powders treated by H_2SO_4 solution was also investigated in the paper. The results are shown in Figure 13 and Table 3. By comparing Figure 13 with Figure 11, it is noted from that the photocatalytic activity of all the catalysts is improved after H_2SO_4 treatment. The reaction rate constants of Rx-SMT (Rx = 0, 0.05, 0.1, and 0.2) after sulfuric acid treatment are 0.0094, 0.0295, 0.0405, and 0.0194 min^{-1} , respectively. The photocatalytic degradation rate of methyl orange over 0.1-SMT after sulfuric acid treatment was 2 times of that of Degussa P-25 titania and 1.37 times of that 0.1-SMT without sulfuric acid treatment. FTIR results (Figure 7) showed that all samples after H_2SO_4 treatment demonstrate enhanced acidity on their surface. It was reported that the enhancement in surface

acidity improves the activity of a photocatalytic system [28]. Therefore the photocatalytic activity of all samples after H₂SO₄ solution treatment was higher than that of the samples without H₂SO₄ solution.

3.9. Oxidants Affecting the Photodegradation of MO over 1%-FST_(Rx = 10%). The effect of different oxidants such as in aqueous solutions on the photodegradation efficiency of MO in aqueous 1%-FST_(Rx = 10%) suspensions was investigated here, the addition concentration of the oxidants all was 0.01 M and reaction time all was 60 mins. When these oxidants were separately added into reaction solutions, the photodegradation efficiencies corresponding to KIO₄, (NH₄)₂S₂O₈, H₂O₂, and control were 95.1%, 87.5%, 93.2%, and 82%, respectively, which indicated that these oxidants enhance the photodegradation of MO. The higher degree of degradation with the oxidants may be ascribed to formation of highly reactive radical intermediates and the electron capture by these oxidants in the following equations [28].



It was well documented that the electron reduction potentials of different species such as $E(\text{O}_2/\text{O}_2^{\bullet-})$, $E(\text{H}_2\text{O}_2/\bullet\text{OH})$ and $E(\text{S}_2\text{O}_8^{2-}/\text{SO}_4^{\bullet-})$ are -115 mV, 1150 mV, and 1100 mV, respectively. It showed that all added oxidants should be more efficient electron acceptors than molecular oxygen to inhibit the electron-hole recombination.

4. Conclusion

The Rx-SMT powders calcined at 550°C had pure anatase phase without other phases, except that pure titania showed pure rutile phase. XRD and FT-IR results showed that the silicon formed segregated amorphous silica and embedded into anatase titania matrix. BET results indicated that specific surface area increased with increasing the ratio of silica to titanium. Embedding silica into titania matrix increases the thermal stability by suppressing the increase of anatase crystallites and makes it possible to calcine the prepared Rx-SMT powders at high temperature without reducing surface area.

The photocatalytic activity of Rx-SMT powders for the degradation of methyl orange increased with increasing the ratio of silica/titanium up to 0.1. The highest photocatalytic activity was obtained at 0.1-SMT and 1.5 times greater than that of Degussa P-25 titania. It can be confirmed that the quantization of particle size and large surface area by embedding silica into anatase titania matrix are beneficial to improve the photocatalytic activity of samples. The optimum ratio of silica to titania was 0.1. The photocatalytic

degradation of methyl orange was affected by calcination temperatures. The rate constant at 550°C was higher than that at other temperature. This may be ascribed to higher specific surface area, small crystallite size, and improvement in the crystallinity of anatase.

Sulfuric acid treatment can enhance photocatalytic activity of SMT powders. The photocatalytic activity of 0.1-SMT after treatment by H₂SO₄ solution was improved 37%. This increase in activity can be ascribed to high acidity. These oxidants such as KIO₄, (NH₄)₂S₂O₈, H₂O₂ enhance the photodegradation of MO.

Conflict of Interests

The authors declare that there is no conflict of interests.

Acknowledgments

The authors would like to thank Zhejiang Provincial Natural Science Foundation of China (no. Y5080232, no. Y4090605) and International Cooperation Funding of the Ministry of Science and Technology (2010DFA92050) and the Foundation of Zhejiang Provincial Top Key discipline of Environmental Engineering (no. 20080213) for financial support.

References

- [1] T. Peng, A. Hasegawa, J. Qiu, and K. Hirao, "Fabrication of titania tubules with high surface area and well-developed mesostructural walls by surfactant-mediated templating method," *Chemistry of Materials*, vol. 15, no. 10, pp. 2011–2016, 2003.
- [2] F. U. Xianzhi, L. A. Clark, Q. Yang, and M. A. Anderson, "Enhanced photocatalytic performance of titania-based binary metal oxides: TiO₂/SiO₂ and TiO₂/ZrO₂," *Environmental Science and Technology*, vol. 30, no. 2, pp. 647–653, 1996.
- [3] A. A. S. Alfaya, Y. Gushikem, and S. C. De Castro, "Highly dispersed phosphate supported in a binary silica-titania matrix: preparation and characterization," *Chemistry of Materials*, vol. 10, no. 3, pp. 909–913, 1998.
- [4] K. Y. Jung and S. B. Park, "Anatase-phase titania: preparation by embedding silica and photocatalytic activity for the decomposition of trichloroethylene," *Journal of Photochemistry and Photobiology A*, vol. 127, no. 1–3, pp. 117–122, 1999.
- [5] D. W. Lee, S. K. Ihm, and K. H. Lee, "Mesostructure control using a titania-coated silica nanosphere framework with extremely high thermal stability," *Chemistry of Materials*, vol. 17, no. 17, pp. 4461–4467, 2005.
- [6] R. Mariscal, M. López-Granados, J. L. G. Fierro, J. L. Sotelo, C. Martos, and R. Van Grieken, "Morphology and surface properties of titania-silica hydrophobic xerogels," *Langmuir*, vol. 16, no. 24, pp. 9460–9467, 2000.
- [7] N. Hüsing, B. Launay, D. Doshi, and G. Kickelbick, "Mesostructured silica-titania mixed oxide thin films," *Chemistry of Materials*, vol. 14, no. 6, pp. 2429–2432, 2002.
- [8] V. Lafond, P. H. Mutin, and A. Vioux, "Control of the texture of titania-silica mixed oxides prepared by nonhydrolytic sol-gel," *Chemistry of Materials*, vol. 16, no. 25, pp. 5380–5386, 2004.

- [9] Z. M. El-Bahy, A. A. Ismail, and R. M. Mohamed, "Enhancement of titania by doping rare earth for photodegradation of organic dye (Direct Blue)," *Journal of Hazardous Materials*, vol. 166, no. 1, pp. 138–143, 2009.
- [10] D. Z. Li, Y. Zheng, X. Z. Fu, and P. Liu, "SO²⁻/TiO₂ catalyst prepared by microwave method and the research of its photocatalytic oxidation activity," *Acta Physico*, vol. 17, no. 3, pp. 270–272, 2001.
- [11] S. Brunauer, P. H. Emmett, and E. Teller, "Adsorption of gases in multimolecular layers," *Journal of the American Chemical Society*, vol. 60, no. 2, pp. 309–319, 1938.
- [12] J. C. Yu, J. Yu, W. Ho, Z. Jiang, and L. Zhang, "Effects of F doping on the photocatalytic activity and microstructures of nanocrystalline TiO₂ powders," *Chemistry of Materials*, vol. 14, no. 9, pp. 3808–3816, 2002.
- [13] J. Lin, Y. Lin, P. Liu, M. J. Meziani, L. F. Allard, and Y. P. Sun, "Hot-fluid annealing for crystalline titanium dioxide nanoparticles in stable suspension," *Journal of the American Chemical Society*, vol. 124, no. 38, pp. 11514–11518, 2002.
- [14] S. Iwamoto, S. Iwamoto, M. Inoue, H. Yoshida, T. Tanaka, and K. Kagawa, "XANES and XPS study of silica-modified titanias prepared by the glycothermal method," *Chemistry of Materials*, vol. 17, no. 3, pp. 650–655, 2005.
- [15] S. R. Yoganarasimhan and C. N. R. Rao, "Mechanism of crystal structure transformations: III. Factors affecting the anatase-rutile transformation," *Transactions of the Faraday Society*, vol. 58, pp. 1579–1589, 1962.
- [16] A. Duran, C. Serna, V. Fornes, and J. M. Fernandez Navarro, "Structural considerations about SiO₂ glasses prepared by sol-gel," *Journal of Non-Crystalline Solids*, vol. 82, no. 1–3, pp. 69–77, 1986.
- [17] D. C. M. Dutoit, M. Schneider, and A. Baiker, "Titania-silica mixed oxides. I. Influence of sol-gel and drying conditions on structural properties," *Journal of Catalysis*, vol. 153, no. 1, pp. 165–176, 1995.
- [18] L. J. Zhao, S. S. Yan, B. Z. Tian, J. L. Zhang, and M. Anpo, *Materials Letters*, vol. 60, pp. 395–399, 2005.
- [19] A. Amlouk, L. El Mir, S. Kraiem, and S. Alaya, "Elaboration and characterization of TiO₂ nanoparticles incorporated in SiO₂ host matrix," *Journal of Physics and Chemistry of Solids*, vol. 67, no. 7, pp. 1464–1468, 2006.
- [20] J. Rubio, J. L. Oteo, M. Villegas, and P. Duran, "Characterization and sintering behaviour of submicrometre titanium dioxide spherical particles obtained by gas-phase hydrolysis of titanium tetrabutoxide," *Journal of Materials Science*, vol. 32, no. 3, pp. 643–652, 1997.
- [21] Z. Zhang, C. C. Wang, R. Zakaria, and J. Y. Ying, "Role of particle size in nanocrystalline TiO₂-based photocatalysts," *Journal of Physical Chemistry B*, vol. 102, no. 52, pp. 10871–10878, 1998.
- [22] C. Anderson and A. J. Bard, "Improved photocatalytic activity and characterization of mixed TiO₂/SiO₂ and TiO₂/Al₂O₃ materials," *Journal of Physical Chemistry B*, vol. 101, no. 14, pp. 2611–2616, 1997.
- [23] E. K. Luo, B. S. Zhu, and J. S. Luo, *Semiconductor Physics*, Electronics Industry Press, Beijing, China, 2003.
- [24] M. M. Rahman, K. M. Krishna, T. Soga, T. Jimbo, and M. Umeno, "Optical properties and X-ray photoelectron spectroscopic study of pure and Pb-doped TiO₂ thin films," *Journal of Physics and Chemistry of Solids*, vol. 60, no. 2, pp. 201–210, 1999.
- [25] C. Kormann, D. W. Bahnemann, and M. R. Hoffmann, "Preparation and characterization of quantum-size titanium dioxide," *Journal of physical chemistry*, vol. 92, no. 18, pp. 5196–5201, 1988.
- [26] J. C. Yu, J. Lin, D. Lo, and S. K. Lam, "Influence of thermal treatment on the adsorption of oxygen and photocatalytic activity of TiO₂," *Langmuir*, vol. 16, no. 18, pp. 7304–7308, 2000.
- [27] Y. T. Kwon, K. Y. Song, W. I. Lee, G. J. Chio, and Y. R. Do, "Photocatalytic behavior of WO₃-loaded TiO₂ in an oxidation reaction," *Journal of Catalysis*, vol. 191, pp. 192–199, 2000.
- [28] E. Evgenidou, K. Fytianos, and I. Poullos, "Semiconductor-sensitized photodegradation of dichlorvos in water using TiO₂ and ZnO as catalysts," *Applied Catalysis B*, vol. 59, no. 1–2, pp. 81–89, 2005.